An Air-Breathing, Portable Thermoelectric Power Generator Based on a Microfabricated Silicon Combustor

by

Christopher Henry Marton

B.A.Sc. Chemical Engineering, University of Waterloo, 2005
M.S. Chemical Engineering Practice, Massachusetts Institute of Technology 2008

Submitted to the Department of Chemical Engineering
in partial fulfillment of the requirements for the degree of

DOCTOR OF PHILOSOPHY IN CHEMICAL ENGINEERING
AT THE
MASSACHUSETTS INSTITUTE OF TECHNOLOGY

FEBRUARY 2011

Signature of Author: _____
Department of Chemical Engineering
October 22, 2010

Certified by: _____
Klavs F. Jensen
Warren K. Lewis Professor of Chemical Engineering
Professor of Materials Science and Engineering
Thesis Supervisor

Accepted by: _____
William M. Deen
Carbon P. Dubbs Professor of Chemical Engineering
Chairman, Committee for Graduate Students

An Air-Breathing, Portable Thermoelectric Power Generator Based on a Microfabricated Silicon Combustor

by

Christopher Henry Marton

Submitted to the Department of Chemical Engineering
on October 22, 2010 in partial fulfillment of the requirements
for the degree of Doctor of Philosophy in Chemical Engineering

ABSTRACT

The global consumer demand for portable electronic devices is increasing. The emphasis on reducing size and weight has put increased pressure on the power density of available power storage and generation options, which have been dominated by batteries. The energy densities of many hydrocarbon fuels exceed those of conventional batteries by several orders of magnitude, and this gap motivates research efforts into alternative portable power generation devices based on hydrocarbon fuels. Combustion-based power generation strategies have the potential to achieve significant advances in the energy density of a generator, and thermoelectric power generation is particularly attractive due to the moderate temperatures which are required.

In this work, a portable-scale thermoelectric power generator was designed, fabricated, and tested. The basis of the system was a mesoscale silicon reactor for the combustion of butane over an alumina-supported platinum catalyst. The system was integrated with commercial bismuth telluride thermoelectric modules to produce 5.8 W of electrical power with a chemical-to-electrical conversion efficiency of 2.5% (based on lower heating value). The energy and power densities of the demonstrated system were 321 Wh/kg and 17 W/kg, respectively. The pressure drop through the system was 258 Pa for a flow of 15 liters per minute of air, and so the parasitic power requirement for air-pressurization was very low. The demonstration represents an order-of-magnitude improvement in portable-scale electrical power from thermoelectrics and hydrocarbon fuels, and a notable increase in the conversion efficiency compared with other published works.

The system was also integrated with thermoelectric-mimicking heat sinks, which imitated the performance of high-heat-flux modules. The combustor provided a heat source of 206 to 362 W to the heat sinks at conditions suitable for a portable, air-breathing TE power generator. The combustor efficiency when integrated with the heat sinks was as high as 76%. Assuming a TE power conversion efficiency of 5%, the design point operation would result in thermoelectric power generation of 14 W, with an overall chemical-to-electrical conversion efficiency of 3.8%.

Thesis Supervisor:	Klavs F. Jensen
Title:	Department Head, Chemical Engineering Warren K. Lewis Professor of Chemical Engineering Professor of Materials Science and Engineering

Acknowledgments

I would first like to thank Prof. Klavs Jensen for his tremendous support throughout my thesis research. During my first meeting with Klavs to discuss the possibility of my joining his research group, I described the type of project I was looking for as one that incorporated both my interest in systems engineering and my core chemical engineering fundamentals, hopefully with an energy application. His responded that he thought he had just the project I was looking for, and he was absolutely right. But it is important to find an advisor whose leadership style suits your personality, and in that way the fit was also ideal. I very much appreciated Klavs's pragmatism, his dedication to rational research, and his tremendous knowledge base, as well as his willingness to give me freedom to maneuver.

I would like to thank my thesis committee of Prof. Paul I. Barton and Prof. William H. Green for their guidance. I would also like to thank Prof. Martin Schmidt and Dr. Hanqing Li for their assistance with the development and trouble-shooting of my silicon microfabrication process. And I am grateful to the staff of Microsystems Technology Laboratories and the Center for Materials Science and Engineering for assistance with fabrication and characterization. Special thanks to Alina Haverty and Christine Preston for all of their help and kindness.

I thank MIT Lincoln Laboratories for funding. Several collaborators from Lincoln Laboratories were instrumental in this work, particularly Dr. George Haldeman, Dr. Todd Mower, Dr. Christopher Vineis (now at Wakonda Technologies), Dr. Robert Reeder, Jon Howell, and Keith Patterson (now at Caltech). I would very much like to thank my collaborators at MIT's Institute for Soldier Nanotechnology, with particular thanks to Walker Chan, Dr. Ivan Celanovic, Dr. Peter Bermel, and Professor John Joannopoulos.

I am deeply indebted to the students and postdoctoral researchers in the Jensen group. Having an informed, collaborative research group to rely on was essential for the accomplishments in this thesis research. Particular thanks go to Jerry Keybl for his seemingly-endless support in the design, set-up, operation, maintenance, and trouble-shooting of my experimental system and to Dr. Nikolay Zaborenko for his guidance in all things silicon.

I am grateful to the David H. Koch School of Chemical Engineering Practice for providing me with exceptional experiences as a student and as a Station Director. I would particularly like to thank my Station Directors, Dr. Robert Fisher and Dr. William Dalzell, for their guidance and encouragement. I owe great thanks to Prof. Alan Hatton for placing his trust in me as a Director, allowing me to represent the Department and guide the development of eight students. I would also like to thank those students (Amrit, Christian, Eric, Jason, Jen, Juhyun, Sashikant, and Vivian) for their hard work and positive attitudes. And I thank Prof. Emeritus Gregory McRae, and the rest of the Morgan Stanley sponsors, for a tremendous opportunity to see the application of chemical engineering in a unique and nontraditional setting.

My achievements at MIT would not have been possible if not for the assistance of the Faculty in the Chemical Engineering Department at the University of Waterloo. I would especially like to thank Prof. Ali Elkamel for his guidance, friendship, and the faith that he had in my capabilities. His impact on my professional development cannot be overstated.

This work would not have been possible, and certainly the journey would not have been worthwhile, if not for my friends. An attempt at complete enumeration would be foolish. However, I would like to thank Dr. Jonathan McMullen for being a great friend, as well as for always being a half-step ahead of me so that he could teach me what I needed to learn to be an effective graduate student. I would also like to thank Kristen Farn for her immeasurable impact on my life, and for being so supportive through the challenges as well as the good times. To all my friends, at MIT and elsewhere, thank you for making life more enjoyable.

And finally, I thank my family for all of their affection and support through this process, and for keeping me grounded. To my Grandparents, Parents, Brother, Sisters, Aunt, Uncle, and Cousins: thank you! From my parents, I learned to work hard and to work until the job is finished. And from my Brother, my first role model, I continue to learn a host of lessons that make me a better person.

I dedicate this thesis to the man who first saw the engineer in me – Henry Skinner.

Table of Contents

List of Tables

List of Figures

1. Introduction

1.1. Motivation

The global consumer demand for portable electronic devices is increasing. Between 2002 and 2006, the global sales of laptop computers increased from 36 million to 72.5 million units[1, 2]. Wireless phone sales experienced a similar increase over the same time period, rising from 600 million units in 2002 to over 1 billion in 2006[1, 3]. The battery source of choice for many popular devices is the lithium-ion battery, and these batteries are produced in the billions of units per year[4].

In order to capture these expanding markets for portable electronic devices, significant efforts have been made to provide more sophisticated devices in increasingly smaller, lighter packages. The emphasis on reducing size and weight has put increased pressure on the power density of available power storage and generation options, which have been dominated by batteries. Consumer demand for longer battery life has emphasized the need for power systems with better energy density than those currently available[5, 6].

The US Army is focused on the development of portable power generators with improved energy density. The reasons for this focus are three-fold: to reduce the burden (weight) carried by a dismounted soldier due to powered equipment, to increase the amount of useful powered equipment that can be carried by a dismounted soldier, and to reduce or eliminate the dependency of soldiers in the field on large-scale electrical power generation (particularly if portable power generation can be driven by a logistics fuel). Clearly, there is a significant consumer and military demand for new portable power generation devices which are superior to batteries.

The focus of this research has been the development of a combustion-based, portable thermoelectric (TE) power generator to provide power in a usable range (5 – 20 W) with as high an energy density as possible. The need for a demonstration of efficient TE devices was described as “urgent in the next 2 – 5 years” by a panel of nanotechnology experts[7].

1.2. Portable Power Generator Metrics and Definitions

There are several metrics that are used to evaluate portable power generators. Two of the most important metrics are the energy density and the power density of the system, where the density can be based on either the system volume or mass. The power density, given in units of (or equivalent to) W/kg or W/L, describes the rate at which energy can be drawn from the system compared to the mass that must be carried, and gives an indication as to what types of loads may be powered from the generator. That is, generators with low power densities may not be suitable for providing large bursts of energy, such as for the rapid acceleration of a vehicle or to provide torque for an electric drill. The power density is calculated as the ratio of the power produced (often peak power) to the mass of the system. Often the term power density is used to describe the flux of power through some active surface, such as an electrode area for fuel cells or a photocell for photovoltaic or thermophotovoltaic power generators. While this form of the term is useful for comparing generators in development, where the complete system has not yet been selected, it does not provide an indication of how much mass must be carried to power a useful device. The term power flux will be used here for this concept to avoid confusion with the mass- or volume-based power density.

The energy density of the system, with units of (or equivalent to) Wh/kg or Wh/L, gives an indication of how much energy is provided for a given amount carried, either system weight or volume. The energy density is calculated as the ratio of the energy provided by the generator from a fuel charge to the total system mass, including the fuel. Provided that the power generator is able to satisfy the necessary demand, the energy density determines how long the load can be satisfied for a given mass or volume to be carried, and is a critical metric for comparison of systems.

For fuel-based power generators, the conversion efficiency is another common metric of comparison. The conversion efficiency, η_c, typically given as a percentage, is calculated according to Equation 1, where the subscript "i" refers to each fuel species, n_i is the flow rate of the species, and LHV is the lower heating value of the species. The LHV is appropriate for combustion-based generators, though in the case of some generator types

(such as PEM fuel cells), the higher heating value of the species may be more appropriate for calculating conversion efficiency. The energy density of the system for "infinite mission duration" approaches the product of conversion efficiency of the generator and the energy density of the fuel. The infinite-mission-duration-limit is a useful metric for remote, stationary power generators such as remote sensor applications. Both the infinite mission limit energy density and the fuel conversion efficiency are useful metrics to compare systems in development, where not all of the system components have been made portable or the end application (and, thus, the "mission duration") has not been identified.

$$\eta_c = \frac{PW}{\sum_i \left(n_i \, LHV_i\right)} \times 100\% \qquad [1]$$

For multi-stage power generation systems, such as combustion-based thermal generators or fuel cell systems which incorporate an on-board reformer to produce hydrogen from a stored fuel, it is often useful to consider the efficiency of an individual system component. This component efficiency is typically determined as the fraction or percentage of the input energy entering the component that is transmitted in the desired path to the next system. For example, in a combustion-based thermoelectric power generator, the combustor efficiency, $\eta_{combustor}$, can be determined according to Equation 2, where Q_{TE} is the rate of heat transfer to the thermoelectric modules and, as before, the denominator represents the total heating value of the fuel. Similar efficiencies are used to evaluate thermoelectric modules, fuel reformers, and other systems.

$$\eta_{combustor} = \frac{Q_{TE}}{\sum_i \left(n_i \, LHV_i\right)} \times 100\% \qquad [2]$$

1.3. Limitations of Electrochemical Cells

Currently, most portable electronic devices use a battery to store energy, and this technology is limited in several respects. Batteries have long recharging procedures and relatively low energy density, as compared with desired performance. And both the cost and environmental impact of batteries are relatively high. These limitations motivate this research effort into alternative portable power devices that are better able to meet the requirements of the future generations of portable electronics.

Secondary cells (rechargeable batteries), such as the currently popular lithium-ion cell, must be connected to an external power source for some time in order to drive the electrochemical reaction used to store electrical energy. This recharge procedure requires access to an energy source (usually on the timescale of minutes to hours), which can be problematic for the consumer (e.g., during lengthy travel) and the dismounted soldier (e.g., while on mission, or at outposts far from base). Primary cells (single-use batteries), such as the predominant alkaline batteries, must be periodically replaced, which poses economic and environmental concerns for the consumer market, and supply chain concerns for the military[6].

The energy density available in current battery technology is limited compared with desired levels. Secondary cells are limited to a few hundred Wh/kg[5, 8-10] (e.g., novel lithium-based cells have been reported to achieve 180[4] – 263[11] Wh/kg). As well, many have suggested that the improvement of energy density in batteries has reached a plateau because the list of attractive materials have been exhausted[12]. The current workhorse battery for the US Army is the BA-5590, which has an energy density of 150 Wh/kg (with a mass of 1 kg), and is a primary cell. Recently, a transition to a secondary cell (BB-2590) with an energy density of 81 Wh/kg (with a mass of 1.4 kg) has been initiated[9]. Typical electrochemical cells provide power at 1 – 4 V[4, 13].

There are a variety of consumer electronics which require power on the order of 1 – 10 W, such as cellular phones, digital camcorders, and toys, and they are powered by batteries with costs on the order of US$10 – 100[14]. In addition, there are military devices which are desired for the US Army with power requirements on the order of 5 – 50 W[15], such as AN/PAS-13 thermal weapon sight that requires 5 W nominal and 8 W peak power, or the ASIR radio that requires 5 W nominal and 18 W during transmission[13]. Given that the energy density available in lithium-ion or lithium-polymer batteries is on the order of 10^2 Wh/kg, and the limits of portability are on the order of a kilogram (though this is an overestimate of what is tolerable for many consumer devices), the “mission duration” of powered electronics from battery power is on the order of 10 h.

Clearly, there would be significant interest in both consumer and military circles for power generators capable of providing significantly longer "missions" with the same mass as a battery, or for the significant reduction of mass for the same duration with near-instantaneous recharging. Such is the promise of hydrocarbon-fueled power generators, given the high energy density stored in liquid fuels, as shown in Figure 1-1. A fuel-based generator with the ability to convert even a few percent of the energy stored in a hydrocarbon fuel would provide a greater energy density than the best lithium-based batteries.

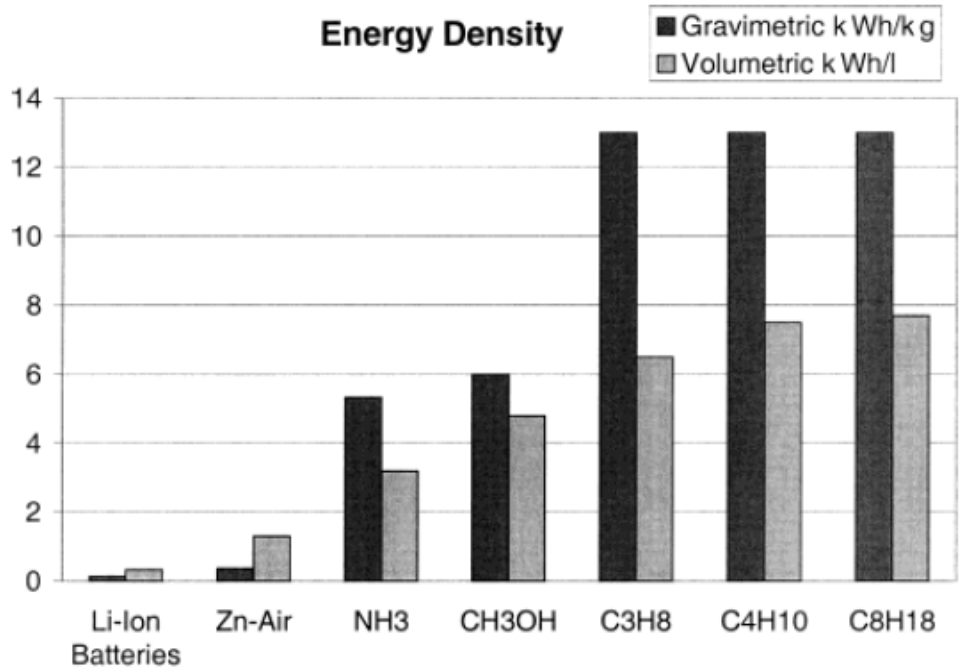

Figure 1-1: Comparison of state-of-the-art batteries with theoretical energy density of fuels in a perfect fuel cell at ambient temperature, in which all the Gibbs free energy of reaction is used to produce power (i.e., HHV). From Mitsos, et al.[16]

1.4. Fuel-based Portable Power Generation Strategies and Demonstrations

There are two main categories of fuel conversion strategies for portable power generation: combustion-based systems and fuel cells. The basis for these methods will be discussed here, along with the advantages and challenges of select methods. This discussion is not intended to be an exhaustive list of possible portable power generation platforms. The focus of this work is on combustion-based systems, and specifically portable thermoelectric power generation; however, a brief comparison with competing technologies is presented.

1.4.1. Combustion-based Power Generation Strategies

Combustion-based portable power generation systems involve direct conversion of the heat released during the combustion of fuel into electrical energy. Three main types of combustion-based systems are described here: thermoelectric (TE) generators, thermophotovoltaic (TPV) generators, and heat engines. Some claim that combustion-based systems have higher potential electrical energy densities than fuel cells[17, 18].

Conventional macroscale power generation is based on homogeneous (flame) combustion. However, as the length scale of the system decreases below a critical reactor dimension, on the order of a few millimeters, it becomes difficult to sustain homogeneous combustion due to increasing radical and thermal quenching at the wall[19]. There has been significant interest in novel design and management strategies that can overcome the thermal and radical quenching at small length scales[20, 21]. The typical approach is to use materials which do not quench radicals (such as quartz or cordierite) and to insulate the combustor walls to allow for temperatures above 1000°C[22, 23]. Other approaches to stabilize flames below the traditional quenching limit have also been developed, such as the use of a porous structure to provide a film of unburned fuel and air as a "sheath" around the flame[24].

However, many authors have concluded that increased stability and fewer materials complications can be obtained using catalytic combustion[25-27]. At small length scales, the attractiveness of catalytic combustion increases as the surface area to volume ratio is large. Catalytic combustion is particularly well suited for TE power generation because of the relatively low temperature[28], which corresponds with the limitations imposed by many current TE materials. Flame temperatures for hydrocarbon combustion in air often exceed 1000°C, whereas commercial BiTe-based TE modules are limited below 350°C[29, 30]. Several works have described a combination of hetero- and homogeneous combustion within small scale combustors; however, the predicted wall temperatures in such arrangements are also typically in excess of 1000°C[26, 31].

1.4.1.1. Thermoelectric Power Generation

Electric current flows around a closed circuit made up of different electrical conductors when the junctions are subject to different temperatures. This effect was first described by Seebeck in 1822 as "the magnetic polarisation of metals and ores produced by a temperature difference"[29]. The Seebeck effect describes the electrical potential difference that can be produced by bridging a hot source (at temperature T_2) and a cold sink (at temperature T_1) with two materials (termed A and B) that have different Seebeck coefficients (S_A and S_B, with S_{AB} being the difference between values of S_A and S_B), according to Equation 3. The linear approximation can be used when the Seebeck coefficients are not strong functions of temperature over the temperature range in question. Thermoelectric (TE) power generation utilizes the Seebeck effect to generate electricity when a temperature difference between two areas (i.e. a hot source and a cold sink) is maintained, and the two areas are bridged by thermoelectric materials.

$$V = \int_{T_1}^{T_2} \left[S_A(T) - S_B(T) \right] dT \approx S_{AB}\left(T_2 - T_1\right) \qquad \textbf{[3]}$$

The potential difference is built due to different charge-carrier (electron and hole) diffusion rates from the hot side of the material to the cold side. In doped materials such as semiconductors, the diffusion of either electrons (for n-type semiconductors) or holes (for p-type semiconductors) from the hot side to the cold side results in an excess of the charge carrier at the cold side. This build-up of charge carriers at the cold side imposes a potential difference that can be used to drive an external load, given the proper electrical connections, as shown in Figure 1-2. As current flows around the electrical circuit shown in the figure, heat is removed from the hot source and released at the cold sink due to a combination of thermal conduction through the TE materials and the Peltier effect (Q_P), which is described in Equation 4. The amount of Peltier heat removed is proportional to the current, I, that flows through the two materials. The result of these combined effects is the ability to directly convert thermal energy to electrical energy, given the appropriate materials. Connected differently (with an applied voltage), similar systems are often used as solid-state coolers or heaters. The principles of thermoelectrics are described with great clarity, and in detail, by Rowe[32], and also discussed by Wood[29].

$$Q_P = S_{AB} I T \qquad [4]$$

Combustion-based TE power generation is an attractive option for portable devices because it offers a direct, passive conversion of heat to electricity that is quiet and generates only CO_2 and water. A TE power generation system consists of a constant heat source such as a combustor, a cold region connected to either a passive or active cooling system (e.g., a forced or free convection-cooled fin), and the appropriate TE materials connecting the two temperature zones. Given these parts, the peripheral systems required to operate a TE power generator are quite simple, compared with other portable power generation options. TE power generators are also desirable due to the high power fluxes that can be achieved (e.g., Venkatasubramanian, et al.[33], have estimated the power density (flux) of their thin-film TE material at 700 W/cm^2). For the most part, the development of TE power generators has been limited by the conversion efficiency of the available TE materials. Recently, however, cascaded BiTe-based thermoelectrics have been demonstrated at 8% conversion efficiency for a temperature difference of ~400°C[34].

The theoretical maximum energy conversion efficiency, η_{max}, of a TE power generation system, operating between a hot source at temperature T_H and a cold sink operating at temperature T_C, is given in Equation 5, where T is the average temperature between T_H and T_C[29]. In this equation, the Carnot efficiency is modified by the dimensionless figure of merit, ZT, which is a material-specific performance metric for thermoelectrics. The figure of merit can be calculated from the Seebeck coefficient, the electrical conductivity (σ), the electronic contribution to the thermal conductivity (κ_e), and the lattice contribution to the thermal conductivity (κ_L) according to Equation 6. The efficiency of a TE system increases as ZT increases, approaching Carnot efficiency as ZT gets large. In metals, the electronic contribution tends to dominate, whereas in semiconductor materials, the lattice contribution typically dominates. Though high compared to current demonstrations, a material with a ZT value of 2 could reach conversion efficiency as high as 19.5% between a heat source at 700K and a cold sink at 298K.

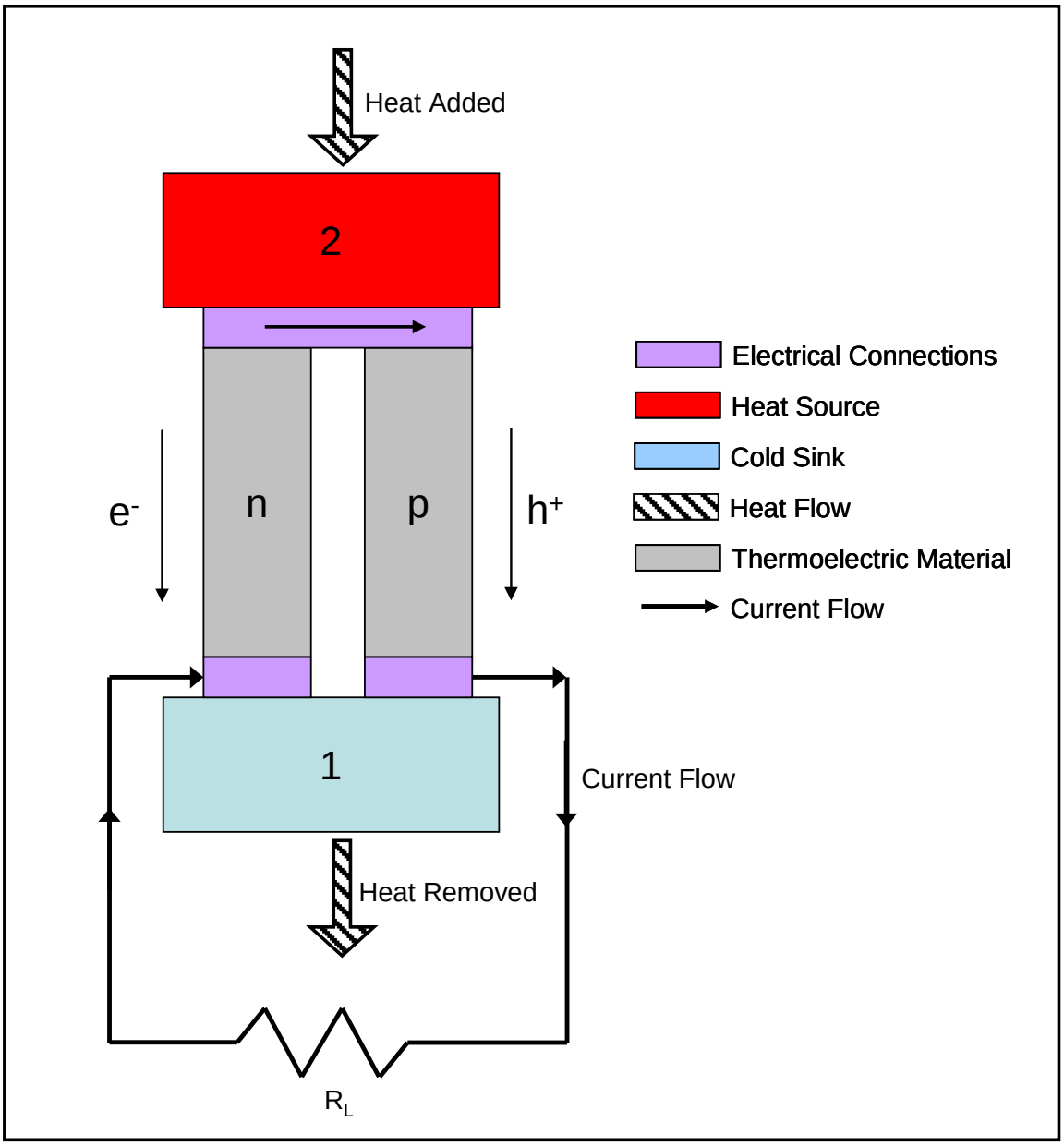

Figure 1-2: Conceptual diagram of a two-junction thermoelectric power generator. The hot source (2) and the cold sink (1) are bridged by n- and p-type semiconductor materials. An electrical circuit is connected along the black lines, such that current flows from the interface of the p-type material and the cold sink, through the load (R_L) to the interface of the cold sink and the n-type material, through the n-type material to the hot source, through to the p-type material completing the circuit. The hot and cold materials are electrically insulated.

$$\eta_{\max} = \left(\frac{T_H - T_C}{T_H} \right) \frac{\sqrt{1+ZT} - 1}{\sqrt{1+ZT} + T_C / T_H} \qquad [5]$$

$$ZT = \frac{S_{AB}^2 \sigma}{\kappa_e + \kappa_L} \left(\frac{T_H + T_C}{2} \right) \qquad [6]$$

Bulk TE materials with a ZT of 0.75 at 300K were identified in 1958; however, the progress in ZT for bulk materials since then has been modest[33, 35]. Conventional TE materials are bulk solid solution alloys such as Bi_2Te_3, Bi_2Se_3, and Sb_2Te_3, with the best materials having room temperature ZT values of approximately 1.0[36]. The approximate relation of Seebeck coefficient, electrical conductivity, and thermal conductivity with the concentration of charge-carriers is shown in Figure 1-3 to illustrate the competitive nature of these factors, leading to a maximum in ZT that can be achieved by adjusting the bulk material properties alone.

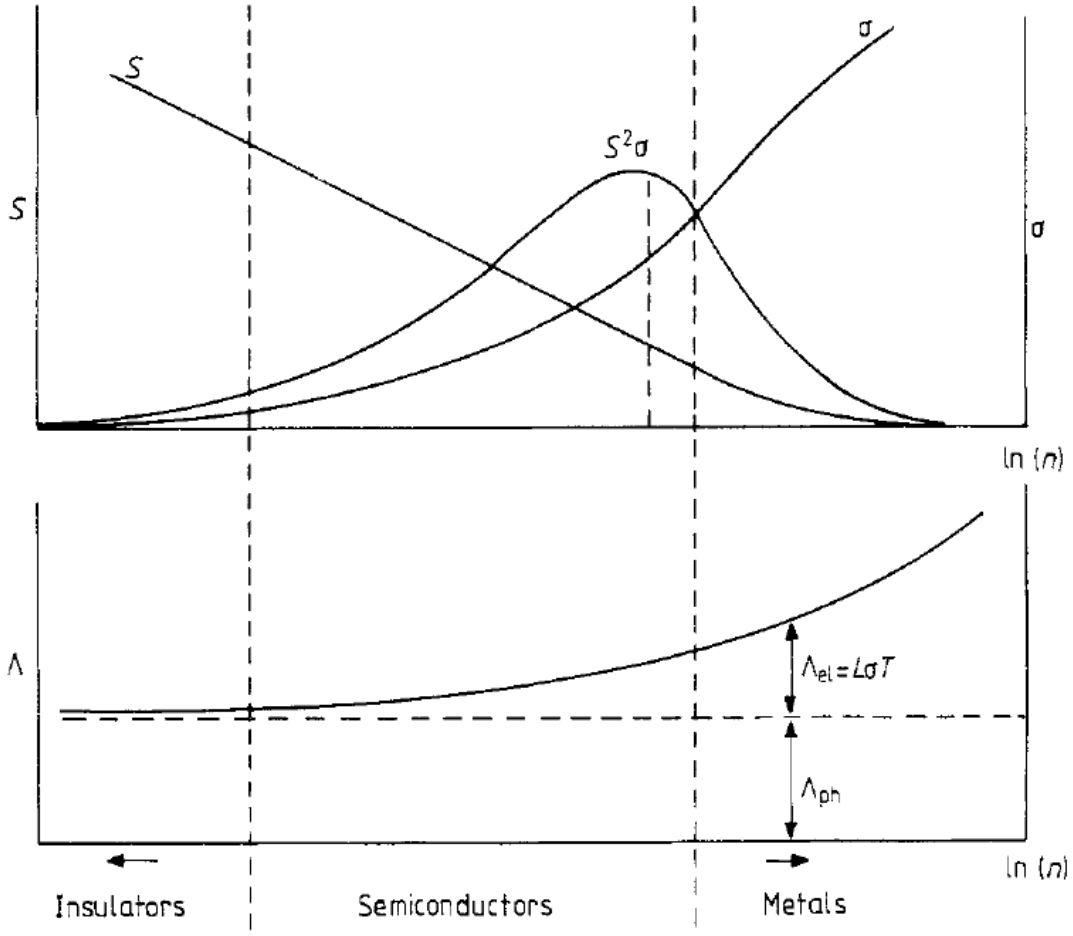

Figure 1-3: Dependence of Seebeck coefficient (S), electrical conductivity (σ), and thermal conductivity on the charge carrier concentration (n). The figure of merit (Z), which is determined from the ratio of the power factor ($S^2\sigma$) to the total thermal conductivity (Λ), exhibits a maximum. From Wood[29].

Recent efforts to improve the figure of merit for TE materials have focused on reducing the lattice thermal conductivity through nanostructuring[36, 37] or increasing the power factor ($S_{AB}^2\sigma$) through quantum filtering or lattice confinement[35]. A recent review of

nanostructured thermoelectrics has been prepared by Pichanusakorn[38]. Nanodot superlattices (NDSLs), comprised of periodic PbSe nanodots in a PbTe matrix, have been reported to reduce the lattice thermal conductivity of PbTe from ~2W/mK to ~0.4W/mK as a result of phonon scattering due to an acoustic mismatch. Compared with bulk PbTe, it was reported that the NDSL materials exhibit a decrease in electrical conductivity of only ~30%, and no significant change to the Seebeck coefficient, which implied a significant improvement in ZT for the NDSL[37]. However, more recent work has shown that the thermal conductivity of these materials is >0.85 W/mK, and that the ZT value of the materials represent only a 30% increase over optimized n-type PbTe at 300K[39]. The Kanatzidis group at Northwestern has focused on improvements to thermoelectric performance through bulk properties, such as La/Ag cosubstitution in PbTe[40] yielding a ZT of ~0.8 at 500K and ~1.2 at 720K. At 500K, the thermal conductivity of these cosubstituted materials is ~1.5 – 2 W/mK, which indicates that the heat flux through these materials would be increased compared to that of the NDSL materials or commercial BiTe materials (~1.15 W/mK).

A limitation of TE power generation systems is the low operating temperature for which TE materials are mechanically stable. The typical BiTe-based materials are limited to a maximum temperature of approximately 600K[29]. It is difficult to design a heat source operating at this temperature using a hydrocarbon fuel, and there are several examples in the literature of unsuccessful attempts at achieving a stable temperature that is suitably low for TE power generation (e.g., [30, 41]). The heat source for a TE power generation device should generate a high heat flux at a low temperature (for catalytic combustion of hydrocarbons) while minimizing heat loss to the surroundings. The design of such a heat source poses a significant engineering challenge.

The general layout of a TE power generation system is shown in Figure 1-4. At the center of the system is a combustor used to generate heat from the combustion of a hydrocarbon fuel. The top and bottom surfaces of the combustor are covered by the TE materials, which are placed into junction assemblies (also shown in the figure) with copper thermal concentrators and diffusors. Each pair of TE elements (one n-type

material, one p-type material) is connected thermally in parallel and electrically in series. The elements are connected electrically in series because the typical voltage gain over a given pair is low, and so the addition of pairs in series provides a usable system voltage.

The TE elements are also connected to a heat sink, which may be actively or passively cooled. Because of this layout, and the fixed footprint of each junction assembly, the number of TE junction assemblies in the system determines the minimum surface area that must be heated by the combustor. The typical geometry for a combustor used with TE elements is that of a thin box, with the TE junctions placed on one or both of the large sides, and the thickness minimized to reduce heat losses to the environment through the faces not in contact with the TE materials. Given that the elements are distributed across the surface of the heat source, the maximum temperature is limited due to material properties, and the power generation increases as the temperature difference across the element increases, it is desirable to have the heat source temperature be uniform and as close to the maximum limit as possible to achieve the highest power production.

There are many examples of micro- and mesoscale thermoelectric power generators powered by catalytic combustion in the literature. Cohen, et al., patented an integrated TE device based on a ceramic "Swiss-roll" structure, with the TE elements positioned between the hot exhaust stream and the cold inlet stream[18]. Vican, et al., also developed a TE power generation system based on an alumina ceramic "Swiss-roll" using a stereolithography process; however, the maximum power output reported from this system was 52 mW from a hydrogen input of 9.1 W-equivalent (0.57% efficiency). A TE generator fabricated from silicon bonded to glass was developed by Yoshida, et al., but the high heat loss from the device prevented the autothermal combustion of butane[41]. The device was able to produce 184 mW of electrical power with an efficiency of 2.8% using hydrogen.

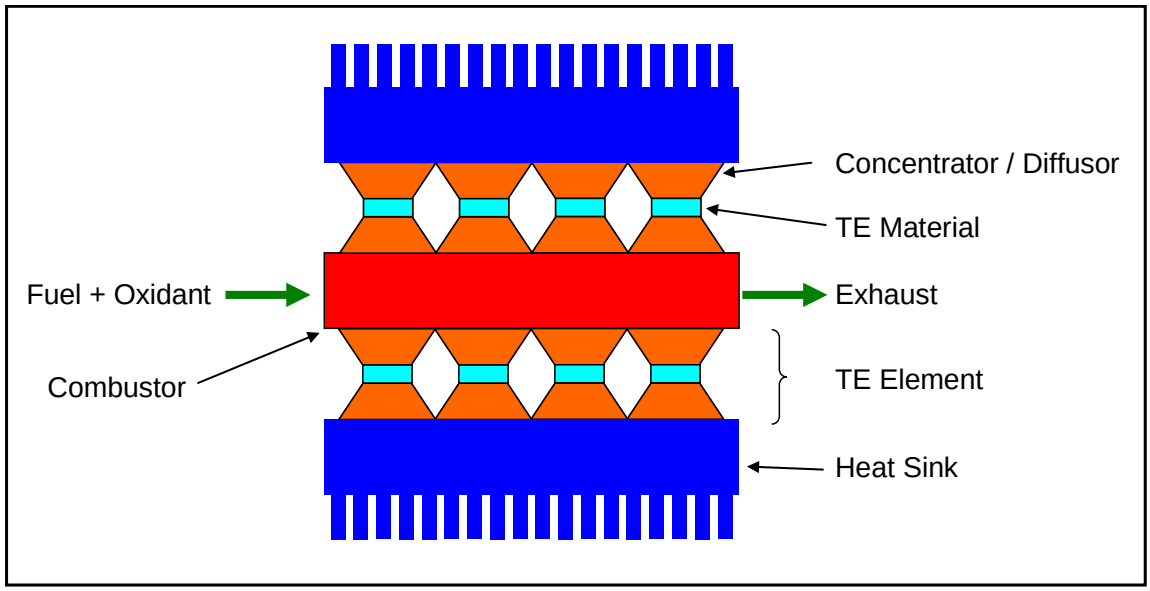

Figure 1-4: General structure of TE power generator.

The most significant recent efforts directed towards the design and understanding of an integrated combustor-TE power generator have come from the Vlachos group at the University of Delaware. Their stainless steel combustor has been used to combust hydrogen, propane[30, 42, 43], and methanol[44]. The combustor was integrated with a commercial BiTe-based TE device from Hi-Z Technology, Inc. The group has reported the production of 1 W maximum power and a thermal-to-electrical conversion efficiency of 1.08% with hydrogen as the fuel, with energy and power densities of 67 Wh/kg and 5 W/kg, respectively. The group has also reported the generation of 0.45 W electrical power with propane as the fuel at 0.66% conversion efficiency. The group reported 0.65 W power generated from methanol combustion, and claim that the 1.1% conversion efficiency is the highest reported for TE power generation using a liquid fuel. The demonstration of a fuel-based TE generator suitable for portable power with energy density comparable to that of a battery remains an open challenge.

1.4.1.2. Thermophotovoltaic Power Generation

Thermophotovoltaic (TPV) generators convert radiation energy emitted by material at an elevated temperature (heated by the combustion of fuel, in this case) to electricity using a low-bandgap photocell. These devices have been researched since low-bandgap photocell materials became available in the late 1980s. Typical photocell materials include GaSb (with a bandgap of 0.72 eV) and GaInAsSb (0.53 eV). Heated materials

emit photons with energy larger than the bandgap of the photocell, and can evoke free electrons and produce electrical energy under the action of a PN junction. However, most systems emit the majority of thermal photons with energy less than the bandgap of the TPV cell, which greatly reduces the conversion efficiency. The idea of spectral shaping has been proposed as a way to suppress undesirable photons and enhance the emission of photons with energy higher than the bandgap[45, 46].

TPV portable power generation involves the combustion of a fuel (either through homogeneous or catalytic combustion) within a device made from a material (or coated with a material) with a high emissivity in the desired wavelength (such as Co-doped MgO or photonic crystals). Typically, the desire is to obtain the highest possible temperature, as the energy radiated scales with temperature to the fourth power. The combustor is placed in proximity to the photocell, which must be either passively or actively cooled. A suitable arrangement of a TPV system is shown in Figure 1-5.

There are three significant efforts towards a portable-scale, fuel-based TPV generator in the literature. The first is a previous effort in the Jensen group by Nielsen, et al.[47], based on the SμRE I microcombustors. In this work, 1 mW of electrical power was produced from the catalytic combustion of propane in air, with a conversion efficiency of 0.08%. The second is from National University of Singapore, where homogeneous hydrogen combustion in a SiC tube was used to generate 810 mW at a conversion efficiency of 0.66%[48-51].

Working with collaborators at MIT's Institute for Soldier Nanotechnology, we have developed a propane-combustion-based TPV system for portable-scale power generation. The system is based on the SμRE IV microcombustors designed by Blackwell[52], with 1-D photonic crystals used to shape the spectral emission, as described elsewhere[46]. The system has generated 220 mW of electrical power with 2.2% chemical-to-electrical conversion efficiency, based on the LHV of the propane fuel. This work represents a major step towards an attractive fuel-based power generator. However, several technical

challenges remain, such as the reduction of the system pressure drop and the improved packaging to enable vacuum packaging.

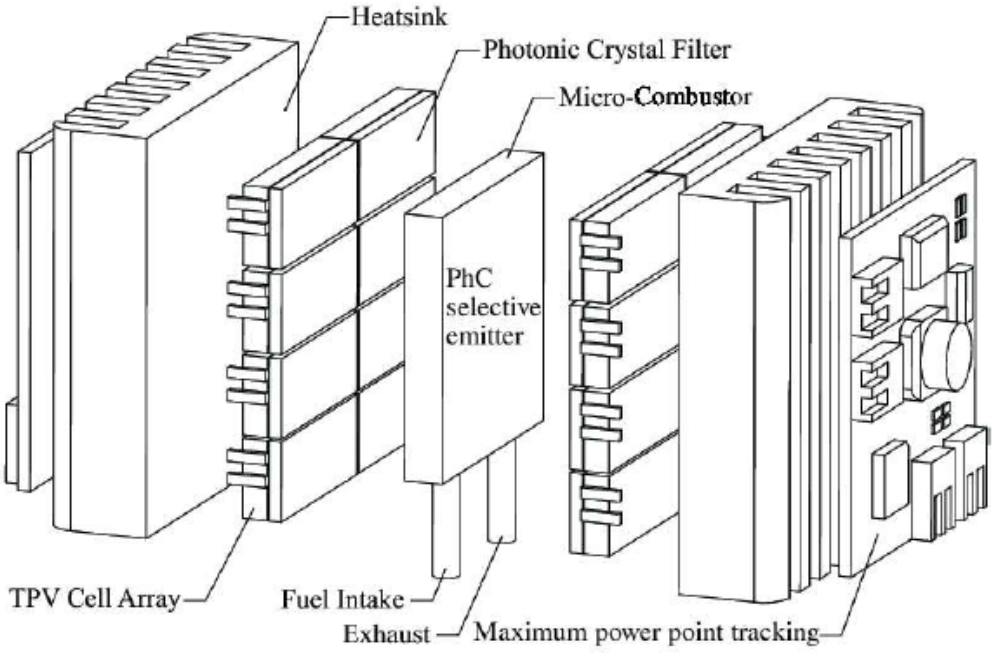

Figure 1-5: Arrangement of a high-efficiency TPV system developed at MIT. The silicon microcombustor serves as a heat source, with spectral shaping provided by photonic crystals. The TPV cells are mounted on heat sinks in close proximity to the combustor. From Bermel, et al.[46]

1.4.1.3. Heat Engines

There have been a number of attempts to develop microscale heat engines to generate portable power, with the most notable being the MIT MEMS micro gas turbine and the "P3" external combustion engine from Washington State University[53]. More detailed reviews of microengines are provided by Jacobson and Epstein[54], Fernandez-Pello[55], and Chia, et al.[51] The MIT project has been in development for some time, with the intention of producing a 10 g device capable of 10 – 50 W power generation from 7 g/h of jet fuel (JP-8)[56]. The general layout of the micro gas turbine, made from stacked silicon wafers, is shown in Figure 1-6. To date, significant advancements have been demonstrated in the construction of various system components, but the generation of electrical power has not yet been demonstrated[53]. The P3 system is based on an external heat engine[57] and a flexible membrane[58]. The heat supplied from the external combustor (which is a "Swiss-roll" system) is used to expand a saturated fluid, which expands the membrane. The schematic of the system timing, based on a thermal switch which controls the heat transfer into and out of the system, is shown in Figure 1-7. The system has been

demonstrated to provide 2.5 mW of mechanical power, with a 0.2% chemical-to-mechanical conversion efficiency. A piezoelectric generator has been coupled to the system to demonstrate 0.8 μW of electrical power[59].

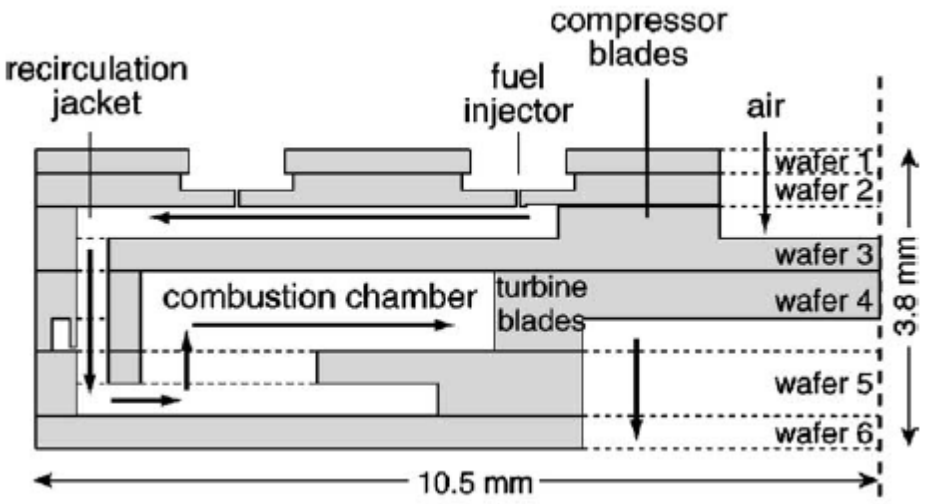

Figure 1-6: Schematic of cross-section of MIT MEMS micro gas turbine. From Spadaccini, et al.[60]

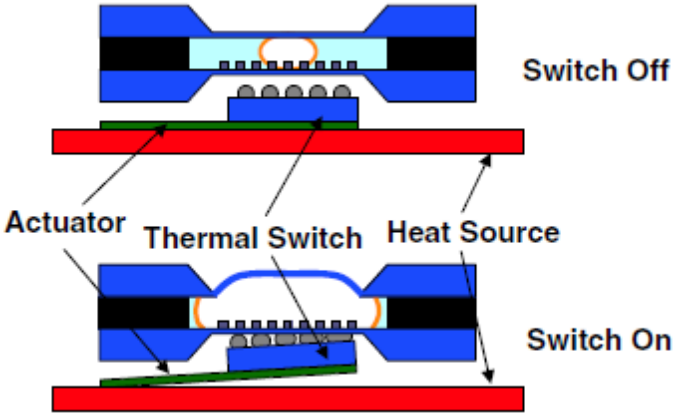

Figure 1-7: Schematic of micro heat engine with thermal switch. From Cho, et al.[58]

1.4.2. Fuel Cell Power Generation Strategies

There are several different types of fuel cell systems for power generation using different fuels and materials. The general principle behind fuel cell power generation is the use of coupled reduction-oxidation reactions to generate free electrons that can be used to drive a load. The general construction of a fuel cell is an electrolyte sandwiched between a porous anode and a porous cathode. The fuel reacts at the anode-electrolyte interface, and the oxidizer (oxygen) reacts at the cathode-electrolyte interface. The electrode allows ions to pass between the anode and cathode but prevents the passage of electrons, which instead are forced out of the cell to power the load. Some of the different fuel cell

systems that can be used for portable power generation are introduced here; however, there are several reviews[6, 9, 61, 62] and texts[53] which provide a more detailed treatment.

1.4.2.1. Hydrogen-Fueled Proton Exchange Membrane Fuel Cells

Proton exchange membrane (PEM) fuel cells typically involve the reaction of hydrogen and oxygen to form water. The half-cell reactions are given in Equation 7.

$$\begin{aligned} &Anode: \quad H_2 \rightarrow 2H^+ + 2e^- \\ &Cathode: \; O_2 + 4H^+ + 4e^- \rightarrow 2H_2O \end{aligned} \qquad [7]$$

Typical PEM fuel cells use platinum or platinum/ruthenium electrocatalysts and a Nafion polymer electrolyte membrane, and the operating temperature is usually between 60 and 120°C. The relatively low operating temperature is an advantage for system dynamics, safety, and thermal efficiency; however, the low temperature necessitates the current electrocatalyst material, which dominates system cost (~50%) and limits the potential for widespread application[7].

There has been considerable development towards hydrogen-fed micro-fuel cells for portable power applications[6]. A review of the field by Kundu, et al.[9], summarizes the results from nine different proposed systems, particularly for small (<10 cm^3) systems. The reported maximum power flux of these small systems was in the range 30 – 120 mW/cm^2 using air (as opposed to pure oxygen) at the anode. The review by Cowey, et al.[6], describes ongoing commercial and military efforts to design PEM fuel cells for portable systems in the 1-100 W range. In 2005, the Nippon Telegraph and Telephone Corporation demonstrated a PEM fuel cell mounted in a cellular phone which was able to power phone start-up and a video call[63], though performance details were not reported. Typical hydrogen PEM fuel cells operate between 40-60% conversion efficiency[10, 52], and systems operating with energy densities greater than 500 Wh/kg have been reported[8].

The main challenge for portable PEM fuel cells is the safe storage of hydrogen and its impact on the energy density of the system[64]. Due to the low volumetric energy density of hydrogen gas at atmospheric pressure, hydrogen must be compressed significantly to achieve an acceptable volumetric energy density for the system. However, in order to

safely store hydrogen at such elevated pressures, and given the explosion hazard presented by hydrogen leaks, thick metal tanks are required to store the hydrogen, increasing system weight and severely limiting energy density. This storage issue serves to motivate much research into on-line hydrogen generation to couple with PEM fuel cells. Another significant challenge to PEM fuel cells is the sensitivity to contaminants including CO, CO_2, H_2S, NH_3, NO_x, SO_x, Fe^{3+} and Cu^{2+} [65]. Significant efforts are ongoing to attempt to reduce the sensitivity to these species, particularly CO.

1.4.2.2. Reformed Hydrogen Fuel Cells

The high available conversion efficiency, power density and moderate operating conditions (temperature, pressure) of PEM fuel cells offer significant motivation to investigate portable power systems involving PEM fuel cells without stored hydrogen[66]. There are a multitude of ongoing research efforts related to the on-line generation of hydrogen for use in a PEM fuel cell, either from metal hydrides or reformed hydrocarbons. The systems designed through these efforts have been termed reformed hydrogen fuel cells (RHFC). A review of different hydrogen production systems for portable fuel cells has been prepared by Holladay, et al.[64], and a review of reformers for biomass-derived fuels is presented by Xuan, et al.[67]

There are literature examples of hydrogen generation systems operating from 0.01 – 300 W-equivalents aimed towards portable power generation via RHFC. For systems intended to generate power on the order of 200 W or less, methanol was the most common fuel. This was likely due to the ability to achieve nearly complete conversion of methanol at moderate temperatures (200 – 400°C), and the low impurity levels of PEM fuel cell-poisoning species such as (H_2S) compared with blends like jet and diesel fuel[68].

Several groups have demonstrated systems capable of converting methanol or other hydrocarbons to hydrogen at moderate temperatures[8, 10, 68-76]. Although some systems have integrated catalytic burners with the reformer, for the most part this reforming has been performed using a local electrical heat source, or with the device placed in a hot environment such as a furnace. Many systems with integrated burners have suffered from low thermal efficiencies due to heat loss, and the heat loss to fluidic connections

remains a significant difficulty for small reactors. The system developed by Kwon, et al., for the autothermal operation of a methanol steam reformer lost ~80% of combustion heat generated to the surroundings[72]. Arana, et al., were able to develop a thermally isolated reformer through the use of thin-walled silicon nitride tubes[76]. Work by Keui-Sung, et al., used trench-refilled silicon dioxide to thermally isolate the catalytic combustor from the external environment in an integrated combustor and methanol steam reformer to achieve good thermal efficiency[73]. However, the device was only able to convert 1% of methanol due to temperature gradients in the combustor and uneven catalyst distribution in the reformer. Moreno, et al, have developed a self-thermally-isolated methanol reformer for the autothermal production of hydrogen, with low cost and low resistance to flow, using a compression-sealed cordierite monolith[71, 77]. The system, which utilizes the catalytic combustion of methanol to provide heat for steam reforming, has been demonstrated to provide >70% hydrogen yields while maintaining a large gradient between the reaction zone (400°C) and the external packaging temperature (50°C). A 25W RHFC commercial system has been developed commercially by Ultracell Power, with a system weight of 1.27kg. A methanol-based RHFC has been demonstrated in a silicon MEMS with an energy density of 225 Wh/kg from 0.24 W-equivalent heating value of hydrogen produced[78].

One of the impediments to connecting the product stream from the previously demonstrated reformers to a PEM fuel cell for portable power generation is the high levels of membrane- and catalyst-poisoning species - particularly CO - present in the gas stream. The level of CO in reformed methanol gas streams in the literature is on the order of 103 ppm, and must be reduced to ~10 ppm for current PEM fuel cells. Traditionally, two methods have been used to obtain a hydrogen stream suitable to feed to a PEM fuel cell: reactive conversion of CO (to CO_2 or CH_4), or membrane separation of hydrogen. Reactive conversion can still lead to problems, as CO_2 can be converted back to CO by the reverse water-gas shift reaction at the PEM fuel cell anode. Reactive conversion to CO2 has been incorporated after a reformer by Kim and Kwon[78]. Palladium membranes have been used successfully to separate hydrogen from other gases[69, 74].

1.4.2.3. Direct Alcohol and Acid Fuel Cells

Direct alcohol fuel cells, such as direct methanol fuel cells (DMFC), operate with an alcohol fed directly to the anode (with water). For methanol fuel, the reaction is as shown in Equation 8. DMFC have been used in several efforts to produce a portable power device[6].

$$\begin{aligned} &Anode: \quad CH_3OH + H_2O \rightarrow CO_2 + 6H^+ + 6e^- \\ &Cathode: \; O_2 + 4H^+ + 4e^- \rightarrow 2H_2O \end{aligned} \qquad [8]$$

DMFC compare favorably with PEM fuel cells in that they can operate directly using a fuel with a moderately high energy density (both mass- and volume-based). As well, they do not require an integrated reformer system, which greatly simplifies the balance of plant required for operation. Significant research efforts have been directed towards the development of DMFC-based portable devices.

Several companies, including Fujitsu, Hitachi, LG, NEC, Samsung, Sanyo, and Toshiba have developed prototypes of portable electronic devices powered by DMFC[9, 52]. A review of DMFC development and remaining challenges by Kamarudin, et al.[79], describes many different approaches to the design of DMFC and identifies several works that have achieved maximum power fluxes on the order of 50 mW/cm^2. DMFC conversion efficiency can reach 41%[6].

DMFC have been limited by several issues, including low power flux (compared with hydrogen-fed PEM fuel cells), required fuel dilution with water, and methanol cross-over. The power fluxes available from the methanol oxidation at the anode is approximately 10% of the equivalent hydrogen-fed PEM fuel cell[79] due to slower kinetics[6] and mass transfer issues[9] (such as the build up of CO_2 bubbles at the anode and formation of water droplets at the cathode). Due to material compatibility issues, methanol must be diluted with water, and typically this is done prior to storage (though in-situ dilution strategies are being investigated). Typical methanol concentrations have been limited less than 10 M, which greatly reduces the energy density of the stored fuel. According to Kamarudin, et al.[61], methanol cross-over (the transport of methanol from the anode to the cathode through the electrolyte membrane) has been the most important fundamental problem for

DMFC. Methanol cross-over generates waste heat at the cathode and leads to drastically reduced cathode voltage.

Direct formic acid fuel cells (DFAFC) have also been investigated as potential portable power sources. Formic acid has several advantages compared to methanol, given that it is non-flammable at room temperature and is sufficiently benign to be used as a food additive at lower concentrations. However, the energy density of formic acid (1870 Wh/L) is less than half that of methanol and about an order of magnitude less than other hydrocarbon fuels. The power flux which can be generated in a DFAFC (255 mW/cm^2) is considerably higher than that of a DMFC (~50 mW/cm^2) and is similar to that of a hydrogen PEM fuel cell (~320 mW/cm^2)[80]. A miniaturized DFAFC power generator system has been developed at UIUC, and it provides 70 Wh/L from a 1.3 mL system[81]. Also at UIUC, a laminar flow-based membraneless DFAFC has been developed[82], though these devices have produced a power flux of 55 W/cm^2. However, the flowing electrolyte design requires that the electrolyte must also be stored "on-board", and given the ratios considered, 1:1 to 8:1 electrolyte to fuel flow, this significantly reduces the energy density of the system. A larger DFAFC power generator was developed by Miesse, et al., which is capable of generating 13.7 W from a 1440 mL system, with an energy density of ~20 Wh/kg[83].

1.4.2.4. Micro-Solid Oxide Fuel Cells

There is considerable interest in microscale solid oxide fuel cells, though to date these have been limited by thermal management issues[53]. The system must operate at high temperatures in order to raise the performance of the ceramic oxygen conductor to the necessary level. The microfabrication of the membranes[62, 84] and other system components[85] are currently being studied. A system demonstration was made by Shao, et al., in which 350 mW was generated with at 1% efficiency from propane with a system volume less than 2.25 mL[86].

1.5. Thesis Objectives and Outline

The usefulness of portable electronic devices is limited by the current state of portable power generation. Batteries have low energy densities, high recharging times, and high environmental impact. The large energy densities of common hydrocarbon fuels and the

possibility of instantaneous recharging has motivated significant research efforts to develop a small power generator which can produce usable power while surpassing the energy density of a battery. While major advancements have been made in a number of power generation strategies, none have progressed to the point where they form the basis for demonstrated systems which significantly exceed the performance of batteries.

The focus of this thesis research was to develop a combustion system which could be used to demonstrate the performance of novel thermoelectric modules. The goal of these demonstrations was to produce a usable amount of power (5 – 20 W) with an energy density significantly superior to that of conventional batteries. The combustor was intended to operate using a hydrocarbon fuel, in order to capitalize on the high energy density and to allow for the instantaneous refueling (even when "off-grid"). The system was also intended to be "air-breathing" (i.e., to use ambient air as an oxidant) to further improve the "off-grid" appeal of the generator. The combustor was intended to accommodate thin-film TE materials (<1 mm), which require a large heat flux from the combustor surface.

The structure of the remaining thesis chapters is as follows: the concepts critical to the design of a small-scale combustor, as well as literature examples of some common approaches in this design, are discussed in chapter 2. The design of the mesoscale combustor for TE power generation is discussed in chapter 3. The silicon microfabrication used to produce the combustor is presented in chapter 4, and the packaging of the combustor (such as catalyst loading, and system integration) is presented in chapter 5. The testing of the combustor with a specially designed heat sink to investigate performance with a high-heat flux is discussed in chapter 6, and the testing of the combustor using commercial TE modules is discussed in chapter 7. Finally, some concluding remarks, along with recommendations for system improvements, are presented in chapter 8.

2. Design Concepts for Catalytic-Combustion-Based Power Generators

In the design of a micro- or mesoscale catalytic combustor for integration into a power generation system, many aspects of the system must be considered. Proper thermal management, which is the careful comparison of all heat transfer pathways between the system and the surroundings, and an understanding of all the energy inputs to, and outputs from, the system are essential to the successful design of a small-scale, high-temperature autothermal system. Given the large ratio of surface area to volume that is characteristic of small devices, it can be difficult to limit the amount of heat lost to the environment, which scales with the external surface area, as compared with the heat generated, which scales with the internal volume, without the use of complicated structures[55]. Further complicating matters are the needs to achieve sufficient mechanical robustness to allow for use as a portable (consumer or military) device and to limit the pressure drop through the system to enable the use of ambient air as an oxidant. In this chapter, some of the critical concepts for the design of a catalytic combustor for power generation will be discussed. Some of the prominent designs from the literature will be examined to exemplify these concepts.

2.1. Heat Transfer Pathways and Energy Inputs

2.1.1. Conductive Heat Transfer

Any material which bridges two areas with different temperatures will conduct a flow of heat in proportion to the temperature gradient, as described by Fourier's law in Equation 9, simplified for one-dimensional Cartesian heat conduction in the right-most form. In this equation, $Q_{conduction}$ is the heat transferred by conduction, k is the thermal conductivity of the material, A is the area for conduction, T is the temperature, and x is the distance variable in the direction of heat transfer. A linear approximation is often useful, as given in Equation 10, for conduction between hot and cold regions (subscripts H and C, respectively) over a distance L.

$$Q_{condustion} = -k\,A\nabla T \quad \left[= -k\,A\frac{dT}{dx}\,in\,1-D \right] \qquad [9]$$

$$Q_{condustion} \cong -k\,A\frac{T_H - T_C}{L} \qquad \textbf{[10]}$$

Conductive heat transfer plays a role in several aspects of small-scale combustion systems. The fluidic connections, which transport reactants to (and in many cases, from) the combustor, bridge a sizable temperature difference (on the order of several hundred degrees Kelvin) between the high-temperature combustor and the ambient-temperature external system (such as the fuel tank). Depending on the cross-sectional area, the conductivity of the material, and the length scale over which the temperature difference is bridged, the conductive heat transfer from the combustor through the fluidic conduits can be very large[52]. Conductive heat transfer is also important within the combustor to distribute heat from regions of high reactivity (and thus, high rates of heat release) to regions of lower reactivity. In the special case of thermoelectric power generation, conductive heat transfer through the TE materials should be the dominant pathway of heat removal from the system.

In designing a high-temperature system with significant conductive heat transfer, such as a thermoelectric generator, it is likely to be important to consider the temperature dependence of the thermal conductivity of the materials. The thermal conductivity of silicon decreases significantly as the temperature increases above room temperature, as shown in Figure 2-1[87]. The thermal conductivity of some other materials increases as the temperature increases above room temperature, such as with high alloy steels (like 316 stainless steel used as tubing in this work), as shown in Figure 2-2. The temperature dependence can be extremely important, for example, when considering a "high conductivity" material such as silicon compared with stainless steel for use at 900°C, where both have similar thermal conductivities (~30 W/mK).

2.1.2. Convective Heat Transfer

A surface which is in contact with a fluid at a different temperature will experience convective heat transfer due to circulation of the fluid. This heat transfer can be described by Newton's law of cooling, given as Equation 11. In this equation, h is the convective heat transfer coefficient (1 – 20 W/m^{2}K for natural convection, higher for

forced convection), A is the heat transfer area, T_s is the surface temperature and T_∞ is the ambient fluid temperature, and the heat transfer is defined from the surface to the fluid.

$$Q_{convection} = h A \Delta T \quad = h A (T_s - T_\infty) \qquad \textbf{[11]}$$

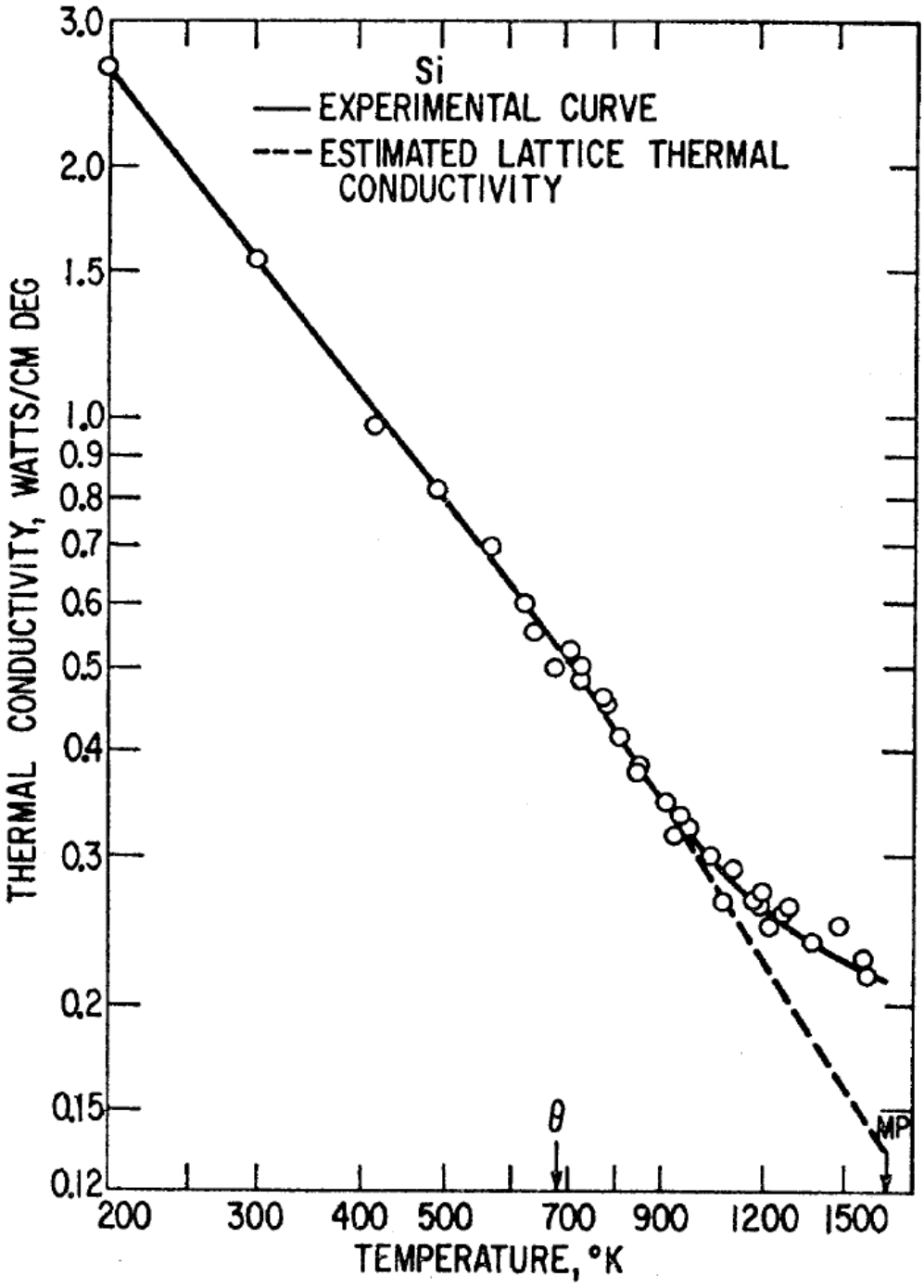

Figure 2-1: Temperature dependence in the region of interest of the thermal conductivity of silicon. From Glassbrenner and Slack.[87]

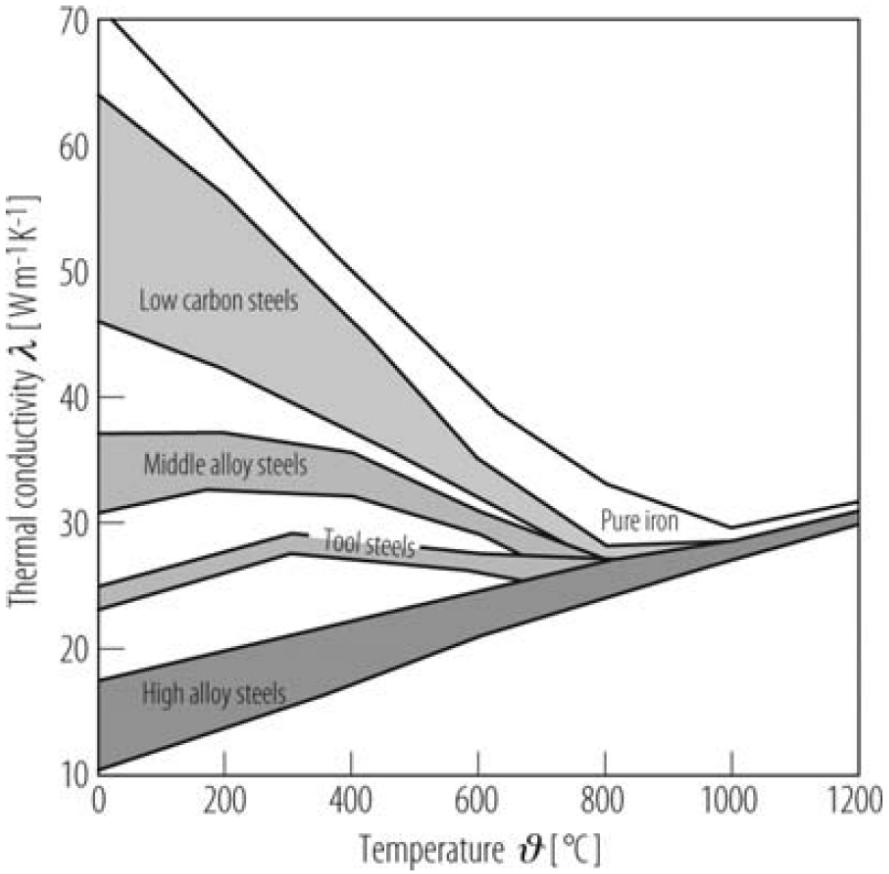

Figure 2-2: Temperature dependence of the thermal conductivity of steels. High alloy steel (316 ss) was used for fluidic conduits in this work. From Landolt-Börnstein[88].

In nearly all combustor systems for portable power generation, convective heat transfer is involved only as a mode of loss from the system. The convective heat transfer from the system can be influenced by the size of the exposed area, by the temperature of the exposed surface, and by the fluid properties of the ambient medium. Three common techniques for reducing convective heat transfer from the system capitalize on one of these influencing factors. One common approach, particularly for a combustor for TE generation or for an integrated combustor/reformer, is to use a structure with a large aspect ratio, such that the surface involved in the "active" (productive) heat transfer pathway is much larger than the surface exposed to the atmosphere. A second common approach is to cover hot surfaces with low-thermal-conductivity insulation, which reduces the temperature of the surface exposed to the atmosphere (likely with an increase in exposed area). The third approach, and one that has been considered for micropower generators, is to use vacuum packaging to reduce the density of the "ambient" medium to

the point where the mean free path is less than the distance from the hot combustor to the cold wall.

2.1.3. Radiative Heat Transfer

The heat loss due to radiation from a heated surface of area A, assumed to behave as a grey body emitter, to the ambient environment, assumed to behave as a black body emitter, is calculated according to Equation 12. In this equation, ε is the emissivity of the material (0.63 – 0.7 for silicon, ~0.3 for 316 stainless steel, and ~0.5 for 17-7 PH stainless steel) and σ_b is the Stefan-Boltzmann constant (5.7×10^{-12} W/cm^{2}K^4). Given the 4th-order dependence on surface temperature, radiative heat transfer becomes much more significant as the surface temperature of the combustor increases. Similar to convective heat transfer, radiation depends on the total exposed surface area of the device. However, radiation is a much stronger function of the surface material (through the emissivity) than convection, and so low-emissivity materials (or coatings) may be used to reduce this pathway. Radiative heat transfer is involved in the active pathway for TPV generators, and is a loss pathway in all other combustion-based systems.

$$Q_{radiation} = \varepsilon A \sigma_b \left(T_s^{\,4} - T_\infty^{\,4} \right) \qquad \textbf{[12]}$$

2.1.4. Parasitic Energy Loss for Flow Pressurization

The pressure profile within a combustor, and associated limitations, can have a significant impact on the design. Most portable power generation devices are designed to be air-breathing, that is they are operated using air from the surrounding environment as the oxidant. As such, they must incorporate some system to force air through the device (e.g., a fan or an ejector nozzle), which can serve as a parasitic load on the generated power. The energy required to provide air flow must be considered when designing a combustor. As well, a combustor which is designed for liquid fuels would require power input for vaporization based on the system pressure drop.

For ejector nozzle systems, the combustor pressure drop must be very low in order to ensure that the vapor pressure of the fuel is sufficient to entrain enough air to reach a desired equivalence ratio. Satoh, et al. [89], developed a micro-ejector for use with butane in a TE power generator system, but found that it was limited to a pressure drop of less

than 31 Pa to achieve an equivalence ratio less than 1. Microscale ejector systems have also been developed recently for use with ethanol vapor that can achieve a flow efficiency of 93% compared to isentropic calculations; however, the packaging of the ejector with a combustor in a compact manner remains an open challenge[90].

For systems that use a fan or compressor to supply a forced stream of air, the parasitic power load will be proportional to the flow work required. The power required is calculated according to Equation 13, where P_{fan} is the fan power, η_{fan} is the fan efficiency, W_{flow} is the flow work for air pressurization, v is the volumetric flow rate of air, and ΔP is the pressure drop in the system. Particularly at the small size required for portable power generators, the fan or compressor efficiency is likely to be much less than 100%, and a conservative estimate of 10% was used in this work. The parasitic power loss for air pressurization is particularly challenging because it must be satisfied by the electrical power generated from the device, and the efficiency of portable power generators is typically quite low.

$$P_{fan} = \frac{W_{flow}}{\eta_{fan}} = \frac{v \Delta P}{\eta_{fan}} \qquad \textbf{[13]}$$

2.1.5. Fuel Heating Value and Combustion Heat Release

The complete combustion reaction for an arbitrary hydrocarbon (with air as the oxidant) is shown as Equation 14. The amount of energy which is released in the form of heat is determined by the heating value of the hydrocarbon fuel. Two different heating values, the lower heating value (LHV) and higher heating value (HHV), are used to describe combustion of fuels. The LHV of the fuel is calculated as the difference between the total heat of formation of the products and that of the reactants, all calculated at some standard state (typically 1 bar, 25°C) and with the water in the remaining in the vapor phase. The HHV of the fuel is calculated similarly, except that the water is considered as liquid.

$$C_x H_y + z O_2 \left(+ \frac{21z}{79} N_2 \right) \rightarrow x CO_2 + \frac{y}{2} H_2O \left(+ \frac{21z}{79} N_2 \right) \qquad \textbf{[14]}$$

Depending on the system, either the LHV or the HHV may be more appropriate to be considered. Given that combustors typically operate at temperatures above 100°C, it is

rare that the system would be designed such that the heat of vaporization of the produced water could be extracted in a usable way. The LHV is commonly used as a comparative value in the literature for small-scale combustors. For fuel cells or other devices operating at lower temperatures, the HHV may be a more appropriate comparison. The specific choice is not, however, important so long as consistent comparisons are made.

2.1.6. Heat Loss through Enthalpy of Exhaust Stream

The enthalpy loss from the system refers to the amount of heat released in combustion that is required to increase the enthalpy of the exhaust gas from the ground state (usually ambient temperature, though pressure effects could potentially be included) to the state at which the stream exits the system. The enthalpy loss could otherwise be described as the wasted exergy of the system, in that it is the amount of energy available which has not been captured in some useful way. The enthalpy loss for comparison with the LHV (i.e., water condensation not considered) is calculated according to Equation 15, considering only temperature effects on enthalpy. In this equation, subscript "i" refers to each species in the exhaust gas (including nitrogen, if air is used as the oxidant), H(T) refers to the specific enthalpy at temperature T, n refers to the molar flow rate, T_{ex} refers to the temperature of the exhaust stream, T_∞ refers to the ambient temperature, and C_P refers to the specific heat capacity at constant pressure. Tabulated values of the specific enthalpies of common exhaust gases can also be used, such as those given in Table 2-1, from Felder and Rousseau[91].

$$Q_{enthalpy} = \sum_i n_i \left[H_i(T_{ex}) - H_i(T_\infty) \right] = \sum_i n_i \left[\int_{T_\infty}^{T_{ex}} C_{P,i}\, dT \right] \qquad \textbf{[15]}$$

The enthalpy of the exhaust gas could be involved in the active pathway for heat transfer, for example, in a turbine engine or in a combustor/reformer system where the two systems were thermally isolated from one another. In systems where it is a pathway of heat loss, the enthalpy loss can be reduced by decreasing the gas temperature, provided that the heat is put to some useful task. Typically, the enthalpy "recovery" from the exhaust gas is attempted through heat exchange with the inlet gas, though in an integrated system other process intensification schemes may be possible. Enthalpy recovery can be

difficult to achieve in a small system, as the length scales for conductive heat transfer in the solid materials tends to be quite small.

Table 2-1: Specific enthalpies of selected gases, referenced to 1 atm and 25°C, in units of KJ/mol. From Felder and Rousseau[91].

Temperature [C]	O_2	N_2	CO	CO_2	H_2O (v)
25	0	0	0	0	0
100	2.24	2.19	2.19	2.9	2.54
200	5.31	5.13	5.16	7.08	6.01
300	8.47	8.12	8.17	11.58	9.57
400	11.72	11.15	11.25	16.35	13.23
500	15.03	14.24	14.38	21.34	17.01
600	18.41	17.39	17.57	26.53	20.91
700	21.86	20.59	20.82	31.88	24.92
800	25.35	23.86	24.13	37.36	29.05
900	28.89	27.19	27.49	42.94	33.32

In order to achieve enthalpy recovery in a catalytic combustor, a heat exchanger would have to be thermally isolated from the combustion zone, which requires separation by some low-conductivity material (e.g., air, vacuum, glass, certain ceramics, etc.). The fluid channel should be free of any catalyst, at least on the inlet gas side where the temperature would approach or exceed the ignition temperature. And the *net* impact on the total system energy balance (or energy density) should be used to assess the merit of the enthalpy recovery, considering the extra mass of the recuperator, the (possible) additional heat loss to the environment due to convection and radiation from the additional surface area, and the additional power requirement for air pressurization due to added system pressure drop. Any gain in the efficiency of the system should be compared with the additional manufacturing complexity, additional cost, and any possible change to the mechanical robustness of the system.

2.2. Design Objectives for Catalytic Combustors

The design of a catalytic combustor for portable power generation depends on many factors, but none is more important than the identification of the active thermal pathway which will be used to transfer the heat released in combustion towards some useful purpose. As described in chapter 1, the efficiency of the combustor within the larger

system is determined from the proportion of the input energy (i.e., the heating value of the fuel) which is transmitted through this active path. Different combustor designs may be appropriate for an efficient design, depending on the active pathway. As a simple example, a compact chamber made from thick layers of an insulating material may be appropriate for an external combustion engine or an integrated combustor/reformer because the convective, radiative and conductive heat losses from the relatively cold exterior would be small; however, the same system would be exceptionally ill-suited to serve as a radiator in a TPV system, as the heat released would be dominated by the enthalpy loss.

The general schematic for a catalytic combustor is shown in Figure 2-3. The catalytic combustion occurs in a heated zone (at temperature T_c), and one (or more) of the thermal pathways serves as the active pathway. The combustor is connected to the ambient environment by, at least, a fluid conduit that introduces fuel and oxidant into the chamber, and often by another conduit that removes exhaust gases. These conduits also provide some structural support to the combustor, and conduct heat from the combustor to the ambient environment (at temperature T_∞). The combustor may also be in direct contact with some heat sink (at temperature T_s), such as the connection to a thermoelectric module and heat sink or to a reformer and endothermic reaction. The exposed, heated surfaces will also experience convective heat loss to the environment and will radiate energy.

The design objective of such a system is to generate heat from the combustion of a fuel in the combustion chamber and to transmit as much of that energy as possible through the active pathway, with as little energy transmitted through the other pathways as is possible. For portable systems, it is also typically desired to limit the size and mass of the system, which can reduce the design space for techniques to limit the heat loss from the system. Another important design aspect for portable systems is the mechanical robustness of the device, where the desire is to develop a system which is capable of accommodating modest physical stress, such as vibrations, external forces, or thermal stresses.

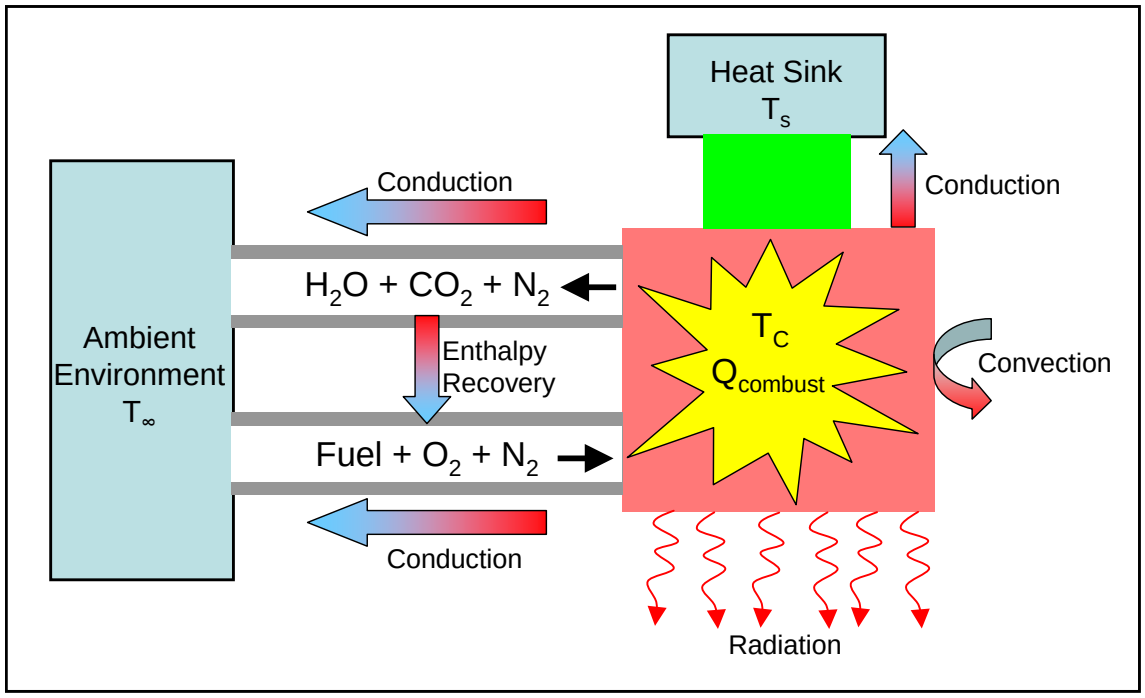

Figure 2-3: Interactions between catalytic combustor and environment.

2.3. Specific Design Challenges

As its primary function, the ability of a combustor to convert a significant portion of the input fuel is critical to the design. The primary design drivers for reactant conversion in the catalytic combustor are the flow rate of the mixed fuel and oxidant, the temperature, surface area, and activity of the catalyst, and the volume and characteristic length for bulk diffusion of the reactor. As the heat loss from convection and radiation is proportional to the external surface area of the system, typically catalytic combustors are designed for small internal volumes, and, thus, short catalyst contact times and short residence times. As such, the internal structure should be designed to provide a large catalyst area given the external dimensions, while considering the pressure drop imposed by the internal structure. The traditional design for a gas-solid heterogeneous catalytic reaction is a packed bed of catalyst particles; however, it is not likely to be possible to accommodate the large pressure drop through a packed bed of micron-scale particles. On the other end of the design spectrum, simply coating a thin layer of catalyst on the walls of a large, open chamber is unlikely to provide sufficient catalyst area to allow a high gas throughput.

There are two typical approaches to providing internal catalyst surface area enhancement with a manageable pressure drop. One approach is to fill the void with a highly porous material with high void fraction, onto which the catalyst layer can be deposited. Externally prepared metal[92, 93] and ceramic[94] foams have been used as catalyst supports in short-contact-time reactors, and they exhibit relatively large surface area (~1 m^2/g) and large void fraction (>80%). Also, porous alumina structures prepared in a microchannel with very large void fractions have been demonstrated for catalytic combustion. These supports were made using an inverse template of PMMA spheres, forming either an inverse opal structure[95] or a random porous structure[96] (with much less effort). The alumina structures were deposited in stainless steel microchannels, and are shown in Figure 2-4. The inverse opal structures have ~300 nm pores with a void fraction of 0.74, and the reported pressure drop through the coated channel was 1350 Pa for 200 sccm. The other approach is to use multiple channel passes through the reactor length, either with many parallel channels as in a catalyst monolith[97, 98] or with a single serpentine channel, as shown in Figure 2-5. Catalyst monoliths have been shown to impose less pressure drop than ceramic foam supports for equivalent performance as a catalyst support[99]. However, the use of parallel channels necessitates some flow distribution to avoid channeling.

Another challenge for many catalytic combustors is the reduction of surface temperature gradients, or "hot spots" near the inlet of combustion channels. The catalytic combustion reaction rate is typically positive order in the fuel concentration, and the activation energy is typically ~20 kcal/mol, so there is positive reinforcement in the reaction rate of increased heat release due to high fuel concentration leading to increased local temperature. An example of the resulting surface temperature gradient is shown in Figure 2-6, from propane combustion in a silicon microreactor with an observed temperature gradient of 100°C/cm. The surface temperature gradients are undesirable for several types of power generation, particularly TE generators[30], where the materials limitations typically limit the maximum temperature, and in TPV generators, where the electrical connections between photocells can limit the ability to make full use of the photons generated from the hot spot.

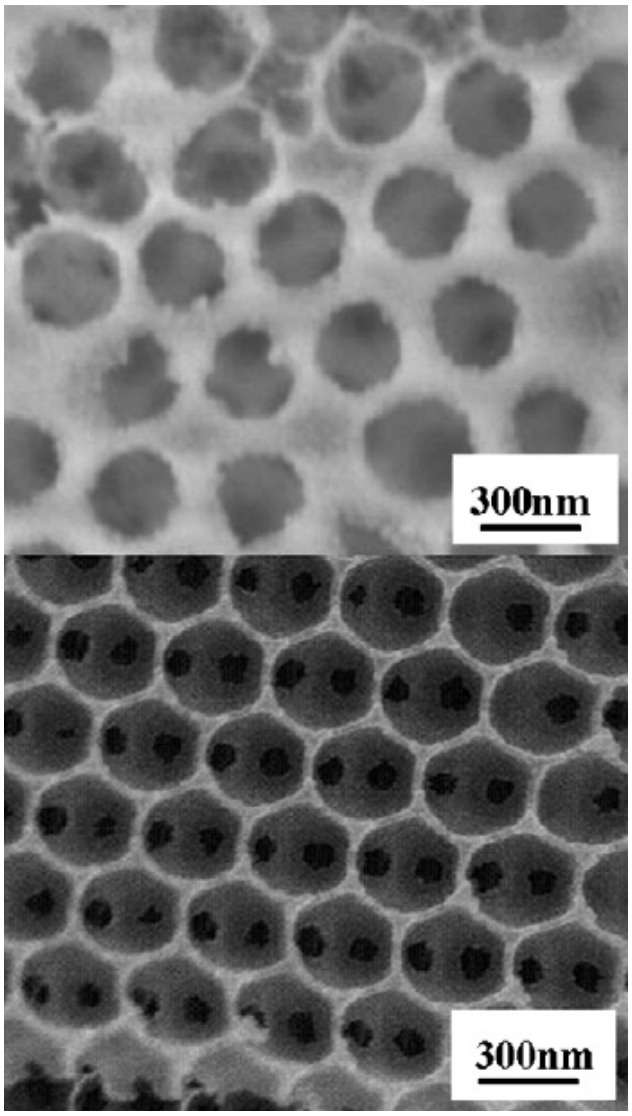

Figure 2-4: SEM images of alumina structures formed in a stainless steel channel using an inverse template of PMMA microspheres. The top image shows a random porous structure and the bottom layer shows an ordered inverse opal structure. From Guan, et al.[96]

The thermal conductivity of the combustor wall material has been shown to have a significant impact on the magnitude of surface temperature gradients in small combustors. Chen, et al.[100], conducted a numerical study of hydrogen combustion in a tube with catalytic walls (including both homo- and heterogeneous combustion), and reported that the thermal gradient could be reduced from ~700 to <200°C/cm with an increase in wall conductivity from 3.3 to 78 W/mK, as shown in Figure 2-7. A similar effect was observed through numerical[101] and experimental[42] investigation of catalytic combustion of propane by the Vlachos group at the University of Delaware. In their work, thermal spreaders of different materials were attached to the external walls of the combustor to

increase the effective thermal conductivity of the stainless steel. The thermal spreader consisted of one or more 3.2-mm-thick sheets of copper or stainless steel. The reported benefit of the copper thermal spreader was to reduce the temperature gradient over 5 cm from >300°C to <100°C, as shown in Figure 2-8.

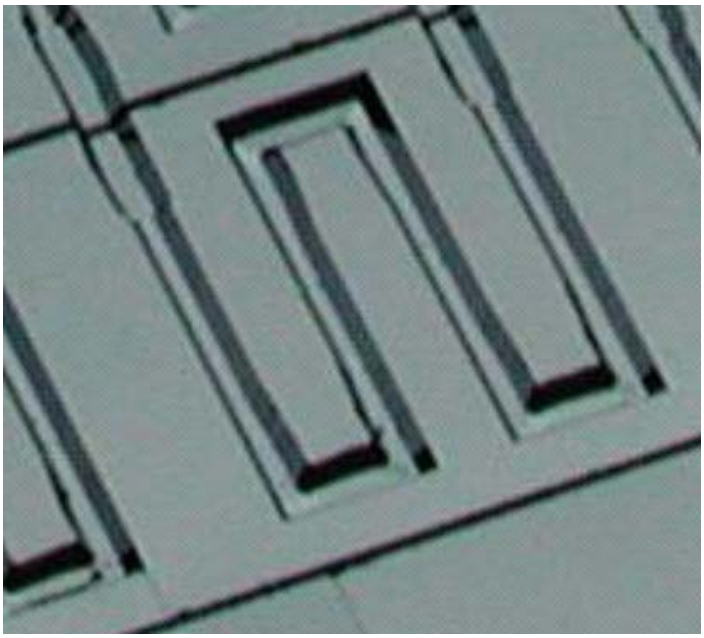

Figure 2-5: Image of a serpentine half-channel for catalytic comustion. From Blackwell[52].

Figure 2-6: Image of the catalytic combustion of 13 sccm of propane in a silicon microreactor (surface dimensions of 1 x 1 cm^2). The increased surface temperature on the right side corresponds to inlet region. From Blackwell[52].

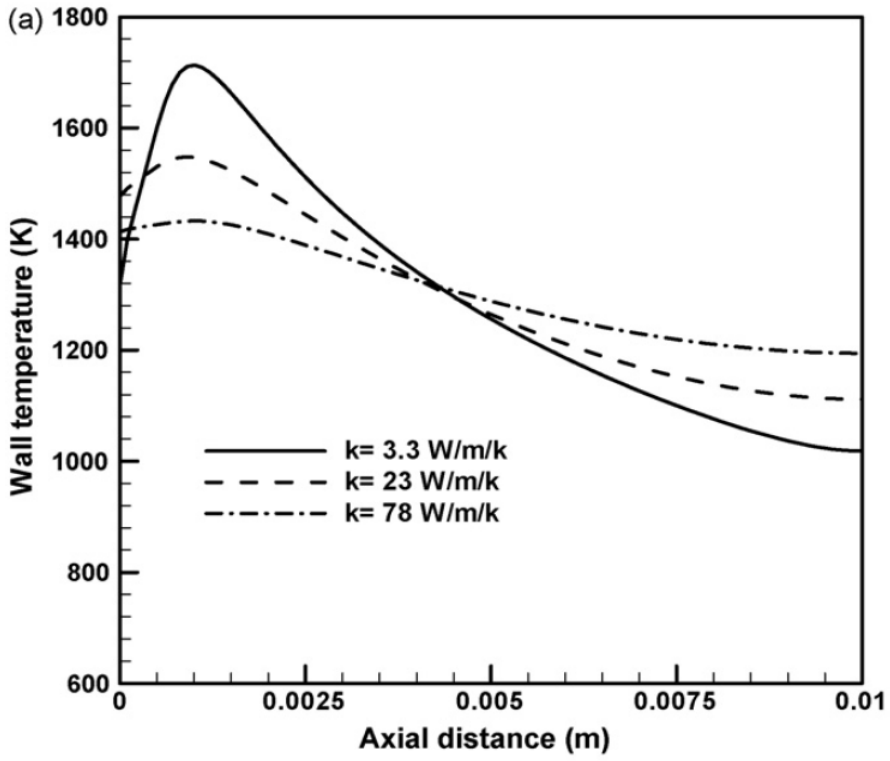

Figure 2-7: Effect of thermal conductivity of wall material on axial temperature gradient for combustion of hydrogen. From Chen, et al.[100]

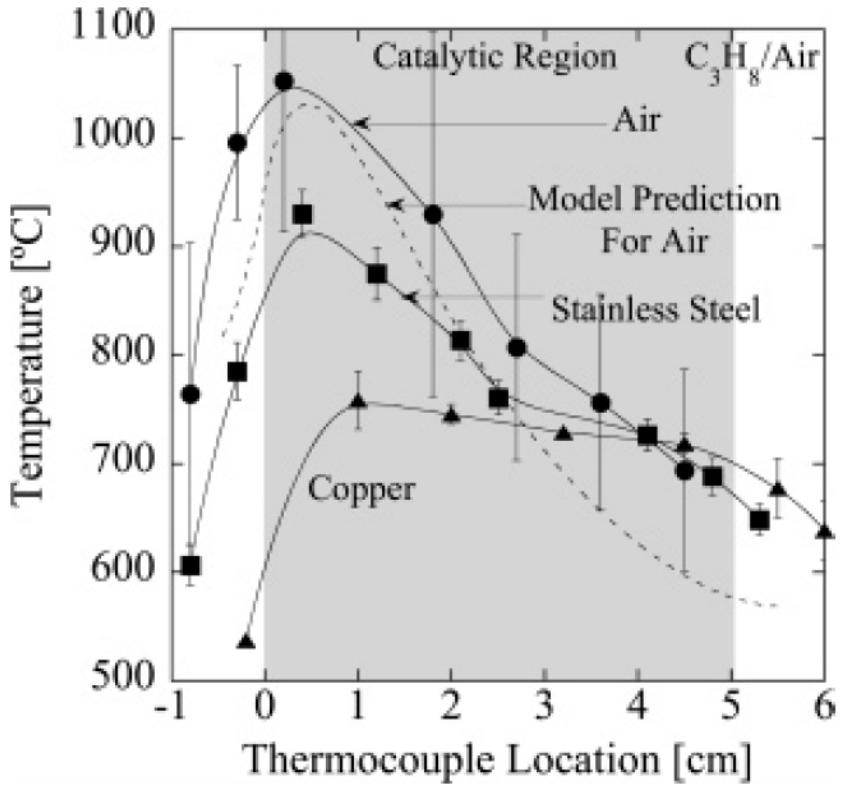

Figure 2-8: Axial temperature profiles for stoichiometric propane/air combustion with conducting thermal spreaders of different materials. From Norton, et al.[42]

2.4. Examples of Combustor Designs

Examples of microcombustor devices in the literature span a range of fabrication schemes, internal flow paths, reactants, operating conditions, and efficiencies. While this section is not intended to provide an exhaustive review of the field, an understanding of some of the different microcombustors in the literature is useful to consider different design compromises and consequences. In the following sections some illustrations of previous designs will be presented and discussed.

Microcombustors have been made using a number of different materials and techniques. Ceramic structures have been made using stereolithography[102] and high-precision tape casting[17], though the low thermal conductivity of ceramics can promote thermal gradients. Stainless steel devices have been made from sandwiched plates and gaskets[42, 103], machined microchannels[95], and steel tubes[10], although the high density of steel is not ideal for light-weight devices. A variety of different designs have been produced using silicon processing techniques[47, 72, 73, 76].

2.4.1. "Swiss Roll" Excess Enthalpy Combustor

The excess enthalpy burner concept was first proposed by Weinberg[104], and has more recently been used as the basis of a device patented by Cohen, et al., for thermoelectric power geneartion[18], as well as an external combustion engine by Cho, et al[57]. The principle of the combustor has been described in detail by Ronney[105], and the general concept is that a "Swiss roll" channel arrangement enables heat transfer between the hot exhaust stream and the cool inlet stream, as shown in Figure 2-9. As shown in the figure, the external temperature of the device is significantly lower than the combustion zone, which leads to reduced enthalpic losses and heat loss from the perimeter. The "Swiss roll" combustors have been made from γ-Al_2O_3 using a stereolithography process and from Vespel polyimide (with conductivity of ~0.29 W/mK and able to accommodate 500°C) using CNC milling, as well as other materials. The combustion and heat transfer within a "Swiss roll" has also been investigated numerically by Chen and Buckmaster[106]. The TE power generator patented by Cohen, et al., employs TE elements integrated into the walls between the hot exhaust stream and the cool inlet stream. The integrated system design is quite interesting, though the performance has not been reported.

Vican, et al., developed an alumina ceramic "Swiss roll" microreactor for TE power generation[102]. A schematic of the design concept, which is similar to the concept used in this work, is shown in Figure 2-10, and an image of the integrated system is shown in Figure 2-11. From a 12.5 x 12.5 x 5 mm^3 combustor, integrated with commercial BiTe arrays, 52 mW of electrical power was generated from the catalytic combustion of 9 W LHV hydrogen in air. A catalyst support layer of γ–Al_2O_3 was deposited within the channel using a washcoat technique, and subsequently the layer was impregnated with platinum. Fluidic connections were made to the reactor using stainless steel capillaries and sealed with glass welds. Reaction ignition was achieved through external heating of the device in an oven.

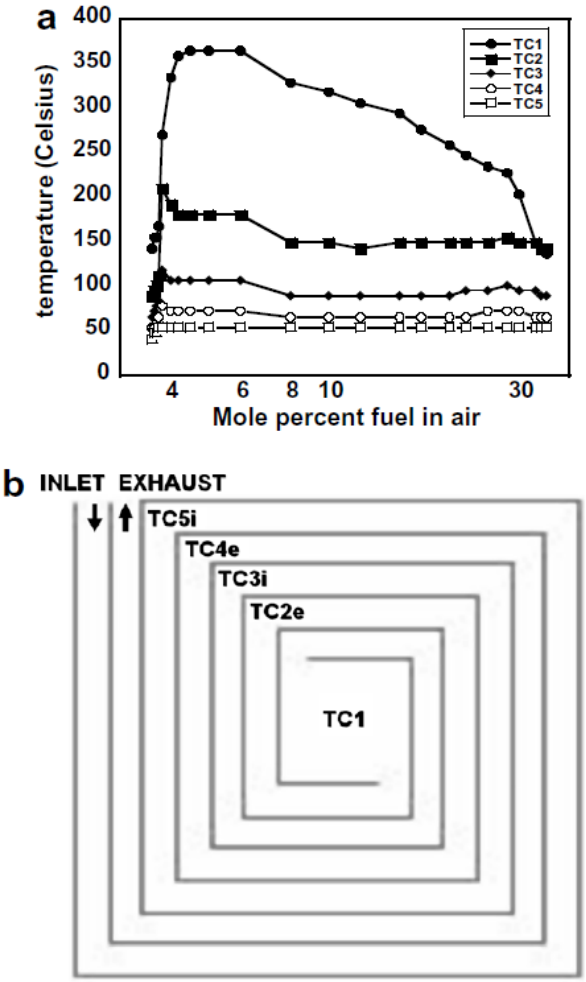

Figure 2-9: (a) Temperature profile at different spots in a "Swiss roll" combustor compared with the fuel concentration (propane with balance air). (b) 2-D schematic of "Swiss roll" combustor flow path with labels for temperature measurements corresponding to figure (a). From Cho, et al.[57]

The reactor was designed to achieve thermal energy transfer from the exhaust heat to preheat the reactants, to provide a large internal surface to volume ratio for effective catalyst performance, and to have large top-and bottom-face surface area for heat transfer to TE devices. Through use of a spiral channel layout, the surface temperature of the reactor was very uniform (within 1.5°C). However, the combustor was not able to operate in the excess enthalpy mode, due to the low Biot number of the system and the homogeneous application of the catalyst coating. The resistance to flow within the system was prohibitive, with a measured pressure drop of 96.5 kPa for a flow rate of 210 sccm. A significant flow resistance was attributed to the capillaries, which had a diameter of 350 μm. Given the pressure drop and flow rate of air, the flow work requirement was ~330 mW, and thus even with ideal compression the system would not produce net electrical power.

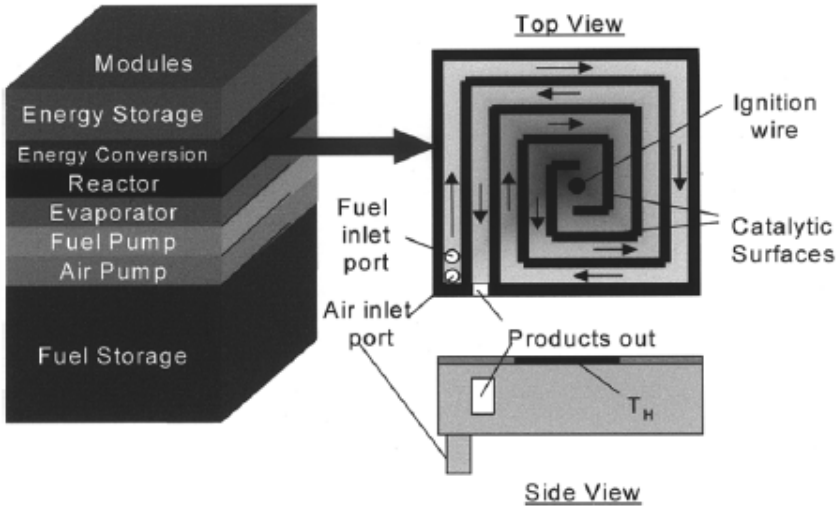

Figure 2-10: Schematic of a conceptual TE power generator using a "Swiss roll" combustor. From Vican, et al.[102]

The "Swiss roll" combustor is an intriguing design for portable power generation, and it has been applied in several different systems (e.g., internal TE, surface TE, external combustion engine, etc.). The concept of insulating the combustor from external heat loss (by conduction, convection, and radiation from the cooled sides) while simultaneously reducing the enthalpy loss from the system with minimal additional system mass is quite attractive. The design appears better suited to homogeneous combustion, as it is typically used by the Ronney group at USC, as opposed to catalytic

combustion, as in the work of Vican, et al., because of the difficulty in selective catalyst deposition which prevents enthalpy recovery.

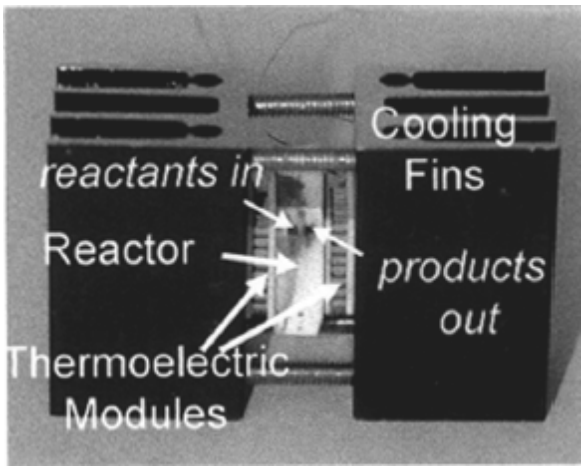

Figure 2-11: Image of the integrated combustor with commercial TE modules and heat sinks. For scale, the combustor has dimensions 12.5 x 12.5 x 5 mm^3. From Vican, et al.[102]

2.4.2. Silicon and Glass Open-Chamber Combustor

A catalytic combustor was designed by Yoshida, et al., using two silicon wafers which were anodically-bonded to a central glass wafer, with two open chambers etched using TMAH, as shown in Figure 2-12[41, 107]. The combustor was designed for TE power generation, with two BiTe modules to sandwich the chambers. Each chamber was 8 x 8 x 0.4 mm^3, and was coated with Pt/TiO_2 catalyst using a sol-gel deposition. The exterior of the combustor was 14 x 10 x 1.8 mm^3, and the fluidic connections were made with 2-mm-long, 1/16-inch-OD, and 100-µm-thick-walled glass capillaries. Given the internal dimensions, the surface area for catalyst deposition is ~3 cm^2. The measured pressure drop through the system, which was designed with a target of 31 Pa in order to interface with a micro-ejector, was 113 Pa for a flow of 150 sccm at ambient conditions.

The performance of the combustor was analyzed for the catalytic combustion of butane in air without the TE modules connected, and heat removal primarily by natural convection of air (typically with a heat transfer coefficient <20 W/m^{2}K). In this configuration, the combustion of 2.5 – 5 W LHV butane was successful to high conversion (>95%), with combustor temperatures between 300 and 400°C, and residence times between 40 and 50 ms (based on standard conditions, so the actual residence time was approximately half as long). However, when the TE modules were connected, it was reported that autothermal

butane combustion could not be maintained. The effective heat transfer coefficient through the TE modules was reported (based on the thermal resistance and the surface area of the combustor) as ~120 W/m^2K. It is likely that either the catalyst surface area or the catalyst activity was not sufficiently high in this design for TE power generation from sustained butane combustion. This result highlights the pitfalls of analyzing a catalytic combustor with thermal pathways that do not reflect the final application.

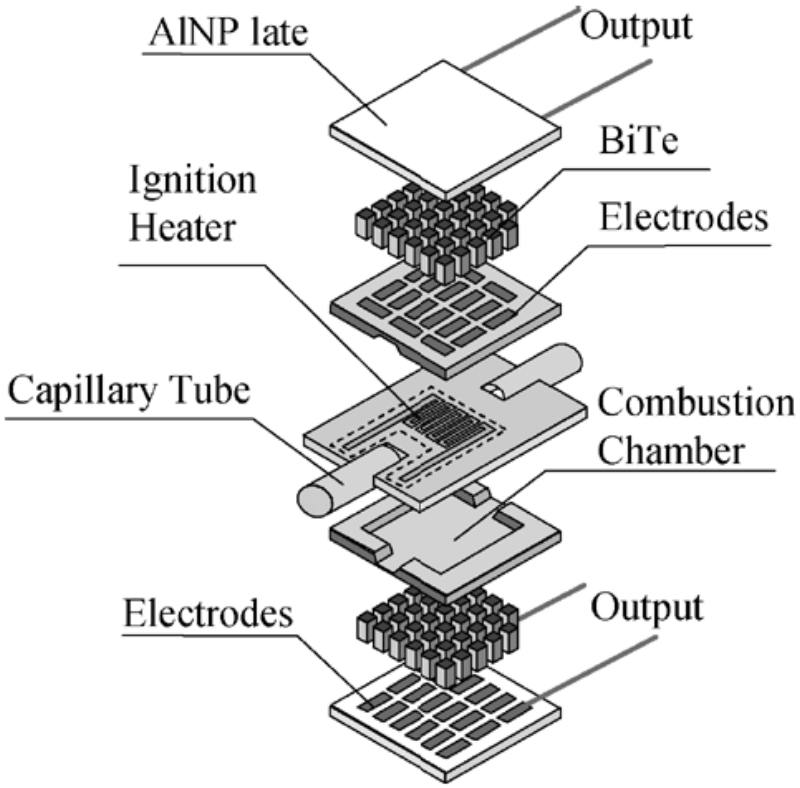

Figure 2-12: Illustration of the components of the open-chamber combustor interfaced with TE modules. From Yoshida, et al.[41]

The combustor integrated with the TE modules was tested with catalytic combustion of hydrogen (with stoichiometric air), with complete conversion observed at all conditions. For an input chemical energy was 6.6 W LHV, 184 mW of electrical power was generated (for a conversion efficiency of 2.8%, which is the highest reported efficiency for a portable-scale combustion-based TE generator). A partial heat balance was estimated for the combustion of 7.2 W LHV of hydrogen, with 4% estimated for enthalpy loss, 0.1% estimated for conductive losses through the tubes, and 10% estimated for radiative losses. The combustor is estimated to be ~50% efficient based on the generated

power and the estimated efficiency of the TE modules (5%). And so the remaining 36% is estimated as convective heat loss from the exposed combustor surface.

The sandwiched design of the open-chamber combustor has been demonstrated to be effective for TE power generation, at least in terms of the combustor efficiency. And the open-chamber design, as well as the relatively large, thin-walled tubes, proved to be effective in achieving a relatively low pressure drop, particularly compared with the work of Vican, et al. However, the catalyst surface area was quite small, and it is likely that this proved to be the factor which prevented the success of the device as a butane combustor.

2.4.3. Suspended-Tube Microreactor (SμRE)

Previous work at MIT by Arana, et al., led to a suspended-tube microreactor for thermally efficient fuel processing[47, 76]. The layout of the suspended-tube reactor is shown in Figure 2-13. Thin, silicon-rich silicon nitride (2-μm-thick-walled SiN_x) tubes were used to suspend the reaction zone and greatly reduce the conductive heat loss. Silicon slabs were used to bridge the inlet and outlet tubes in order to provide some enthalpy recovery. Silicon features were defined using a plasma-etch technique, and SiN_x tube release was accomplished using a fluorine etch. Two separate U-turn channels were provided, and an array of silicon posts was patterned in the reaction zone in order to increase the available surface area for catalyst deposition (while ensuring that the catalyst was in good thermal contact with the exterior of the device). An image of the reaction zone and catalyst posts is shown in Figure 2-14. The use of vacuum packaging and the possible incorporation of radiation shields greatly reduced all heat loss pathways from this reactor. The pressure drop through the SμRE I is shown in Figure 2-15.

Another version of the suspended tube reactor (SμRE IV) was developed by Blackwell, in order to simplify the fabrication and enlarge the device[52]. The external dimensions of the device were 1 x 1 x 0.13 cm^3 and a serpentine channel was used to provide catalyst surface area. The channels had a diamond cross-section, with a width of 500 μm and a depth of ~350 μm, and a total channel length of ~6 cm. The fluidic connections were made using thin-walled borosilicate glass capillaries, which had 550-μm-OD and 400-

μm-ID and a length ~1 cm. The capillaries were sealed to the reactor using a glass braze technique. An image of the fabricated SμRE IV is shown in Figure 2-16.

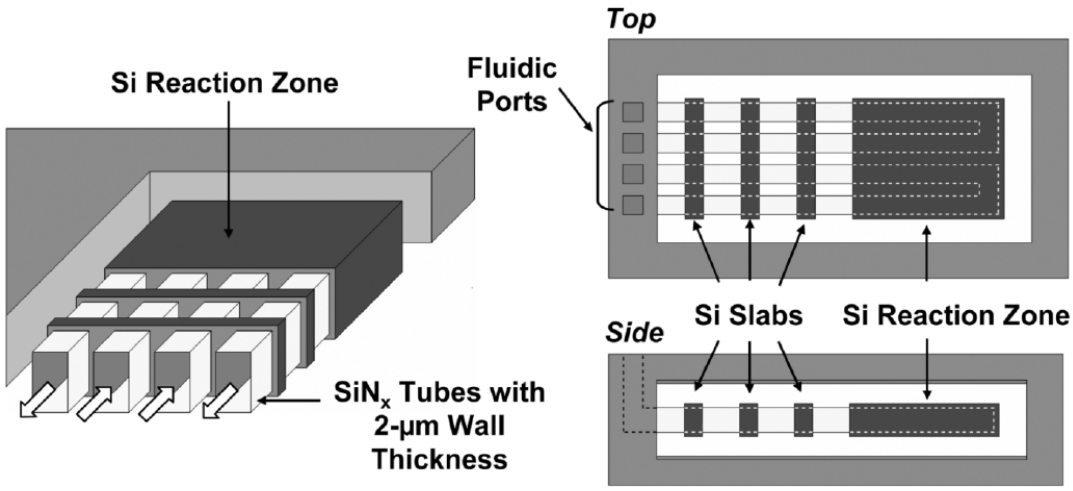

Figure 2-13: Schematic of the original suspended-tube reactor (SμRE I). The reaction zone is 1.5 x 2.5 mm^2. Each tube is 200 x 480 μm. The silicon slabs are used for enthalpy recovery, and the SiN_x tubes are the only connection with the surrounding environment. From Arana, et al.[76]

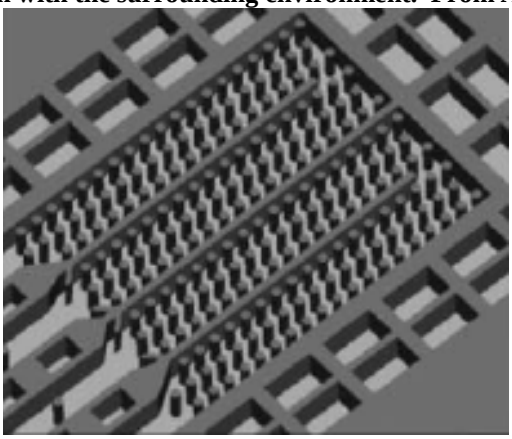

Figure 2-14: Illustration of the reaction zone of SμRE I, showing silicon posts for catalyst washcoat support. Representation of system prior to release of the reactor and silicon nitride tubes from surrounding silicon. From Arana, et al.[76]

The SμRE designs were intended as catalytic combustors for either TPV power generation[46, 47] or to serve as integrated fuel processors for hydrogen production[76]. The concept of the design was that each of the heat transfer pathways from the reaction zone could be made to be quite small with changes to the packaging (save for enthalpy losses in SμRE IV, which did not include silicon strips between the conduits). The thin-walled, low-thermal-conductivity tubes prevented significant conductive heat loss. Vacuum packaging has been demonstrated to reduce heat loss from the device by 60%, by drastically reducing the convective loss. Without radiation shielding, at a reactor

temperature of 800°C approximately 90% of the combustion heat generated would be released as radiation from SμRE I. And, as mentioned previously, the SμRE IV reactor has been integrated into a TPV system, and without modification (i.e., no photonic crystals to shape the radiative emission) the device was used to produce 220 mW of electrical power at 1.8% chemical-to-electrical conversion efficiency.

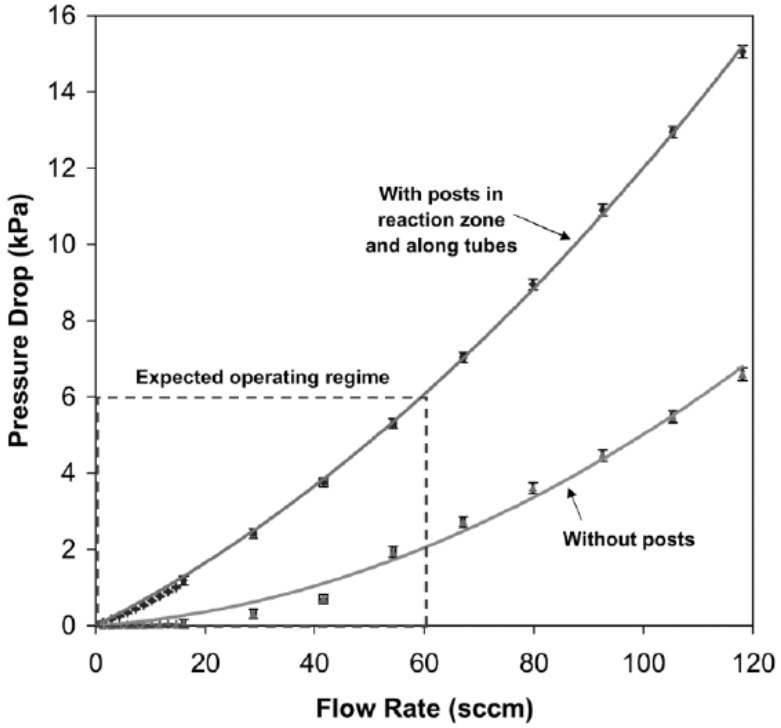

Figure 2-15: Pressure drop as a function of flow rate through SμRE I for nitrogen flow at 25°C in one channel of the device. Silicon posts contribute a significant flow resistance. From Arana, et al.[76]

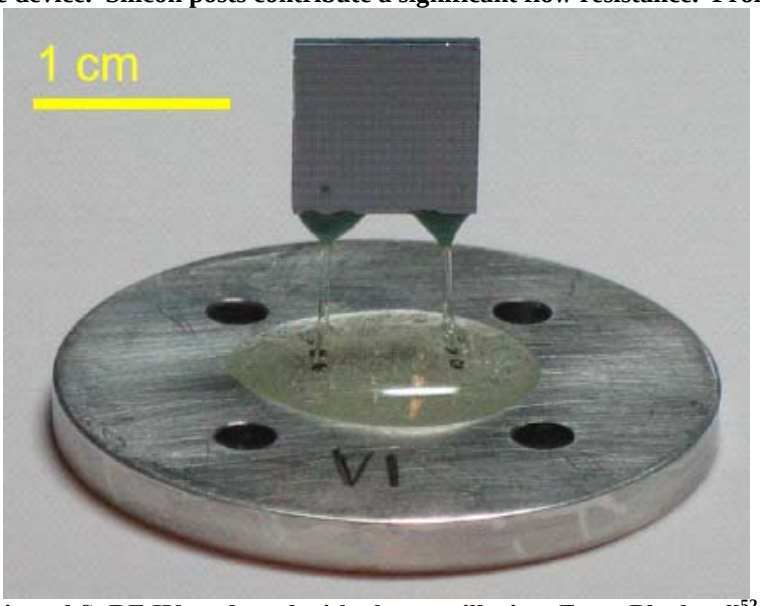

Figure 2-16: Fabricated SμRE IV packaged with glass capillaries. From Blackwell[52].

The suspended-tube reactors were able to achieve very high values for combustor efficiency for either radiative heat transfer or for hydrogen production in an integrated combustor/reformer system, and their success underscores the value of proper thermal management in the design of combustors. However, the applicability of the design is limited by two factors: the fragility of the devices challenges their use as portable generators, and the large pressure drop through the reactors drastically reduces the net power production for an air-breathing device with pressurization by mechanical means. However, it is not trivial to maintain the design concept and correct these two problems. The fragility of the devices directly results from the thin-walled capillaries which prevent significant conductive heat losses (and in the case of SμRE I, allow for light-weight and efficient enthalpy recovery). And the pressure drop is related to the small diameter of the tubes and the internal flow path intended to provide sufficient catalyst area with small diffusion lengths. This difficulty in redesign highlights the many trade-offs that are inherent in the design of a combustor.

2.4.4. Stainless Steel Sandwiched-Gasket Reactor

A relatively simple combustor has been designed in the Vlachos group at the University of Delaware, with a thin, open chamber for catalytic combustion[30, 42-44]. The combustor used in their work consisted of a 316-stainless steel gasket (500-μm-thick) sandwiched between two stainless steel plates (790-μm-thick) to define a channel of 5 cm length, 1 cm width, and 500 μm height. A series of 10 nuts and bolts were used to seal the channel. Catalyst inserts of platinum-coated anodized alumina (4 cm by 1 cm by 100 μm) were welded to the top and bottom steel plates, with ~1% by weight platinum and ~85 mg catalyst loaded in the burner. Static mixing screens were used at both ends of the channel to provide even flow distribution across the width (though the usefulness of the downstream screen seems questionable and the added pressure drop is likely significant). And fluidic connections were made using welded stainless steel tubes (of undefined diameter or length, though from images they appear to be 1/8-inch diameter and several inches long). The system was insulated using layers of 6.4-mm-thick fibrous alumina. As discussed previously, the combustor was interfaced with thermal spreaders composed of 3.2-mm-thick copper or steel with a 1 x 6 cm^2 footprint to reduce thermal gradients considerably. The layout of the combustor is shown in Figure 2-17. The system was

ignited using either external heating, such as from a resistive heater, or the selection of an appropriate fuel system, such as hydrogen/air or methanol/air.

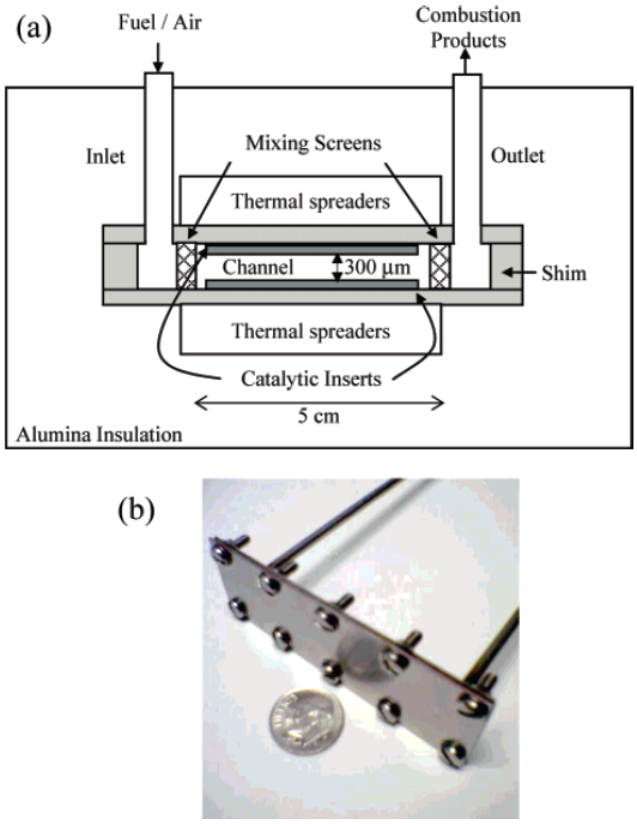

Figure 2-17: Stainless steel sandwiched gasket reactor. (a) Schematic of the system. (b) Image of the assembled system before insulation or thermal spreader integration. From Norton, et al.[42]

As described in chapter 1, the stainless steel sandwiched-gasket reactor has been used for thermoelectric power generation (with leading power demonstrations for hydrocarbon fuel combustion). The combustor was integrated with a second thermal spreader (i.e., a 3.2 mm x 3 cm x 3 cm copper block), a BiTe-based commercial TE module, and an aluminum-finned heat sink. The layout of the integrated system is shown in Figure 2-18, though the external C-clamp that was used to compress the entire device is not mentioned. An estimated system energy balance was provided for a heat input of 74.5 W LHV, with 70% of the total heat released lost to convection, 17% transferred to the TE module (i.e., conversion efficiency of 17%), and 7% lost to the enthalpy of the exhaust gas. However, this energy balance does not include any conductive heat loss through the tubes, which, along with radiative loss, is likely part of the 70% attributed to convective heat loss. The outer surface of the insulation was ~84°C, which suggests that the additional mass and volume of extra insulation would likely significantly improve performance. The system

mass was not reported, though it is likely >140 g given the dimensions of the metal structure. The pressure drop through the device was also not reported.

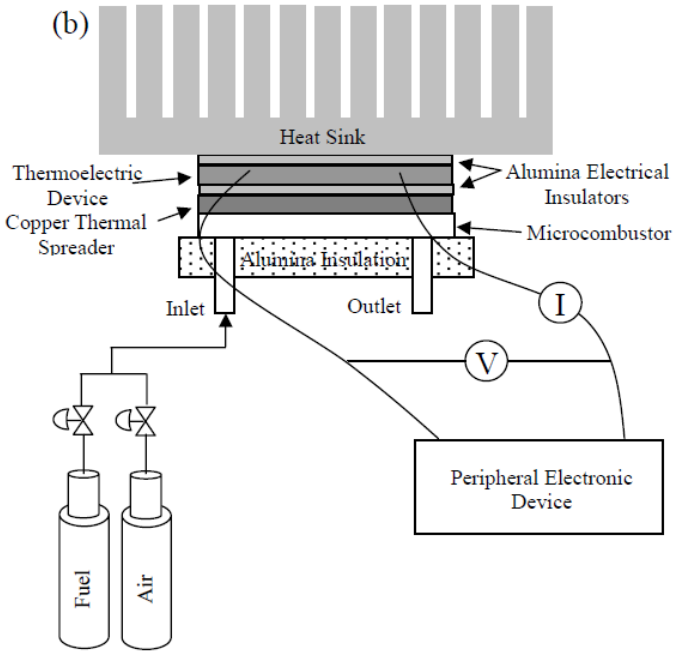

Figure 2-18: Integrated combustor and thermoelectric generator system. From Norton, et al.[43]

The stainless steel sandwiched-gasket combustor design has several attractive features. Aside from some spot welding, the fabrication and packaging is quite simple. The aspect ratio is very large, with a thickness of 2.08 mm compared with a length of 6 cm, which should lead to efficient heat transfer to the TE module. However, the maximum combustion heat released is quite low (~120 W) given the large size of the system, which calls into question the efficacy of the open chamber design (with ~12 cm^2 surface area for catalyst). The reasoning for not sandwiching the combustor between two TE modules is not clear, but the heat transfer through two conducting faces would certainly not perform at twice the heat flux of the single module, so the combustor would not reach 46% efficiency without modifications to the design. And as explained by Blackwell, the conductive heat loss through steel tubes is not likely to be negligible[52] without considerable length, at which point the pressure drop for ~1.4 slpm gas flow through 1/8-inch tubing is likely to impose significant parasitic power losses.

2.5. Concluding Remarks

To design an effective catalytic combustor for portable power generation, there are many aspects which must be considered simultaneously. The mode of power generation to be integrated with the combustor is of prime importance, as there is no all-encompassing solution. The reason for this is that efficient design involves a large heat transfer rate through an active pathway, to achieve high power density, and low heat transfer rates through all other pathways, to achieve high efficiency and, thus, energy density. Given the active pathway, the system must be designed such that the implication of each decision on all aspects of the performance is considered. The interrelation of the different performance drivers, such as catalyst surface area provided compared with system pressure drop or thermal isolation compared with mechanical robustness, demands that design of the system be identified with adequate consideration for all concerns. Often, the consideration of a single variable, such as the desire to reduce system pressure drop, leads to the design of a sub-optimal system, such as the open chamber structures, which do not provide sufficient surface area to facilitate significant short-contact-time catalytic combustion. Such a systems engineering view, leading to an optimal design of the power generation device, has been recommended elsewhere[53, 108].

In this chapter, some of the critical aspects for the design of an effective catalytic combustor for portable power generation, and in particular for TE power generation, have been identified. And some of the notable designs put forth in the recent literature have been discussed, with the goal of highlighting how different groups have approached these issues. Thermal management is a key aspect of the design of any high-temperature, autothermal micro- or mesoscale device, and this is certainly true for catalytic combustors. Through an understanding of the design challenge associated with catalytic combustion for portable power generation, the use of a system-level, model-based design approach was motivated.

3. System Design and Modeling

The design of microsystems for portable power generation exhibits a new set of engineering challenges, as scaled-down conventional systems are often unsuitable and new aspects of design, such as heat loss to the environment, become critical[16]. In this work, the focus was to design a combustor that would provide a suitable heat source for novel, high-heat-flux TE modules to produce a generator of usable electrical power (1 to 20 W) from a light-weight, chemical-fueled device. In particular, this design challenge was focused on achieving a thermally isolated, low- and uniform-temperature combustion heat source, while minimizing parasitic power losses related to reactant flow.

It has been demonstrated that the design objective for a portable power generation device can have a significant impact on the resulting design, and that energy density is a more suitable design objective than the chemical-to-electrical conversion efficiency for portable power generation devices[5]. For a system with only one stored component, such as an air-breathing, combustion-based TE power generator, the long-run (fuel-based) energy density and the energy conversion efficiency are proportional. However, the two are not equivalent in terms of design objectives for portable power generators, as can be observed from the simple case of fuel selection. A system which converts a lower percentage of a fuel with a higher energy density can provide higher energy density than one which converts a greater percentage of a fuel with less energy density. In this work, the simultaneous achievement of attractive energy and power densities was used as the design target. However, for a combustion-based system, the chemical-to-electrical conversion efficiency remains a useful comparison with similar systems, provided that reasonable consideration is given to the system-mass-implications of any design features which boost conversion efficiency (such as the use of compressed oxygen in lieu of air as an oxidant) in a way that is unlikely to be advantageous for a typical terrestrial system. A discussion of the relationship between application and design objectives for portable power generation systems is given by Mitsos, et al.[14]

The design efforts used in this work resemble, at least in basic structure, the process suggested by Mitsos, et al.[108], for the design of man-portable power generation devices,

as shown in Figure 3-1. Initial system-level models and scaling arguments of heat transfer, fluid mechanics, and energy balances were used to screen design concepts, with input from previous experimental efforts as to achievable structures, approximate fuel and catalyst performance, and possible material integration issues. Once a design concept was selected, more detailed timescale analyses, reaction modeling and pressure drop calculations were performed to identify precise system dimensions and flow rates, and identify limiting factors. And subsequently, a 3-dimensional computational fluid dynamics (CFD) simulation of the combustor was developed to examine the finer points of the system, such as temperature and concentration gradients, to assess parameter sensitivity and to identify potential avenues for improvement.

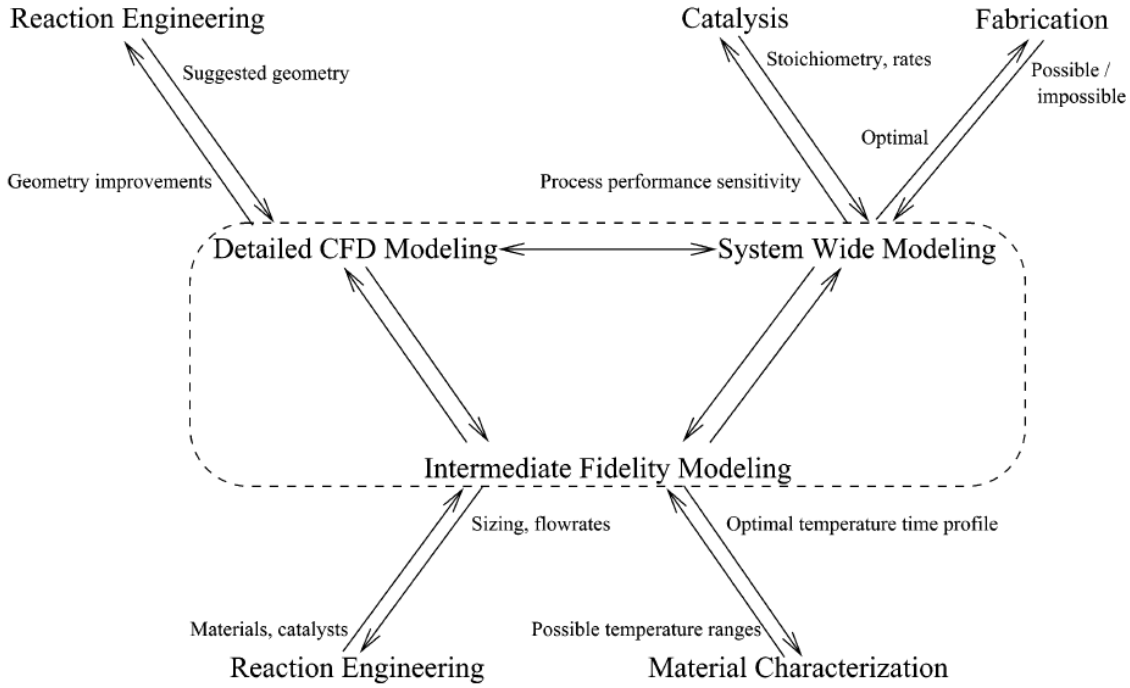

Figure 3-1: Example methodology for the design of man-portable power generation devices including potential interactions with experimental efforts. From Mitsos, et al.[108]

3.1. System Targets and Constraints

Initial design work by our collaborator, Dr. George Haldeman from MIT Lincoln Laboratories, was used to develop some specifications for the combustor system required for integration into an attractive device for portable power generation based on advanced TE materials. The primary targets for the combustor were to provide 280 W of heat to two TE modules, each with an area of 2.75 x 2.75 cm^2 (for a heat flux of 18.5 W/cm^2), with a total system mass less than 1 kg. A target of 80% was specified for the combustor

efficiency based on the desired energy density and the selection of a light hydrocarbon fuel, which refers to the proportion of the chemical energy in the fuel that is transferred through the TE materials. The design of the TE–combustor interface, arranged as described in Figure 3-2, combined with the desire to minimize combustor surface area not covered by the TE module, nominally fixed the combustor surface dimensions (length and width) to 3.1 x 2.85 cm^2. The effective heat transfer coefficient of the TE module is ~675 W/m^2K, on a basis of the module area. The design concept was that the combustor should have a large aspect ratio, such that the flat surfaces which coupled with the TE modules should be much larger than the other four surfaces combined, as the heat transfer from a given face scales with the area.

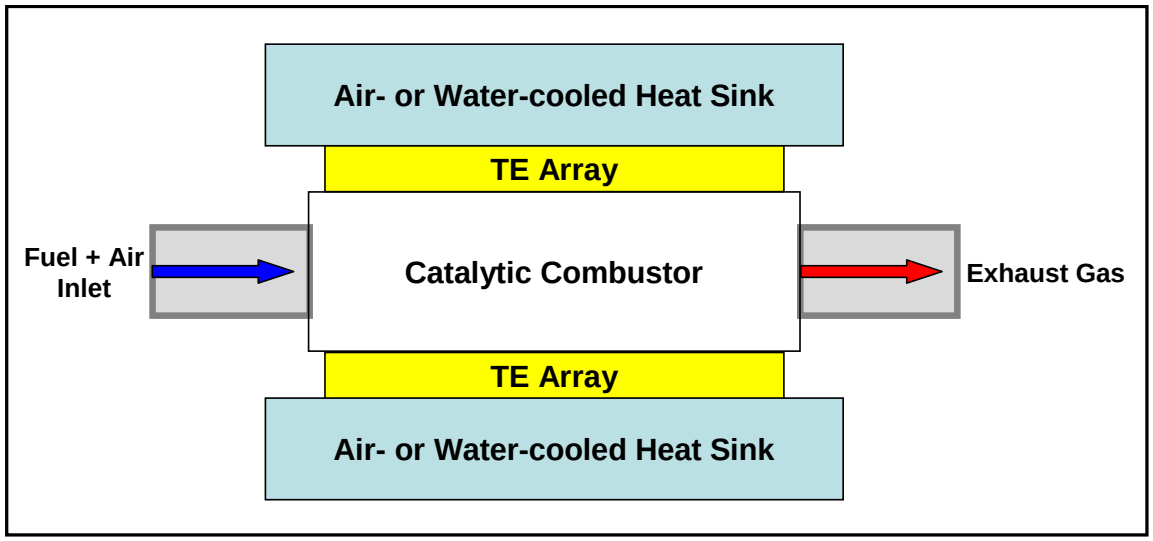

Figure 3-2: Nominal configuration of the TE power generation system components.

A significant limitation of many TE power generation systems is the low operating temperature for which TE materials are mechanically stable[30]. Given the thermal properties of many TE materials, the maximum temperature for the exterior wall of the combustor was nominally fixed at 700K, with a small reduction of temperature between the combustor surface and the TE surface anticipated for electrical insulation. It is difficult to design a heat source operating at this temperature using a hydrocarbon fuel, and there are several examples in the literature of unsuccessful attempts at achieving a stable temperature that is suitably low for TE power generation[30, 41]. The heat source for a TE power generation device should generate a high heat flux at a low temperature (for catalytic combustion of hydrocarbons) while minimizing heat loss to the surroundings.

In order to obtain the best performance from the TE materials, the hot side of the TE material-combustor interface must be maintained as close as possible to the maximum temperature across the entire surface. This implies that thermal gradients in the combustor temperature profile must be reduced, at least at the interface with the TE materials. The design of such a heat source posed a significant engineering challenge.

The design concept for the TE power generator involved the use of air from the environment as the oxidant, which would be forced through the system using a fan or some other system. In order to minimize the parasitic power consumption by the air handling system, the total pressure drop was limited to 500 Pa. This target was based on an assumed 10% compression efficiency and the design air flow rate, with a limit of 0.5 W electrical power for air handling. The pressure drop limit is significantly lower than pressure drop reported for previous microcombustors (e.g.,[76]), and represents a significant limitation of the design space. As well, it is difficult to achieve thermal uniformity with an exothermic reaction in a catalytic reactor without a large pressure drop resulting from a complicated internal flow path. The use of the vapor pressure of the fuel in a nozzle to entrain the required air flow has been investigated for n-butane; however, the maximum reactor pressure drop which could be tolerated while providing at least stoichiometric air was 31 Pa[89], which would represent an even more stringent design constraint. Other investigations have produced microscale ejectors with 93% mass flow efficiency compared with isentropic behavior, though the compact packaging of the ejector remains an open challenge[90].

There were additional design targets for the combustor, based on engineering intuition and the anticipated application as a consumer or military power device. The first design target was that the fluidic connections should be made using mechanically robust materials, such as steel or another metal, as opposed to those used in previous works for improved thermal isolation[52, 109, 110]. It was desired to use a catalyst system that was in good thermal contact with the reactor housing, so that the combustion temperature would not be significantly higher than the temperature at the hot-side of the TE module. This decision was intended to avoid unnecessary enthalpy loss from the system and reduce

catalyst sintering, as slow heat transfer out of the catalytic support results in temperatures near that of the adiabatic temperature rise[97]. And it was desired to produce the system using fabrication techniques which would, at least in principle, be suitable for low-cost, high-volume production.

3.2. Fuel and Catalyst Selection

The volume-based and mass-based energy densities of many hydrocarbons, such as those given in Table 3-1, are significantly higher than the energy density available from batteries. These values are based on the lower heating value of these fuels, defined as the enthalpy released from the complete combustion of the fuel with oxygen, forming gaseous products at 25°C. Hydrogen has some attractive properties as a fuel, such as extremely fast combustion kinetics over precious-metal-catalysts (proceeding at room temperature in most cases) and very high mass-based energy density. However, the storage of hydrogen requires significant mass to achieve sufficient compression, and the recharging of a hydrogen tank is not nearly as simple or rapid as those of several other fuels, making hydrogen an unlikely choice for a portable generator. Methanol is also an attractive fuel due to its fast low-temperature kinetics over platinum catalyst; however, the storage of neat or highly-concentrated methanol is difficult given its corrosive behavior. Light hydrocarbons, such as propane and butane, are attractive sources for portable power generation because they can be stored as a liquid under modest pressure (allowing for possible light-weight storage in plastic or thin metals). The catalytic oxidation kinetics of alkanes has been reported to be less than that of similar alcohols, aromatics, and alkenes[111]. However, the vapor pressure of an alkane fuel could be used to eliminate the need for a fuel pump, and possibly that for an air-compressor, which is a distinct advantage for a portable system.

In saturated alkanes, the activation of the C-H bond is known to be the crucial step in the oxidation reaction on a variety of catalysts[112]. As a result, the general trend is that the higher the number of carbons in the molecule, the higher the oxidation rate over noble metals[113]. In the series of straight-chain alkanes, the light-off temperature (which corresponds to the temperature at which 50% of the fuel is converted) trends similarly with the first ionization potential, as observed in from Diehl, et al[113]. Absent from the

previous figure, the butane "ignition" temperature was reported in the range 227 - 267°C over Pt-wire[114, 115], and <200°C over Pt/Al_2O_3[116], which is less than the design combustor temperature limit of <423°C. Similarly, a light-off curve for butane combustion over Pt/Al_2O_3 from Garetto, et al.[117], is shown as Figure 3-4. For the TE generator, the desire for extremely short contact times with low oxidation temperature was balanced against the desire for the fuel to be self-propelled (i.e., normal boiling point below room temperature), and so n-butane was chosen as the fuel. The vapor pressure of n-butane at 298K is 242 kPa, which provided sufficient pressure for flow control. Neglecting the mass of the convertor required, a power generation device processing butane, converting approximately 1.2% of the lower heating value to electrical energy, would have an energy density comparable to that of a lithium-ion battery.

Table 3-1: Mass- and volume-based energy densities of some common fuels. Values based on lower heating values. Hydrogen density at STP. From Blackwell.[52]

Fuel	Energy Density (Mass) [Wh/kg]	Energy Density (Volume) [Wh/L]
Hydrogen	33300	3
Methanol	5530	4370
Ethanol	7460	5885
Propane	12870	6320
Butane	12700	7280
Isooctane	12320	8540
Ammonia	5167	3110

There are several catalyst options reported in the literature for the combustion of alkanes, and catalysts for lower alkanes have been reviewed by Choudhary[118]. Common catalysts for combustion are Pt[117] and Pd[17], but some of the many other catalyst options include Cu- and Mn-doped ceria-zirconia[119] and $CuMnO_x$[75]. In many cases, the catalyst is a composite of a metal (such as Pt) adsorbed on a supporting material (such as a mineral oxide like Al_2O_3). The supporting material is used to increase the exposed surface area of the metal, provide structural support, and change the catalytic properties of the metal. A detailed procedure for catalyst preparation by metallic complex adsorption on mineral

oxides is presented by Brunelle[120] and more general preparation procedure by Pinna[121]. Zeolites have also been shown to be effective supports for platinum catalysts for combustion of C2 – C4 alkanes, due to increased alkane adsorption on the surface compared to an alumina or MgO support[117]. Noble metal catalysts have been widely considered for lower alkane combustion due to higher specific catalytic activity and resistance to sulfur poisoning, particularly Pt and Pd due to their lower volatility[118]. And Pt/Al_2O_3 has been reported to be a more effective catalyst than Pd/Al_2O_3 at higher conversions in stoichiometric mixtures[116, 122]. Many of the examples of combustion systems for small devices in the literature have used platinum on γ-alumina (Pt/ γ-Al_2O_3) as the catalyst[52, 72, 102, 110, 123, 124]. The long term stability of Pt/Al_2O_3 catalyst has been investigated by Nishibori, et al., and the activity was maintained for more than 250 days after some initial heat treatment to prevent sintering[125].

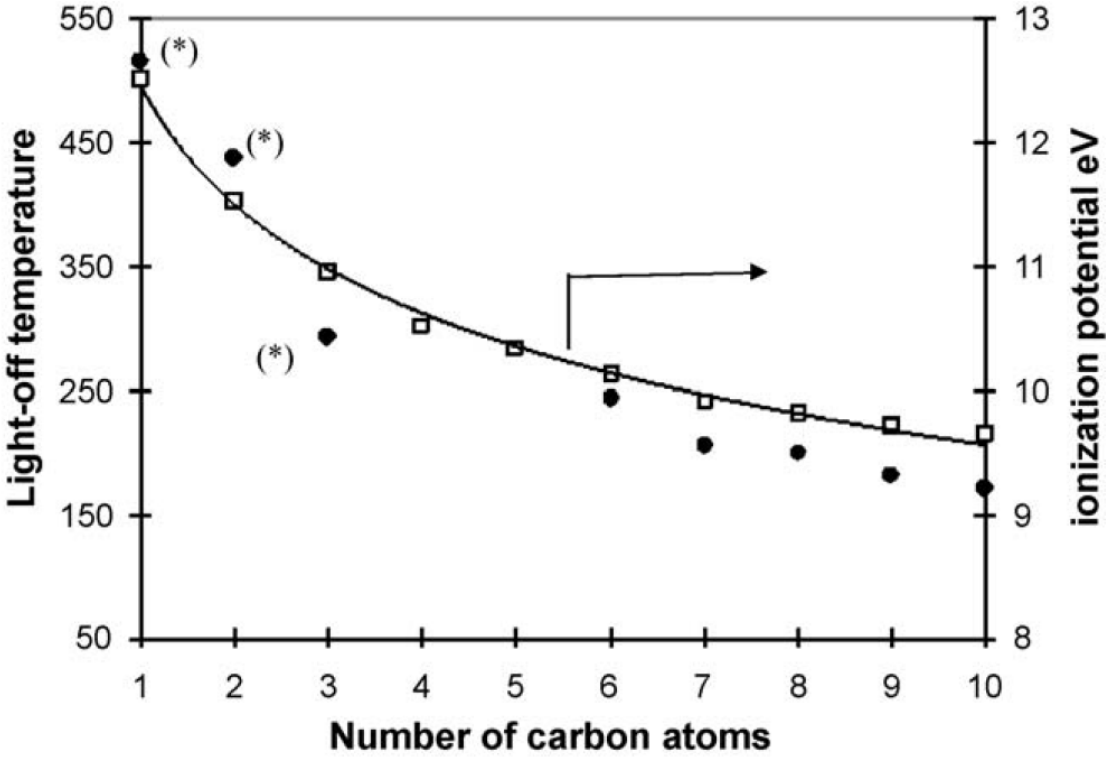

Figure 3-3: Correlation between the light-off temperatures of n-alkanes and their ionization potential. Black circles: T_{50} values; open squares: ionization potential in eV. From Diehl, et al.[113]

The impact of platinum concentration in (Pt/ γ-Al_2O_3) on the reaction rate of propane oxidation was reported by Otto, et al.[126] Fitting a first-order rate expression, they reported ~6.4 times increase in the observed rate constant for an increase in Pt from 0.03

to 30%. The rate increase was attributed to larger platinum particle sizes, which are known to have increased oxidation kinetics for alkanes[113] (with an increase of ~100 times in the reaction rate adjusted for surface platinum as total Pt concentration increased from 0.03 to 30%), and mitigated by an increase in subsurface Pt atoms. In this work, a commercial Pt/ γ-Al_2O_3 catalyst (Sigma Aldrich) was employed, and, given this trend, the highest available platinum concentration was selected (5% by weight).

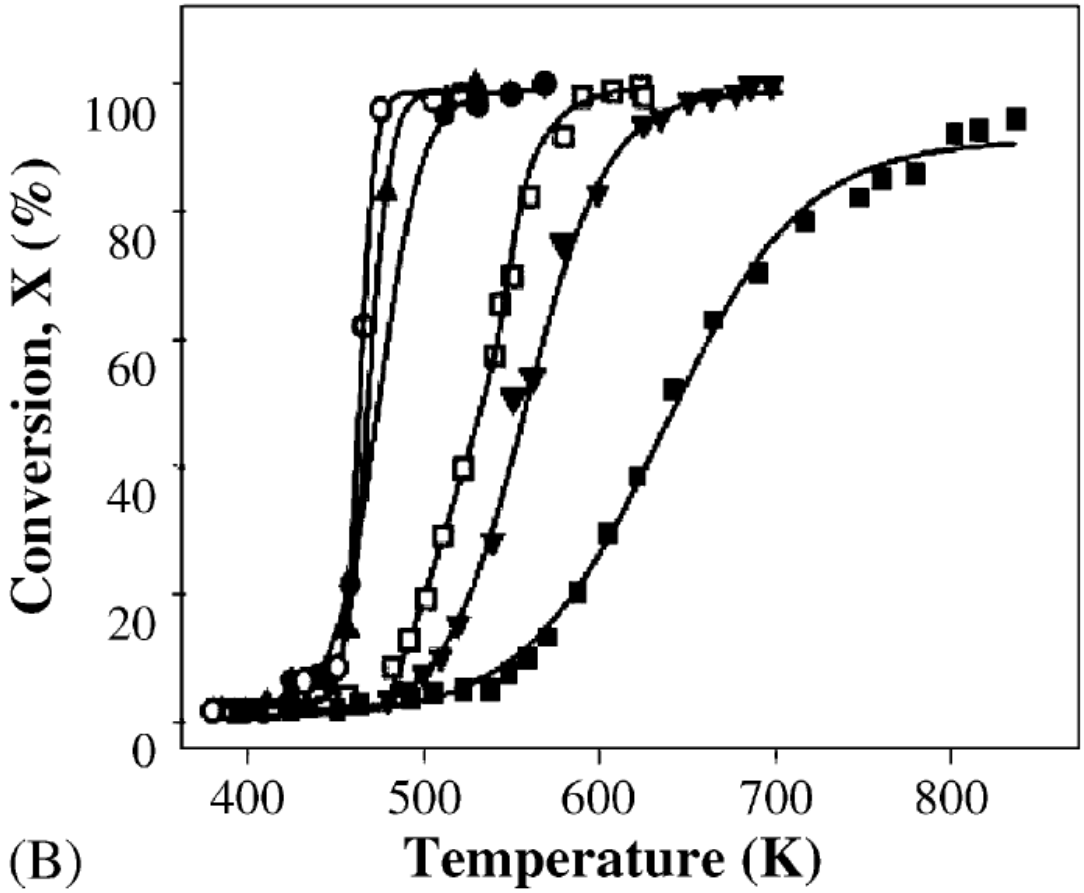

Figure 3-4: Light-off curves for butane combustion over various supported platinum catalysts. Pt/Al_2O_3 is shown as ▼ symbols, with 0.33% Pt by weight. The other symbols represent Pt on different zeolite (higher activity) and MgO (lower activity) suppots. From Garetto, et al.[117]

In the past decade, there have been a number of methods developed to improve the performance of Pt/γ-Al_2O_3 catalysts for the oxidation of alkanes. One approach has focused on the impact of the catalyst support properties on the catalytic activity. It has been shown that the increased acidity of the support material results in greater resistance to platinum oxidation, and thus enhanced activity[127-129]. Support materials with improved performance include SiO_2-Al_2O_3 and sulfated alumina. It is important to note that these

support effects are believed to be most pronounced for low temperature combustion (<700K). Another approach to improve catalytic activity is the addition of electronegative atoms, such as tungsten or vanadium, using an impregnation process[95, 130]. Similar to the acidic supports, these electronegative additives increase the oxidation-resistance of the platinum.

The performance of the combustion catalyst can only be improved to the point where the system becomes mass transfer-limited. Mass transfer limitations have been reported in several examples of catalytic alkane combustion from the literature[52, 64, 101, 123, 131]. To overcome these mass transfer limitations, structured packing placed in the flow field has been used to reduce the characteristic diffusion length in the system. Arana, et al.[76], patterned an array of silicon posts throughout the width of a microchannel, and these posts were catalyst-coated using a wash coat technique. Guan, et al.[95], developed a free-standing Al_2O_3 inverse-opal porous structure in a microchannel from a template of PMMA spheres using a sol-gel procedure. The structure had a high surface area per unit volume with a pressure drop two-orders of magnitude less than a packed bed structure with the same geometric surface area.

3.3. Reactor Design

The reactor design challenge to produce a combustor capable of significant heat release (~350 W) with a low operating temperature from within a small footprint area was considerable. Given the relatively low conversion efficiency of TE modules (<10%), there was only a small margin for reduced efficiency in the combustor, either from heat loss or unconverted reactants, or for tolerated parasitic power losses (such as for air pressurization), while producing a device that would be competitive with the energy density of batteries.

3.3.1. Material Selection

There are several characteristics which supported the selection of crystalline silicon as an attractive material for a combustor in the TE power generator. First, silicon is a light-weight material, with a density 30% of that of stainless steel, which is attractive for a portable device. Second, silicon has a moderately high thermal conductivity at the

intended operating temperature (61.9 W/mK at 600K); roughly double that of steel and significantly more than that of ceramics. It has been demonstrated that materials with higher thermal conductivity can improve stability and enhance catalytic combustion relative to homogeneous combustion[25] as well as reduce thermal gradients that can occur within exothermic catalytic reactors[42]. Third, the low coefficient of thermal expansion (CTE) of silicon leads to less thermal stress on TE materials than would be experienced with a metal combustor, and also promotes adherence of catalyst coatings during thermal cycling. Last, parallel processing techniques for silicon that enable microstructured devices have been demonstrated[132], which is advantageous compared to serial processes such as micromachining of metals. And these processes are well suited to producing the high-aspect ratio structures that are desired for a TE generator.

3.3.2. Selection of Internal Structure

Given that the footprint area of the combustor was roughly fixed by the TE module size, the thickness of the combustor and the dimensions and arrangement of the internal structure were the most impactful variables that could be selected to obtain the desired combustor performance. The desired heat generation to the TE modules (280 W), the approximate combustor efficiency (~80%), and the properties of butane combustion (such as the reaction stoichiometry and the lower heating value) established a total flow rate of approximately 6 standard liters per minute (slpm, referenced to 1 atm and 0°C). Correcting for the gas expansion at reactor temperatures, the initial design flow rate was approximately 15 lpm at 423°C. Given the footprint area of the TE modules, 2.75 x 2.75 cm, and assuming that the reactor would be formed from two standard silicon wafers, the approximate size of a simple combustion chamber was estimated to be 2.75 x 2.65 x 0.1 cm^3. The pressure drop for laminar flow of ~15 lpm of air through a channel of these dimensions is ~10^2 Pa, and this indicated that there was not much margin in the pressure drop limitation (500 Pa) for the use of internal structures for catalyst support or gas distribution.

Several chamber designs were considered for the combustor in order to provide surface area for catalyst deposition without sacrificing too much of the open area for gas flow. Serpentine channels had been used with some success in previous microcombustors;

however, the design target of minimal surface temperature gradient motivated the use of an internal structure where the region of high fuel concentration was more dispersed across the reactor than was possible with a serpentine design. For example, Blackwell observed temperature gradients as high as 100°C/cm in a silicon combustor with a serpentine channel[52]. An open chamber with internal features to provide some catalyst surface, such as the silicon posts used by Arana, et al.[76], was also considered. However, there were concerns of channeling within the chamber without the use of a distribution manifold (that could not be accommodated given the pressure drop limitation), which would result in a reduction of the effective residence time in the reactor. Because of the relative magnitude of the air flow rate compared with the TE module footprint and the thickness required to achieve thermal isolation, a relatively short contact time was anticipated (GHSV ~10^5 h^{-1}) that made it highly unlikely that significant channeling within the reactor could be tolerated. A comparison of posted reactors with channel reactors was made by Ni, et al., and it was reported that a posted reactor behaved more like a continuous stirred tank reactor than as a plug flow reactor[133]. Significant consideration was given to an integrated device with a low-flow-resistance distribution section, multiple reaction channels, and possibly an enthalpy recovery section. This type of integrated system has been used in the past for catalytic combustion; however, significant challenges associated with selective catalyst deposition were identified, such as the challenges with fluidic stop valves encountered by Nielsen[109], or the manual loading of catalyst in a clean-room environment[60] that limited the type of catalyst support that could be used in the micro gas turbine project. In order to simplify the fabrication of the device, such that the fabrication procedure would be more suitable for a large-production-volume device, these complicated designs were not pursued.

Design inspiration was drawn from the monolithic reactors that are commonly used for catalytic combustion, and other reactions, in the automotive industry. Monolithic reactors, whether ceramic or metal, offer high geometric surface area for catalyst deposition and low resistance to flow due to their open structure[134]. Since ~1980, essentially all automobile manufacturers design catalytic converters using monoliths, and high-performance vehicles use metal monoliths with open frontal areas of 90% to reduce

the pressure drop across the reactor to negligible levels (for that application)[135]. The general monolith structure of close-packed channels is shown in Figure 3-5, from Geus, et al[97]. Monoliths with the largest open frontal area have wall thicknesses from 50 to 100 μm and channel diameters ~1 mm[135, 136]. One disadvantage of the typical monolith structure is that the majority of (internal) channels function as adiabatic reactors[135] given their isolation from the environment, which can lead to catalyst sintering, NO_x formation, and poor temperature control.

The catalytic combustor designed for the TE power generator was essentially a silicon monolith, meant to mimic the large catalyst surface area and low flow resistance of monolithic reactors; however, the device was also designed with the large aspect ratio characteristic of many silicon microreactors. The basic structure of the reactor was a chamber, formed by etching two silicon wafers and subsequently bonding them together, which would have a footprint similar to that of the TE modules and an internal height of 1 mm. The height was chosen to provide significant flow area while leaving sufficient material to preserve the strength of the silicon support based on previous microfabrication experience at MIT. Within the chamber, thin silicon supports were evenly distributed along the width of the chamber, forming parallel rectangular channels, as illustrated in Figure 3-6. The straight, parallel channels distribute the inlet flow to avoid the creation of a single hot spot and avoid the added pressure drop associated with turns in the flow path.

The width of the open chamber was 2.75 cm, and the length of the combustors used in this work ranged from 3.1 to 3.5 cm, where the additional length was provided to simplify the reactor packaging. The thickness of the side walls was 100 μm, which was selected as low as possible under the constraints imposed by alignment precision during fusion bonding and mechanical strength of the etched structure prior to bonding. The width of each individual channel, w, is given by Equation 16 in units of mm, where N is the number of channels, w_t is the total chamber width, and w_s is the side wall width. The total surface area of exposed silicon within the volume, SA, is given by Equation 17 in units of cm^2, where L is the chamber length and h is the chamber height. Clearly, the

width of the channels decreases and the surface area for catalyst deposition increases as the number of channels (and side walls) increases.

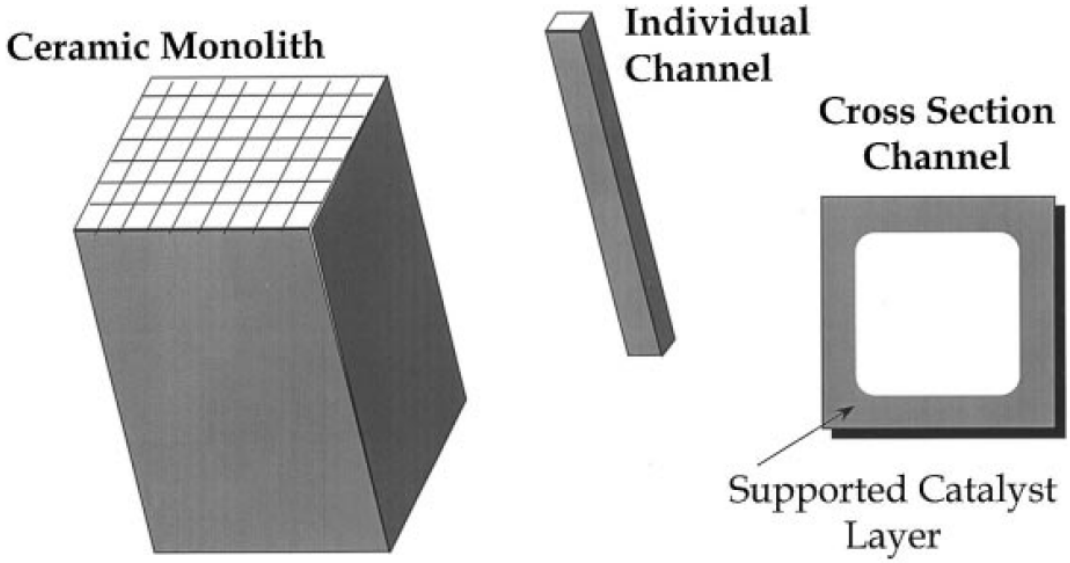

Figure 3-5: Schematic of a ceramic monolith, showing arrangement of channels and cross-section of channel with deposited catalyst washcoat. From Geus, et al.[97]

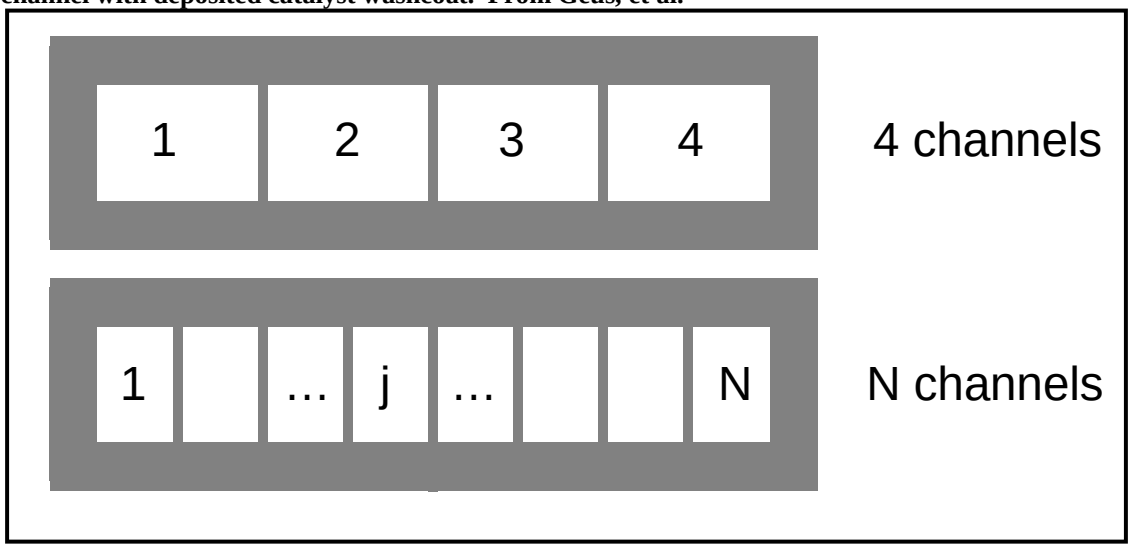

Figure 3-6: Illustration of side walls added to combustor chamber. The cross-section of the chamber is shown with a variable number of parallel channels. The top image shows four channels, separated by three side walls. The bottom image shows "N" channels, with N-1 side walls.

$$w = \frac{w_t - w_s\left(N-1\right)}{N} = \frac{27.6}{N} - 0.1 \qquad \textbf{[16]}$$

$$SA = N\,L\left(2w + 2h\right) = 19.32 + 0.63N \qquad \textbf{[17]}$$

The flow in the reactor channel was determined to be laminar, as the Reynolds number was ~10^2. The pressure drop for ideal gas laminar flow in a rectangular channel was calculated using the Darcy-Weisbach equation (Equation 18) as described in Janna[137], which is suitable for low pressure differences[138] and is a function of the hydraulic diameter, D_h. In the equation, u is the average velocity, ρ is the density and f is the friction factor (determined from Janna for a specific ratio of w/h). The hydraulic diameter of a rectangular channel is calculated according to Equation 19. In the event that w << h, it is clear that $D_h \sim 2w$, and if w >> h then $D_h \sim 2h$. The average velocity is related to the total gas flow rate, Q, and the open flow area as given in Equation 20.

$$\Delta P = \frac{\rho f L u^2}{2D_h} \qquad \textbf{[18]}$$

$$D_h = \frac{4A}{P} = \frac{2wh}{(w+h)} \qquad \textbf{[19]}$$

$$u = \frac{Q}{whN} \qquad \textbf{[20]}$$

Most of the design options to increase the catalyst surface area, including the use of side walls to decrease the width of parallel channels, result in a trade-off of increasing the system pressure drop. One way to increase catalyst surface area which also decreases the system pressure drop was to add a second set of channels in a parallel reactor. Of course, the trade-off for this increased area and decreased flow resistance (due to a reduction in the total flow rate through each reactor) was an increase in the external surface area for heat transfer (and an insignificantly small added mass). However, given the large aspect ratio, the added external area was only 10% of the total surface area of the combustor in order to obtain an increase in internal surface area by a factor of 2 and a pressure drop decrease by a factor of 4. And unlike catalyst monoliths, all channels are in good thermal contact with the desired thermal pathway for power production.

The total internal surface area for catalyst deposition and the pressure drop in the two reactors as a function of the number of channels is shown in Figure 3-7. The sharp increase in the pressure drop around 24 channels is observed because the width of the

channel becomes the dominant length scale (i.e., the width becomes less than 1 mm). Thus, for each reactor, 24 nearly square channels (1.05 mm wide and 1 mm high) were chosen to balance the desires for large surface area and low pressure drop.

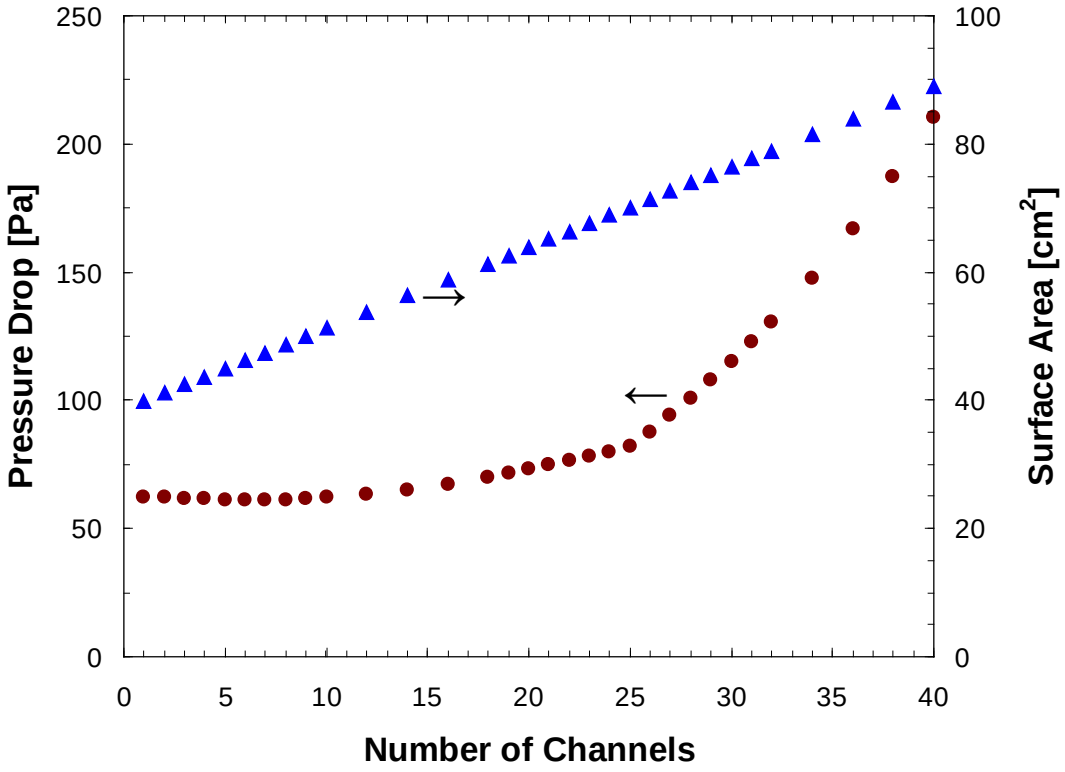

Figure 3-7: Pressure drop through channels (brown circles) and internal silicon surface area (blue triangles) as a function of the number of parallel channels. Assumes flow divided evenly between two identical combustors. Pressure drop calculated using Darcy-Weisbach equation for 188 sccm of butane and stoichiometric air, corrected to 400°C and for gas expansion for complete combustion.

The dimensions of the catalytic combustor, using the two-stacked-reactor design, are shown in Figure 3-8 (drawing not to scale). Each reactor was formed from two 1-mm-thick silicon wafers through an etching and subsequent bonding process, described in detail in chapter 4. An exterior silicon wall of 500 μm surrounded the channels on all sides to provide mechanical stability and to provide sufficient surface on the exterior of the reactor to allow for consistent, gas-tight bonding of the silicon wafers. The TE modules were intended to align with the center of the "top" and "bottom" faces, covering the width of the channel area (2.75 cm) without overlapping the external walls. The external dimensions of the combustor were 3.5 cm x 2.85 cm x 4 mm in length x width x height. The total internal surface area was 68.88 cm^2, and the internal volume was 1.764

cm^3. The design resulted in 9.9 cm^2 of external surface area not covered by the TE modules. It is worth noting that the combustor is more appropriately termed a "mesoreactor", as the smallest length scale is ~100 μm, though it has been microfabricated.

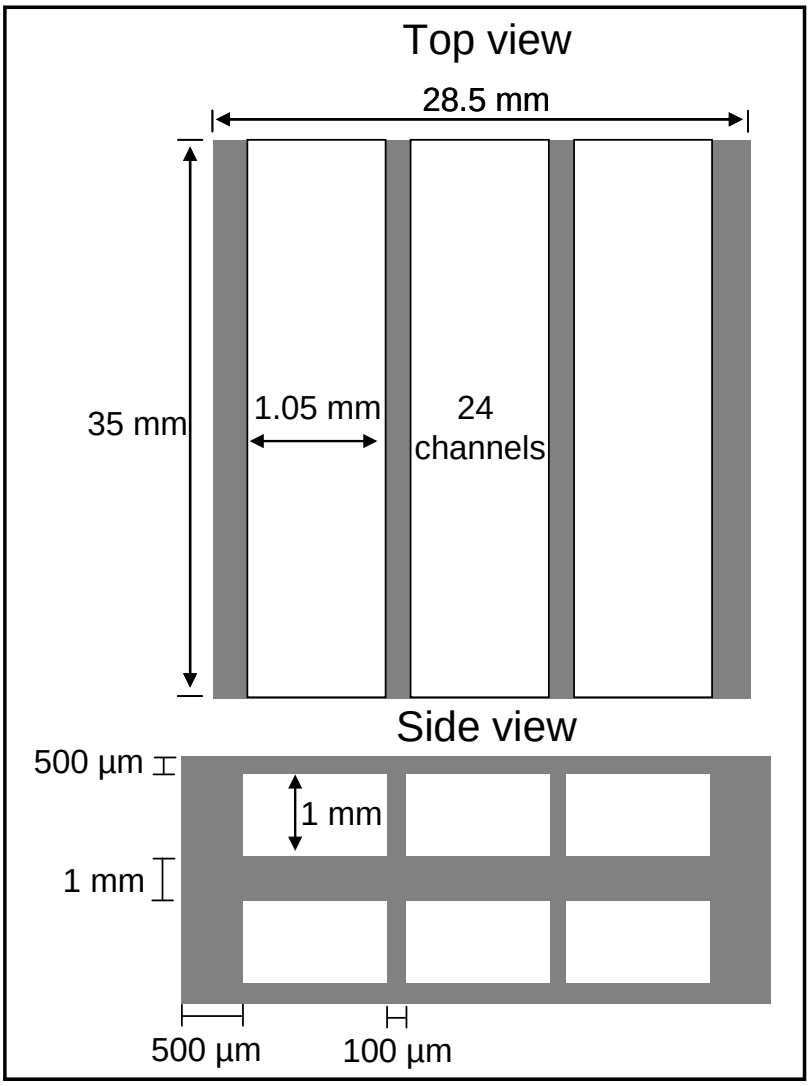

Figure 3-8: Dimensions of combustor made from two stacked reactors. Drawing not to scale.

Another attractive feature of the parallel channel and parallel reactor structure was the ability to implement a counter-current flow arrangement to improve thermal uniformity of the surface. Catalytic combustion channels typically experience increased temperature near the inlet of the gas stream, as the reaction rate is positive order in fuel concentration and the activation energy of the catalytic oxidation is considerable. Through a counter-current arrangement of flow channels, some of the "hot spots" could be located at one

edge of the combustor, while others are located at the opposite end. This arrangement would capitalize on the good thermal conductivity of silicon to provide heat transfer from hot to cold sections of the combustor. It would be possible, and desirable, to implement a channel-by-channel counter-flow arrangement[77], such that the temperature gradients would be separated by only a 100-µm-thick silicon wall. However, in order to simplify fabrication of the combustor and fluidic connections, in this work a reactor-by-reactor counter-current flow arrangement was implemented, as shown in Figure 3-9.

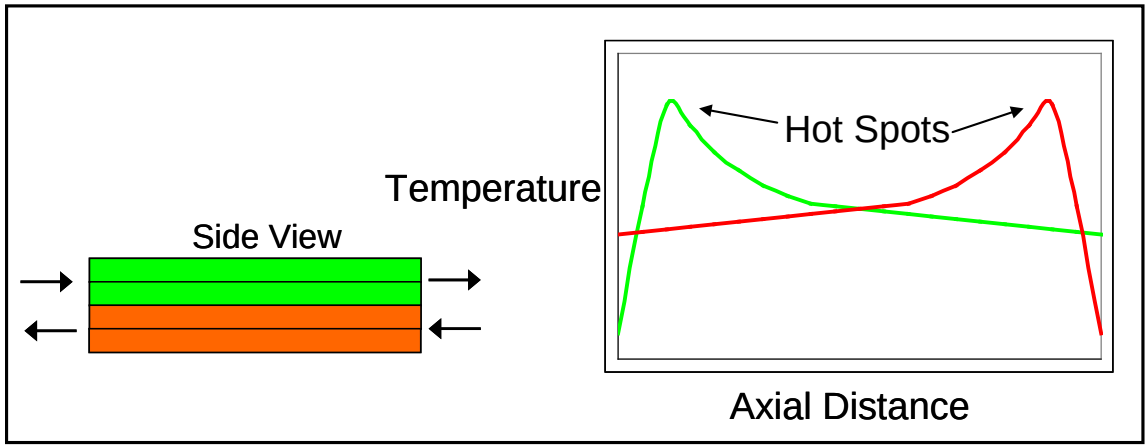

Figure 3-9: Reactor-by-reactor counter-current flow arrangement. The image on the left shows the gas through the top reactor from left to right, and the reverse direction through the bottom reactor. The figure on the right shows the shape of the temperature profiles in the two reactors independent of their interaction, in order to show the two regions where heat transfer between hot and cold sections would be expected to occur.

3.3.3. Fluidic Connections

It has been demonstrated in previous works that the design of fluidic connections for a small-scale combustor can have a major influence on the thermal isolation[52, 76] and flow resistance[102]. The typical approach for small fuel processors has been to interface with capillary tubing, often from the side of the device to limit exposed surface area for heat loss. The identification of a suitable sealant can be a challenge for high-temperature silicon devices, though glass braze techniques have been developed for tube materials such as glass[52] or Kovar[139]. Unless a single serpentine channel is used, the use of capillary tubing necessitates an integrated gas distribution manifold. The on-chip distribution of gases has been demonstrated, using a designed flow restriction that dominates the pressure drop in the reaction zone to achieve even flow. A pressure drop channel for this purpose, developed in silicon for a differential packed bed reactor by

Ajmera, et al.[140], is shown in Figure 3-10. The optimal design of on-chip flow distribution has been studied for parallel channel reactors, where the objective is to precisely design the flow distribution and collection channels such that the pressure drop is equivalent without the imposition of a dominant resistance[141, 142], as shown in Figure 3-11.

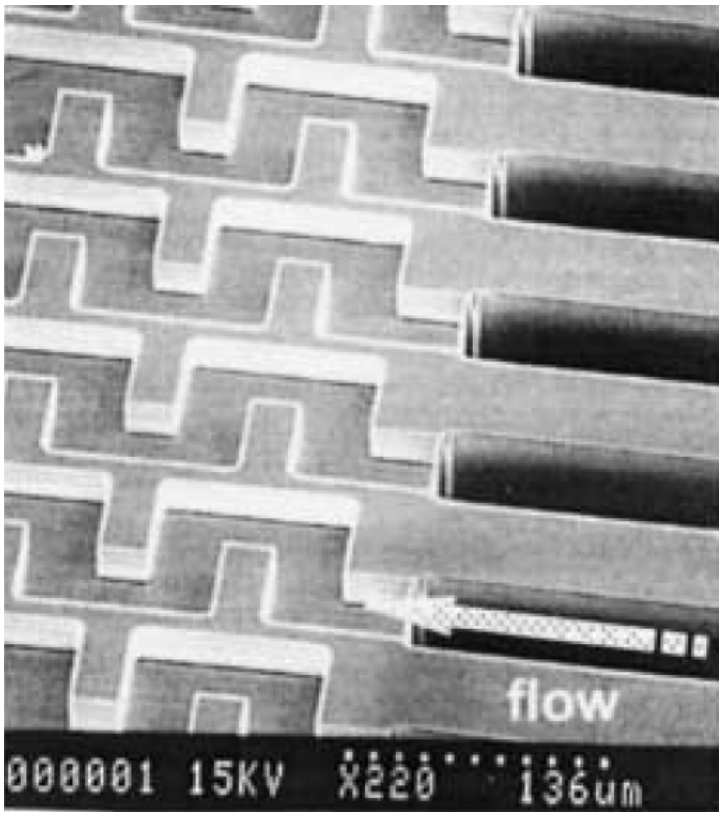

Figure 3-10: SEM image of a shallow flow distribution channel in a silicon microreactor. From Ajmera, et al.[140]

The use of capillaries was considered for the design of the combustor, at least at an early stage. In order to interface with the side of the device, the capillary is typically of the same dimensions as the channel height, which in this case was 1 mm. However, given the considerable flow rate required, in part because of the use of air as the oxidant, the pressure drop was determined to be unmanageably large for a manageable number of tubes (such that could be packaged successfully). The Reynolds number of the flow in the outlet tube was ~10^4, even when considering three outlet tubes per reactor (for a total of 12 tubes attached to the combustor). With 12 tubes (1-mm-diameter), the pressure drop in the inlet tubes was estimated as 112 Pa/cm, which was high considering the 500 Pa total system pressure drop target. Additionally, the pressure drop in the outlet tubes

was estimated as 612 Pa/cm, which was almost certainly unmanageable (though outlet tubes could possibly be eliminated from a final design). A total of 80 capillary tubes were determined to be necessary to reduce the pressure drop through 1 mm conduits to acceptable levels (5 Pa/cm in the inlet tubes, 23 Pa/cm in the outlet tubes); however, the successful packaging of 80 tubes to the combustor was unlikely to be successful. Even with tube diameter increased to 1.7 mm, at least six capillaries were required to achieve an estimated pressure drop below 50 Pa/cm in the outlet tubes. Given this analysis, other fluidic packaging options were considered.

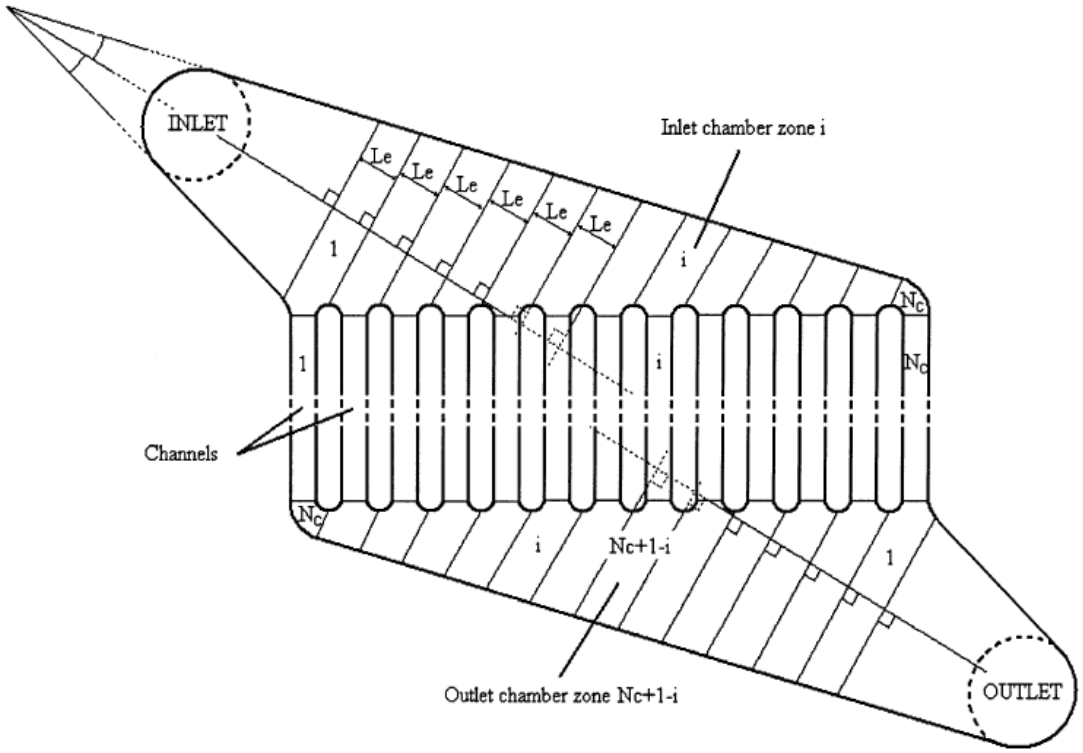

Figure 3-11: Design framework for flow distribution in a channel reactor. From Commenge, et al.[142]

An alternative packaging scheme for forming fluidic connections that was identified, and one that has been used for catalyst monoliths, is the use of compression packaging. With compression packaging, the use of an "external" manifold (that is, one that is not integrated with the channels in the silicon) is common. A recent example of such a packaging scheme, from the University of Connecticut, involved the use of multiple machined brass plates (four per side) for gas distribution, a steel frame for compression, and silicone or graphite gaskets for compliance, as shown in Figure 3-12[71, 77]. The gas distribution was performed on each side of a ceramic monolith with ~1.4 x 2 x 2 in^3 of

brass, and the compression packaging was accomplished by manual adjustment of four bolts. Even distribution of flow was obtained through the use of 1/32-in holes, to dominate the pressure drop differences within the channel. Due to the low thermal conductivity of the ceramic monolith (~2 W/mK), the manifolds were held at ~50°C while methanol was combusted in the center of the monolith.

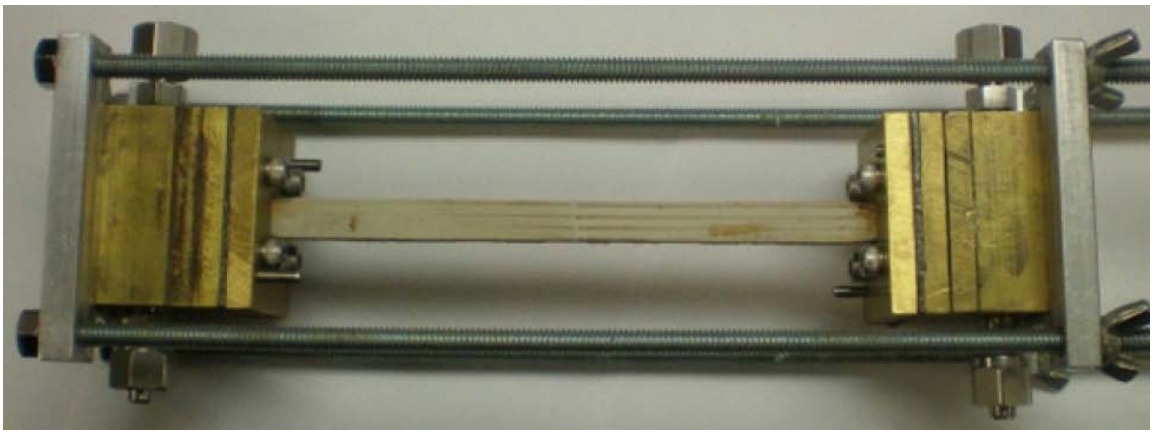

Figure 3-12: Ceramic monolith (150 mm long) with fluidic connections via compression seal using machined brass plates (each 1/8 x 2 x 2 in^3). A metal compression chuck was used to provide sealing force. From Moreno and Wilhite[71].

With the help of collaborators at MIT Lincoln Laboratories, a compression packaging scheme including a low-flow-resistance gas distribution structure was developed for the combustor. The reaction channels were open on both sides of the silicon structure, similar to a monolithic reactor. The concept for the packaging system was to allow the gas to flow through 3/8-in-diameter tubing, within which the pressure drop was extremely low, until just before entering the reaction channel. The design concept for the manifold is shown in Figure 3-13, where one half of the combustor and manifolds is shown. The flow path within the manifolds was designed by our collaborators using CFD simulations to ensure low pressure drop (235 Pa) and uniformity of distribution across the channels (<25 Pa difference through each channel). Additionally, the manifold was designed to provide reactor-by-reactor counter-current flow. A drawing of the designed manifold is shown in Figure 3-14, with a cut out to show the internal flow path. The inlet portions are 10-mm-diameter cylinders, and the flow is smoothed down to a 1-mm-high gap to interface with the combustor. The manifolds were manufactured from 17-4 PH stainless steel using direct metal laser sintering, which is a 3-dimensional printing technique for rapid prototyping. Given the smooth internal layout of the

distribution manifold, this process provided an inexpensive alternative to precision machining. However, the uncertainty surrounding the manufacturing process led to extra material being included in the design, and, as a result, added mass.

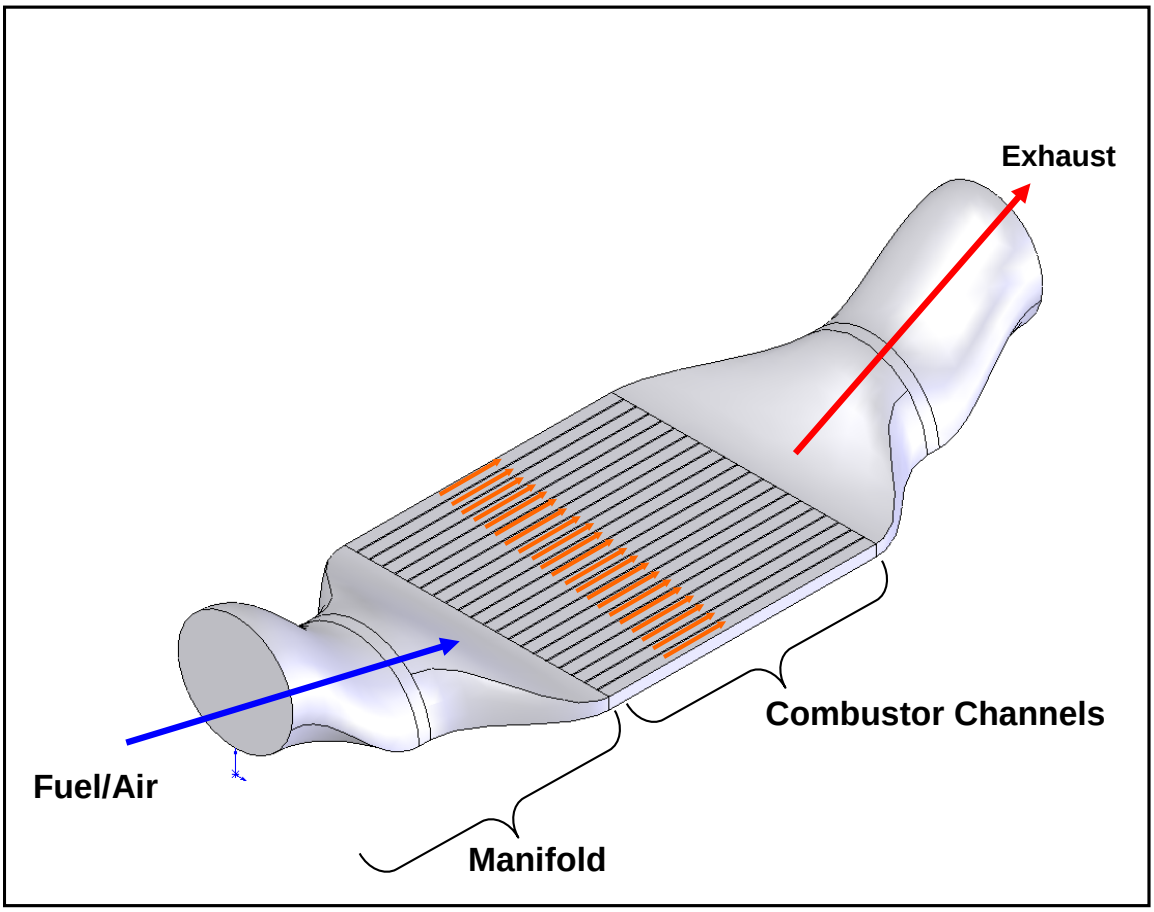

Figure 3-13: Half reactor and manifold design concept. Gas flow is contained in large tube until it is distributed to the reaction channels. Drawing provided by collaborators at MIT Lincoln Laboratories.

The manifolds were designed to be compression-sealed to the sides of the combustor. Unlike the example presented earlier, the manifolds were designed to operate near the combustor temperature (~300°C). A soft 99.999% pure-Al gasket (ACI Alloys and Newcut, inc.) was used to facilitate a gas-tight seal between the steel and the silicon reactors at the operating temperature. One downside of the manifold design is the large increase in surface area operating at an increased temperature, which adds significant potential for heat losses from the manifolds and fluidic connections to dominate the system energy balance. However, calculations performed at MIT Lincoln Laboratories

suggested that the heat loss from the manifolds, after some insulation, would be in the tens of Watts, which could be accommodated within the reactor heat balance.

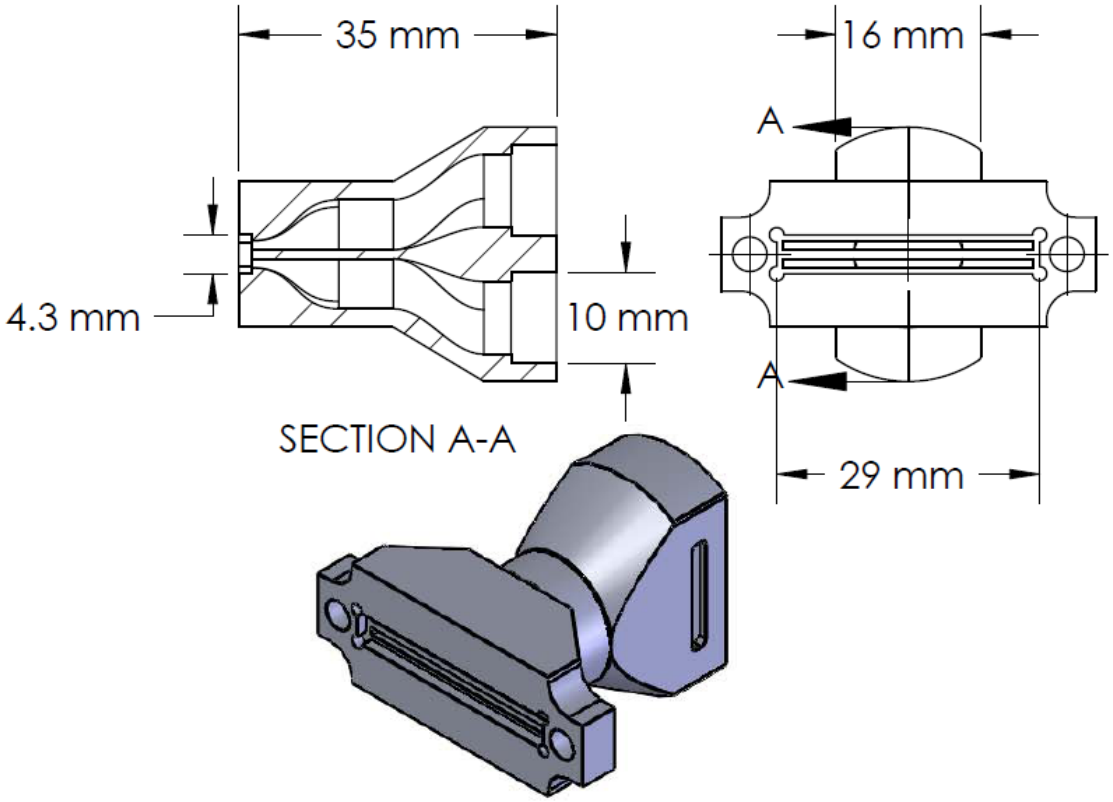

Figure 3-14: Drawing of designed gas distribution manifold for compression packaging of silicon combustor.

3.4. Design of Heat Sinks and Supporting Systems

3.4.1. TE-Mimicking Water-Cooled Heat Sinks

Two heat sinks were developed to mimic the thermal resistance through a high-heat-flux TE module, such that the heat conducted out of the combustor at a given temperature profile would be similar to that of the combustor interfaced with the TE modules. Previous work by Yoshida, et al.[41], in which a butane combustor was successfully operated while insulated but failed after TE module integration due to the increased heat removal, highlights the importance of testing under the proper thermal pathways. The TE-mimicking heat sinks were developed to allow testing of the combustor under "design" conditions while the high-performance TE modules were in development.

The thermal resistance of the heat sink consisted of a copper layer (27.5 x 27.5 x 1.27 mm^3, with a thermal conductivity at 700K of 373 W/mK) on top of a titanium block (27.5 x 27.5 x 12.2 mm^3, with a thermal conductivity at 700K of 10 W/mK), both of which are attached to a water-cooled copper CPU heat sink (Thermaltake). The structure and dimensions of the copper and titanium layers is shown in Figure 3-15. The gaps in the titanium and the copper helped to better mimic the performance of the TE modules, preventing conductive heat transfer within the heat sink from providing additional smoothing of combustor surface thermal gradients. Using a model of heat transfer resistances in series, the effective heat transfer coefficient based on the external area of 2.75 x 2.75 cm^2 is 673 W/m^2K, and correcting to the full surface area of the combustor (3.5 x 2.85 cm^2), the effective heat transfer coefficient is 510 W/m^2K.

The holes in the heat sink were added to provide wells for thin K-type thermocouples, which were positioned at the hot surface and held in place with a polyimide adhesive. The positioning had some errors, and as a result some thermocouples were not functional or were observed to lag the surface temperature as they were withdrawn into the heat sink. The maps of functional thermocouples, along with the labels used to reference them and the direction of gas flow, are given as Figure 3-16 and Figure 3-17. It was observed that the surface temperature measurements were sensitive to variation in the applied compressive force, where some thermocouples that were not adequately compressed against the reactor would measure a lower temperature.

The titanium and copper structures were mounted on a water-cooled CPU heat sink in order to remove the combustion heat. The flow rate of water used to cool each heat sink was on the order of 500 mL/min, which was high enough to eliminate any noticeable impact of water flow rate on heat extraction from the combustor. The temperature of the water entering and exiting the heat sink was measured using K-type thermocouples, and the flow rate of water was measured by timing the collection of water in a graduated cylinder. With these measurements, the heat extracted from the combustor through the heat sink (which served as a proxy for heat transferred through the TE modules) was determined from calorimetry, based on the temperature rise observed in the water.

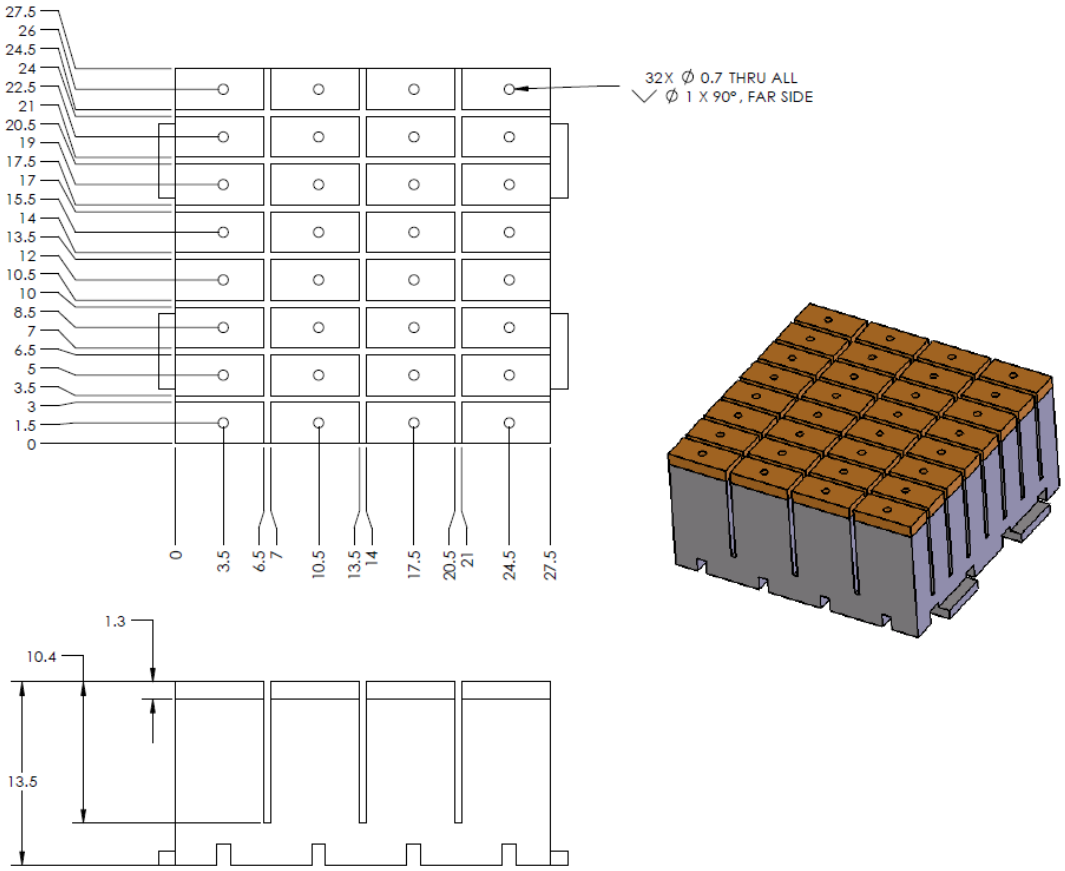

Figure 3-15: Dimensions of TE-mimicking heat resistance, with integrated thermocouple wells for combustor surface measurements. The light brown color indicates the copper layer, and the grey layer indicates the titanium layer. Drawing provided by collaborators at MIT Lincoln Laboratories.

3.4.2. Commercial TE modules and Air-Cooled Heat Sinks

In order to demonstrate the performance of the catalytic combustor as a TE generator, commercial TE modules were obtained from Hi-Z technology, Inc. The HZ-2 modules were used, which are designed to generate 2.5 W electrical power with a temperature difference from hot to cold sides of 200°C. The reported thermal-to-electrical energy conversion efficiency of the bismuth-telluride-based modules at the design conditions is 4.5%. The reported temperature limits of the modules are 400°C intermittently and 250°C for continuous operation; however, the vendor claimed that 300°C operating temperature would be tolerated for a significant length of time (on a timescale of months) without a notable degradation of module performance.

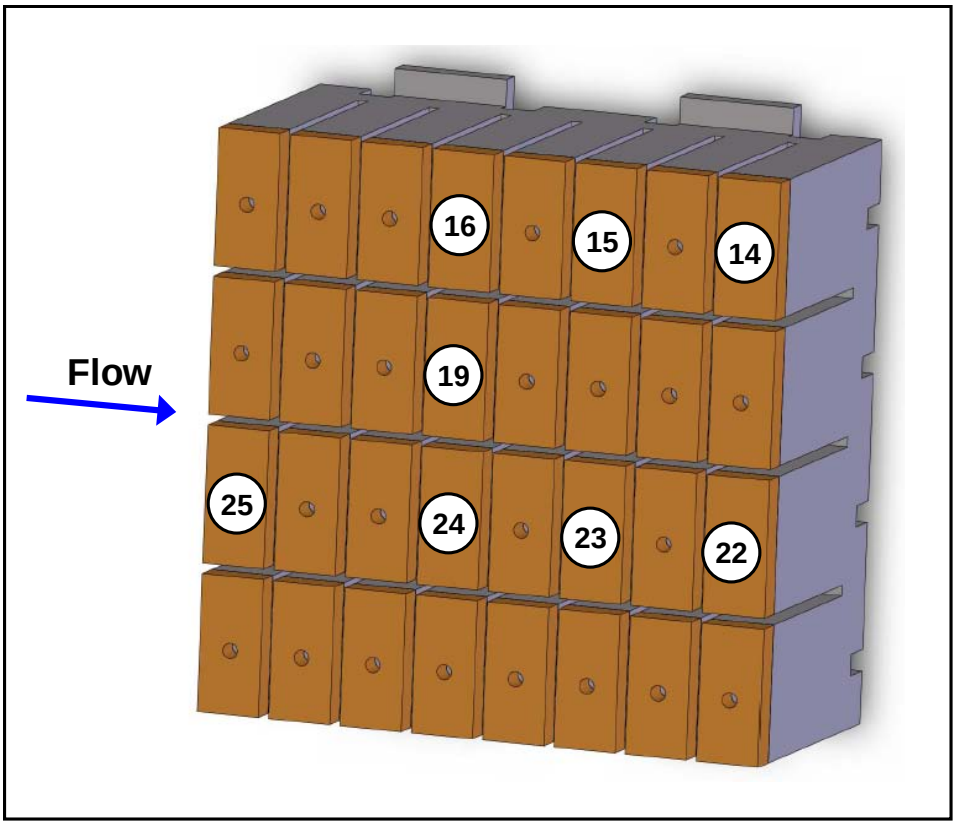

Figure 3-16: Thermocouple labels and positions relative to flow direction for heat sink 1.

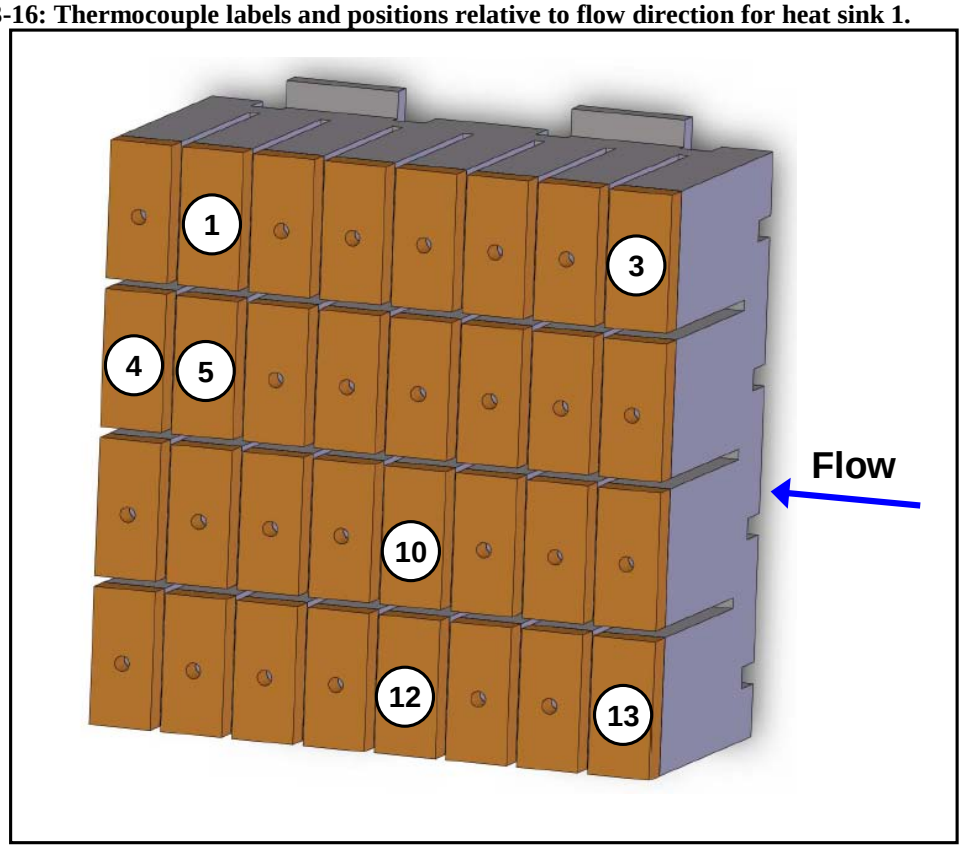

Figure 3-17: Thermocouple labels and positions relative to flow direction for heat sink 2.

The HZ-2 modules have been used in the leading portable-scale TE power generation demonstrations in the literature, from the Vlachos group at the University of Delaware[30, 43, 44]. The module was selected based on the footprint area, which is similar to that of the design modules at 2.9 x 2.9 cm^2. Based on the reported heat flux through the TE module at the design temperatures (230°C on the hot side, 30°C on the cold side) of 9.54 W/cm^2, the effective heat transfer coefficient based on the total area of the combustor is 398 W/m^2K, which is only 78% of that of the design modules.

In order to remove the heat transferred through the TE modules, two light-weight air-cooled heat sinks were obtained from Aavid Thermalloy to dissipate ~260 W of heat with a temperature less than 100°C. The heat sinks consisted of a solid block of metal, which had similar footprint dimensions as the TE module, with copper heat pipes connecting to a large array of aluminum fins (~8 x 8 cm^2 finned area). The heat sinks were cooled by air from a CPU-case fan (Delta AFB0805H), which consumed an estimated 1.35 W of electrical power; however, experiments by Aavid Thermalloy confirmed that the heat sinks would provide adequate cooling with a reduced power consumption of 0.8 W for the fan. The heat sinks and TE modules were compressed on either side of the reactor using two machined aluminum clamp plates.

3.4.3. Exhaust Water Condenser

In order to measure the exhaust gas composition using a mass spectrometer (MS), the water from the exhaust needed to be condensed. While the MS is capable of accommodating the water, a long (25 ft), narrow (~50-μm-diameter) capillary tube was used to provide adequate pressure drop between the MS and the system, and condensed water in this capillary was very difficult to remove. However, it was desired not to impose significant back-pressure on the combustor system, as the compression seal was designed to operate near ambient pressure and was not as effective at elevated pressures. The typical condenser design to provide sufficient heat transfer is to bubble the exhaust through water. The pressure head imposed by one inch of water is 249 Pa, which is similar to the pressure drop in the reactor. As such, a different condenser design capable of accommodating significant heat transfer from large gas flows and continuous operation (as the experimental timescale was on the order of hours) was desired. The

condenser was developed using stainless steel ball bearings inside a glass jar to provide surface area for heat transfer without imposing a large flow resistance. A copper tube was coiled inside the jar, in contact with the stainless steel bearings, through which cold water was circulated to control the temperature. The exhaust stream was introduced to the jar at the bottom of the ball bearings, and the gas was removed from the jar through an opening at the top. In order to avoid condensed water from covering the exhaust inlet, the jar was angled at ~45° so that the water would pool without obstructing the inlet. A flexible tube was placed at in this "pooling" region, and the condensed water was removed using a syringe.

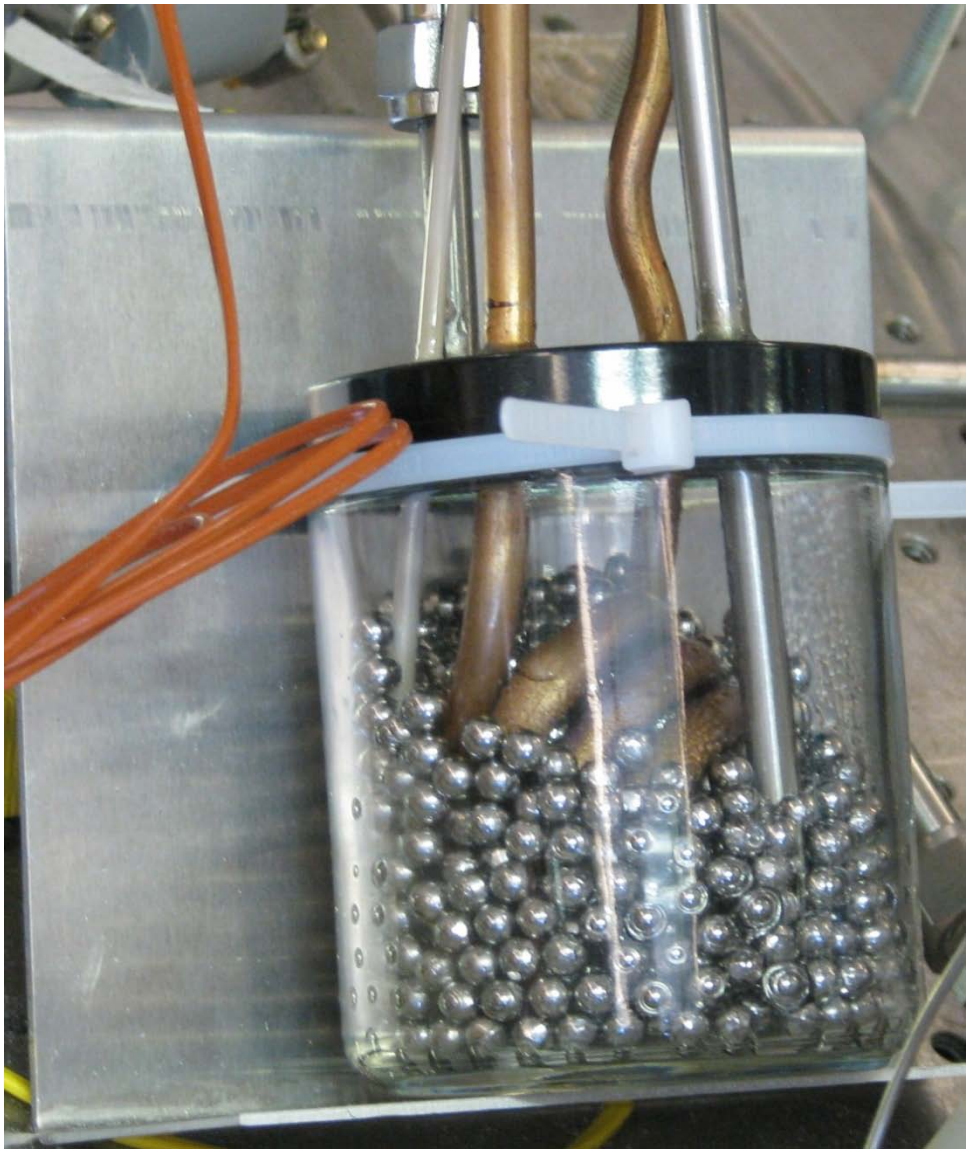

Figure 3-18: Condenser designed to remove water from exhaust stream and protect MS-sample capillary.

3.5. System Models

3.5.1. Simple Heat Transfer Models for Estimating System Heat Balance

Thermal management is critical for small scale autothermal devices like the combustor. Because heat loss scales with the external surface area and heat generation scales with the volume, the heat loss becomes a much larger component of the heat generated at small length scales. The possibility for heat loss to the environment to dominate the system energy balance meant that one of the first steps to evaluate the impact of any design concept or modification was to use simple heat transfer models. During the design of the combustor, many such calculations were performed; however, in this section the focus is on the simple models which describe the final combustor design.

The amount of exposed area which is available for a given heat transfer pathway is a critical aspect of the system energy balance. For the combustor, the external features are two large faces (2.85 x 3.5 cm^2) which interface with the TE modules (2.75 x 2.75 cm^2 for the design case, though slightly larger for the commercial modules), two side faces (3.5 cm x 4 mm) which are open to the environment, and two channel faces (2.85 cm x 4 mm, with 48 channels of 1.05 x 1 mm^2 open area) which are connected to the gas distribution manifolds. However, the conductive losses through the fluidic connections depends also on the tube sizes and thicknesses, which in the design system consisted of four 3/8-inch stainless steel tubes (each having ~19.7 mm^2 surface area, and thermal conductivity ~19 W/mK). The convective heat transfer coefficient for natural convection is typically in a range from 1 to 20 W/m^2K, and in these simple models the top of this range was used. While this was not necessarily representative of the experimental set-up, located in a ventilated hood with significant air flow, it was appropriate for the end-use as a consumer or military device. For radiative heat loss, the emissivity of silicon was assumed to be 0.65. To calculate enthalpic losses to the exhaust gas, specific enthalpies were obtained from Felder and Rousseau[91].

The estimated convective heat loss from the exposed side faces and the portions of the large faces not covered by the TE modules, assuming an isothermal reactor temperature of 423°C and an air temperature of 27°C, was 6.1 W, which is 1.7% of the estimated total

350 W heat released. The estimated radiative heat loss from the same silicon surface was 6.6 W (1.9% of 350 W). From these two estimates, it was confirmed that the aspect ratio of the combustor was sufficiently large that radiation shields (on the reactor sides) or vacuum packaging were not required. It was also noted that area, and thus the heat loss, of the portion of the large faces not covered by the TE module was larger than that of the side faces. If this heat loss were to become a concern, it would likely be easier to improve the packaging and manufacturing precision to allow the TE to cover more of the combustor surface than to attempt to reduce the heat loss from the sides.

The heat loss to the enthalpy of the exhaust gas is dependant on the air excess (or the air equivalency, which is its inverse) that is used in the combustor, as well as on the temperature of the reactor. For an air-breathing combustor, the enthalpy loss is a significant component of the total heat released because of the large amount of nitrogen that passes through the system. The stoichiometry of the butane combustion reaction is such that the 24.45 moles of nitrogen are heated to the combustion temperature for every mole of butane combusted at the stoichiometric air flow. The enthalpy loss to exhausted nitrogen, as a function of the ratio of air flow to the stoichiometric air flow and assuming 25°C ambient temperature, is shown in Figure 3-19. Based on this relationship, it is clear that an enthalpy recovery zone could be required to achieve very high combustor efficiencies, and that there is a significant penalty for operation with excess air. For stoichiometric air flow at 423°C, the enthalpy loss to nitrogen was estimated to be 40 W (11.5% of 350 W), and the total enthalpy loss from the exhaust (including nitrogen) was estimated to be 56 W (16% of 350 W).

Depending on the insulation over the gas distribution manifolds, the heat loss from the system could change significantly. However, heat loss model assumed that sufficient insulation could be provided such that the heat loss from the manifolds would occur primarily through conduction along the 3/8-in-diameter tubes (which were also designed to be insulated in order to increase the length over which the temperature would be reduced from 423°C to room temperature. Given an insulated length of 5 in (12.7 cm), the conductive loss through the four stainless steel tubes was estimated to be 4.7 W (1.3%

of 350 W). Obviously, any conductive heat loss from the insulated surface would add to this amount; however, it is also likely that the hot exhaust gases will transfer some heat to the tubes and the manifolds, possibly reducing the error from the neglected convective and radiative loss.

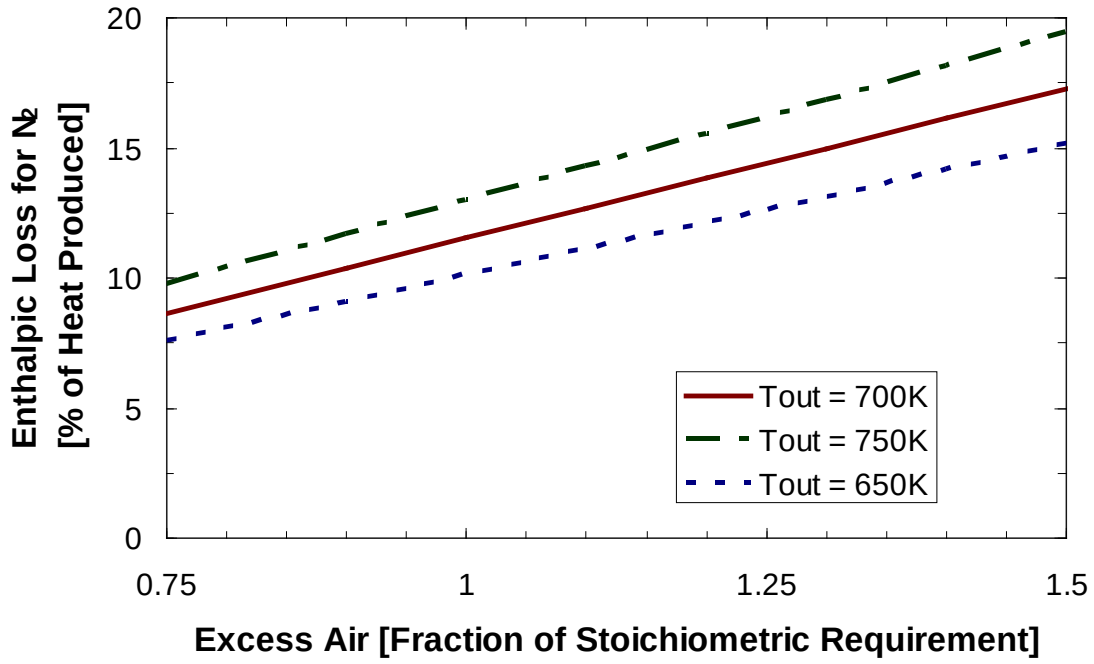

Figure 3-19: Enthalpy loss to nitrogen, assuming ambient temperature of 25°C, as a percentage of the heat released from butane combustion, for various reactor temperatures (Tout) and air excesses.

The estimated heat loss from an isothermal reactor at 423°C was 73.4 W, or 20.9% of 350 W. This indicated that the designed combustor was likely in the neighborhood of the design target for efficiency, at least within the accuracy of these simple models. The simple models also provided some sensitivity information for slight modifications to the design during implementation.

3.5.2. Kinetic Model of Butane Combustion over Platinum Catalyst

Kinetic parameters for butane combustion on a Pt/Al_2O_3 catalyst were scarce in the literature. The most relevant data was published by Yao[116], and included some simplified models for butane over platinum foil and $Pt/\gamma\text{-}Al_2O_3$. The reported rate equation for butane combustion had a first order dependence on the butane partial pressure, and an inverse dependence (exponent of -1) on the oxygen partial pressure. The activation

energy (17 kcal/mol) and turnover number for 0.22% by weight platinum on γ-Al_2O_3 were reported. Similar activation energy was reported for butane combustion over platinum foil (18kcal/mol)[143], (17kcal.mol)[144], (20.1kcal.mol)[114] and platinum wire (23.9 kcal/mol)[115, 145]. A more detailed, reduced surface mechanism for butane combustion on platinum was proposed by Deshmukh and Vlachos; however, the model requires parameters not readily available for butane[146]. The turnover numbers reported by Yao were adjusted to account for the higher platinum loading (5% by weight), and the one-step model used to predict conversion in this work is given as Equation 21. The reaction rate predicted with standard conditions in the reactor is on the order of 10^{-5} mol /s/cm^2.

$$-r = 38.93 \frac{mol}{s\,cm^2} \exp\left(\frac{8560.4\,K}{T}\right)\left[C_{butane}\right]^{1}\left[C_{oxygen}\right]^{-1} \qquad \textbf{[21]}$$

3.5.3. Three-Dimensional CFD Reactor Model

A three-dimensional CFD model was developed to predict the performance of the combustor using the CFD-ACE+ software package. This package has been used previously by Blackwell to obtain reasonable predictions of catalytic combustor performance, including steady-state temperatures and thermal gradients[52]. The sensitivity of the results to the kinetic parameters was minimal, as the reaction was predicted to be limited by diffusion in the bulk. The model describes an interior channel (i.e., assumed symmetry at the side wall and middle of the channel), and the geometry is illustrated in Figure 3-20. The dimensions of the channel were similar to those described previously with the exception that the length of the channel was 2.9 cm (as the simulation was performed before the final length had been selected). The simulation assumed that the inlet gas to the reactor channel was heated to 600K (similar to the observed temperature of the gas distribution manifold at steady state). The model consists of mass, momentum, and energy balances.

The simulation grid consisted of 237350 cells with 267648 nodes. The challenge for the simulation was to provide sufficiently dense mesh to capture the rapid changes in temperature and concentration near the inlet of the channels and near the walls, while maintaining a small enough problem to allow for a solution in a reasonable timescale. In

the “y”-direction (defined in the figure), the grid points were distributed evenly with 25 grid points per 1 mm. In the “x”-direction within the channel volume, 20 grid points were distributed over 0.525 mm, with spacing following a power law distribution with an exponent of 2 in order to provide more points near the wall, and less points near the middle of the channel. In the “x”-direction within the side wall, 7 points were distributed across 0.05 mm, also with a power law distribution and exponent of 2 to allow for more points near to the channel wall. In the “z”-direction, 102 points are distributed across 29.05 mm with a power law spacing exponent of 1.3, to allow more points near the inlet of the channel. A traditional mesh-refinement study was not done, in part because the simulations were quite slow to converge. After some trial-and-error, the largest mesh such that a solution could be achieved within a reasonable timeframe was considered to be acceptable. Ideal gas properties were assumed for the gas species, and a piecewise-linear relationship for the temperature-dependent thermal conductivity of silicon was used.

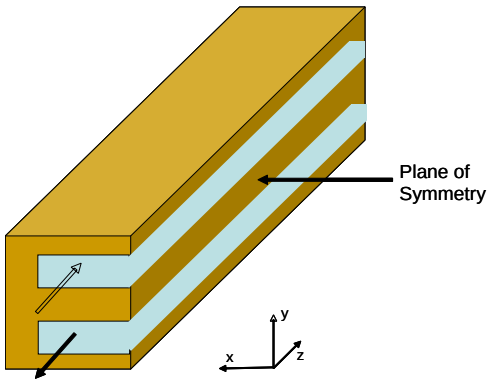

Figure 3-20: Drawing of half-channel modeled in CFD simulation.

The boundaries within the model are illustrated in Figure 3-21, and the corresponding boundary condition equations are given in Table 3-2. The channel was considered to be adiabatic at all of the external faces save for the top and bottom face corresponding to the TE module interface. The assumption of insulated ends corresponding to the fluidic connections is a common simplification applied to small-scale combustor models in the literature (e.g., [101, 147, 148]). In this work, the conductive heat loss to the manifolds was not well known when the models were developed, and so this simulation was used to assess the case of “well-insulated” manifolds. The heat transfer through the two TE modules was modeled with an effective convective heat transfer coefficient of 589 W/m^2K, which

corresponds to the thermal resistance of the heat sinks on a basis of the area of a 29-mm-long channel. The external temperature for the convective heat loss was 380K, which was to account for the anticipated rise of the air-cooled heat sinks as designed.

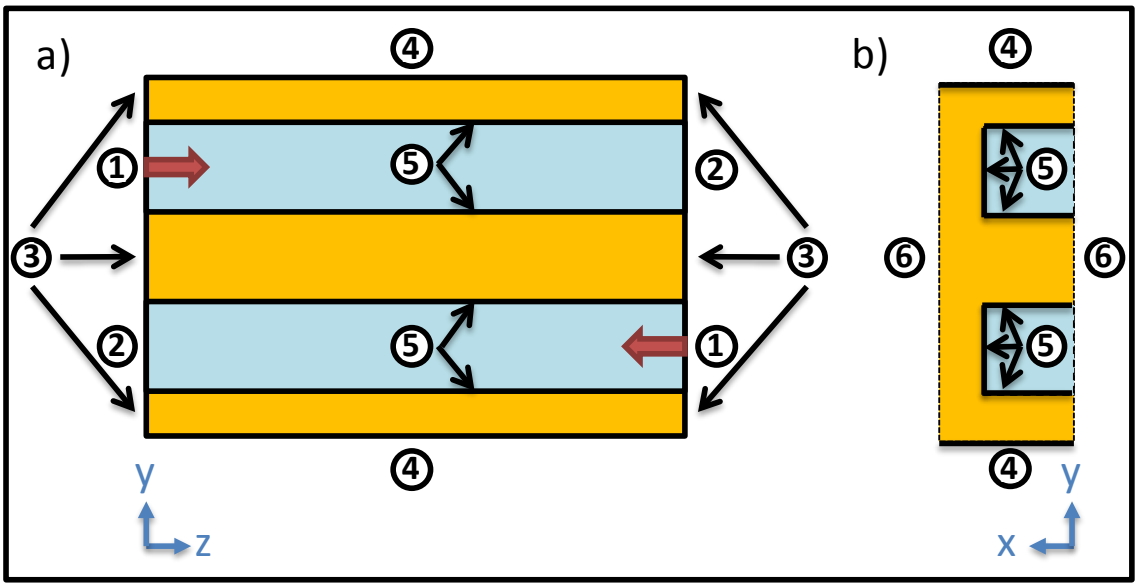

Figure 3-21: Labeled boundaries to identify conditions for CFD model. Circled numbers identify the boundary. Gold-colored regions represent silicon, blue regions represent the gas channel, and the red arrows indicate the direction of gas flow (at the inlet). a) shows the y-z plane (axial slice) and b) shows the x-y plane (channel cross-sectional slice).

The model predicted temperature and butane concentration profiles along the center of the channel are shown in Figure 3-22. The butane conversion in the combustor was predicted to reach 93%, and this result was used to support an increase in channel length from 29 to 35 mm in the final design. The maximum temperature at the external wall of the combustor was predicted to be 798K, which is in excess of the design limitation for TE power generation considered in this work. However, it was believed that the inlet wall temperature in the actual system was reduced (compared with this model) as a result of conductive heat losses through the distribution manifold. The positioning of the hot spot at the entrance of a combustion channel has been reported elsewhere in the literature when insulated fluidic connections are assumed[148], and Blackwell showed that the hot spot would be located further in the channel when conductive loss was included[52]. The maximum temperature difference at the external wall was 120K, which is higher than is desirable. This temperature gradient was reduced as a result of conductive heat losses to the gas manifold in the experimental system, and also by a heat spreading layer of graphite that was placed between the combustor and the TE junctions in the actual device.

The reduction in axial thermal gradients as a result of the counter-flow arrangement was observed in the CFD model, as the surface temperature profile was slightly "U-shaped", increasing as the hot spot from each reaction was approached.

Table 3-2: Boundary conditions for CFD model. Interface labels correspond to images in Figure 3-21. T refers to temperature, u refers to velocity, y_i refers to the mole fraction of species i, k is the thermal conductivity of silicon, D_i is the diffusivity of species i, C_0 is the total gas concentration, A is the pre-exponential factor of the reaction rate, EA is the activation energy of the reaction rate, R is the universal gas constant, and γ_i is the stoichiometric coefficient of species i in the combustion reaction (positive for products and negative for reactants).

Boundary Label	Type of Interface	Boundary Conditions
1	Fluid Inlet	$u(x,y,z_1) = u_0 = 6.23\ \frac{m}{s}$ $y_i(x,y,z_1) = y_{i,0}$ $T(x,y,z_1) = T_0 = 600K$
2	Fluid Outlet	$\frac{\partial}{\partial z}(\theta) = 0\ \forall\ \theta(x,y,z_2)\ \epsilon\ \{u, y_i, T\}$
3	Insulated Solid Surface	$\frac{\partial}{\partial z}T(x,y,z_3) = 0$
4	Flux Matching "TE" Heat Removal From Solid Surface (Modeled as Convection)	$k\frac{\partial}{\partial y}T(x,y_4,z) = -h(T - T_\infty)$ $= -589\ \frac{W}{m^2K}(T - 298K)$ *Note that sign changes for top vs. bottom surface
5	Surface Reaction	$-D_i \left.\frac{\partial y_i}{\partial a}\right\|_{surface} = \gamma_i\ A\ exp\left(\frac{-E_A}{RT}\right)\left.\frac{C_{butane}}{C_{oxygen}}\right\|_{surface}$ *Note that "a" is a dummy variable to indicate the Cartesian direction normal to the surface. Also note that the sign changes for top vs. bottom surfaces. Of course, there is also a reaction heat source term at the wall surface proportional to the reaction rate.
6	Symmetry Boundary	$\frac{\partial}{\partial x}(\theta) = 0\ \forall\ \theta(x_6,y,z)\ \epsilon\ \{u, y_i, T\}$

3.5.4. System Timescales

In order to achieve high fuel utilization rates in a catalytic combustor, the residence time, τ_f, should be on the greater than the relevant timescale for diffusion, τ_d. These timescales can be estimated according to Equations 22 and 23, where D_b is the diffusivity of fuel in

air, Q is the volumetric flow rate of the gas, L is the length of the reactor, and d_h is the hydraulic diameter. The reaction time, τ_R, is estimated according to Equation 24, where C_{bo} is the initial fuel concentration, V is the reactor volume, $-r_m$ is the maximum reaction rate, and A_{cat} is the surface area of catalyst.

$$\tau_f \sim \frac{L d_h^2}{Q} \qquad [\ 22\ ]$$

$$\tau_d \sim \frac{d_h^2}{4D_b} \qquad [\ 23\ ]$$

$$\tau_R \sim \frac{C_{bo} V}{(-r_m) A_{cat}} \qquad [\ 24\ ]$$

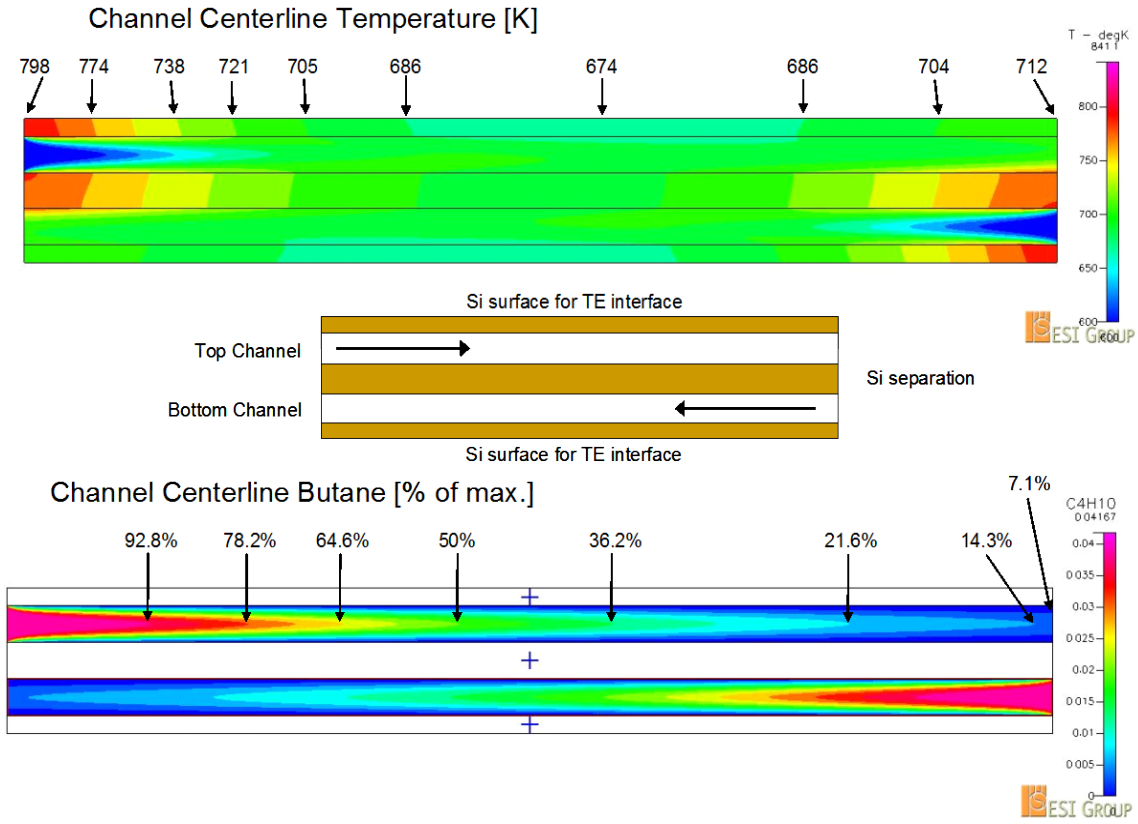

Figure 3-22: Temperature (top image) and butane concentration (bottom image) profiles at the center of the channel, as predicted by CFD simulation.

Given the reactor dimensions, the diffusion time was on the order of 6 ms. The volumetric flow rate of the gas depends on the temperature of the gas stream, and as such the assumed temperature impacts the residence time calculation. For 6 slpm, over a range

of 25 to 400°C, the residence time varied from 16 ms to 7 ms, and this indicates that the reaction may become diffusion limited for flow rates and temperatures above 6 slpm and 400°C. The reaction time at 700K was estimated to be on the order of 2 ms, and so the reaction was expected to be bulk diffusion limited. This provided valuable insight into the benefit of various design modifications, such as longer channels, higher platinum concentrations, or catalyst additives. Internal features which would decrease the characteristic length scale for diffusion (such as internal posts or more narrow channels) would be likely to increase the potential throughput of the reactor.

3.5.5. Model of Electrical and Thermal Transport in Thermoelectric Module

In order to predict and understand the electrical and thermal transport in the TE modules, a model was developed that included the major heat transfer processes involved in TE power generation. A schematic of the system is shown in Figure 3-23, which shows the TE modules as a series of "N"- and "P"-type elements connected electrically in series (as shown by the copper-colored interconnects between alternating elements) and thermally in parallel between the hot combustor, at a temperature T, and the cold heat sink, at a temperature T_c. Also shown in this schematic is the electrical insulation shim between the TE modules and the reactor or the heat sink, with a temperature drop across the shim of ΔT_s. The simple model was adapted from Rowe[32] to represent an autothermal reactor. A similar model to that of Rowe has been used by Shakun to predict the performance of Peltier coolers[149]. A more detailed, discretized model was used by Rodriguez, et al., to describe a TE power generator with considerable success, as demonstrated in Figure 3-24[150]. However, the terms in the model were the same as those used in this work, with the exception that the Thompson effect was explicitly included by Rodriguez, et al. In this model, as described by Rowe, the error resulting from the neglecting of the Thompson effect is mitigated by the use of material properties (i.e., Seebeck coefficient, thermal conductivity and resistivity) evaluated at the average temperature.

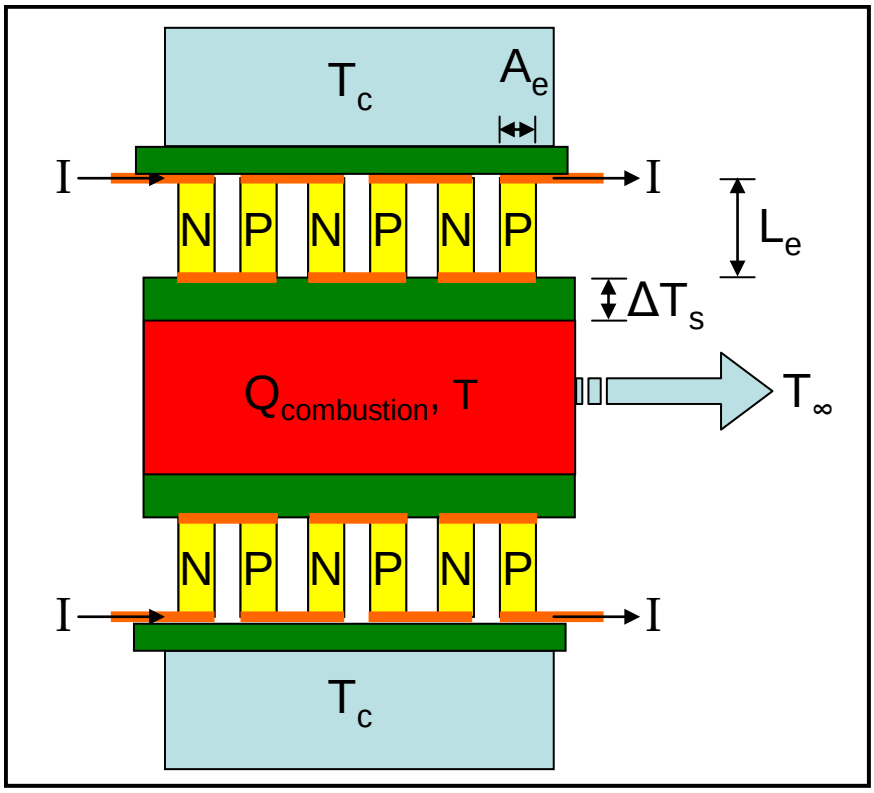

Figure 3-23: Schematic of the TE modules interfaced with the combustor and the heat sinks.

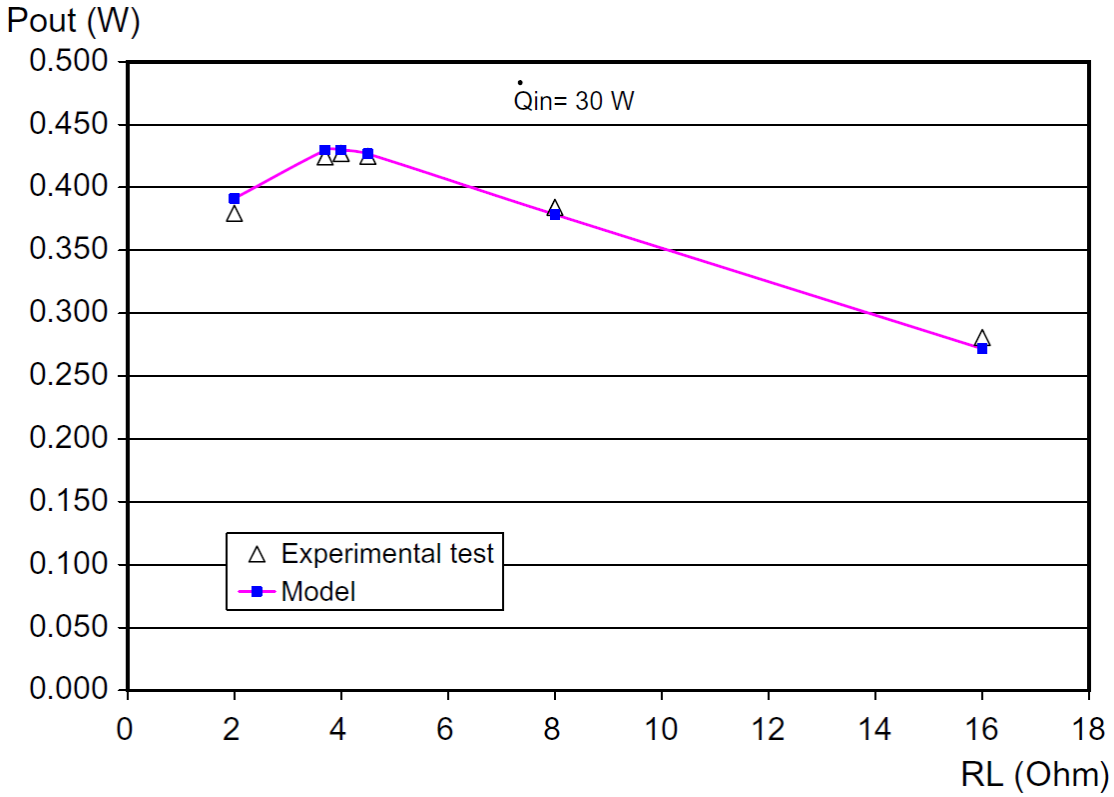

Figure 3-24: Comparison of model prediction and experimental observation of power generation using the discretized model from Rodriguez, et al.[150]

Given that the TE materials bridge two different temperature zones in the combustor and the heat sink, there is convective heat transfer from the hot to the cold side. The conductive heat transfer through one TE element is given by Equation 25, where the subscript "j" refers to either N- or P-type material, k_j is the thermal conductivity of material j, assumed to be isotropic, A_e is the cross-sectional area of the element (assumed to be the same for N and P), and L_e is the length of the element (assumed to be the same for N and P). The heat loss from the sides of the elements is neglected in the model, as is the heat transferred through the packaging materials. The conductive heat transfer is the largest pathway from the combustor to the heat sink.

$$Q_{conduction,j} = \frac{A_e k_j}{L_e}\left(T - T_C - 2\Delta T_s\right) \qquad \textbf{[25]}$$

The second largest heat transfer pathway is the Peltier effect, which is the heat released or absorbed by the charge carriers accompanying a change in entropy as they undergo a reversible process of crossing a junction (from one TE element to the other). As the Peltier heat is proportional to the charge carrier transport, the effect is related to the current flow in the electrical system, as described in Equation 26, where the subscript j refers to the N- or P-type elements, I is the current, and α is the Seebeck coefficient. The Peltier heat in this equation refers to that removed from the hot side, rather than that released on the cold side. As mentioned above, the Thompson effect, which is often described as an effect related to the heat capacity of the charge carriers, has been neglected.

$$Q_{Peltier,j} = \left|\alpha_j\right|\left(T - \Delta T_s\right)I \qquad \textbf{[26]}$$

The smallest of the heat terms, for common TE materials, is that of the Joule heating of the TE materials, given the non-negligible resistivity of common materials. Half of the heat generated from Joule heating in the element reaches the hot side, and is calculated according to Equation 27, where ρ_j is the resistivity of material j. The Joule heating effect is typically small compared to that of conduction and Peltier heat.

$$Q_{Joule,j} = \frac{L_e \rho_j}{2A_e} I^2 \qquad \textbf{[27]}$$

These heat transfer pathways can be compared with the combustor performance, given by the heat released from combustion, $Q_{combustion}$, and the heat loss to the environment which is represented here with a lumped heat transfer model as $(UA)_{loss}$. It is also possible to break the lumped heat transfer coefficient into its component conduction, convection, and radiation loss terms, as was described for the simple energy balance. The energy balance on the combustor can be solved to estimate the heat loss from the system, as shown in Equations 28 to 32, where T is the reactor temperature, T_∞ is the ambient temperature, Q_i is the heat flux through pathway "i", H(T) is the enthalpy at temperature "T", N is the number of TE pairs in the two modules, and the other terms have been previously defined. The temperature drop across the electrical insulation shim was assumed to be 18°C.

$$(UA)_{loss} = \frac{1}{(T - T_\infty - 2\Delta T_s)}\left(Q_{combustion} - Q_{enthalpy} - Q_{conduction} - Q_{Peltier} + Q_{Joule}\right) \quad \textbf{[28]}$$

$$Q_{enthalpy} = H_{exhaust}(T_H) - H_{exhaust}(T_C) \quad \textbf{[29]}$$

$$Q_{conduction} = \frac{N A_e (k_n + k_p)}{L_e}(T_H - T_C) \quad \textbf{[30]}$$

$$Q_{Peltier} = N(\alpha_p - \alpha_n) T_H I \quad \textbf{[31]}$$

$$Q_{Joule} = \frac{N L_e (\rho_p + \rho_n)}{A_e} I^2 \quad \textbf{[32]}$$

3.6. Mass of System Components

For the design of a portable device, the mass of system components is a critical target. Given its small size and low density, the silicon combustor had a mass of 5.6 g, which made it especially well suited to the production of a portable power generator. The mass of the gas distribution manifolds and the bolts used to compression-seal the combustor was 147 g, which is considerable. However, there is significant margin for weight reduction from the current manifold design. The combined mass of the air-cooled heat sinks used to cool the TE modules was 159 g, and the mass of the TE modules was 28 g. Therefore, the mass of "critical" system components was 338 g, which is suitable given the design target of <1 kg for the total system.

3.7. Concluding Remarks

An iterative process was used to design a combustor and system that could meet the aggressive design targets and constraints of the portable TE power generator. Simple models were used to sort through design concepts, details of fabrication techniques and their associated limitations were investigated to refine these designs, and detailed models were used to improve and verify the utility of the final designs, as well as to identify sensitivity to design changes.

A silicon monolithic reactor was designed to interface with external gas distribution manifolds using a compression seal and a soft metal gasket. A configuration of two stacked reactors was used to increase catalyst surface area, decrease channel pressure drop, and enable a simple counter-current flow arrangement to reduce axial temperature gradients. Suitable models were used to confirm that the design was likely to achieve the release of ~350 W (based on LHV) from the combustion of butane in air with ~80% of the heat transferred through two TE modules, and requiring less than 500 Pa of pressure for forced-air flow through the device.

4. Silicon Reactor Fabrication

The design and execution of a silicon microfabrication process can pose a significant challenge for MEMS-based research efforts. The basic design of a fabrication process involves the selection of an etch technique for the definition of features, the selection of an appropriate etch mask, the definition of features in the etch mask (typically using photolithography), the removal of silicon to form the desired features, and the enclosure of channels with some capping material such as Pyrex or another silicon wafer. The selection of process steps can have a significant impact on the processing time, cost, mechanical robustness and chemical properties of a silicon reactor. The goal in this work was to develop a reliable, inexpensive, and parallelizable fabrication process to produce combustors according to the design presented in chapter 3.

4.1. Silicon Etching Techniques

For devices made from silicon, channels have often been defined using proximity or contact photolithography and a subsequent chemical etch, though other methods exist. Channels can be etched using an anisotropic etchant such as potassium hydroxide or an isotropic etchant such as a deep reactive ion etch (DRIE). The appropriate etch technique is determined by the specific layout of the flow path, as certain geometries cannot easily be accessed using anisotropic etching. Details on silicon etching can be found in Plummer, et al[151]. A wide variety of features have been demonstrated using DRIE, which is a common term for multiple time-multiplexed inductively coupled plasma etches[152] that has been developed to provide etched features in silicon with large aspect ratios. Features of interest for combustors demonstrated with DRIE include gas distribution manifolds[140], fuel injection nozzles[153], catalyst support structures[154], and thermal isolation zones[73, 155, 156]. Typically, vertical features are formed in silicon using DRIE, including the common design of channels with rectangular cross section. As demonstrated by the example structures listed above, DRIE features can take any number of widths or directions on the wafer, allowing for curved or expanding features. As well, features can be arranged with very narrow spacing between them, allowing for highly efficient utilization of chip area. However, in a given etch process all features must be etched to similar depth, necessitating multiple masks to achieve multiple etch depths. The major

drawback of DRIE features for a device intended for large-scale production (such as a portable power generator) is that it is an expensive, serial process (per wafer).

Wet etching techniques are much less expensive than DRIE, and allow for large parallelization of wafer processing; therefore, the relative etching cost per reactor is very low. Characteristics of several anisotropic wet etchants, such as potassium hydroxide (KOH), ethylenediamine pyrochatechol (EDP) and tetramethyl ammonium hydroxide (TMAH), have been described by Maluf[132]. Isotropic wet etchants, such as a combination of hydrofluoric, nitric and acetic acids, have also been developed[157] and used for the definition of channels[158]. For the anisotropic etchants, the etch rate of the {111} plane is significantly slower than that of the {100} plane, and this is used to form features of defined geometry bounded by {111} planes. For KOH etching, which along with TMAH is the most common etchant used[158], the selectivity of {100} to {111} is as high as 100:1[159].

With the most common, and thus least expensive, (100)-silicon wafers, KOH-etched features form "V-shaped" cavities with the top defined by the opening in the etch mask, and sides formed by {111} planes at an angle of 54.74° from the horizontal {100} planes, as shown in Figure 4-1. The typical features are pyramidal pits or long channels with triangular or trapezoidal features aligned along the <110> direction (i.e., parallel to the standard flat on a (100) wafer). Different etch depths can be achieved in a single etching step through the use of self-terminating features where the {111} planes defining a feature intersect on all sides. This aspect of KOH etching can be very useful for microfabrication of reactors, as channels and alignment marks of significantly different depths can be defined in the same lithography and etching process. The standard etch mask for KOH etching is silicon nitride, which exhibits an extremely low etch rate at standard conditions (<1 nm/min[132]). Though silicon nitride deposition is not inexpensive, low-pressure chemical vapor deposition can be done in large batches, thus maintaining a relatively low cost per reactor.

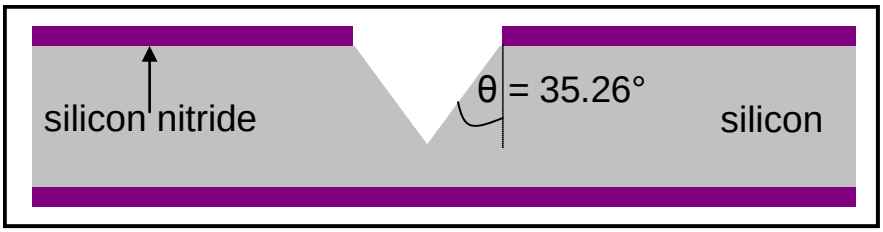

Figure 4-1: Cross-section of typical self-terminated feature defined with KOH etch. Etched feature (shown in white) projects down from opening in silicon nitride mask along {111} crystal planes.

Given the design objectives for the combustor of low resistance to flow and limited exposed surface area for heat loss to the environment, it was desirable to provide as much flow area for a given surface area of silicon as possible. Channels of rectangular cross-section can be formed with KOH etching by aligning long rectangular features to the <100> direction (i.e., 45° from the standard flat for a (100)-silicon wafer)[160]. The terminating {111} crystal planes are at 45° to the feature sides, and the {100} planes are parallel to the features. From a long rectangular opening in the silicon nitride mask, the etch rate in the vertical direction is equal to the etch rate undercutting the mask perpendicular to the edge of the opening, as shown in Figure 4-2. This technique produces rectangles of fixed aspect ratio, where the width of the rectangle is always twice the depth plus the width of the mask feature. The possible size of the mask feature is dependent on the lithography technique used, but can be as small as a few microns if so desired.

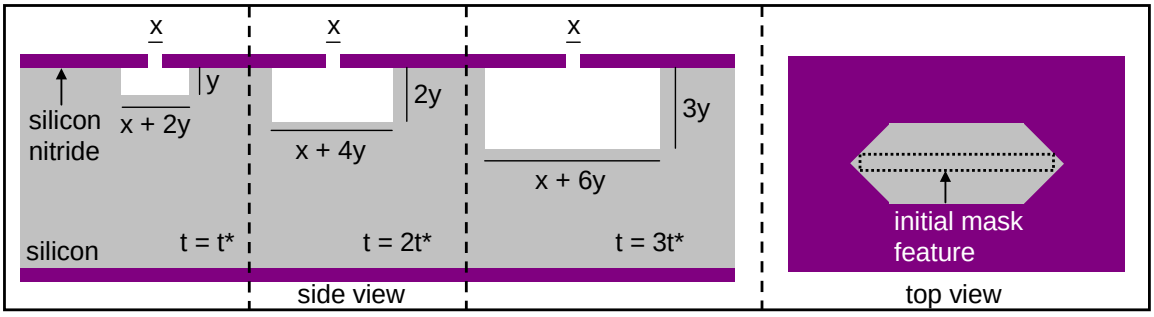

Figure 4-2: Cross-section and top view of KOH-etched feature aligned to <100> crystal plane. Time-series of etched feature (shown in white) shows lateral etch rate is same as vertical etch rate (y/t*). Top view shows initial mask feature and underetched silicon nitride.

The etch rates of silicon in KOH vary primarily with the concentration and temperature of the etching solution (as the etch is kinetically limited), and some correlations for the dependence are presented by Seidel, et al.[159]. However, other variables such as wafer doping can also impact the etch rate. Etch rates of 60 to 80 μm/hour are typical of 25%

(by weight) KOH solutions at 80°C, which is similar in rate to DRIE. However, features on both sides of a wafer can be defined in one etch step, which may be advantageous for some feature sets. If it is desired to protect one side of a wafer from the KOH etch, specially designed Teflon holders have been developed for this purpose[161]. Given the sensitivity of the etch rate to the temperature, it is important that thermal gradients within the bath are minimized through the use of a good-quality temperature control system.

For the KOH etch of features aligned to the <100> plane, the veracity of the lithography process can be critical to overall process yield. The mask features are typically very long and thin, to accommodate the lateral etch, and thus in the thin dimension the process is not as robust to mask errors (related to print quality or particles attached to the surface) or incomplete photoresist development. Any break or obstruction in the mask feature will result in a narrowing or a break in the etched channel. It is also important that the alignment of the lithographic mask to the wafer crystal plane is good.

One limitation for reactors defined with KOH etching, particularly those with rectangular features aligned to the <100> plane, is that there are high stress concentrations along the etched corners lying on crystal planes[158]. This aspect renders rectors processed in this way more fragile and less robust to stress than DRIE-processed reactors. It is possible, however, to post-process the KOH-etched features with a short amount of an isotropic etch such as DRIE or HNA to reduce this fragility.

4.2. Wafer Bonding Techniques

Wafer-level packaging of MEMS devices is highly advantageous from a cost-minimization perspective[162]. As well, wafer-level bonding can reduce or eliminate the need for other fasteners, which add significant system mass and surface area for heat loss. The ability to bond two (or more) wafers of silicon or of silicon and glass has enabled a broad range of microstructures to be formed[163]. The general principle involves the patterning of one or more wafers, followed by the alignment and bonding of two or more wafers to enclose microstructures with some form of bond between the layers. Sophisticated structures such as pressure sensors[162], mixers[164], and valves[165] have been formed with these techniques.

The main classes of wafer bonding techniques are direct silicon fusion bonding (also termed silicon wafer bonding), anodic bonding, and intermediate layer bonding. Anodic bonding typically occurs between silicon and a sodium-baring glass in the presence of an electric field and at elevated temperatures. Anodic bonding is not well-suited for high temperature devices, as there are thermal stresses resulting from mismatched coefficients of thermal expansion (CTE) between the silicon and the glass. Anodic bonding is particularly ill-suited to a thermoelectric power generation device due to the low thermal conductivity of glass (typically ~1 W/mK). The other two classes, silicon fusion bonding and intermediate layer bonding, are of greater interest for these devices and were considered in greater detail.

4.2.1. Silicon Fusion Bonding

Silicon fusion bonding is believed to involve the formation of Si-O-Si bonds between two surface silanol (Si-O-H) groups on two separate wafers, as shown in Figure 4-3. The wafers adhere upon contact at room temperature due to van der Waal's forces, and the bond is strengthened after annealing at high temperature (>1000°C) in an inert environment. The strength of the annealed bond has been reported to be on the order of the yield strength of silicon[163]. Low-temperature wafer bonding has been reported to provide lower bond strength, and a longer timescale for achieving maximum strength (days rather than an hour)[166]. The resulting bonded structure is of particular interest for high-temperature devices as there is no CTE-mismatch, resulting in no significant thermal stresses.

For successful fusion bonding, the wafers must be of high surface quality (low surface roughness and low bow or warp), as the wafers are reported to deform to match one another during the process[167]. Reported limits for roughness and wafer bow for successful bonding have been reported as 10 Å and 1.5 µm, respectively [162], which may necessitate additional polishing of wafers for processes involving fusion bonding. Similarly, surface cleanliness is of the utmost importance prior to wafer contacting, as any significant particulate matter on the surface will prevent bonding in the surrounding area up to several millimeters in diameter[168]. In many cases, protection layers of silicon oxide or silicon nitride (or both) are used to protect the wafer surface from roughening or

contamination during other process steps. It is difficult to maintain a sufficiently clean and smooth surface for fusion bonding through multiple process steps without such a protective layer.

Immediately prior to bonding, the wafers, with any protective masks removed from the bonding faces, are treated using an RCA-clean process to remove any surface contamination and to provide a high-density of hydroxyl groups on the surface silicon atoms. The wafers are then aligned manually or through the use of an aligner, placed in a vacuum chamber, and contacted at one central point to initiate the bond. A contact wave propagates outwards from this point, bringing the surfaces into intimate contact. After some holding time, the force is removed from the center of the pair. The vacuum chamber is critical to prevent plastic deformation of the silicon during the post-bonding anneal as a result of expansion of trapped nitrogen.

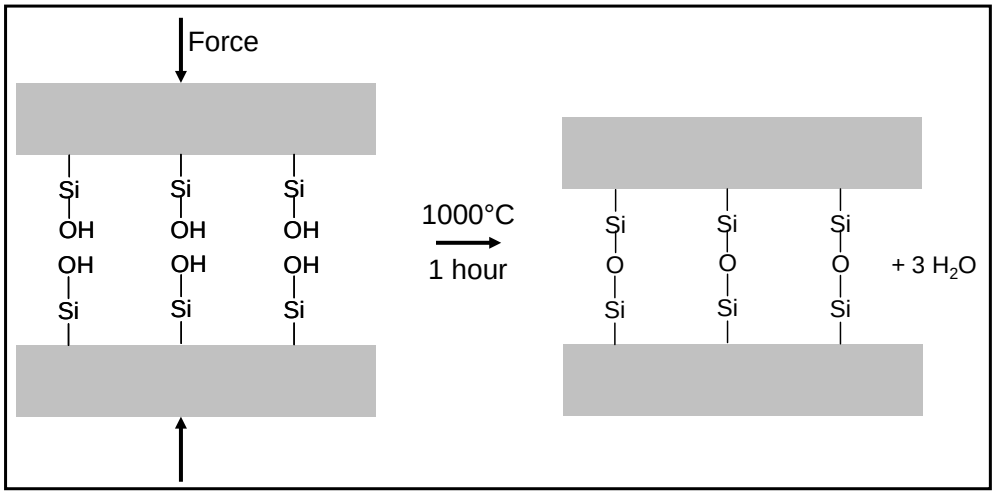

Figure 4-3: General silicon fusion bonding process. Surface silanol groups form covalent bonds at elevated temperature.

After the initial contacting, the bond can be assessed by viewing the IR transmission using an IR source and IR-sensitive camera. Voids in the bond are observed as dark areas or diffraction rings. If critical areas of the wafer are not bonded, the wafers can be separated after soaking for some hours in water by forcing a blade between the two surfaces. Another bond may be attempted between wafers that have been separated in this manner (after an RCA-clean), though the success rate of this second bond is significantly reduced. Successfully bonded pairs are then annealed in a nitrogen environment at 1050°C.

The fusion bonding of multiple wafer stacks has been demonstrated in several instances, such as a three-wafer stack for a microvalve[165], a six-wafer stack for a catalytic combustor[60] or for a micro gas turbine engine[56], and even a 25-layer stack for a chemical reactor[162]. In order to bond multiple wafers with the current equipment, two different approaches are taken. The first approach, which was successful for the micro gas turbine engine project at MIT, is to align and contact all wafers sequentially in ambient conditions, followed by the high-pressure contacting and subsequent anneal steps. This approach requires that no internal volumes be closed from the exterior of the stack, as there is no vacuum used. However, the advantage is that a simple wet process (such as hydrofluoric acid) can be used to remove the protective mask from both sides of all wafers.

The second approach to form multiple wafer stacks is to bond one wafer to the stack at a time (i.e., the first two wafers are bonded and annealed, then a third is added to the stack, and so on). With this approach, the contacting may be carried out under vacuum, so that internal voids can be accommodated. However, with this approach the selective removal of the protective layer from the bonding face alone is advisable to maintain surface cleanliness through multiple bonding cycles. Removal of silicon nitride or oxide from one side of a wafer can easily be accomplished using reactive ion etch (RIE); however, to avoid roughening the bonding surface it is preferable that the final surface release be accomplished using a wet process. Two possible methods of selective release (though many others are possible) are the removal of the majority of a protective layer from one side using RIE followed by a well-timed wet removal using hydrofluoric acid, or the selective addition of silicon nitride using direct chemical vapor deposition to the non-bonding side of the wafer followed by a well-timed wet removal using hydrofluoric acid.

4.2.2. Intermediate Layer Bonding

Intermediate layer bonding is a general term for a number of techniques that incorporate some additional substance to promote or otherwise facilitate a bond between wafers. Many of these techniques can be performed on the die level or at the wafer level. One large area of intermediate layer bonding is adhesive bonding, in which thermoplastic,

thermosetting, or elastomeric polymers have been used to bond silicon wafers[169]. For example, in recent years, bizbenzocyclobutene (BCB) has been used to form void-free bonds between silicon wafers at low temperatures and with high bonding strength[169-172]. However, adhesive bonding is typically of little use for high-temperature devices, as there are few adhesives with desirable properties which are stable at >400°C (BCB, for example, degrades at 300°C). Additionally, the thermal expansion coefficient of most adhesives is significantly higher than that of silicon, and so large thermal stresses would result for adhesively bonded devices at high temperatures.

In this work, a few adhesives which could accommodate the intended reactor temperature (~400°C) were considered for adhesive bonding, including a polyimide adhesive (Epoxy Technology TV1002) and a high-thermal-conductivity ceramic paste (Aremco Pyro-Duct 597A). The intention was to bond two full or partial wafers with the adhesive layer between, then to use the die-saw to cut flat reactor faces for compression sealing fluidic connections. However, the bond formed using both of these adhesives were found to weaken immensely from the water used to cool the die-saw during the cutting process.

Another form of intermediate layer bonding that has been investigated recently is thermocompression bonding[173, 174]. In this type of bonding, a metal such as gold is deposited in a thin layer (<1 μm) on silicon, with a suitable adhesion layer (such as titanium) and diffusion barrier (such as silicon oxide). Two such coated wafers are brought into contact and held at modest pressures and temperatures (0.02 MPa and 300°C) with the metal pads in contact. In this way, a bond is formed between the contacted metal pads, connecting the two wafers. Metal thermocompression bonds could be of use in high-temperature devices, below the melting temperature of the metal and providing that a sufficient diffusion barrier is provided. However, the bond quality has been observed to be very sensitive to distribution of pressure across the wafer.

In this work, a die-level thermocompression-type bond which had been reported previously for high-temperature silicon devices[52] was investigated. The goal was to bond two reactors together with an intermediate copper layer, removing the need for a

multiple-wafer fusion bond and providing a thermally conductive layer between countercurrent reactors. The process involved placing a thin copper foil (0.025 mm-thick, Alfa Aesar) between two silicon reactors (covered only with native silicon oxide) in an alignment jig, compressing the assembly with a weight, and heating at 950°C for two hours. The copper foil was rinsed in 0.1 M acetic acid immediately prior to bonding to remove surface oxide. The alignment jig, shown in Figure 4-4, was made from Macor to minimize thermal expansion and incorporated 304-stainless steel alignment bars. Silicon reactors "bonded" using this process, with reasonably good alignment to facilitate fluidic connections, are shown in Figure 4-5.

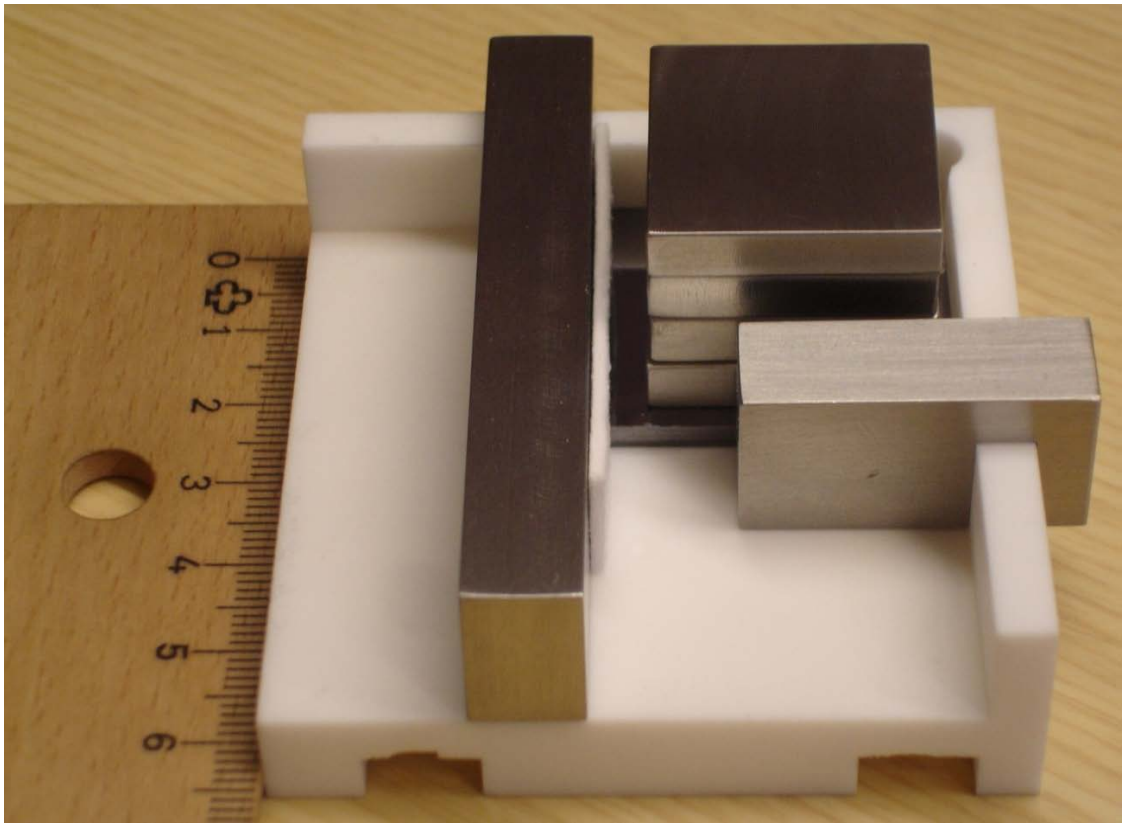

Figure 4-4: Macor alignment jig for copper thermocompression bond between reactors. Approximate dimensions of jig were 6.5 x 6.5 x 2.5 cm. Reactors loaded in alignment jig with alignment bars and ceramic tape for compliance, along with steel weights for compression.

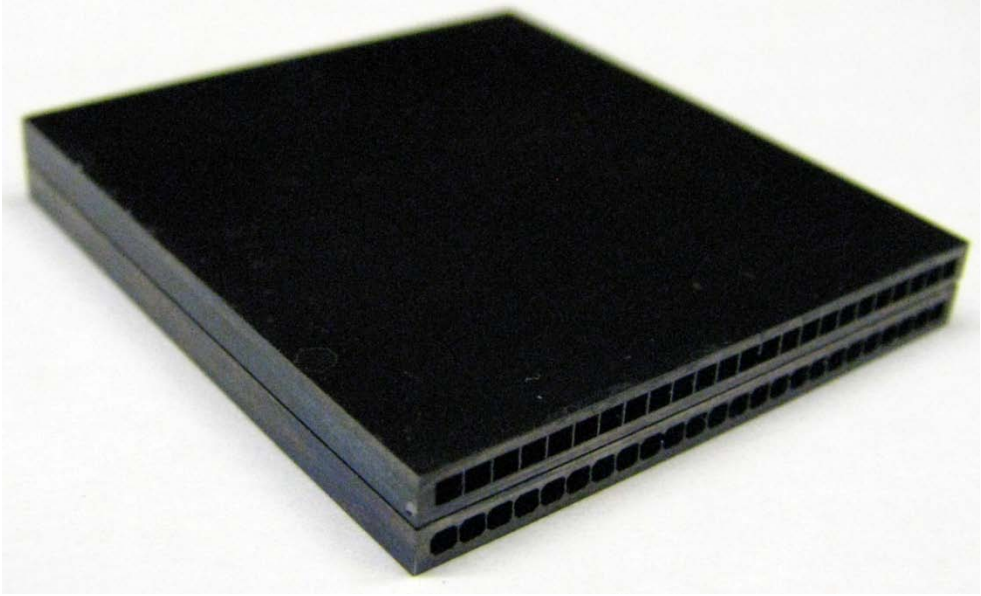

Figure 4-5: Silicon combustors after copper thermocompression bonding in alignment jig. Reactor dimension was 3.1 x 2.85 x 2 cm.

The resulting bond between the reactors from the copper thermocompression bond was sufficient such that they would not come apart under gentle handling. However, the bonded was found to be quite brittle, with the reactors separating under mild torsion or small lifting force normal to the bond surface. As well, the bond surface was observed to include significant gaps, despite the pressure during bonding. The inside surface of the bond after separation is shown in Figure 4-6. It was observed that the copper layer had been entirely discolored, and was well adhered to one wafer or the other in a given location, but not both. These observations were attributed to the formation of copper silicides at the elevated bonding temperatures, as supported by the copper-silicon phase diagram[175]. Copper silicide formation has been studied due to its role in integrated circuit manufacturing[176], and has been observed to form in appreciable amounts on (100)-silicon at temperatures as low as 200°C[177]. The poor adhesion of the layer, and the large gap between reactors that was observed, was a result of the large volume expansion resulting from the formation of Cu_3Si[178], which is one of the three low-temperature equilibrium phases[179]. It was determined that this type of bond would not perform as desired without a significant diffusion barrier between the silicon and the copper, such as sputtered thin films of Ti-Si-N[180]. Given that the diffusion barrier would further complicate the fabrication process, this technique was not pursued.

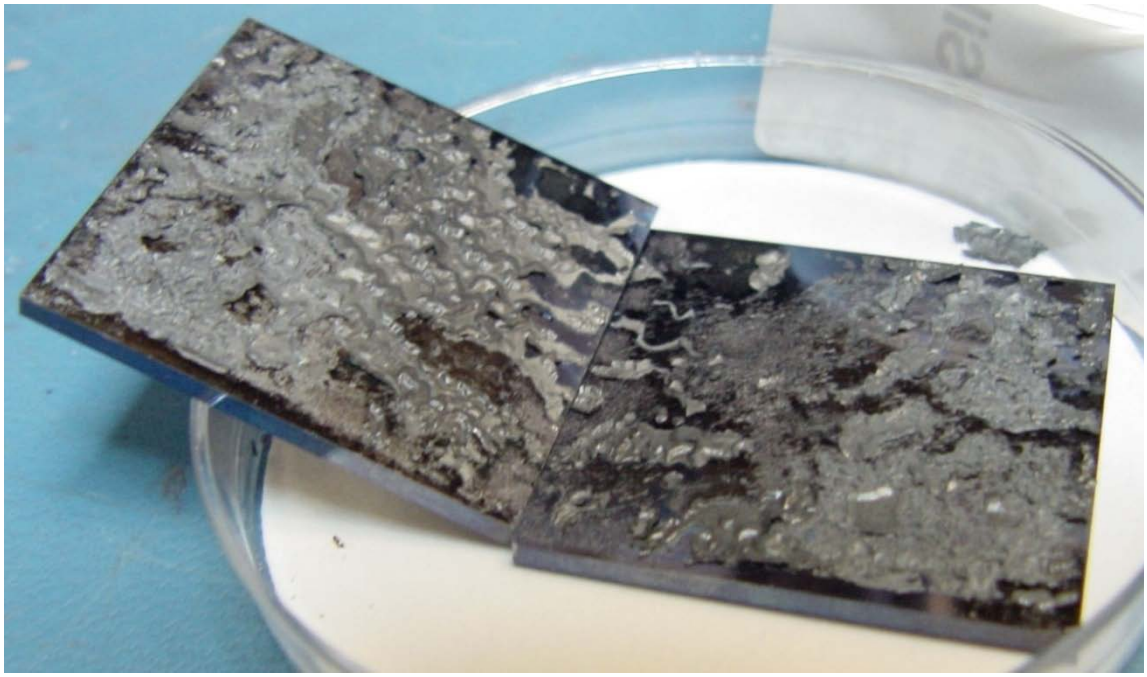

Figure 4-6: Inner surfaces of copper thermocompression bond.

4.3. Silicon Microfabrication Process

The detailed fabrication process and lithography masks used to produce the silicon reactors developed in this work are given in Appendix A. The process consisted of deposition of protective layers, lithography, wet etching, protective layer removal, and silicon fusion bonding. Specifically, a KOH etch with features aligned to the <100> plane for the achievement of rectangular channels was used. Unless otherwise noted, the standard operating procedures developed by MIT's Microsystems Technology Laboratories (MTL) were observed.

Double-side polished 150-mm-diameter n-type (100)-silicon wafers with 1 mm thickness (+/- 50 μm) were obtained from James River Semiconductor. One batch of wafers had flats cut to the <110> plane, and another batch were received with flats cut to the <100> plane. Two different sets of lithography masks were required to facilitate the KOH etch for these two batches, given that the features had to be rotated 45° while the alignment marks had to remain stationary relative to the flat. These wafers were highly polished by the vendor in order to achieve low surface roughness and bow necessary for successful silicon fusion bonding of thick wafers. Thermal (wet) silicon oxide was grown on the bare silicon wafer surface to a thickness of 400 nm (MRL Industries Model 718 System

Atmospheric Oxidation Furnace), and after the appropriate cleaning 400 nm of low-stress LP-CVD silicon-rich silicon nitride was deposited (ASML/SVG VTR Series 6000 furnace) on top of the silicon oxide. These two layers were used in part to balance the stresses imposed on the silicon wafers by the individual layers, in part in an effort to facilitate selective deprotection of bonding surfaces, and in part to ensure that the final deprotection step prior to bonding would consist of a relatively simple and quick wet removal of silicon oxide in hydrofluoric acid. Following the LP-CVD process, ~200 nm of the silicon nitride layer was removed from the wafer "front" (channel) sides using RIE (Lam Research Model 490B Reactive Ion Etch) in a timed etch.

Front and back side lithography was performed sequentially prior to patterning of the silicon nitride mask. Thin (1 μm) photoresist (OCG 825 positive resist) was coated on the back of the wafer, and prebaked for 15 minutes (half the standard time) at 95°C. The front of the wafer was then coated with thin photoresist and prebaked for a full 30 minutes. The photolithography was performed first on the back of the wafer using an Electronic Visions EV620 Mask Aligner, and after exposure the wafer was placed in the developer (OCG 934 1:1 developer) for <10 seconds to make the alignment marks visible. The front side of the wafer was then exposed in the aligner (with alignment to the marks on the back side), and then the wafer was fully developed with features confirmed by the fluoroscope. After development, the rim of the wafer (on both sides) was "painted" with photoresist in order to protect the silicon nitride from the RIE. This was observed to reduce the roughening of the wafer edges during KOH etching.

Considerable care was taken to align both masks to both the crystal plane of the wafer using the horizontal lines at the base of the mask (to match to the flat) and to the center of the wafer using consistent settings on the aligner. Alignment to the center of the wafer was important so that the wafer stack would fit in standard holders after fusion bonding. Two different front masks (A and B, shown in Figure 4-7 and Figure 4-8, respectively) were used in order to have channels aligned when bonded. The back sides of type A had alignment marks and die-saw marks, and the back sides of type B had only alignment marks. Wafer batches contained multiple wafers of each type for process robustness.

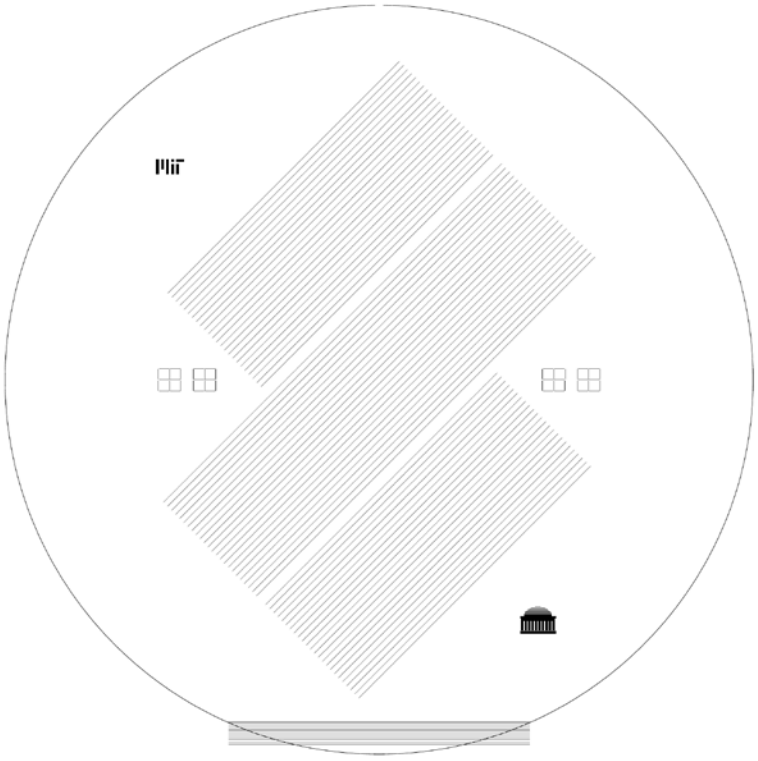

Figure 4-7: Reactor A front mask (negative image) for wafers with flat cut to <110> crystal plane. Each of the parallel lines has a thickness of 50 µm. The box symbols serve as alignment marks.

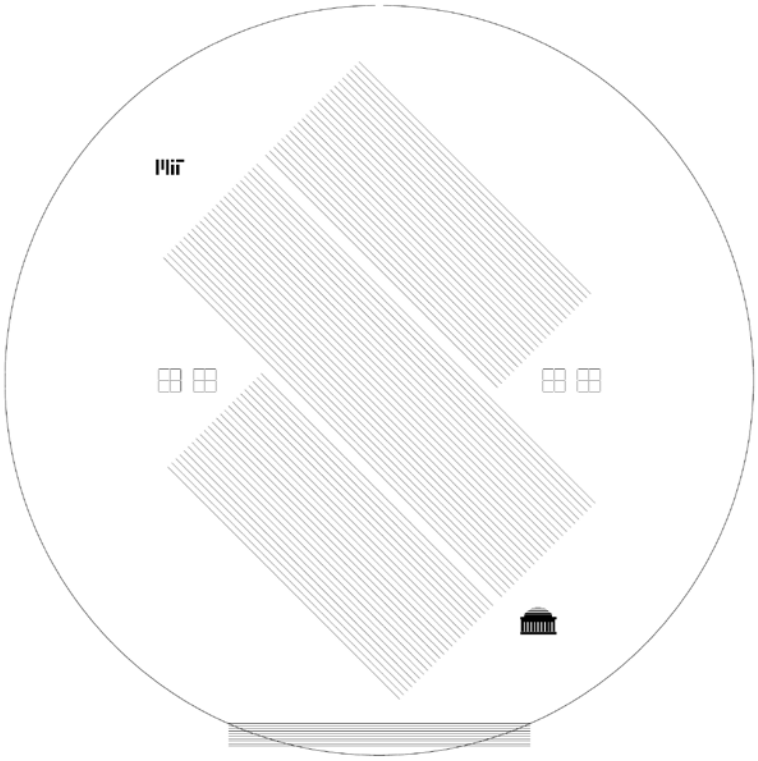

Figure 4-8: Reactor B front mask (negative image) for wafers with flat cut to <110> crystal plane. Each of the parallel lines has a thickness of 50 µm. The box symbols serve as alignment marks.

Following lithography and subsequent postbake for 30 minutes at 120°C, the silicon nitride mask was patterned using RIE, then the silicon oxide was patterned using a buffered oxide etch, and finally the photoresist was removed in a piranha solution. The wafer features were defined in a 25% (by weight) KOH solution at 80°C, which provided an etch rate of ~60 μm/hour. The etch depth was measured after the first hour using an optical microscope to estimate the rate for the process. Approximately one hour prior to etch completion, the etch depth was again measured and the end time was reassessed. Wafers were positioned vertically in the KOH bath, in order to avoid the collection of hydrogen gas bubbles in the features. Care was taken to ensure that the water bath covered the top of the liquid level in the KOH bath, in order to prevent thermal gradients, and if so desired the wafers could be rotated intermittently to minimize the impact of any thermal gradient. With these precautions, up to 25 wafers could be processed with good etch uniformity across and between wafers (as low as 1% variation). Though rare, some errors in lithography were observed in the form of channel impingements.

Each wafer was defined with parallel mask features 50 μm wide and spaced with 1100 μm between the edges of adjacent features within a "set". Each of the three "sets" consisted of 24 parallel features, or lines, which defined the channels of a reactor. The shorter two sets were 65.75 mm in length (allowing for two combustors, each 31 mm in length), and the longer set was 96 mm long (allowing for three combustors, each 31 mm in length). The intended etch depth was 500 μm, which resulted in rectangular impressions in the wafer surface projecting 500 μm from the edge of the mask feature for an array of impressions each 1050-μm-wide with 100 μm walls separating adjacent features, shown in Figure 4-9. The spacing between adjacent "sets" of features was 2500 μm, which provided a side wall of ~500 μm from the edge of the exterior channel to the edge of the die-sawed reactor (allowing 500 μm for material removed by the die-saw blade). While designed to produce seven reactors (of 31 mm length) per bonded pair of wafers, the fabrication process provided effortless flexibility in reactor length (with increased span between die-saw cuts), and this was useful for the final integration with commercial thermoelectric modules that were longer than anticipated. An image of an unbonded, processed wafer is shown in Figure 4-10, though the etch was only ~385 μm

deep. In this image, the flat recessed bottoms of the channels can be observed, along with the dark lines of the shadows cast by the thin side walls projecting up to the original wafer surface. The thin dark lines that are observed in a rectangular pattern are the cut marks from a thin die-saw blade. The lithography process for the wafers with flats cut to the <100> plane was identical, except that only one front and back mask pair was required (as features were horizontal, and thus symmetric, on the wafer).

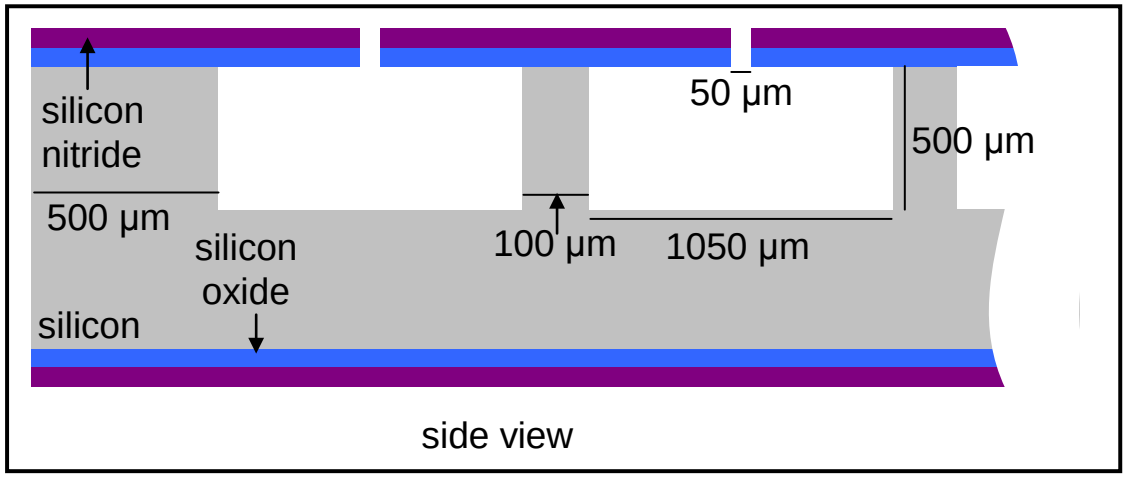

Figure 4-9: Illustration of KOH etched wafer, demonstrating two channels at the edge of a set of 24 which define half a reactor.

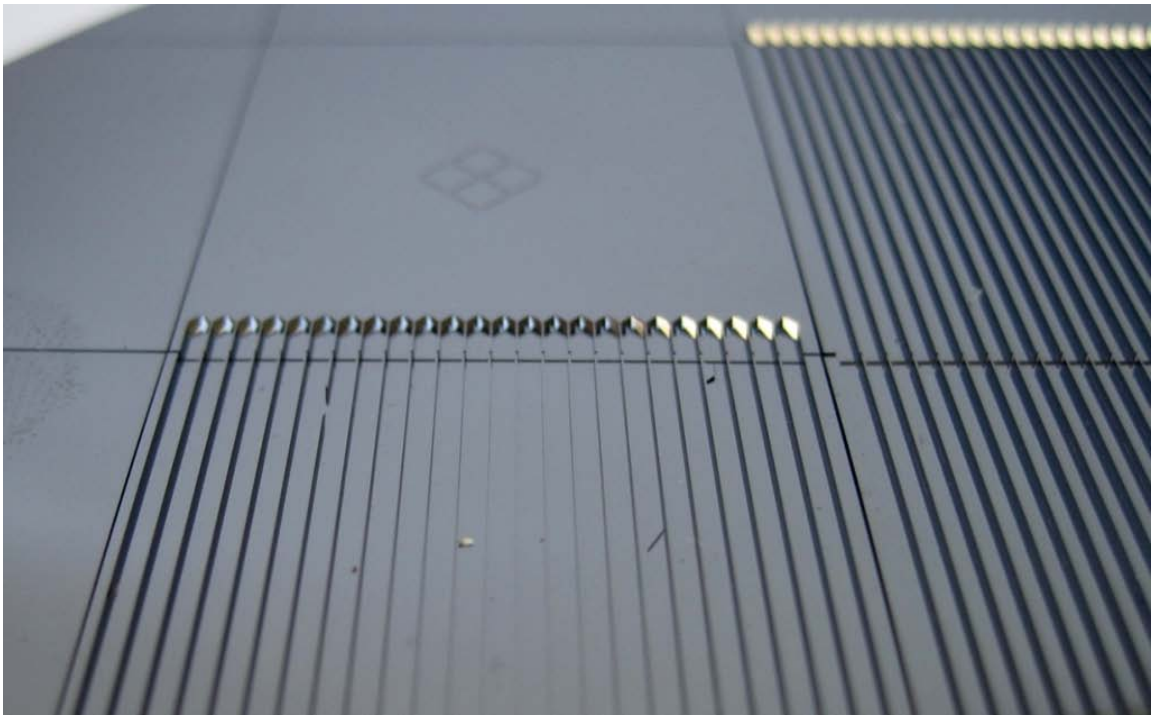

Figure 4-10: Photograph of an unbonded, processed wafer. Rectangular channels were etched to ~385 µm depth. Angular features at the edges of the etched lines are visible, as are alignment marks.

Following the KOH etch and a required cleaning step, the silicon nitride protection mask was removed in phosphoric acid at 165°C. The etch rate for LP-CVD nitride is ~40 Å/min, and the etch rate of thermal oxide is negligible. The intended procedure was to remove the 200 nm of silicon nitride that remained on the front side of the wafers, leaving ~200 nm of silicon nitride on the back of the wafers. The silicon nitride on the back of the wafers was then intended to act as a protective mask during removal of the silicon oxide layer from the front side using 49% hydrofluoric acid. The intention was to selectively remove the protective layers from the wafer fronts to fusion bond the wafers to enclose the channels, while maintaining a protective layer on the back sides to allow for a second fusion bond to create the desired stacked combustors. The final combustors were then to be diced from this four-wafer stack with smooth, aligned edges for compression sealing to fluidic connections and with intimate thermal contact between the two reactor layers. The protective layers were deemed necessary because the enclosed features necessitated a vacuum environment during wafer contacting.

However, the selective nitride removal process could not be completed as intended due to an unanticipated consequence of the KOH etch process. The silicon nitride and silicon oxide layer that had been under-etched during the process – that is, the material between the initial 50 μm feature and the final silicon sidewall – was found to break off from the adjacent, supported layer and form strands of varying sizes. Some of these strands completely broke away from the wafer and were found in the KOH bath, the dump-rinser station used to rinse the KOH solution from the wafer, and even the wafer carrier box. However, some strands would adhere to other parts of the wafer surface and act as an additional mask to the underlying silicon nitride, preventing removal with RIE, hot phosphoric acid, or hydrofluoric acid. Even a treatment for one hour in a sonication bath, including water circulation to remove the released strands from the bath, would not remove the bulk of these strands from the wafer surface. This same issue was observed for wafers that did not include a layer of silicon oxide. Given that the selective removal was based on the removal of half of the total silicon nitride thickness, an effective doubling of the layer thickness in some portions of the surface rendered this technique unworkable as designed.

Several procedures were considered to compensate for the difficulty caused by the strands of silicon nitride and oxide and facilitate a second fusion bond step. One approach considered was to redesign the wafer mask in order to eliminate the enclosed volumes and allow the simultaneous bonding of all four wafers. Though certainly possible, this method was not pursued due to concerns that the wafer fragility, already a concern given the anisotropic etch used, would be considerably worsened with the addition of features etched through the entire wafer thickness. Another approach considered was to use RIE to further thin the front side silicon nitride layer relative to the backside layer prior to KOH etching, enlarging the gap between the two sides and reducing the thickness of the strands. Though attempted, this method was unsuccessful due to the uncertainty in the RIE etch rate variation for silicon nitride across the wafer, the wafer-to-wafer thickness variation of the LP-CVD silicon nitride deposition process (~20% thickness variation within the batch), and the silicon nitride thickness variation over the wafer surface (which was observed to be considerable). Other considered processes which were not attempted include the deposition of a DCVD silicon nitride layer on the back of the wafer prior to hot phosphoric acid nitride removal, the directed deposition of a silicon oxide layer on the back of the wafer prior to hot phosphoric acid etching, or the addition of a buried oxide layer between nitride layers on the wafer back using either DCVD or by selective RIE removal of oxide from the front.

In this work, the intended process was adapted such that a long etch in hot phosphoric acid sufficient for removal of nitride from both sides of the wafer (including all strands) was employed. After an RCA-clean process to hydrate the silicon surface, the wafers were aligned on the front sides to enclose channels (Electronic Visions EV620 Wafer Aligner), and contacted under vacuum with a centrally-applied force of 2500 N for a few minutes. The contact time was varied without any observable effect on wafer bond quality. Following the contacting, the bond quality between the pair of wafers was assessed using IR transmission. Bonded wafer pairs of sufficient quality were annealed at 1050°C for one hour in a nitrogen environment to improve bond strength. Following the anneal step, the wafers were diced at low cut speeds to provide as smooth a surface as possible for the produced reactors. A combustor produced from a two-wafer stack in this

manner is shown in Figure 4-11. As mentioned previously, the length of the reactor could be adjusted based on the step size used during the die-saw process. Initial testing was carried out with 31-mm-long reactors, but the majority of the experimental results were produced with 35-mm-long reactors to accommodate the size of the commercial thermoelectric modules.

Figure 4-11: Image of a fabricated combustor produced using a KOH etch and silicon fusion bonding. The reactor dimensions were 31 x 28.5 x 2 mm, and the channel cross section was 1000 x 1050 µm, with 100 µm walls separating adjacent channels. Adjacent ruler scale is in inches.

The majority of silicon wafer pairs processed were successfully fusion bonded. Typical of other fusion bonding processes[60], the bond quality around the edge of the wafers was not good. The mask features were set at least 1 cm from the edge of the wafer to accommodate this feature of silicon fusion bonding; however, this common issue was exacerbated for this particular process as a result of both the increased thickness (and thus, rigidity) of the wafers and the sharp, jagged wafer edges caused by the KOH etch. Some failures in wafer bonding resulted from these jagged edges, such as interactions between the edges of the two wafers, as a result of foreign material (such as Teflon shards from the wafer carrier) caught in these edges, or as a result of incorrect wafer positioning in the aligner. Occasional issues in wafer bonding were also observed as a result of surface contamination or as a result of silicon nitride shards that had not been completely removed from the surface. The quality of the fusion bond between the 100-µm-thick channel walls was not as good as that of the larger surfaces, as observed by IR transmission and by the fracture of one half-wall with no impact on the opposite half-wall after die-saw and handling (as shown in Figure 4-12). In this work, the bond strength of these internal walls was of no consequence, but this observation confirms that thicker

external walls are advisable to provide a gas-tight seal for the reactor. This would also be of greater significance if a channel-by-channel countercurrent flow reactor was designed, possibly necessitating larger separation between channels.

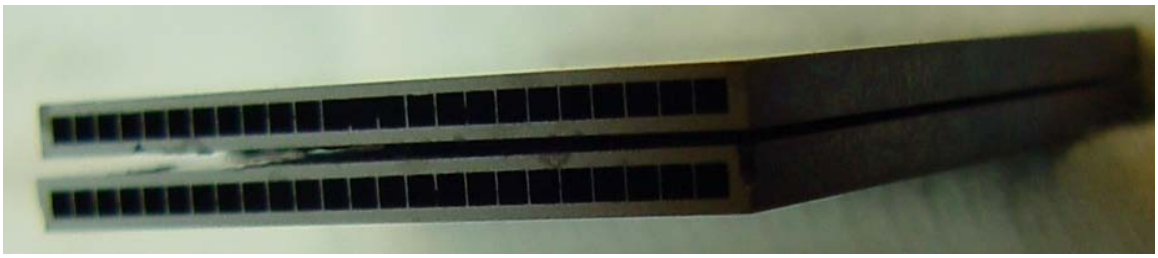

Figure 4-12: Bonded reactor with internal side walls half broken, indicating lack of bond strength on small features.

4.4. Concluding Remarks

In this chapter, some of the silicon microfabrication techniques important to the fabrication of the catalytic combustor have been discussed. The process developed in this work, consisting of wet anisotropic silicon etching and silicon fusion bonding, has been presented. Parallel rectangular channels were patterned in silicon using an inexpensive, parallelizable, non-standard application of potassium hydroxide etchant. The etch depth was consistent and reproducible across the wafer and across a large wafer batch, with as little as 1% observed variation. Silicon fusion bonding was used enclose channels. Selective deprotection schemes were investigated to facilitate a fusion-bonded four-wafer stack, but no successful process was developed to overcome the issues caused by the particular etching scheme.

5. Reactor Packaging and System Integration

The packaging of a MEMS device refers to the methods of packing micromachined structures into a useful assembly which is able to reliably and safely interact with its environment[132]. In this work, the packaging efforts focused on integration of catalyst into the reactor channels, attachment of the compression-sealed gas distribution manifolds, interface with external fluidic connections, and mechanical integration with the TE modules or the TE-mimicking heat sinks. The main challenge was to connect multiple macroscale systems (such as the large-diameter tubing and the water-cooled heat sinks) with the mesoscale combustor without severely hampering the thermal isolation of the device or adding unmanageable mechanical stress to the fragile silicon reactor. In this chapter, the packaging of the silicon reactors is discussed. Unless otherwise noted, all fasteners were obtained from McMaster Carr.

5.1. Catalyst Integration

5.1.1. Standard Catalyst Loading Techniques

As discussed in chapter 3, the catalytic combustor was designed to have a supported-platinum catalyst layer on the internal silicon surface. One approach to catalyst surface integration has been to separately deposit catalyst on some support material, such as a platinum coating on an anodized aluminum shim[30], a platinum[60] or platinum-on-alumina[93] coating on a nickel foam support, or lithium aluminate coated on an α-alumina carrier plate[181], which is subsequently fixed within a reactor. One advantage of this approach is that the catalyst can be localized in the desired positions within the reactor, without risk of deposition on sealing faces or in fluidic connections. A significant disadvantage of such an approach, particularly for a catalytic combustor, is that the catalyst is often not in good thermal contact with the external walls, which can lead to increased enthalpy loss from the system.

The other approach is to deposit the catalyst (and support) material on the surfaces of the device directly. Recent, thorough reviews of methods used to deposit catalysts on structured surfaces are presented by Meille[182], Nijuhuis, et al.[183], and by Holladay, et al.[64] Some of the most common methods for catalyst deposition are sol-gel deposition,

impregnation, chemical vapor deposition, and suspension washcoating (or dip coating). Sol-gel deposition is a useful technique for obtaining thin catalyst layers (< 10 μm), while the suspension-based coating processes have received significant attention, primarily due to the simplicity of the process, for intermediate layer thicknesses (1 – 100 μm)[182]. Catalysts have also been coated on SiC walls through solution combustion synthesis[98], which is similar to dip coating with a higher "evaporation" temperature (600°C). In an interesting application of suspension coating, micro- and nanoparticles have been self-assembled on, and subsequently adhered to, the internal silicon surfaces of MEMS devices[184].

The simplest suspension-based method of depositing Pt/Al_2O_3 in a microreactor is with a "fill-and-dry" washcoat, which has been demonstrated to coat silicon microchannels in several works[52, 185-187]. Catalyst particles are suspended in water (in some cases with acid for pH control, colloidal suspensions for adhesion, or viscosity modifiers). The suspension is drawn into the channels via capillary action or forced flow. The water is then allowed to evaporate from the channels, either at room temperature or an elevated temperature (below the boiling point) such as 80°C. The layer is then calcined to improve adhesion within the layer and to the support at a high temperature (typically 300 – 400°C). A silicon microchannel coated by this fill-and-dry method is shown in Figure 5-1. A wide range of slurry compositions have been reported for fill-and-dry coatings, from <5%[52] to 33%[185] solids (by weight).

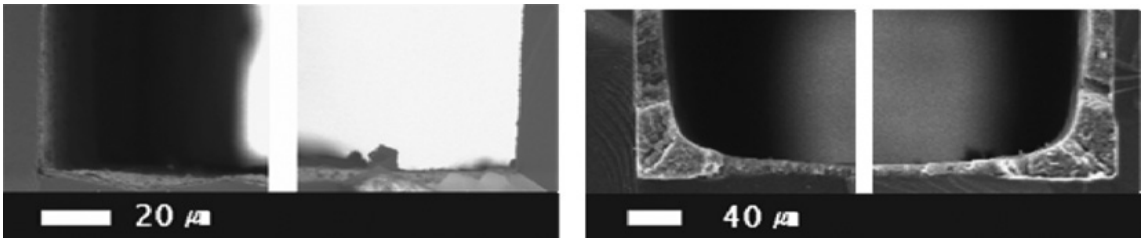

Figure 5-1: Alumina catalyst layers deposited by flow coating (left) and fill-and-dry coating (right) from Hwang, et al.[185] Silicon channels were 600 μm x 240 μm in cross section.

The more commonly used suspension-based coating technique of dip- or washcoating involves the contacting of the surface to be coated with a concentrated solid slurry (typically 20 – 30% solids by weight), and then subsequent removal of the excess slurry from the surface either by gravitational forces or using a forced-air stream to displace the

fluid. The coating procedure for channel structures has been well documented[97, 188-191], in part due to the role of ceramic monoliths in automotive exhaust processing. In dip coating, the structure is immersed in the slurry for a period of time (from seconds to minutes) to allow the solids to adhere to the surface, and then withdrawn at a fixed rate (which is known to strongly influence the coating thickness). Excess slurry is then removed from the channels using an "air-knife" (precise forced air stream), and the structure is allowed to dry either at room temperature or at an elevated temperature (<100°C). Often the structure is rotated during drying to maintain an even distribution of the coating on the channel surface. This process is typically applied to porous supports and solvents that wet both the support and the slurry particles well[183] (such as with water, alumina particles, and ceramic monoliths); however, a similar process has been used to coat smooth surfaces such as silicon and stainless steel[182, 185, 191, 192].

There are several important slurry properties which influence the quality of a catalyst washcoat. The size of particles in the slurry has been reported to have a significant effect on the quality and adhesion of catalyst layers deposited via suspension to the substrate[182, 183]. Alumina particles with diameter of 2 μm were reported to have much better adhesion than particles 17 or 52 μm[193, 194]. Similarly, ceria-zirconia particles were reported to form a better quality washcoat with particles less than 10 μm[188]. Typically, the particles are milled in order to reduce the mean particle size below the desired threshold, usually to an average particle size ~5 μm. Another factor which has been found to affect the adhesion is the use of a binder particle or adhesion promoter, such as colloidal alumina (bohemite) for deposition of larger alumina particles. The small (typically 20 – 50 nm) particles fill the interstices between particles and between the particles and support, improving layer adhesion, as described in Figure 5-2. It is suggested that the concentration of the binder should be low for the deposition of supported-metal catalysts, around 1% of total solids, in order to minimize the covering of active metal sites by the binder[183].

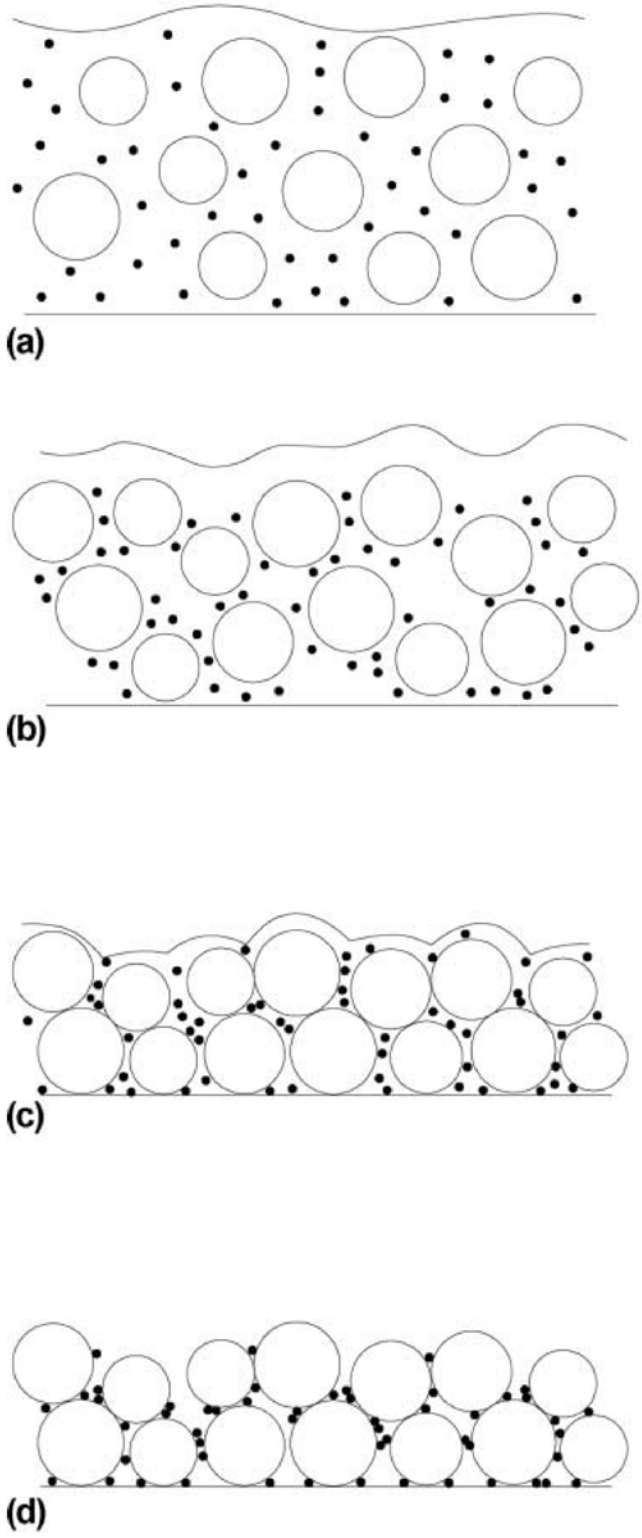

Figure 5-2: Schematic representation of the drying steps in the slurry coating process: (a) wet slurry on surface [large white circles are coating particles (typically 5 μm) and small black dots are binder (typically 20 - 50 nm)], (b) first stages of drying, (c) large particles touch each other, binder still free flowing, (d) binder deposited at interfaces between particles by capillary forces during final drying stages. From Nijhuis, et al.[183]

Other properties of the catalyst slurry which have been reported to influence the washcoat amount and quality include the solids fraction, pH, and viscosity, which are interrelated[195]. The ageing time of the slurry has also been reported to influence the rheological properties of the slurry, particularly for pH-adjusted slurries, with approximately 24 hours providing sufficient ageing time for properties to stabilize[196]. Temperature during slurry processing steps has been reported to influence coating reproducibility[197]. The dependence on these parameters for washcoating is due to the surface film of slurry on the support that is formed after the excess is removed, and as such the "best" properties should be based on the desired coating thickness and the surface properties of the substrate. Typically for alumina slurries, nitric acid is used to adjust the pH of the slurry in the range of 3.5 – 4, which leads to charge stabilization of the alumina particles. However, Triton X100[198], Surfine WNT-A (FINETEX, Inc.) and DOWFAX 3B2 (Dow Chemical)[199] have been identified as suitable anionic surfactants for stabilizing concentrated alumina dispersions in water. Some observed trends for alumina coating load as a function of slurry concentration and nitric acid addition can be found from Valentini, et al., with a recommended "optimum" slurry of ~25% alumina in water with 2 mmol/g HNO_3/Al_2O_3 ratio[191] providing the thickest well-adherent layer.

5.1.2. Catalyst Loading Procedure Development

The fill-and-dry catalyst deposition process was tested, unsuccessfully, with small combustors (770 μm x 820 μm x 3 cm channels) for a 5% (by weight) γ-alumina in DI water slurry. It was also tested with a 5% Pt/Al_2O_3 catalyst slurry (at 5% by weight in DI water) in small combustors which had not been fusion bonded (but were instead held together with tape during catalyst loading) to facilitate observation of the deposited layer. In both cases, the particles were ground (wet) with a mortar and pestle for one hour, filled into the channels with a syringe, and then placed in an 80°C oven to evaporate the water.

The difficulty with the fill-and-dry method for coating long, large rectangular channels is that the catalyst particles tended to collect at the openings, plugging the channel, as shown in Figure 5-3 for the alumina coated reactor, and in Figure 5-4 for the Pt/Al_2O_3-coated half-reactor. To avoid this phenomenon, the evaporation rate of the carrier fluid must be sufficiently fast such that the evaporation front moves into the channel faster

than the slurry from the interior of the channel is drawn out to the edge of the channel (in a "coffee-ring" type effect). This effect is dependent on several variables, including the viscosity of the slurry, the surface tension of the slurry in the channel, the channel dimensions, and the evaporation temperature.

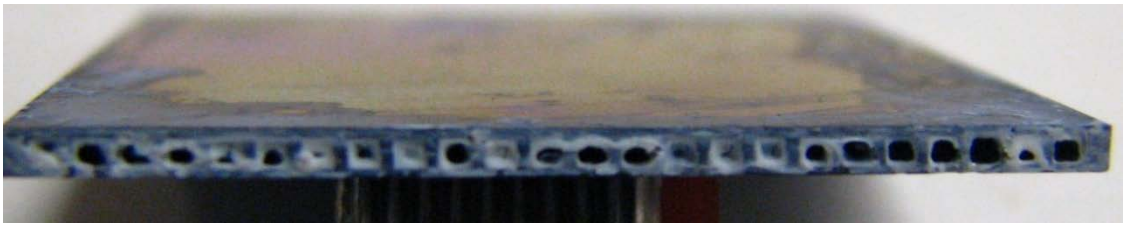

Figure 5-3: Alumina coating of rectangular channels in a silicon microreactor using fill-and-dry method. Channels are ~770 μm x 820 μm x 3 cm, and slurry was 5%-wt alumina in DI water. Drying temperature was 80°C. Channel openings were clogged with alumina due to capillary action during evaporation.

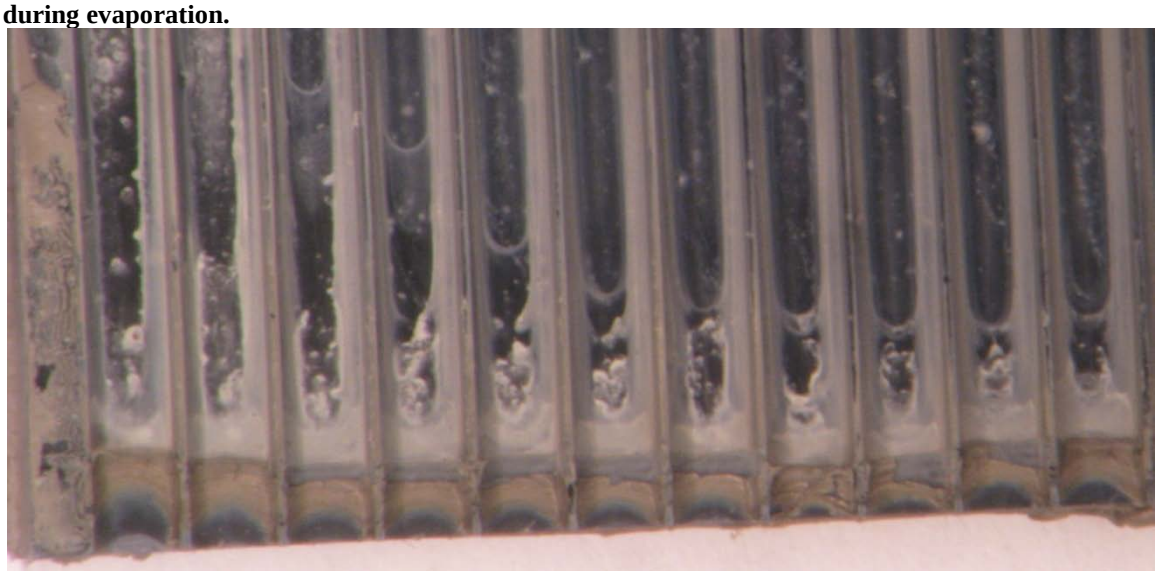

Figure 5-4: Top-view of unbonded (and separated) small combustor after fill-and-dry loading of catalyst. The collection of catalyst near the channel opening can be observed, with a lack of deposition in the bulk of the channel. Preferential deposition in the corners was also observed.

Several variables, such as the milling technique, solids loading, addition of a binder, solvent polarity and volatility, heating temperature, heating source, and heating rate were adjusted, but no satisfactory fill-and-dry process could be obtained. In addition to the accumulation at the channel openings, which could potentially be solved by mechanically clearing each obstruction, a significant limitation was the poor adhesion of layers formed using this method to the silicon walls. The poor adhesion can be observed in Figure 5-5, which shows the catalyst layer resulting from a fill-and-dry coating with a slurry containing Pt/Al_2O_3 at 5% by weight, 2.5 μL of 6N nitric acid per 1 g DI water, a

colloidal alumina binder at 1% of total solids, and ethanol in a 1:1 ratio with DI water (by mass). The ethanol had been added to improve the wettability of the surface by the slurry.

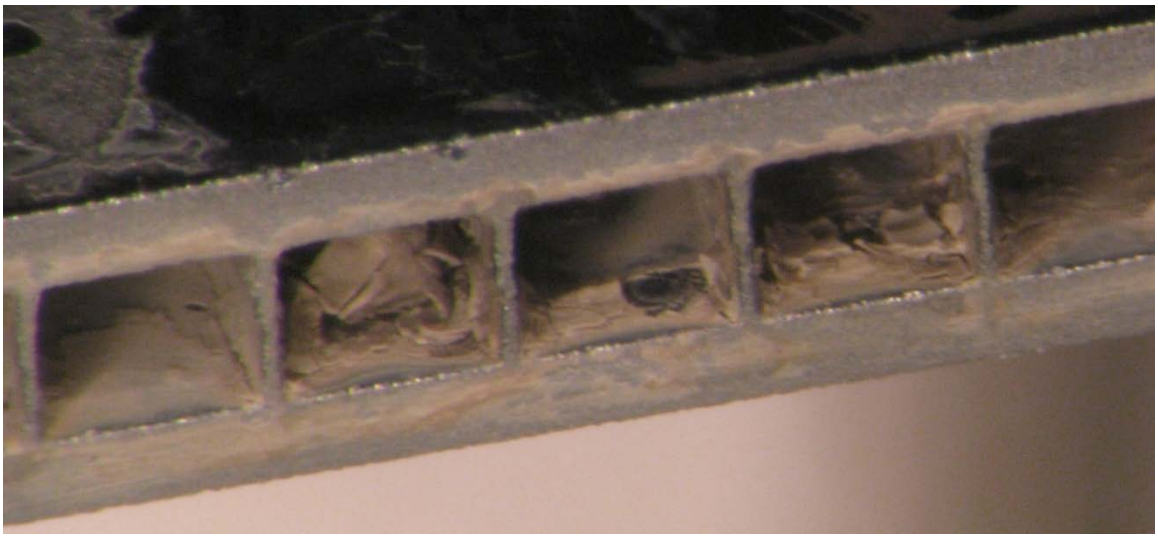

Figure 5-5: Poorly-adherent catalyst layer coated in 1 mm x 1 mm x 3 cm channels using fill-and-dry method with milled, pH adjusted ethanol-water-catalyst slurry.

The adhesion to silicon of the milled slurry prior to ethanol addition was not any better, as can be observed in Figure 5-6 for a drop which was dried on a silicon surface. Notable cracking of the layer and even "curling" away from the surface was observed, and the layer could be removed from the silicon with gentle air currents. Similar behavior was observed for a drop of the colloidal alumina suspension, which was considered as an adhesion layer that could be deposited prior to the slurry, and this observation has also been reported in the literature[192]. However, it was observed that this same slurry could be made to form a uniform, well-adherent layer on the silicon surface, as shown in Figure 5-7, by smearing the slurry across the surface with either a swab or with a gentle application of forced-air. The smearing of the layer was believed to be similar to the removal of "excess" slurry that is performed in the traditional dip-coating procedure. When using forced-air to smear the slurry drop on the silicon surface, it was quite challenging to provide sufficient force to overcome the surface tension without forcing the entire droplet from the surface. This highlights one of the critical differences between the coating of ceramic monoliths and silicon channels – the wettability of native oxide is not sufficient for the formation of a thin surface layer of slurry after aggressive forced-air treatment. These observations directly led to the final coating procedure.

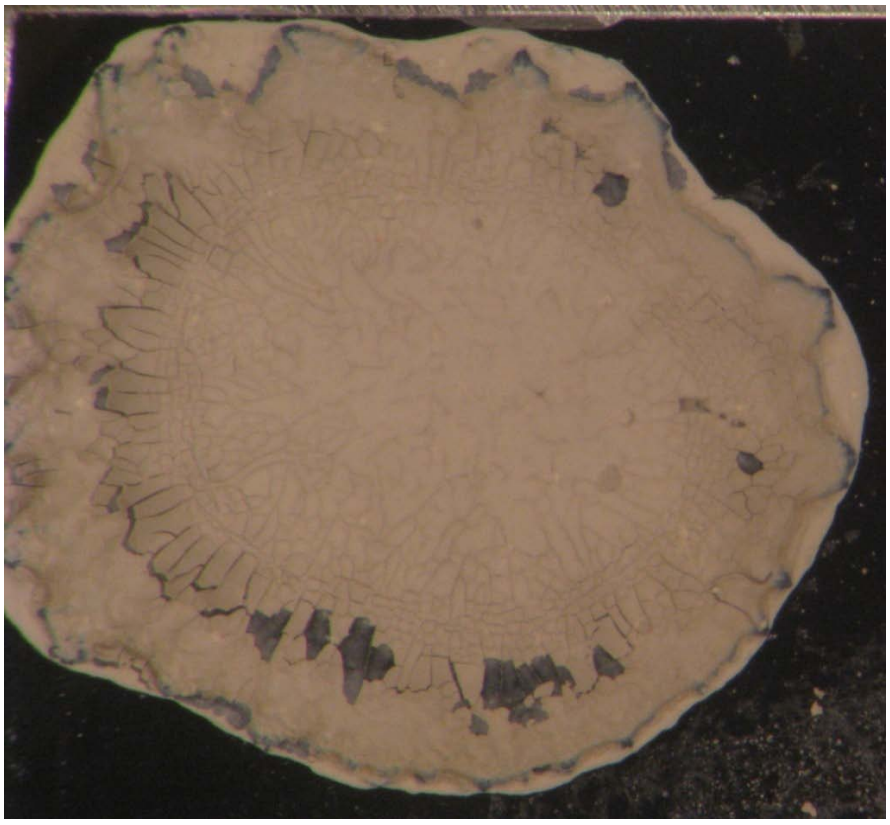

Figure 5-6: Resulting catalyst layer from a drop of catalyst slurry dried on external surface of a silicon wafer fragment.

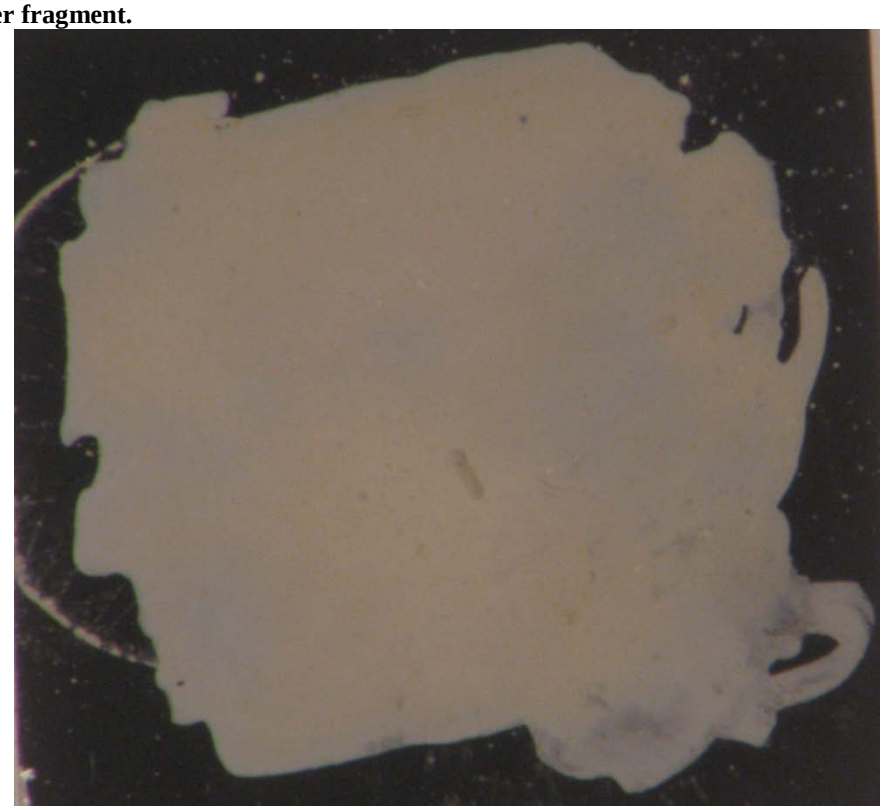

Figure 5-7: Uniform, well-adherent catalyst layer deposited on silicon by addition of a drop and subsequent smearing with a swab.

5.1.3. Final Catalyst Loading Procedure

The catalyst used in this work was 5% (by weight) platinum supported on gamma-alumina (Sigma Aldrich). To prepare the a catalyst slurry, the (wet) powder was ground using a mortar and pestle for approximately one hour, which reduced the mean particle size to from 12.5 to 3.6 µm, as measured by laser diffraction (Malvern Mastersizer 2000). The particle size distribution for the slurry as prepared and after one day of ageing is shown in Figure 5-8. No significant ageing effect was observed, likely related to the absence of any significant pH modifier. The prepared slurry contained 15% solids by weight, and included a colloidal alumina suspension (Nyacol) at 1% of total solids by weight to increase adhesion to the silicon. The particle suspension was not stable for more than a few minutes, and this was essential to allow catalyst coating of such large (and relatively hydrophobic) rectangular channels.

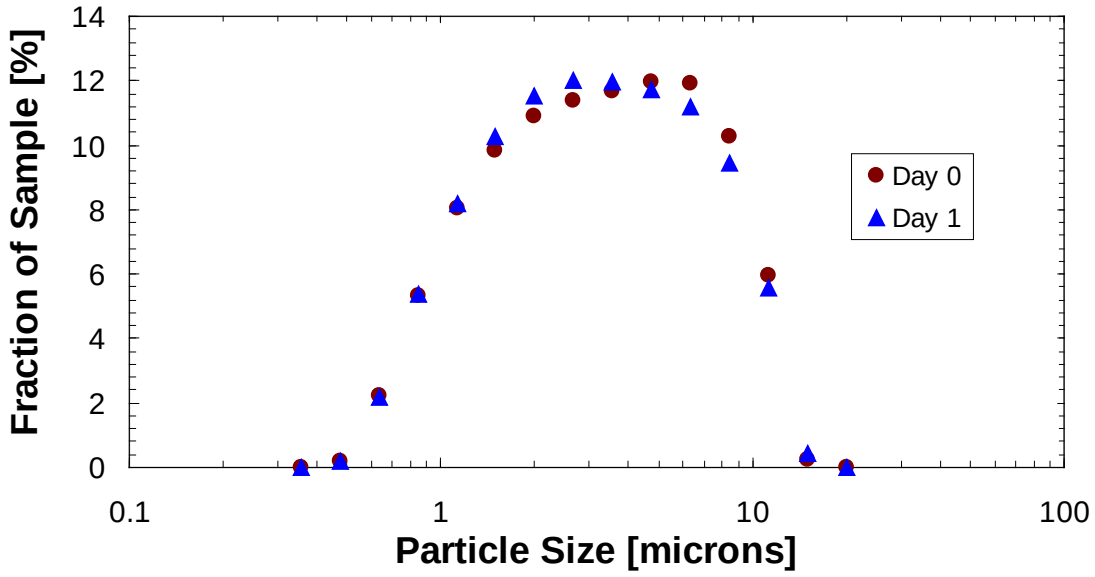

Figure 5-8: Slurry particle size distribution as prepared (Day 0) and after one day of ageing (Day 1).

To coat the channels, a process based on the general washcoating procedure for ceramic monoliths was used[190], with modifications to account for the surface properties of the silicon[200]. The slurry was first injected into the reactor channels using a syringe with the reactor held vertically. The reactor was then "rested" horizontally (such that the large faces were parallel to the bench) for 5 minutes. After this period, excess suspension was forced out of the channels using pressurized air. The reactor was then placed in a furnace

at 80°C for 30 minutes to evaporate the remaining water from the slurry, and a furnace at 400°C for 30 minutes to allow calcination of the catalyst layer. The belief is that some of the catalyst particles settle to the bottom and sides of the channel in the resting time, and then the carrier fluid is removed by the forced-air stream leaving a catalyst-rich layer along the walls, as depicted in Figure 5-9. After calcination, multiple coating steps could be performed without sacrificing the quality of the previous layer. This concept for this deposition process was based on the observation that uniform, adherent layers could be achieved with a smeared catalyst drop.

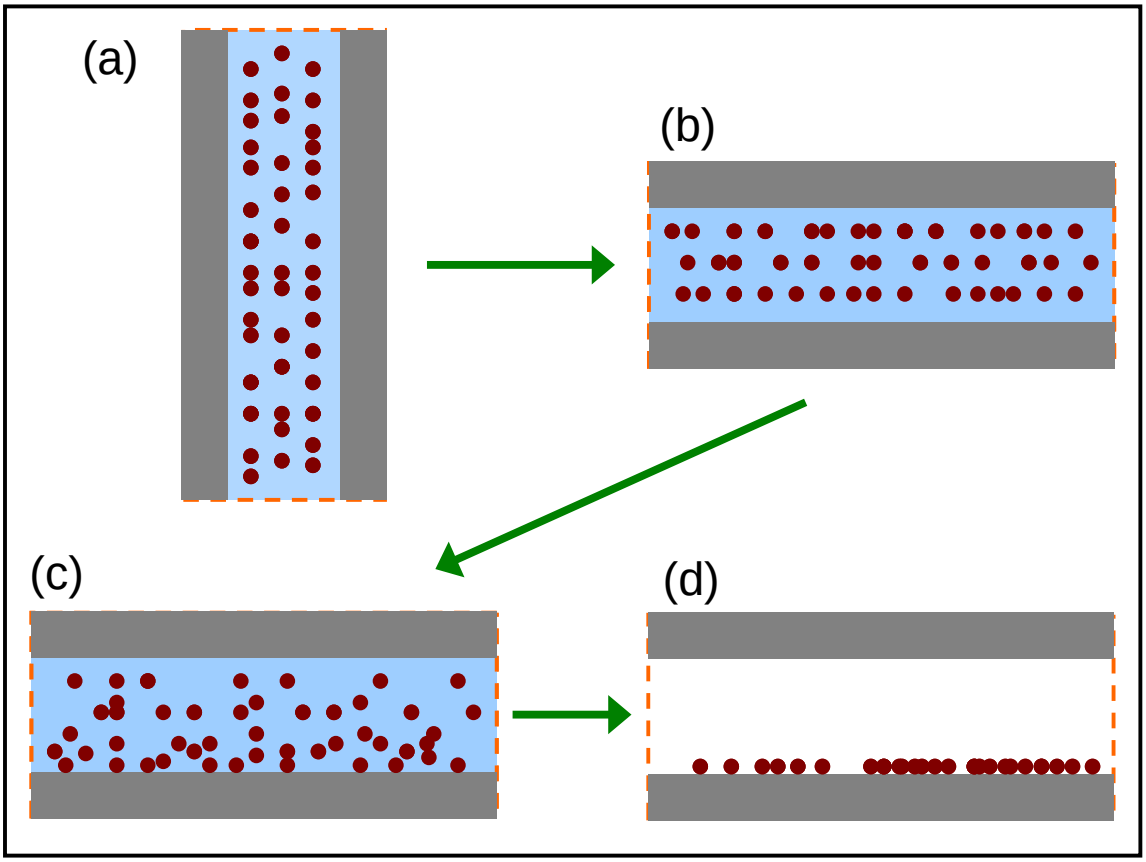

Figure 5-9: Hypothesized mechanism of a single step in the catalyst coating process. (a) Channel is filled vertically with catalyst slurry. (b) Reactor is positioned horizontally and rested for ~5 minutes. (c) Some solid particles begin to settle out of the slurry to the solid surface. (d) The carrier fluid is removed from the channel by forced-air, then the remaining water is evaporated in an oven. A gradient in the catalyst layer is observed such that the layer is thicker at the opening opposite where the slurry is loaded and the forced-air is introduced. The grey rectangles represent the top and bottom silicon surfaces, the brown dots represent the catalyst particles, and the blue represents water.

It was observed that the catalyst layer would be deposited primarily on the "bottom" silicon face – that is the side that had been lower during the resting period, though there was also appreciable deposition on the side walls (and some on the top surface). There

was also a noted axial gradient such that the deposited layer was thicker near the opening opposite where the catalyst slurry was introduced by syringe and the forced-air stream was introduced, as can be observed in Figure 5-10. In this figure, the reactors were coated in two stages, varying which large silicon face was placed on the "bottom" and "top", but with the axial configuration constant to achieve a notable axial catalyst gradient. Also observable in the figure is the appreciable coating on the side walls, particularly in the bottom set of channels (corresponding to the thicker layer). These gradients in catalyst deposition could possibly represent an interesting procedure for localizing catalyst layers within a washcoated structure. To obtain an even catalyst layer, as was used in this work, the catalyst coating procedure was performed a total of four times, alternating the horizontal face at the top and bottom as well as the injection side.

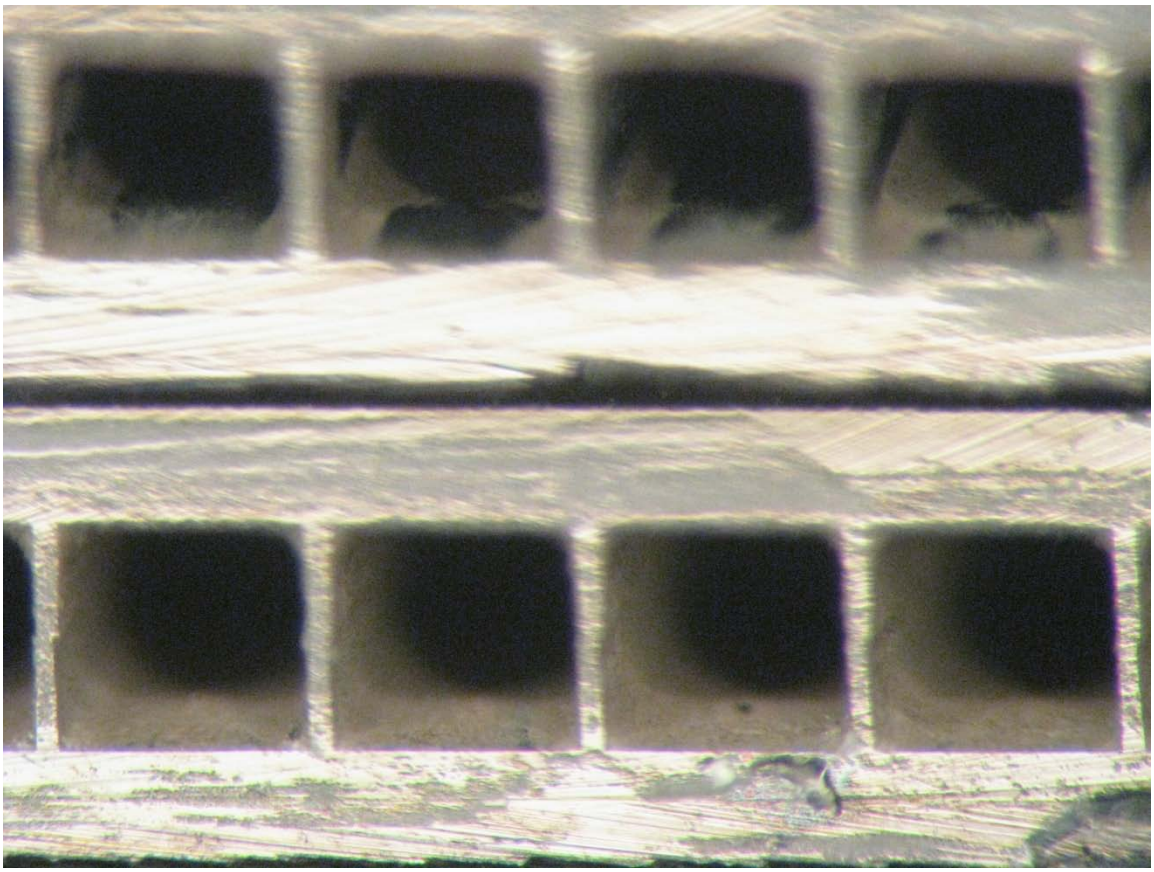

Figure 5-10: Catalyst loaded reactors demonstrating axial deposition gradient. Reactors were coated in two stages (to coat top and bottom faces) with constant axial orientation. Top channels show sparse coating characteristic of the side where slurry and forced air were introduced. Bottom channels show even coating characteristic of the far end.

The catalyst layer obtained through this process resulted in a catalyst mass per reactor of 161 to 243 mg (~28 – 66 mg per addition step), which corresponds to specific loading of

2.3 to 3.5 mg/cm^2 of silicon surface and ~6.5 – 9% of total weight. The deposited amount was proportionally dependant on the number of addition steps, the slurry solids concentration, the resting time during deposition, and the inverse of the slurry ageing time, which was expected given the hypothesized deposition process and the observed slurry properties. Loading densities between 2 and 10 mg/cm^2 have been reported in the literature[182, 201]. No significant loss of catalyst was observed during reactor operation.

Images of the catalyst layer were obtained using an environmental scanning electron microscope (ESEM) (FEI/Philips XL30 FEG ESEM) provided by the MIT Center for Materials Science and Engineering. To prepare the sample, the reactor was filled and surrounded with epoxy (Buehler Epothin) and cut with a diamond saw (Crystalite Corp. Primecut), after which the sample was polished (SBT 920 Lapping and Polishing Machine). The analysis was conducted for the axial center of the reactor, which is expected to have the least amount of catalyst, given the observed trend in deposition. An image of the typical catalyst layer cross-section in the channel is shown in Figure 5-11. The catalyst layer thickness varied from 20 to 70 µm on the top and bottom faces, with a representative image shown as Figure 5-12. The catalyst layer was ~10 µm on the side walls, which indicates that the catalyst distribution could be improved with more addition steps where the reactor was held on its side during the resting period. The observed catalyst layer thickness agrees well with the 10 – 20 µm thickness reported by Cristiani, et al.[196], for coating loads of 1.4 – 2.2 mg/cm^2, particularly when considering the uneven distribution of catalyst between top, bottom, and sides of the channels. Valentini, et al.[191], used a linear fit to experimental results for alumina washcoat thickness and mass to obtain 904 mg/cm^3 as the "coating density", and using this value the expected catalyst layer thickness for the observed loading densities would be 26 – 39 µm, which is also in good agreement.

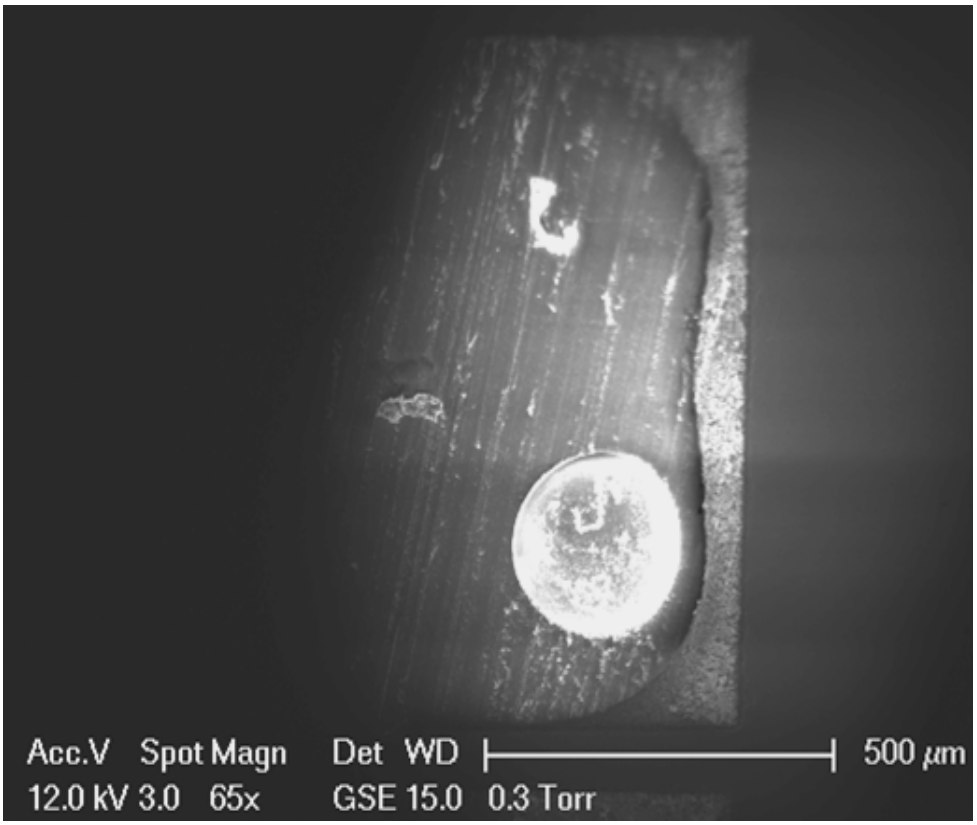

Figure 5-11: ESEM image of a typical channel cross-section from an epoxy-cast, catalyst loaded reactor. The right side represents the outer large face of this reactor, and the left side of the image represents the inner large face (next to the other combustor). The circular feature is a trapped air bubble.

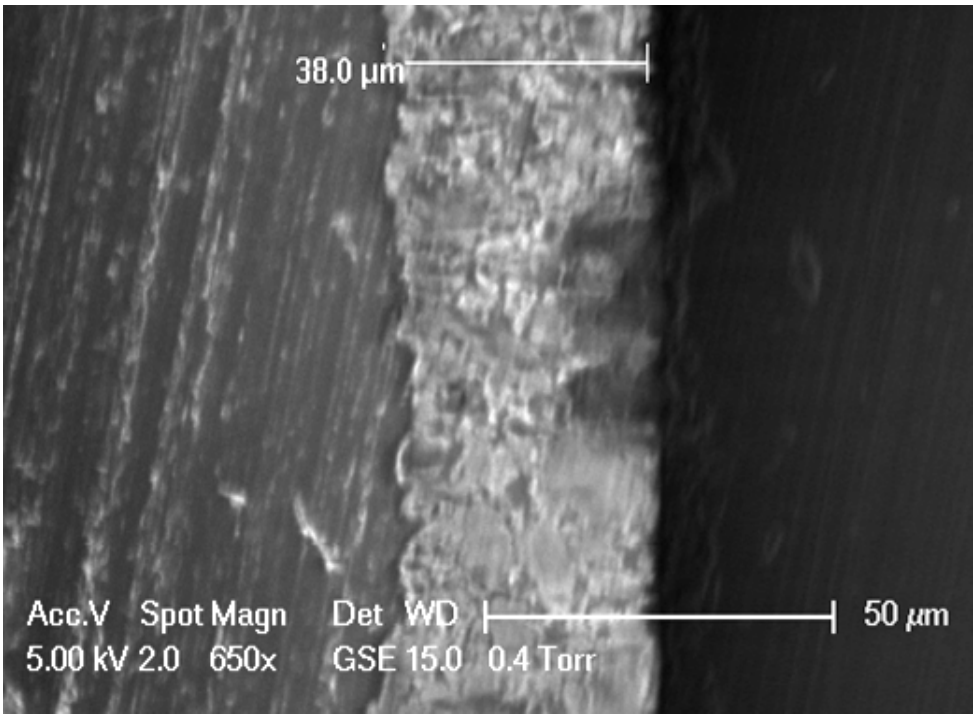

Figure 5-12: ESEM image of catalyst layer on bottom surface of channels. The porous catalyst layer was measured in this image to be 38 μm. The dark region on the right is the silicon combustor wall.

Significant collection of catalyst material was observed in the channel corners, as can be observed from Figure 5-13. This feature of the catalyst washcoat is counterproductive for combustor performance, as it leads to increased flow resistance and essentially wasted catalyst weight (and cost) given that the residence time is unlikely to be sufficient to allow time for diffusion into the corner. However, the accumulation is caused by the surface tension of the slurry in the channel, and has been observed repeatedly in the literature. For example, an image of a 10-μm-thick zirconia washcoat on a cordierite monolith in which similar collection is observed on a length scale of ~150 μm around the corner is presented from Agrafiotis, et al.[201], in Figure 5-14. In order to reduce this accumulation of catalyst in the corner, it is likely that the surface properties of the reactor or the solvent properties would have to be adjusted to increase the wettability of the surface with respect to the slurry.

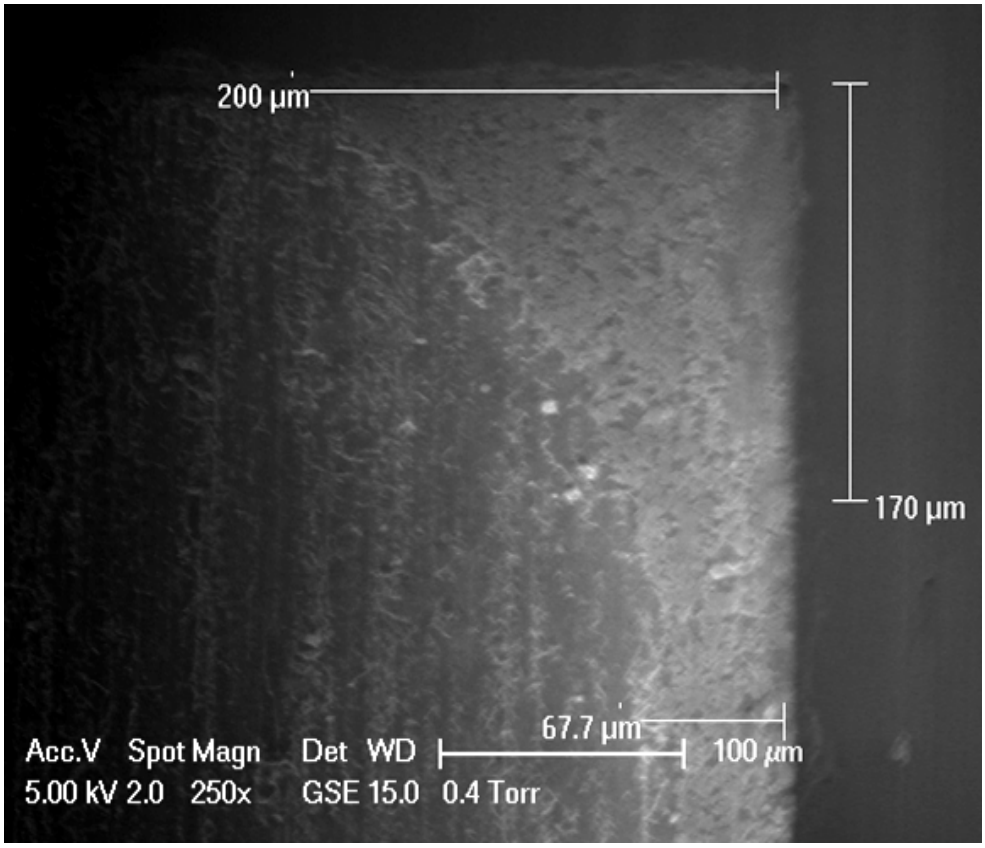

Figure 5-13: ESEM image of catalyst collection in the channel corner between bottom and side surfaces.

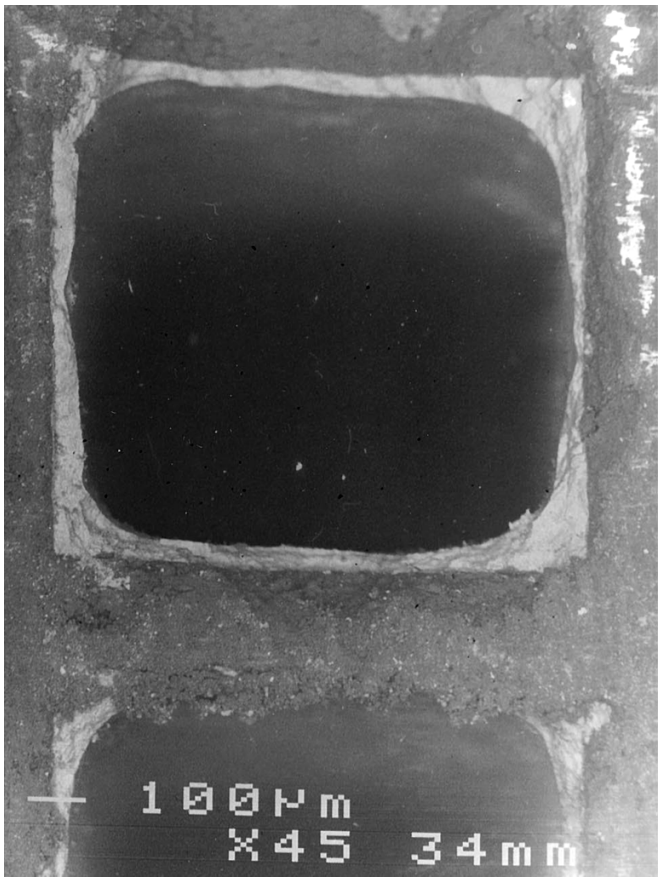

Figure 5-14: Zirconia washcoat on a cordierite monolith exhibiting accumulation of catalyst in corners. From Agrafiotis, et al.[201]

5.2. Compression Packaging of Reactors

As described in chapter 3, gas distribution manifolds were designed at MIT Lincoln Laboratories and fabricated by direct metal laser sintering (DMLS) from 17-4 PH stainless steel. A gas-tight seal between the reactors and the manifolds was created by compression of a soft gasket between the two faces. The gaskets were made from 99.999%-pure aluminum (ACI Alloys, Inc.), and formed to the dimensions specified in Figure 5-15 using a chemical etch (Newcut, Inc.). The manifolds, reactors, and a gasket are shown in Figure 5-16. The gasket was designed to leave the channels open while providing an overhanging seal on all the silicon faces. The aluminum material was selected to minimize material cost while accommodating combustion temperatures and ensuring that the material would deform with less stress than the yield stress of silicon. Gold would also likely have been a suitable gasket material.

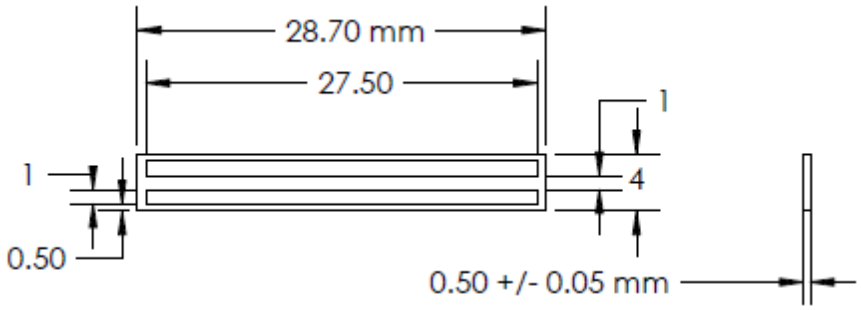

Figure 5-15: Drawing of soft aluminum gasket used to provide a gas-tight seal between combustors and gas distribution manifolds.

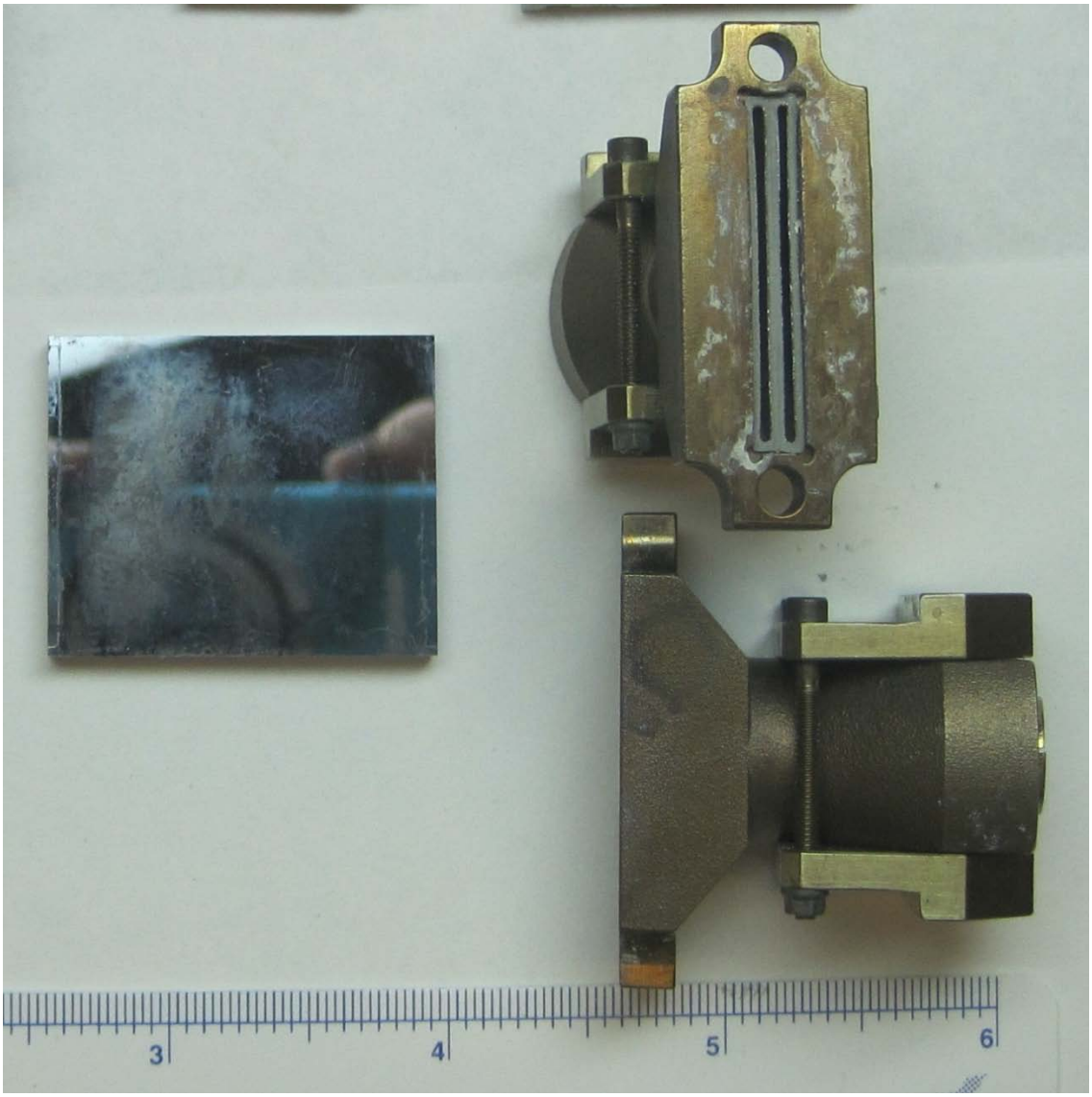

Figure 5-16: Gas distribution manifolds, aluminum gasket, and 35-mm-long silicon combustors. Scale on ruler is in inches. The gasket can be observed inside the recess of one of the manifolds.

In order to provide the proper pressure at the manifold-gasket-reactor interface, the entire assembly was compressed with two 6/32 socket-head bolts, hex jam nuts, and Belleville disc springs (Gardner Spring), which are spring-loaded washers. On each bolt, six Belleville disc springs (each 0.312 in OD x 0.156 in ID x 0.0166 in thickness) were stacked together to provide the appropriate tension when tightened 3/8 of a turn past finger-tight[202]. It was crucial that these bolts were tightened simultaneously and in many stages, to avoid any stress imbalance on the combustor. A drawing of the combustor loaded into the manifolds with the bolts and Belleville disc springs is shown as Figure 5-17.

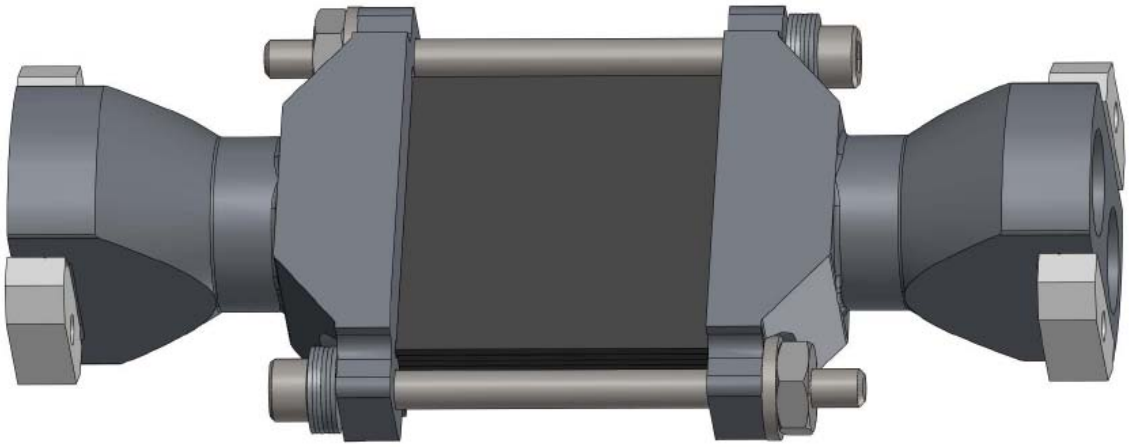

Figure 5-17: Drawing of the designed combustors connected to the gas distribution manifolds with tension provided by Belleville disc springs (shown on socket-cap-end of 6-32 bolts).

To provide the gas-tight seal, the soft aluminum gasket was observed to deform around the silicon features. The deformation can be observed in Figure 5-18, which shows the reactor-facing side of an aluminum gasket after compression and thermal cycling associated with combustor testing. The defined rectangular marks in the aluminum show where the open channel did not compress the metal, and at the very bottom of the image the raised portion of the metal corresponds to part of the gasket that was not covered by the reactor. The gasket shown in this image was used to seal combustors which had been fixed together with a thin film of 5-minute epoxy (DevCon), as part of a series of tests for die-level adhesive bonding (discussed in chapter 4). The resulting gap can be observed as the raised line in the center of the gasket, and was not typical of the gaskets after

compression. During combustion experiments, it was observed that the gas-seal was improved after thermal cycling, likely due to softening of the metal.

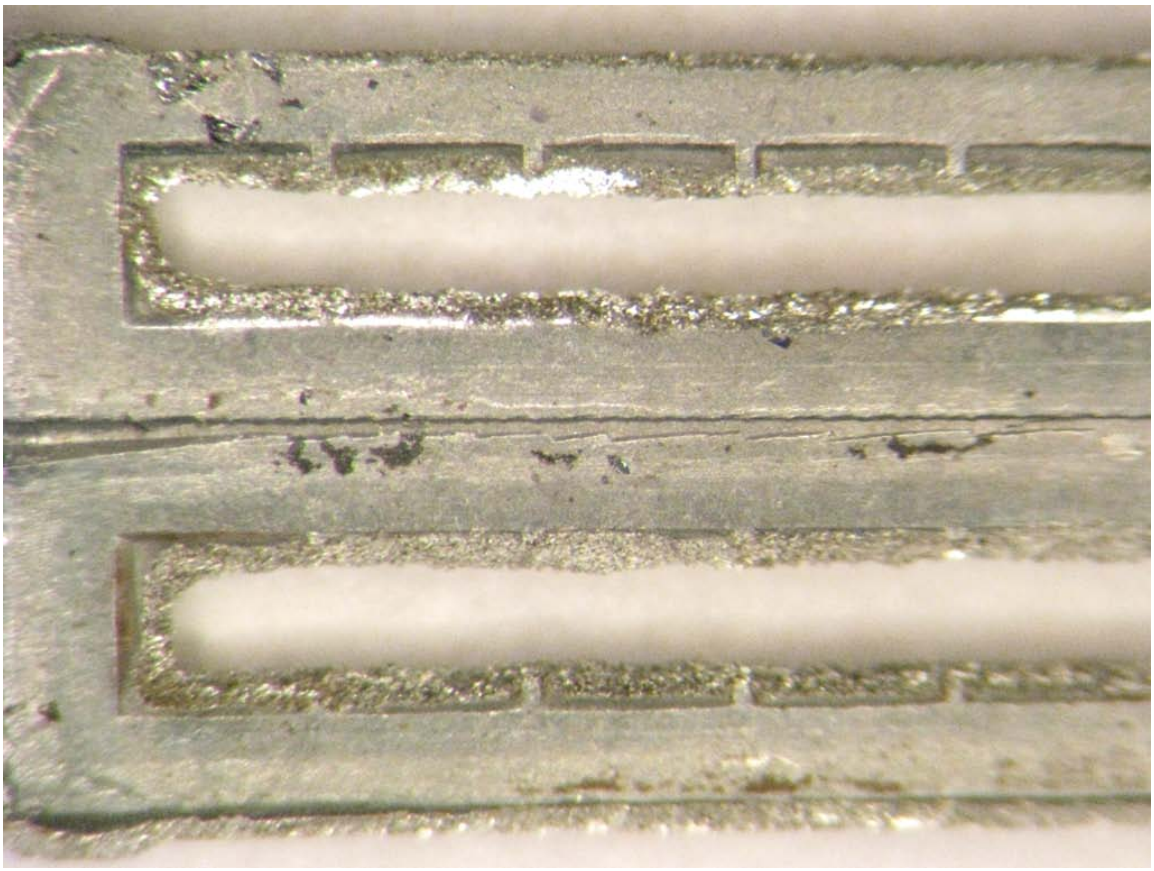

Figure 5-18: Reactor-facing side of aluminum gasket after compression and thermal cycling. Gasket compression is clearly visible from unaltered regions corresponding to reactor channels, to the interface between reactors, and to the top and bottom of the reactors.

The initial design for interface between the gas distribution manifolds and standard steel tubing (for peripheral connections) was to have tubes welded to the manifolds. However, concerns over the mechanical properties of the DMLS-produced-steel led to an altered design using a second high-temperature compression seal. A metal block, referred to as a "tube adapter", was designed to interface with the manifold by compression of a 0.06-in-thick graphite gasket. Flexible graphite (Graftech International GTB grade) was formed into the desired gasket shape, with holes corresponding to the ~3/8-in-diameter inlet and outlet from the manifolds, using a water-jet (OMAX Jet Machining Center) in the MIT Hobby Shop. The produced gaskets, before and after compression, are shown in Figure 5-19. Compression was provided by two socket screws which threaded into a plate that clamped onto the manifolds, and were tightened using a standard hex-key. No

appreciable gas leaks were observed from the compressed gaskets after sufficient tightening. The packaged reactor, including gas distribution manifolds and tube adapters, are shown in Figure 5-20.

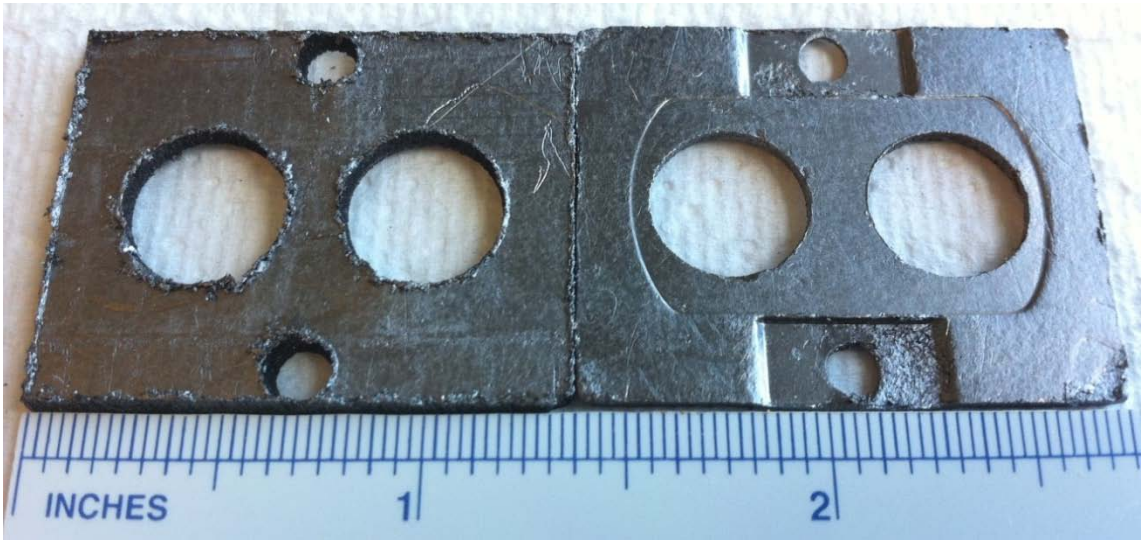

Figure 5-19: Graphite gaskets produced using a water-jet. Gasket on left shows fresh gasket after production, gasket on right shows gasket after compression. Large holes provided for gas flow, small holes for screws.

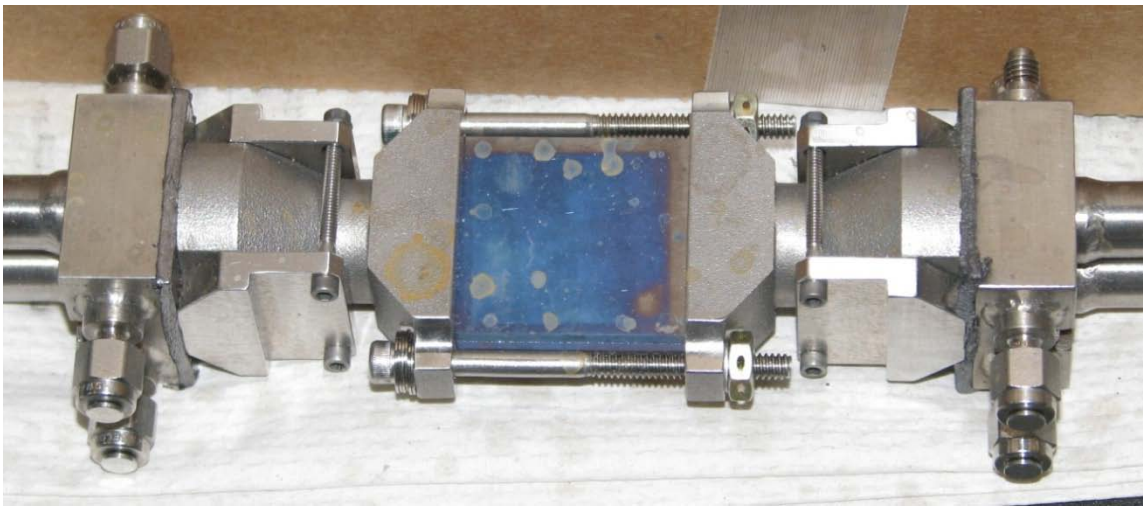

Figure 5-20: Packaged reactors with gas distribution manifolds, original tube adapters, and welded tubes. Plates on gas manifolds to connect to tube adapter facilitated the modified connection. Graphite gaskets can be observed between the manifolds and the tube adapters. Temperature and pressure connection ports can be observed on the original tube adapters. For scale, reactor is 2.85 cm in width (perpendicular to sealing bolts).

5.3. Test Stand Integration for Design Performance with Water-Cooled, TE-Mimicking Heat Sinks

The purpose of the test stand for the combustor was to support the integration between the peripheral systems such as mass flow controllers, pumps, thermocouples, etc., and the

combustor. This stand was not intended to mimic a final portable device, but rather to facilitate consistent and complete analysis of the combustor. The test stand for evaluation of the combustor with water-cooled heat sinks was modified significantly from the original design as a result of integration difficulties between the fluidic connections and the heat sinks. Both the original design, and the modified design required for successful integration are described here. All systems were located inside a ventilated hood with significant air flow to ensure safe handling of all flammable gas mixtures.

5.3.1. Original Test Stand

The original test stand, designed in large part by collaborators at MIT Lincoln Laboratories, was based around a central frame to which both the heat sinks and fluidic connections were mounted. The majority of the stand components were made by the MIT Central Machine Shop, with a few components provided by MIT Lincoln Laboratories. A drawing of the original test stand design, with the outer heat sink removed, is shown in Figure 5-21, and an image of the assembled stand is shown in Figure 5-22. Four rigid 3/8-in-diameter stainless steel tubes were provided for inlet and outlet gas streams to both of the reactors. These tubes were welded to the tube adapter on one (hot) end, connected with Swagelok compression fittings to the external piping on the other (cold) end, and fixed to the central frame close to the cold end with an adjustable clamp. The tubes were bent into a half-square shape after the tube adapter in order to provide additional length to minimize conductive heat transfer between the hot and cold ends. The water-cooled, TE-mimicking heat sinks were also connected to the central frame (through a machinable ceramic insert to provide thermal isolation), and this connection was not adjustable.

The original design for the tube adapter was for a stainless steel piece with two 3/8-in tubes welded for inlet and outlet gas flow and four integrated 1/16-in Swagelok fittings for pressure and temperature measurements. A drawing of the original adapter interfaced with the combustor is shown in Figure 5-23. The machined adapter was shown in Figure 5-20. The design required the fuel and air to be mixed well upstream of the combustor. Fine-tipped thermocouples (Omega TKFT72) were introduced into the gas streams in the adapter to measure the inlet and outlet gas temperatures.

Figure 5-21: Original test stand for evaluation of design performance. Outer heat sink has been removed to show combustor and manifolds. Drawings produced at MIT Lincoln Laboratories.

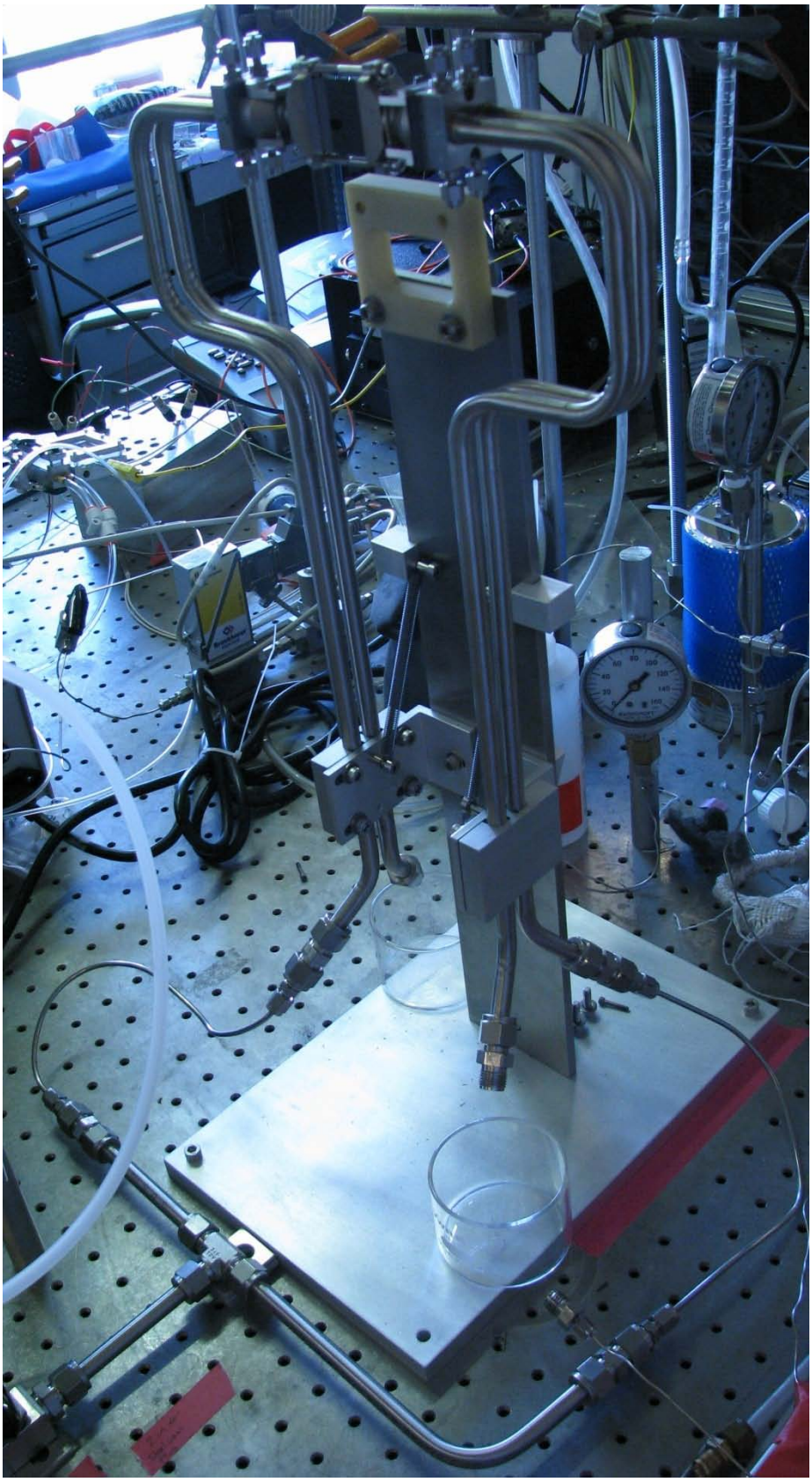

Figure 5-22: Image of original test stand prior to insulation and integration of heat sinks.

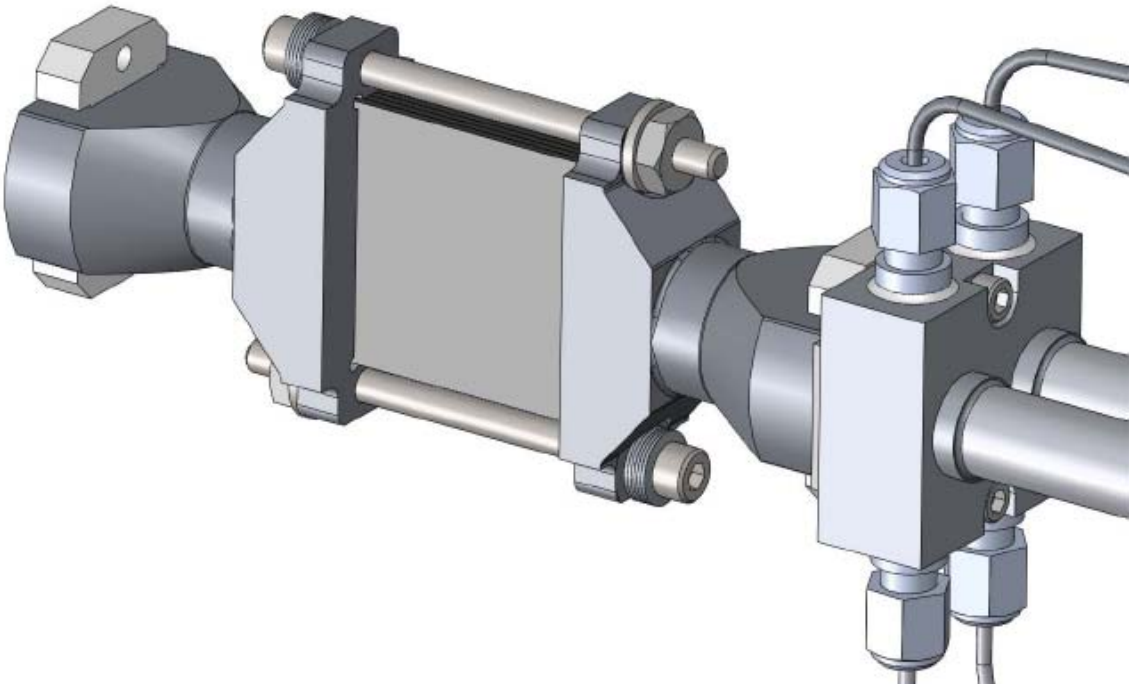

Figure 5-23: Drawing of the original tube adapter connected to the combustor. Two welded tubes transport mixed fuel / air stream and exhaust stream.

The manifolds, tube adapters, and tubes were covered with ceramic insulation in order to provide thermal isolation for the combustor. Immediately next to the metal, a 1/16-in-thick layer of ceramic tape (McMaster Carr, Ultra-Temp.) was provided, which is reported to have a thermal conductivity of 0.055 W/mK at 260°C and can operate at temperatures up to 2600°F. A sturdier, more flexible ceramic tape (Mineral Seal Corp. CeraTex) was wrapped approximately three times outside the first tape to provide a more robust insulation layer. The CeraTex insulation was also 1/16-in-thick, and reported to have a thermal conductivity of 0.12 W/mK at 300°C. When desired, electrical heating tape (Omega Engineering) was incorporated between insulation layers to facilitate reactor ignition (as discussed in chapter 6).

The contact between the water-cooled, TE-mimicking heat sinks and the combustor surface was facilitated by a thermal-spreading graphite layer (Graftech International eGraff SS300). The thermal conductivity within the graphite layer is ~150 W/mK while the thermal conductivity through the graphite layer is ~10 W/mK, as reported by the vendor. The graphite also provided a compliant layer such that the thermal contact

resistances between the heat sink and the combustor could be reduced at high temperature. The heat sinks were compressed against the combustor through four 6/32 bolts using Belleville disc springs to provide the tension, positioned at the corners of the heat sink plate. As with the compression sealing of the combustor and manifolds, it was crucial that the bolts be tightened simultaneously. The amount of clamping force which would compress the graphite without breaking the silicon reactor was determined through trial-and-error to be approximately 3/8-turn past finger-tight. After compression, impressions corresponding to the segments of the heat sink could be observed in the graphite layer, as shown in Figure 5-25. Areas of poorly defined heat sink surface features (as seen in the upper right portion of the figure) indicated uneven heat sink compression.

Figure 5-24: Graphite compliance layer between heat sink and combustor after packaging. Surface features correspond to surface of heat sink. Uneven definition of features indicates uneven compression of heat sinks, and possibly increased contact resistance in region lacking definition.

An image of the integrated test stand, with insulation removed from the tube adapters and manifolds, is shown in Figure 5-25. The original stand was used for combustion experiments, both with and without the heat sinks integrated. However, while the combustor could be loaded into the fluidic connections successfully, there were no successful attempts to integrate the fluidic connections and the heat sinks without breaking the silicon reactor. An image of the typical combustor fracture following an attempt to integrate the system components is shown in Figure 5-26. The nature of the adjustable connection of the tubes to the central frame, which could access a range of positions but was quite difficult to control with precision, combined with the rigidity of the tubes and the heat sink connection resulted in any stress due to misalignment being focused on the silicon combustors. This stress consistently proved to be more than could be accommodated by the silicon reactors, for which the brittleness of silicon was exacerbated by the anisotropic etch used to define the features.

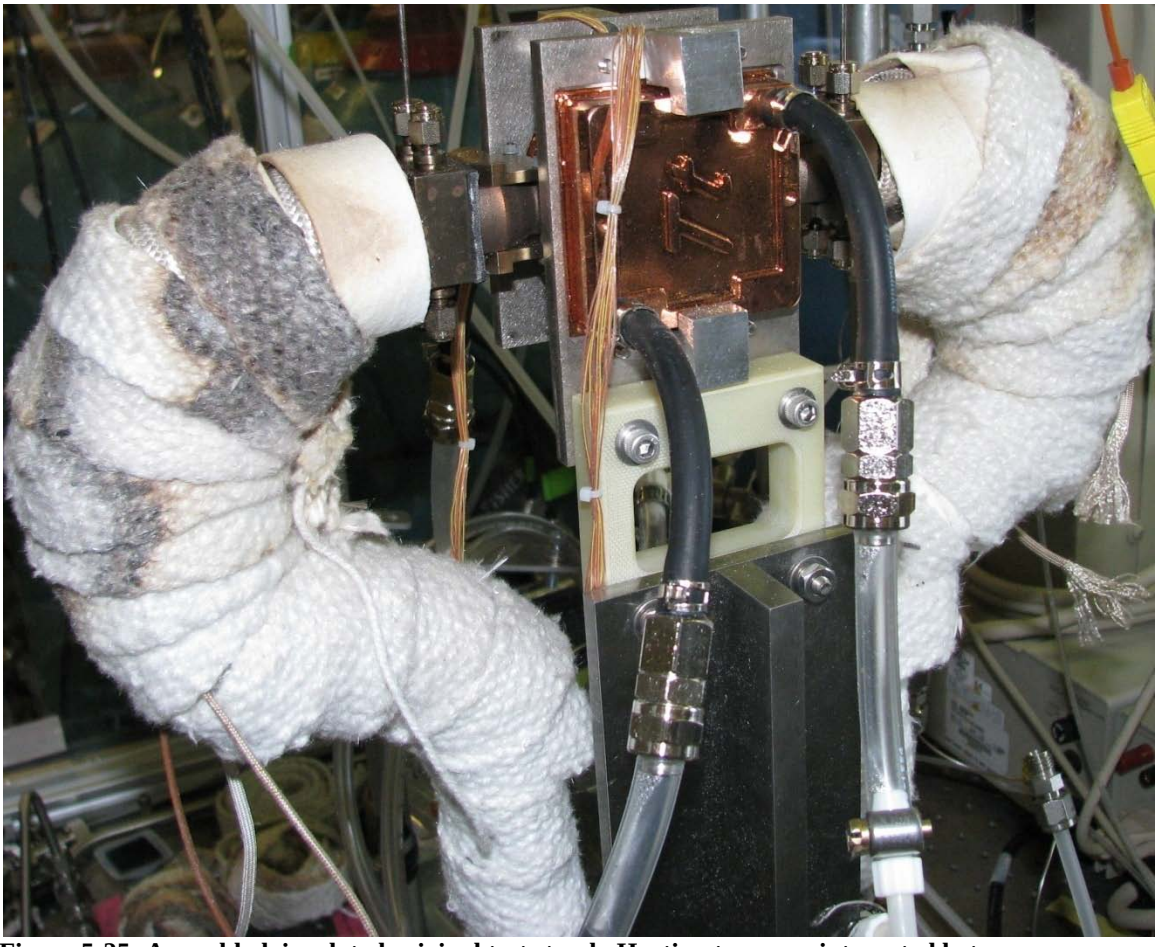

Figure 5-25: Assembled, insulated original test stand. Heating tape was integrated between insulation layers for electrical resistance heating of air stream for reactor ignition.

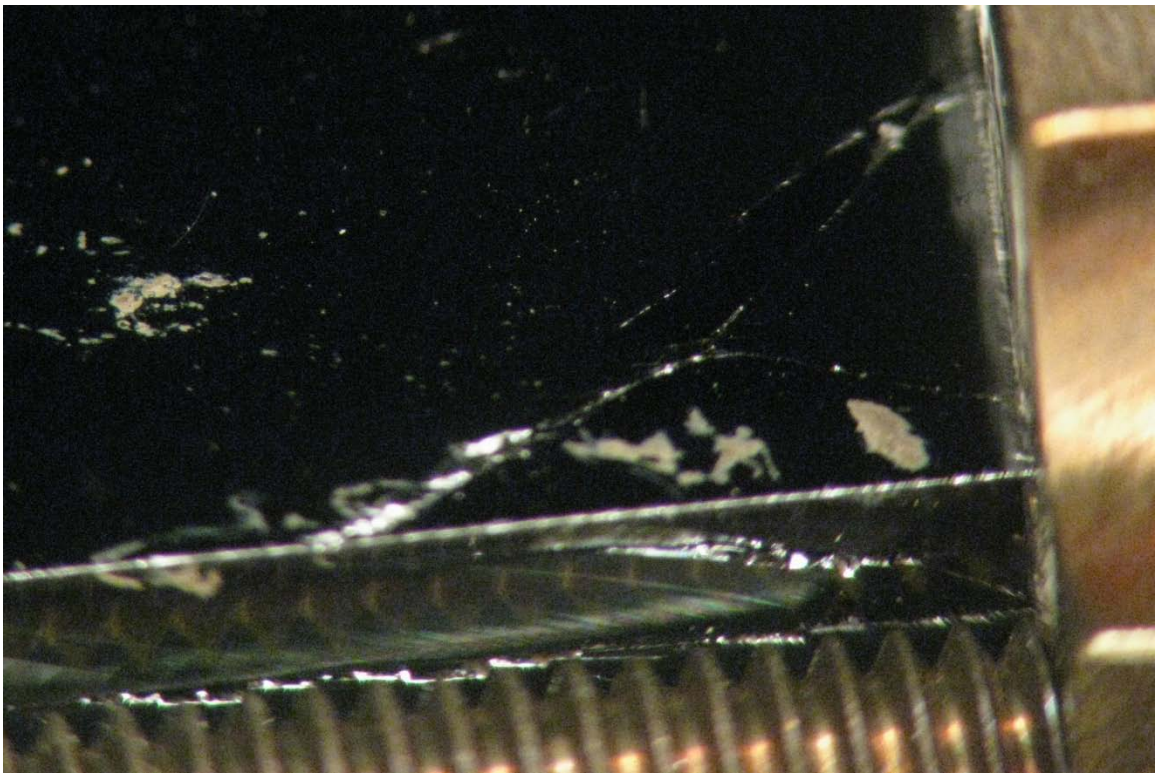

Figure 5-26: Close-up image of cracked reactor after an attempt to integrate with heat sinks and fluidic connections in original test stand.

5.3.2. Final Test Stand

In order to reduce stress due to misalignment of the fluidic connections and the heat sinks on the silicon combustors, the fluidic connections were redesigned to provide some compliance. Flexible steel tubes with 1/4-inch-diameter (Cambridge Valve and Fitting), shown in Figure 5-27, were used replace the rigid 3/8-in tubes, with the idea that the tubes would self-align to the combustor and heat sinks (which remained connected to the central frame). In order to connect these flexible tubes to the tube adapters, threaded NPT fittings were used in lieu of welds (to simplify fabrication). To facilitate a gas-tight seal at the high temperatures that the tube adapters could possibly reach, a high-temperature thread sealant (Esco Products, Inc. Copaltite) was used. Given that new tube adapters were required, the piece was redesigned in order to allow separate fuel and air tubes to be connected. The redesigned adapter, shown in Figure 5-28, was machined from aluminum (Proto Labs). The connection to the NPT fitting was made by a short (~3 in) section of 1/8-in tube (and Swagelok fitting). The flexible tubes were attached to the end of the 1/8-in tubes.

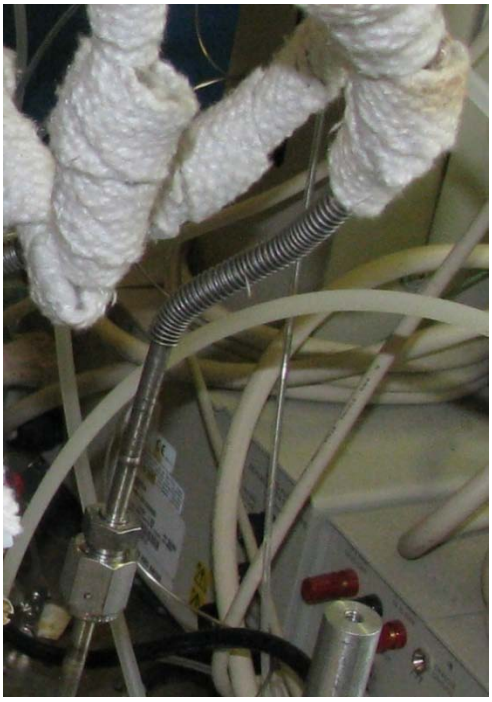

Figure 5-27: Flexible steel tube used to provide compliance in fluidic connections.

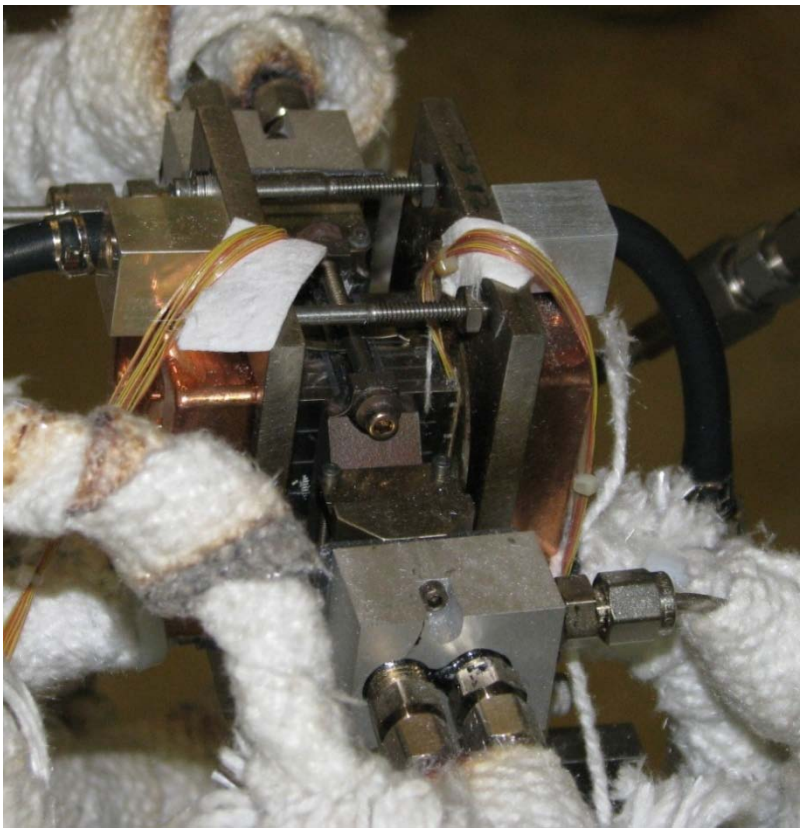

Figure 5-28: Combustor packaged with heat sinks and redesigned tube adapters. The tube adapters have three 1/8-NPT connections to which 1/8-in-swagelock connections are made. The black substance around the NPT connection is the copaltite thread sealant.

The final test stand is shown in Figure 5-29, with the insulation removed from the tube adapters, manifolds and heat sinks for visibility. To assemble the system, first the reactors were loaded into the manifolds, and then the tube adapters were connected to the manifolds. Next, the heat sinks were compressed onto the reactor, and finally the insulation was added to the tube adapters, manifolds, and heat sinks. One to two layers of the CeraTex ceramic tape were used to insulate the flexible tubes and tube adapters, with approximately three layers used to insulate the manifold, the reactor-heat sink interface, and the exterior of the heat sinks (to ensure the accuracy of the calorimetry estimate of the heat removed from the combustor through the heat sinks, as described in chapter 6). The system was packaged successfully, without cracking the combustor, using this final system with the flexible tubing.

5.4. Test Stand Integration for TE Power Generation

The test stand used for the TE power generation system was similar to the final test stand used to evaluate the design performance, described above. The fluidic connections were unchanged, with the slight exception that only one or two layers of ceramic tape insulation were used on the manifolds and tube adapters in order to avoid any interference with the electrical connections made to the TE modules (at the bottom of the system). The changes to the system were related to compression packaging of the TE modules, air-cooled heat sinks, and combustor. A representative cross-section of the TE system is shown in Figure 5-30. The TE modules are sandwiched between the combustor and the air-cooled heat sink. A graphite layer (similar to that used with the water-cooled heat sinks) was included next to the combustor to provide thermal spreading and mechanical compliance, as well as for thermocouple integration (as described in chapter 7). On either side of the TE modules, 0.27-mm-thick alumina insulating shims (Hi-Z Technologies) were used to prevent electrical short circuiting of the TE elements. Thermal paste from Hi-Z technologies was used on all cold interfaces and a high-temperature thermal paste (Epoxy Technologies, Inc. HTG-72) was used on all hot interfaces.

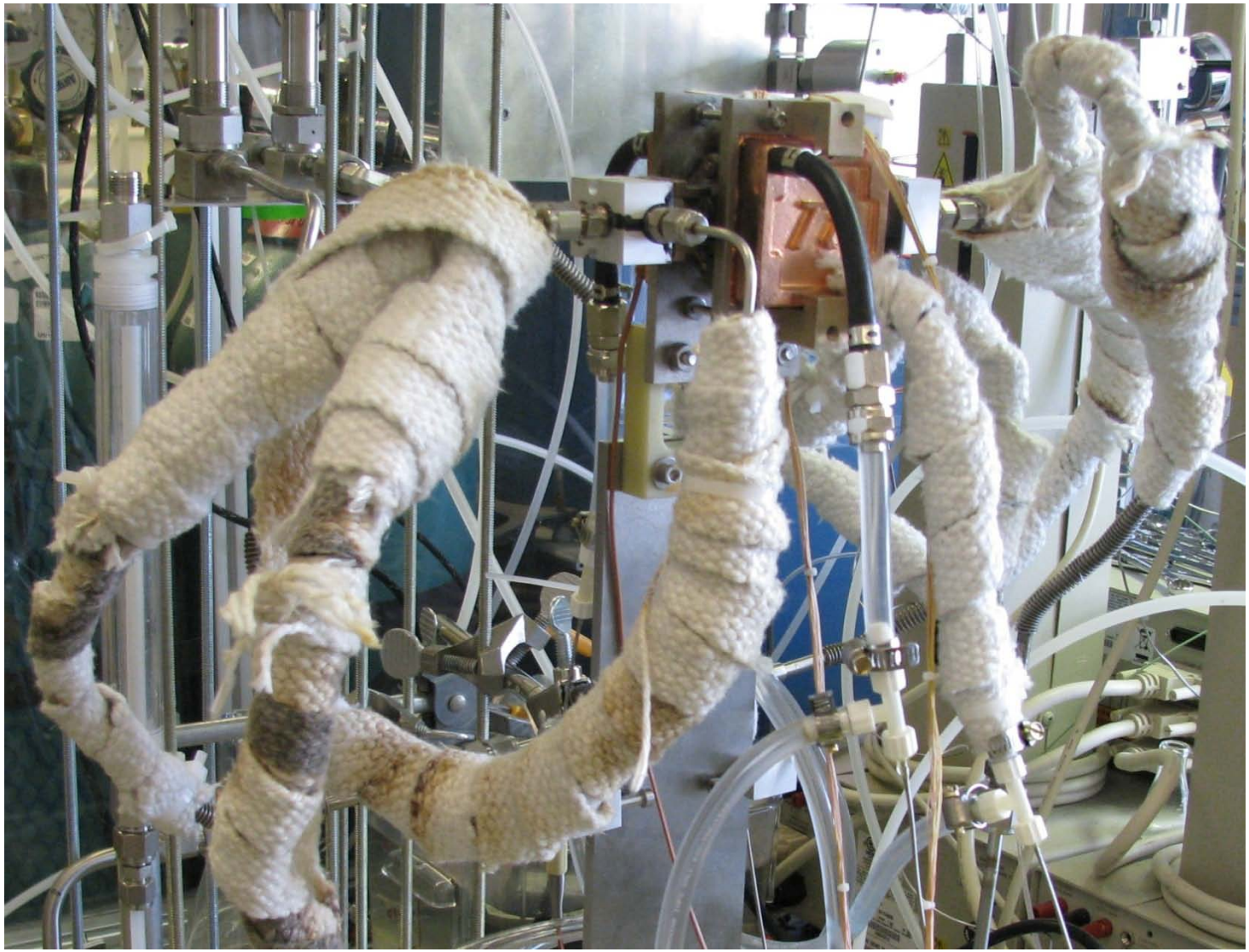

Figure 5-29: Final test stand for evaluation of design performance. Insulation was removed from tube adapters, manifolds and heat sinks.

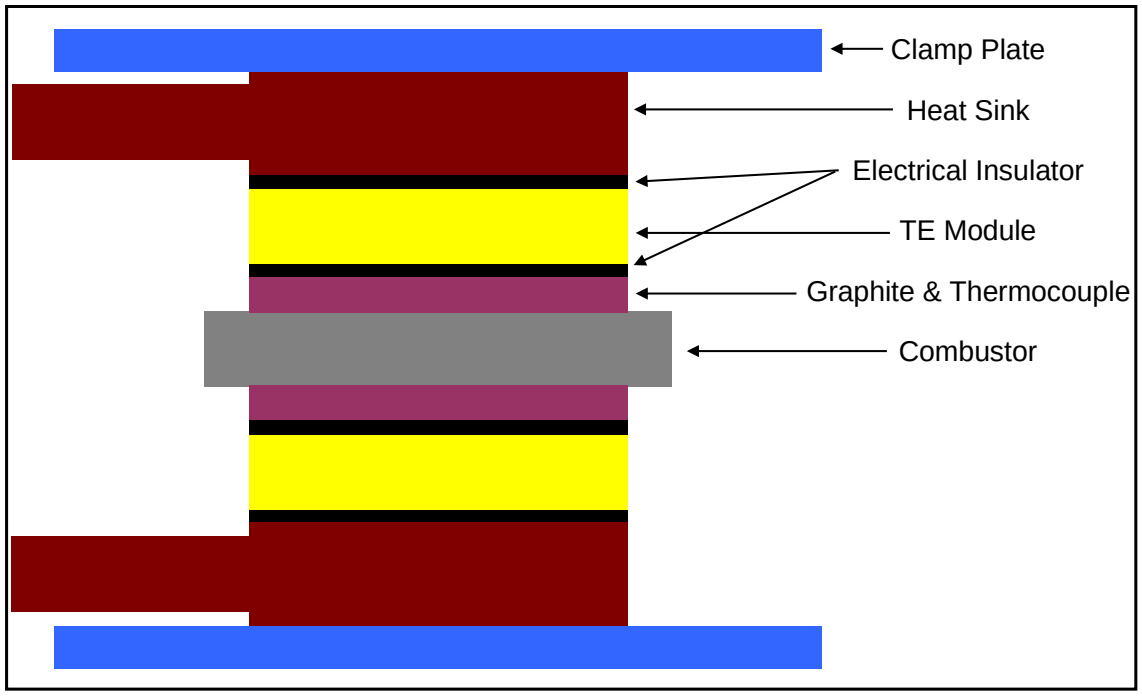

Figure 5-30: Schematic of layered structure of TE power generator.

Some of the key components of the TE power generator system are shown in Figure 5-31. The clamp plates were machined from aluminum (Proto Labs), and the compression was provided by four 6/32 socket cap bolts and hex nuts. To assemble the system, the first clamp plate and heat sink were placed into an elevated holder (that allowed access to the hex nuts), and then the components were added the following order: alumina shim, TE module (cold-side down), alumina shim, graphite layer with thermocouple, combustor (with manifolds attached), graphite layer with thermocouple, alumina shim, TE module (hot-side down), alumina shim, heat sink, and second clamp plate. The four bolts were inserted into the holes and the nuts were attached to finger tight. A torque wrench was used to simultaneously tighten the four bolts to 1.5 inch-pounds of torque, which was determined experimentally to provide similar performance as when bolts were tightened to 2 inch-pounds. Compressive force has been demonstrated to improve thermoelectric performance[30]; however, the desire to improve performance had to be balanced against the possibility of cracking the silicon reactor from an uneven application of compressive force. Following this procedure, the TE power generator was successfully packaged.

Figure 5-31: TE power generator system components. Clockwise from top left: air-cooled heat sink, TE module, clamp plate, gas distribution manifold (with aluminum gasket) top view, manifold side view, and combustor (center of image).

To integrate the packaged TE generator system with the fluidic connections, a suspension system was developed to provide compliance and stability. A nylon rope was fixed to a beam at the top of the hood, and a support was made from two lengths of 3/8-in steel tube and two pieces of 1/16-in-thick aluminum, to which the ends of the rope were attached. These tubes supported the underside of the aluminum fins on the air-cooled heat sinks, providing a flexible support for the TE generator as well as the electric fan used to provide cooling air flow. To assemble the system, the TE generator and fan was suspended using the support, and then the tube adapters were connected to the manifolds.

Once the tube adapters were connected, they were supported by test tube clamps and threaded rods, though care was made to support them far from the tube adapter to maintain a flexible connection. Finally, the electrical connections were made to the TE modules and the system was insulated. The final system (prior to insulation and electrical connection) is shown in Figure 5-32.

5.5. Concluding Remarks

Reactor packaging and system integration is often a significant challenge for MEMS systems, and this was certainly the case in this work. Catalyst washcoating of silicon structures has been studied by several groups, but there is not yet a standardized process which can be transferred between systems, particularly when differences in the fabrication process of the silicon device may prevent or complicate certain steps. For example, the fusion bonding process (with enclosed features) used to form the reactors in this work precluded the deposition of a silicon oxide layer that has been demonstrated to increase the wettability of the surface for aqueous solutions and improve catalyst washcoating. A modified catalyst loading procedure was developed in this work which could be used in the future to selectively deposit catalyst with a washcoat, which may be advantageous for reducing thermal gradients in exothermic reactors.

The integration of system components in a TE power generator was also a significant challenge, particularly to maintain thermal isolation of the combustor while providing proper alignment of system components to avoid the application of stress to the silicon device. It was found that by providing flexibility in the system components, it was possible to assemble a thermally-isolated system in which a silicon device was under compression in two separate directions.

Figure 5-32: Assembled TE power generator system prior to insulation and electrical connections.

6. Design Performance with TE-Mimicking Heat Sinks

As described in chapter 3, the catalytic combustor system was designed to operate efficiently with a large heat flux removed from the two large faces through design thermoelectric (TE) modules. There are several examples in the literature where testing of small-scale combustors was conducted with a significantly different set of thermal pathways from the intended final system, with results that did not reflect the performance of the final device [41, 102]. As the combustor was developed before the design TE modules could be obtained, it was important to validate the design using appropriately designed heat sinks, which have been described previously.

6.1. Experimental Details

6.1.1. System Configuration

A flow diagram for the combustor system with integrated TE-mimicking heat sinks is presented as Figure 6-1. The majority of the piping used was 3/8-inch thin-walled, seamless 316 stainless steel, though some sections of 1/8-inch, 316 stainless steel tube were required to integrate with needle valves on the air inlet lines and NPT-fittings used to connect to the tube adapters (which have been described in chapter 5). Connections between the air, argon, and butane tanks and their respective mass flow controllers were made using 1/4 inch, rigid polypropylene tubing. Unless otherwise specified, all tubing was obtained from McMaster-Carr, and all connections were compression-type using Swagelok fittings from Cambridge Valve and Fitting.

As described in chapter 5, two different piping configurations were used for the heat sink experiments. The original configuration differed from the final system in several aspects of the piping and connections. First, the original configuration did not include valves in the gas lines to balance flow between the two reactors. Considerable care was taken to ensure that the resistances to flow in the two flow paths were similar in this original system. A second difference between the two configurations is that the in original system the air and fuel streams mixed just after the mass flow controllers and check valve, rather than in the tube adapter as in the final system. This early mixing insured that the gases

were well mixed upon entering the reactor; however, on a few occasions, flames were observed to propagate backwards from the reactor in the heated inlet tubes, which was a safety concern. These flames, which occurred during hydrogen combustion, were detected by an audible "pop", observed smoke as the binder in the ceramic tape insulation was released, and notable discoloration on the stainless steel inlet tubes. To avoid this issue in the original system, 1/4–inch-diameter ceramic fiber rope was placed inside the tubes, but this solution was not ideal as it increased the system pressure drop and disrupted the flow balance between the two reactors. No such issues were observed in the final system with fuel and air mixing just upstream of the reactor. A third difference between the two configurations is that the original system had fine-tip thermocouples integrated into the tube adapter to measure exhaust gas temperature. These thermocouples were omitted from the final design, in order to simplify machining and to reduce the opportunities to place additional stress on the silicon reactor.

6.1.2. Instrumentation and Control

Flow of each gas (supplied by Airgas) was controlled by a mass flow meter (MKS Instruments model 1179A for air and butane, UNIT Instruments models UFC-1020 and 1100 for hydrogen and argon, respectively), with set points provided manually and flow readings obtained from a UNIT Instruments (URS 100) controller. Hydrogen, butane, and argon flow meters were calibrated using a 25 mL bubble meter (Chemglass), and air flow was calibrated using a rotameter (Omega Engineering FL-110). The reported accuracy of the mass flow meters was 1% of full scale (500 sccm for butane, 20000 sccm for air), and the accuracy of the rotameter was 2% of reading (calibration provided by Omega). The calibration curves for the air, butane and hydrogen mass flow controllers are shown in Figure 6-2 to Figure 6-4, respectively. Argon was calibrated at the set point where it was used, which was a flow of 10.58 sccm for a set point of 2% of maximum. These calibrations were confirmed periodically to ensure that there was no drift in the mass flow controller operation.

To balance air flow through the two reactors, flow was distributed with two identical needle valves (Swagelok SS-ORS2, maximum Cv 0.09), and identical rotameters (Omega

FL 2040) were used to measure the outlet flow rate from each leg during set-up. The combined flow of the butane, argon and hydrogen stream was distributed to the two reactors with two metering valves (Swagelok SS-4BMG, maximum Cv 0.019), and these were adjusted to equilibrate measured reactor maximum surface temperatures.

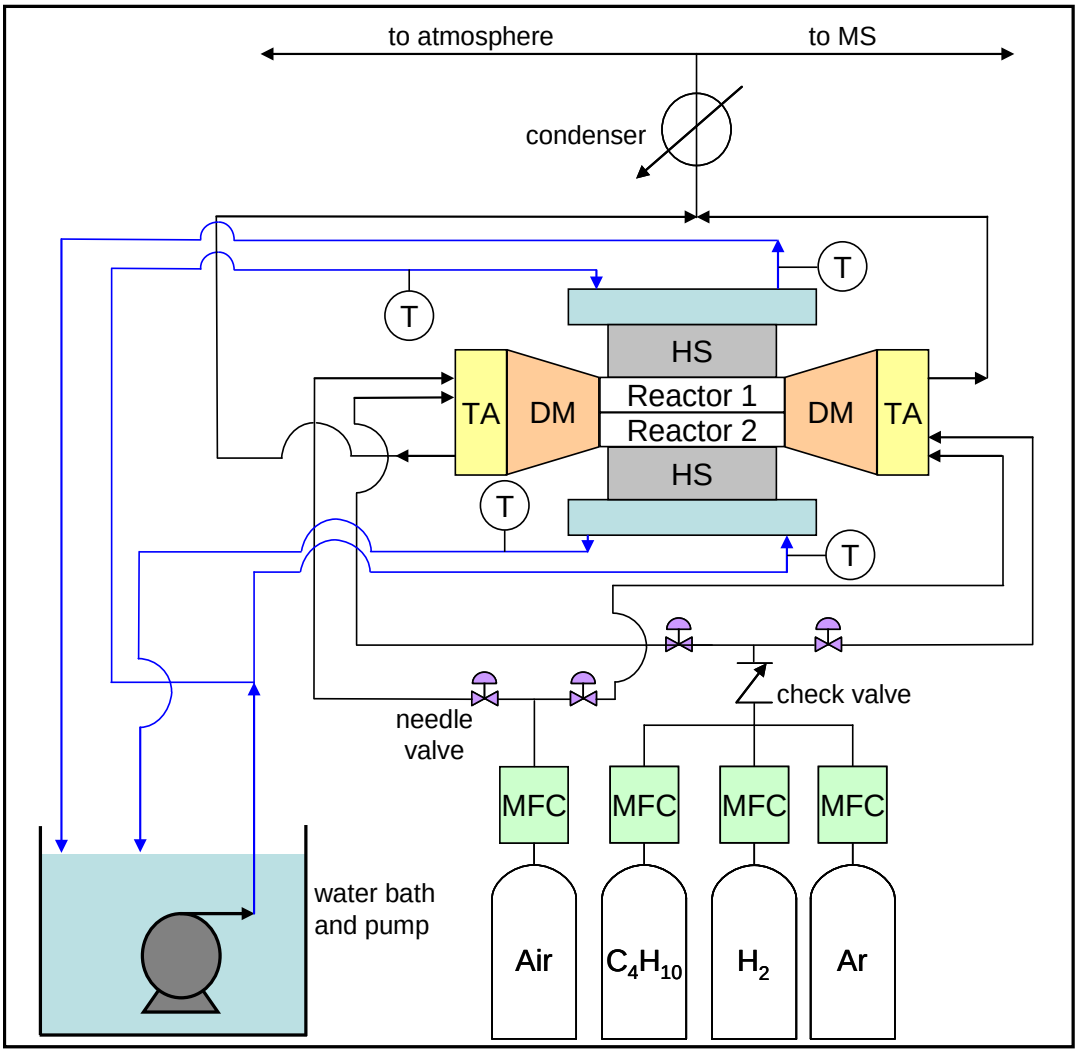

Figure 6-1: Schematic for combustor system with integrated TE-mimicking heat sinks. "MFC" refers to mass flow controllers, "DM" refers to the gas distribution manifolds, "TA" refers to the tube adapters, "HS" refers to the heat sinks, and "MS" refers to the mass spectrometer. The "T" enclosed by a circle identifies a thermocouple. Black lines indicate gas flow and blue lines indicate water flow.

Water flow through the heat sinks was provided by a submerged centrifugal (aquarium-type) pump (VIA AQUA), and the flow rate was determined by timed collection of 946 g of water in a graduated flask. Water flow rate was controlled by the adjustment of pressure drop in the loop using two polyethylene ball valves. The flow path was made

using 1/4-in-inner-diameter PVC tubing and barbed fittings. The appropriate flow rate of water was determined during preliminary experiments by increasing the water flow until no change in heat extraction from the reactor at the same operating conditions was observed. In this way, the flow rate of water was not limiting the heat transfer, and yet the temperature rise of the water was as large as possible to minimize the impact of error in the temperature measurements.

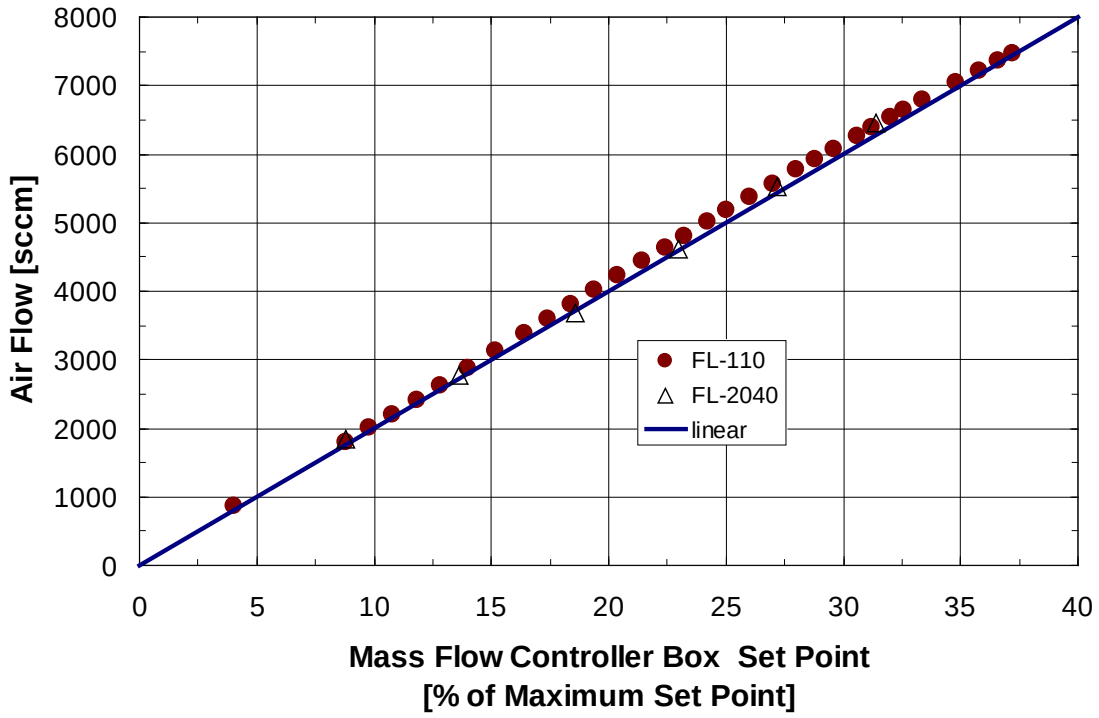

Figure 6-2: Air mass flow controller calibration curve, as determined by two different models of rotameter. Also shown on the curve is the fraction of the calibrated maximum flow rate assuming 100% corresponds to 20000 sccm.

All temperature measurements were made using K-type thermocouples (Omega) and recorded with an Agilent 34970A data acquisition unit and 34910A 20-channel multiplexer cards. For the water temperatures, 0.062-in-diameter thermocouples (Omega KMTSS-062G-6) were drawn through "Luer Lock"-style caps and sealed with 5-minute epoxy (DevCon). These thermocouples were inserted into a "Luer Lock" tee, as shown in Figure 6-5, and the water flow was connected to the other two openings, with care taken that the thermocouple tip was positioned in the center of the water tube.

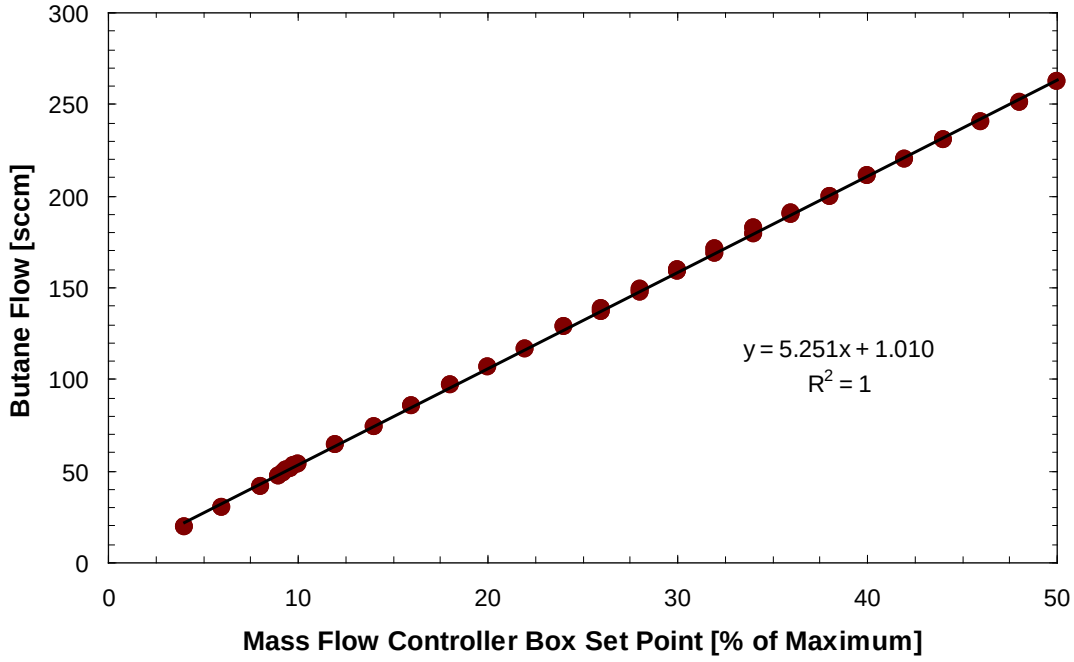

Figure 6-3: Butane mass flow controller calibration curve, as determined by bubble meter. Also shown on the curve is the linear least-squares fit to the data.

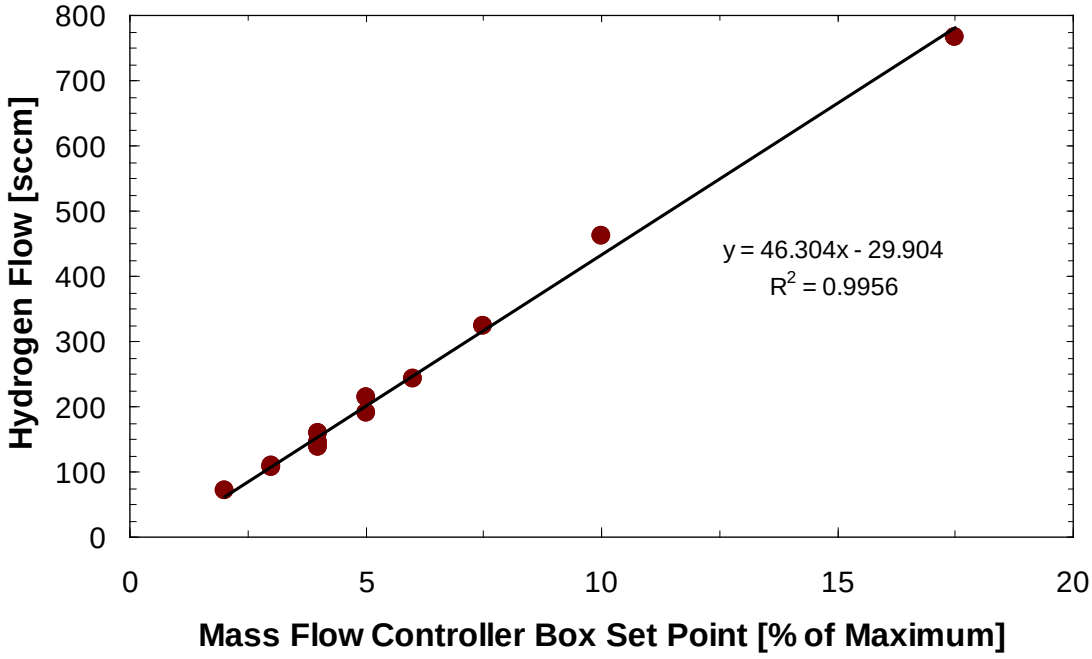

Figure 6-4: Hydrogen mass flow controller calibration curve, as determined by bubble meter.

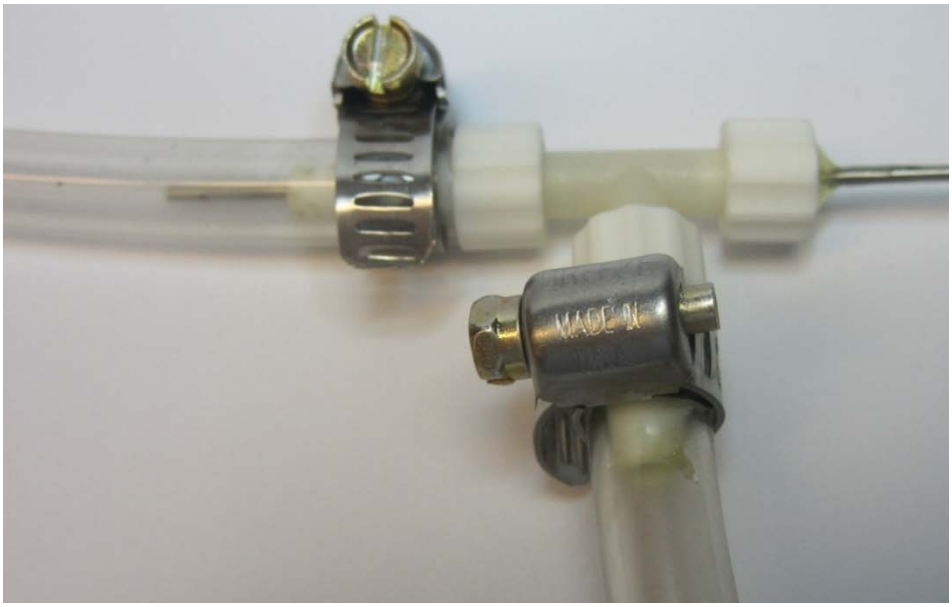

Figure 6-5: Image of thermocouple integrated into water flow path using Luer Lock tee.

Pressure measurements were made using a Honeywell model ASDX ultra-low differential pressure sensor. The sensor had a range of +/- 5 in H_2O (1245 Pa) at ambient conditions, and provided a 0 to 5 V signal that was recorded by the Agilent 34970A data acquisition unit. Due to the temperature limitations of the sensor, the measurements were made at ambient conditions using only air flow.

6.1.3. Experimental Protocols

6.1.3.1. Verification of Reactor and Compression Seal Integrity

As described in chapter 5, the achievement and maintenance of a gas-tight seal at the reactor was a significant challenge, chiefly as a result of cracking of the silicon reactor. With some frequency, it was desired to confirm that the reactor integrity had not been compromised, in a way that would require the least modification to the system. The procedure used was to connect one of the calibrated rotameters to the combined exhaust from the two reactors, and to measure the air flow through the system as a function of the air mass flow controller set point. The typical range over which the flow was varied was from approximately 1000 to 7000 sccm. The flow through the system was then compared with the calibration curve for the mass flow meter to determine if a leak was present in the system and, in such an event, to quantify the leak. An example of this verification is shown in Figure 6-6. In this figure, the air flow through the reactor in the

final configuration (blue squares) is indistinguishable from the mass flow controller calibration with the same rotameter (brown circles), while the leak due to a crack in the reactor can be observed for the original configuration (open triangles). The original configuration leak shown in this figure was quantified as a 10 – 12% of the input air.

6.1.3.2. Reactor Start-up ("Ignition") Procedures

Without an integrated ignition system in the reactor, it was necessary to provide heat to the system in order to raise the temperature sufficiently for the catalytic combustion of butane in air to proceed stably without additional energy input (i.e., autothermally). It is important to note that the "ignition" point in this system is not specifically the point where the butane combustion reaction proceeds over platinum; instead, the term is used here to refer to the set of conditions (i.e., reactor temperature, system heat loss pathways, etc.) such that the rate of heat release from the reaction is sufficient to increase the system temperature towards a stable autothermal operating point at elevated temperature. The concepts of ignition and extinction in nonisothermal reactor design are presented in some detail in Fogler[203]. For considering ignition, it may be useful to consider a lumped heat transfer model for the reactor, similar to those that have been presented in the literature[102] for Biot numbers sufficiently less than 1. The rate of heat generation is primarily a function of butane concentration, oxygen concentration, and temperature at the catalyst surface, although under some conditions mass transfer may also play a role. The rate of heat removal in this system is primarily a function of the reactor temperature, the temperature profile along and rate of convective heat transfer from the fluidic connections, as well as the temperature of and the rate of cooling water flow through the TE-mimicking heat sinks. While system specific, literature values for butane "ignition" have been reported in the neighborhood of 250°C[41, 124].

In this work, two different ignition strategies were used; however, the concept underlying the two strategies was similar: to increase the reactor temperature and the temperature of the fluidic connections from room temperature to approximately 250°C. One approach is to use the catalytic combustion of hydrogen, which proceeds appreciably over platinum at room temperature[204], to assist the ignition of butane in the same reactor in order to

increase the catalyst temperature and to heat the fluidic connections. This technique has been used previously in the Jensen group by Blackwell[52], and has been presented in some detail in the literature[27, 205-207]. Once the reactor temperature has increased, the hydrogen flow was decreased and the butane flow increased to the desired level. The second approach to ignition, used exclusively with the original system configuration, was to electrically heat the inlet and outlet tubes, with air flowing in the system, until the reactor temperature had reached a level such that the addition of butane to the air stream would lead to an increase in reactor temperature. The electrical heating was implemented by wrapping the tubes with heating tape (Omega), and controlling the voltage applied with a Variable Autotransformer unit (Staco Energy Products). The ignition was typically observed with a reactor surface temperature above 200°C. Both of these ignition methods were consistently effective; however, for the final system configuration it was deemed more expedient and simpler to use the hydrogen-assisted combustion ignition.

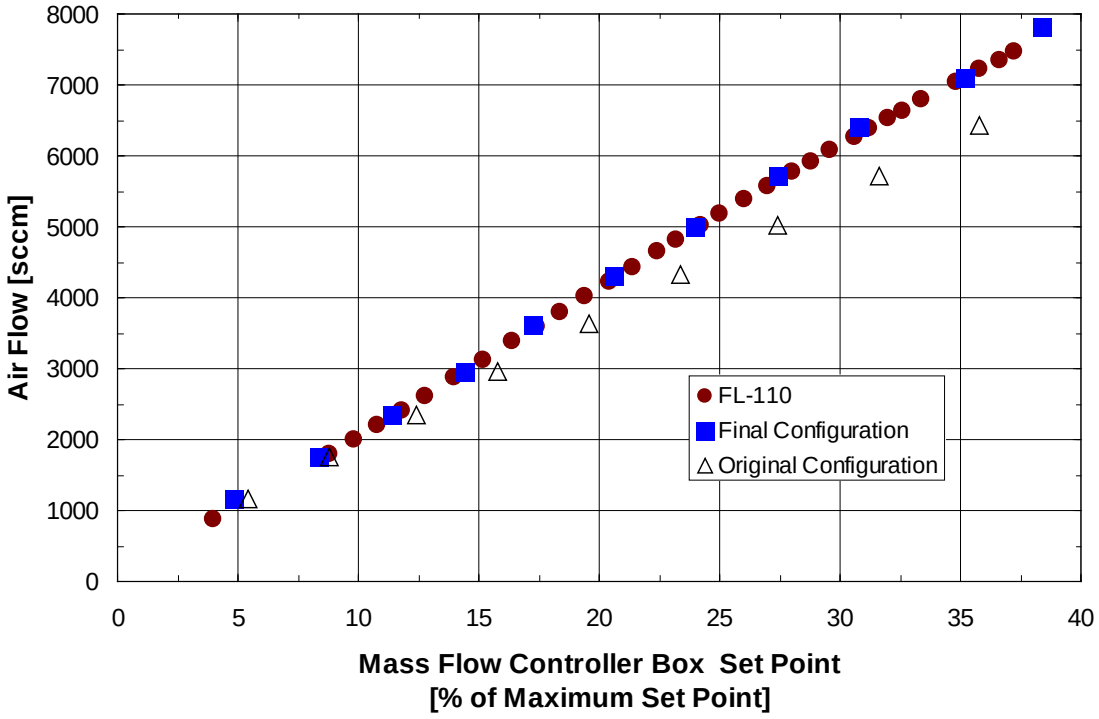

Figure 6-6: Flow verification results for design experiments using TE-mimicking heat sinks. "Final Configuration" data from April 17, 2010 and "Original Configuration" data from November 1, 2009 are compared with the calibration curve for the air mass flow controller.

The typical implementation of hydrogen-assisted ignition was to start a flow of air at the intended experimental flow rate (typically ~6000 sccm), with butane at a moderate flow rate (~105 sccm, or ~210 W LHV) and with hydrogen at a high flow rate (~770 sccm, or ~137 W LHV). To illustrate the process, the maximum reactor temperature profile over time from a heat sink experiment in the final system configuration is shown in Figure 6-7. After the temperature had increased near 200°C, an increase in the slope of reactor temperature over time was typically observed, which seemed to indicate that the butane combustion was increasing the amount of heat released. This slope increase can be observed at approximately the 3-minute point in Figure 6-7, which does not correspond to any change in fuel or air flow rate. After the reactor conditions seemed to be suitable for butane combustion, the flow of butane was increased and the flow of hydrogen was decreased. In the example, this can be observed at the 8-minute mark, where the flow of butane was increased to ~159 sccm (or ~313 W LHV) and the flow of hydrogen was decreased to ~460 sccm (or 82 W LHV). This process of increasing butane flow and decreasing hydrogen flow was repeated until the butane was at the intended experimental condition and the hydrogen flow had stopped. In the example, the butane flow was increased to 180 sccm (354 W LHV) at the 11-minute mark, and the hydrogen flow was decreased to ~211 sccm (38 W LHV) at the 11-minute mark and cut off at the 14-minute mark. The system was then allowed to reach equilibrium, typically requiring another ~30 minutes, depending on conditions.

6.1.3.3. System Dynamics to Steady-State Conditions

As discussed previously, the initial start-up phase (during hydrogen-assisted combustion of butane) required on the order of 10 minutes to transition completely to autothermal butane combustion. The time required to stabilize at a steady condition after this period, or after large changes in system condition, was considerable and varied with the operating condition.

Shown in Figure 6-8 is the temperature profile for one reactor over the course of an experiment, and the experimental controls are given in Table 6-1. In this experiment, the initial steady state was reached after 50 minutes (which was 40 minutes after the

hydrogen flow was cut). The steady state values were then collected for a period of 10 minutes, after which point the butane and air flows were increased. It was preferred to increase the temperature over the course of the experiment, as this alleviated any concerns of the thermal mass of the system causing the efficiency of the combustor to be over-estimated. After reasonably small changes to the system conditions, the system approached steady state after approximately 10 minutes, and then the steady state conditions were collected over an additional 10 minutes. The system was determined to be at steady state when the rate of increase in temperature was low, typically less than 0.1°C per minute.

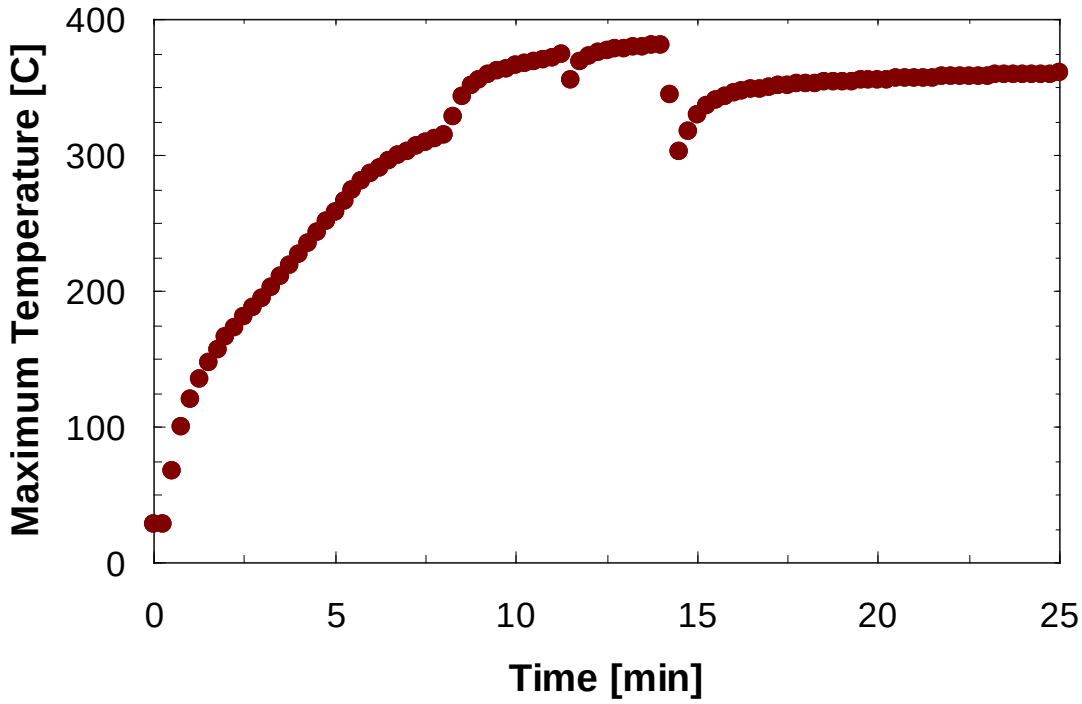

Figure 6-7: Example maximum temperature profile during start-up of reactor for heat sink experiment (from April 1, 2010). Illustrates hydrogen-assisted combustion of butane.

Two main challenges were faced in determining the achievement of steady state operation in this system. The first challenge was the large difference observed in system timescales, likely owing to the relatively large thermal mass of the fluidic connections relative to that of the silicon combustor. The reactor temperature response is much faster than that of the tubing, as can be observed in Figure 6-9. As such, the rate of increase in

the reactor temperature was observed to decrease to a reasonably small amount; however, this temperature increase could persist for some time while the tubing temperature increased. However, provided the temperature of the system was increasing from one steady state to the next, any error in declaring "steady state" before the system had truly equilibrated would lead to an underestimate in device performance, and likely a very small one at that.

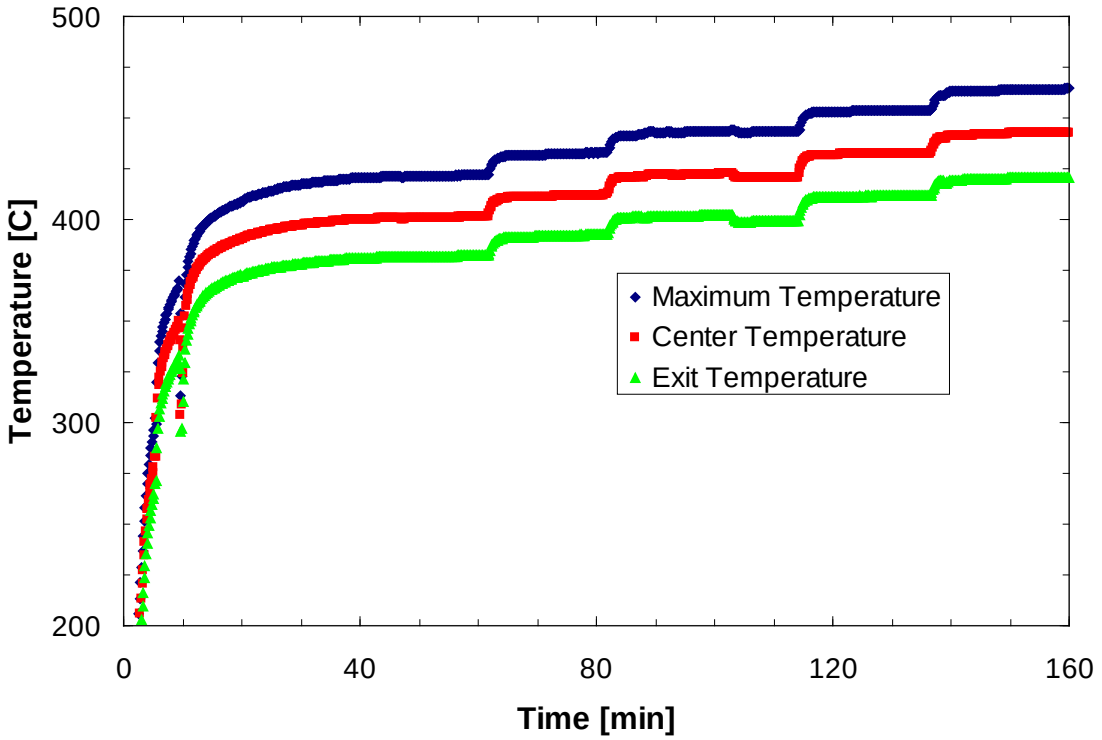

Figure 6-8: Sample dynamic temperature-time profile for a heat-sink experiment. Data from April 10, 2010. Experiment covered butane flows from 211 to 252 sccm. For one reactor, the maximum, center, and exit temperatures are shown.

Table 6-1: Experimental conditions for sample dynamic temperature-time profile.

Time [min]	Butane Flow [sccm]	Air Equivalence Ratio
9.5	211.0	1.00
62	221.5	1.00
82	232.0	1.00
103	232.0	1.04
114	242.6	1.00
136	253.1	1.00

The second challenge was the impact of the heat sink cooling water temperature on the reactor temperature, and the detrimental impact that active control had on the calorimetry estimation. The temperature in the water bath was controlled manually, through the addition of ice. It was desired to keep the temperature of the water above room temperature, such that any error in the calorimetry estimate as a result of heat transfer with the environment would reduce the estimated heat removal from the system. When ice was added to the bath, the measured temperature difference in the water across the heat sinks would increase momentarily. As such, once the system was determined to be approaching steady state, it was important not to disturb the water bath during the 10-minute averaging period. This would result in an increase in the water bath temperature during this time span (typically on the order of 3°C), which could also be observed in the reactor temperature (though to a lesser degree, likely owing to the thermal mass of the heat sink). This temperature increase could, at times, be misconstrued as the reactor temperature not having reached a stable operating point. In the final system configuration, considerable attention was paid to maintain the cooling water within an approximate range of 26 – 33°C, in order to improve the repeatability of steady state conditions between experiments.

6.1.4. Calculations

6.1.4.1. Air Equivalence Ratio

The air equivalence ratio is a common term in combustion literature, used to indicate how much air is mixed with the fuel. The equivalence ratio, Φ, is calculated according to equation 33, where the flow rates of fuel and oxygen should be compared at standard conditions. For butane combustion, the molar stoichiometric ratio of butane to oxygen is 2 to 13. For fuel lean mixtures (with excess oxygen), the equivalence ratio will be less than one. And for fuel rich mixtures (with insufficient oxygen for complete combustion of the fuel), the equivalence ratio will be greater than one.

$$\Phi = \frac{\left(Fuel\ Flow \Big/ Oxygen\ Flow \right)}{\left(Fuel\ Flow \Big/ Oxygen\ Flow \right)_{stoichiometric}} \qquad [\ 33\ ]$$

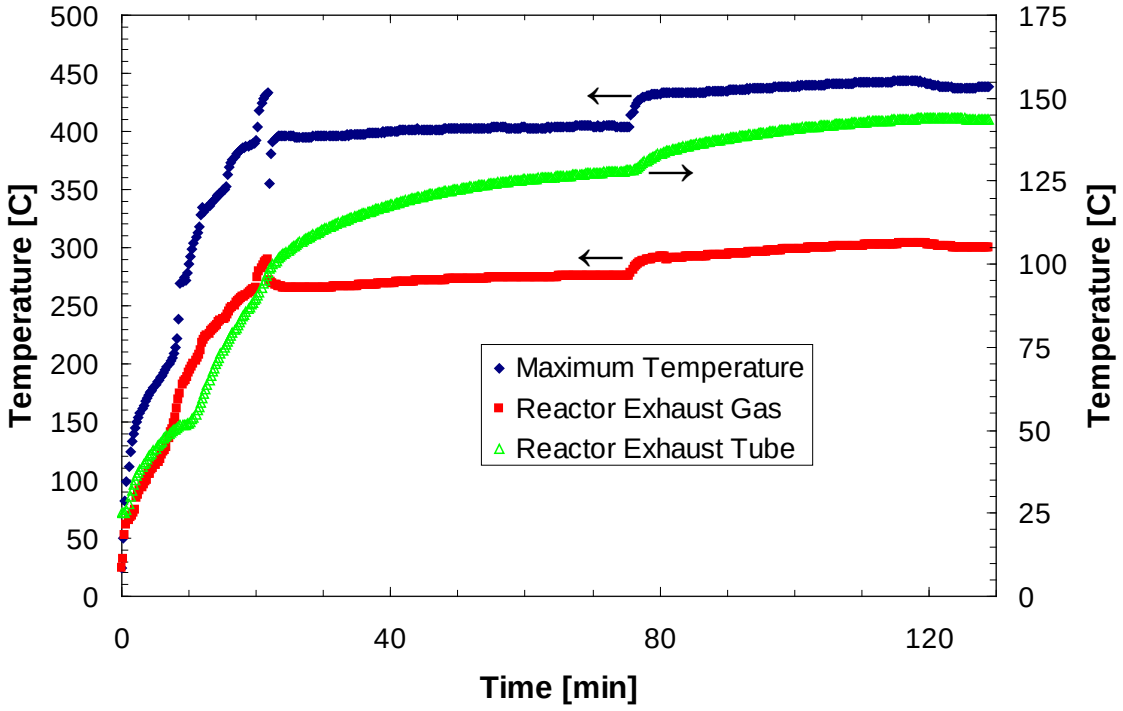

Figure 6-9: Example temperature profile for reactor, exhaust and exhaust tube temperatures. Sample data from November 3, 2009 with original system configuration. Butane flow rate is 180 sccm prior to 77 min, and 200 sccm after. Air equivalence ratio is ~0.93.

6.1.4.2. Heat Removed from Combustor through Heat Sink

The heat transferred through the heat sink from the combustor was calculated from the temperature rise observed for a known flow rate of water. Given that the temperature rise of the water was ~4°C, a constant heat capacity of 4.177 J/g/°C was assumed (for water at 40°C[208]) for a conservative estimate. The heat, Q, extracted by the cooling water, and removed from the combustor through the heat sink, was calculated according to equation 34, where T_{in} is the temperature of the water entering the heat sink, T_{out} is the temperature of the water exiting the heat sink, and m is the mass flow rate of the water.

$$Q = m \cdot C_p \cdot \left(T_{out} - T_{in}\right) \qquad [34]$$

6.1.4.3. Normalized Mean Deviation of Temperature

In order to compare the surface temperature gradient observed in this work with literature results[42], a normalized mean deviation (NMD) of temperature was calculated. The NMD is calculated according to equation 35, where T is the surface temperature at axial

position z, L is the length over which the gradient is measured, T_{max} is the maximum observed temperature, and T_a is calculated according to equation 36.

$$NMD = \frac{\int_0^L |T - T_a| \, dz}{L T_{\max}} \quad \textbf{[35]}$$

$$T_a = \frac{1}{L}\int_0^L T \, dz \quad \textbf{[36]}$$

6.2. Validation Experiments

6.2.1. System Pressure Drop Measurements

Limiting the pressure drop through the reactor and fluidic connections was an important factor in the design of the system. And though the system models predicted that our design would be safely within the 500 Pa limit, it was important to measure the pressure drop through the device to ensure that there were no unanticipated sources of pressure drop, particularly related to the catalyst wash coat which was not included in the original model. However, it is difficult (and costly) to find a pressure sensor with the required precision of measurement that is able to operate at the system temperature, as well as to prevent water condensation from obscuring the measurement downstream of the reactor.

To simplify the experimental requirements, the pressure drop through the reactor and gas distribution manifolds was measured over a range of air flow rates at ambient temperature and pressure. The intention was that the design gas flow (in sccm) could be corrected to an approximate air flow (at ambient conditions). At the design conditions, the gas flow (after the increase in total gas molecules resulting from the reaction) is ~6000 sccm. Correcting the flow for gas expansion at 400°C would correspond to ~14.9 LPM (liters per minute). This does not account for decreased density and viscosity at system temperature, which would increase the pressure drop by a factor of ~1.6, based on the laminar model.

The measured pressure drop through the combustor and manifolds is represented in Figure 6-10. Also shown on in this figure are laminar flow model predictions, corrected

for ambient air properties, for the bare reactor channels alone (dashed line), and for the reactor channels with an assumed catalyst layer (solid line). The catalyst layer was assumed to be uniform across each side and along the length, with a thickness of 70 μm on top and bottom of the channel and a thickness of 20 μm on each side. These catalyst layer thicknesses represent the high end of the observed thicknesses from ESEM images of the layer (described in chapter 5). For the design conditions, the measured pressure drop at 14.9 lpm is 258 Pa. The measurement is in reasonable agreement with the calculated value of 150 Pa for the catalyst-loaded channels alone. However, a nonlinear dependence of pressure drop on flow rate was observed, indicating that the flow is not laminar in all portions of the system. The Reynolds number in the channels is ~600, so it is unlikely that the flow profile in the reactor exhibits turbulence.

It was anticipated that the nonlinear response of pressure drop to flow rate was a result of the contraction or the expansion in the gas distribution manifold (or at the aluminum gasket). To confirm this hypothesis, the pressure drop through one manifold (with aluminum gasket attached) was measured. The measured values for this test are also shown in Figure 6-10, labeled as “Manifold Measurement”. Also shown in this figure is the estimated pressure drop profile that would result from doubling the measured manifold pressure drop (to allow for both manifolds) and adding the laminar model for the catalyst-loaded reactor channels. It can be observed that this estimate is close to the observed trend for the total system, confirming that the pressure drop in the reactor agrees with the laminar flow model.

Given a flow rate at the design point (~5880 sccm for stoichiometric air at 190 sccm butane) and measured pressure drop (413 Pa, after 258 Pa is corrected by a factor of 1.6 for gas properties at reactor temperature), the minimum flow work required for air pressurization would be 0.044 W. Assuming 10% efficient compression, this would correspond to a parasitic power load for air pressurization of 0.44 W, less than the design target of 0.5 W. This system represents a significant step towards an air-breathing fuel processor with low parasitic power loss for air pressurization.

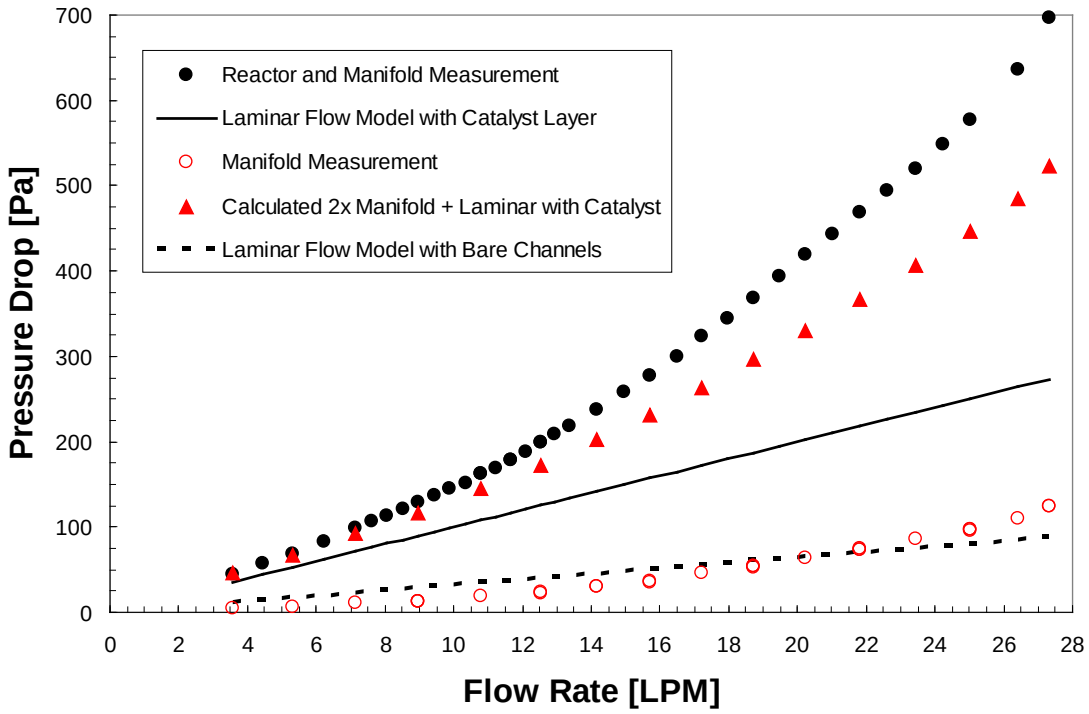

Figure 6-10: Pressure drop measurement and estimate for reactor system as measured with ambient air flow. Catalyst layer thickness based on largest observed values (70 µm on top/bottom of channels, 20 µm on side). Measurements from July 23 and August 12, 2010.

6.2.2. Insulated Testing of Reactor for Estimation of System Losses

With the original system configuration, a reactor was tested without integration with the heat sinks in an "insulated" configuration in order to estimate the heat losses due to conduction through and convection from the gas distribution manifolds, as well as the enthalpy loss from the exhaust gas. The reactor faces (for TE or heat sink contact, in the typical operation) were heavily insulated using ceramic tape. Two thermocouples were held in contact with the reactor faces using two aluminum plates and steel bolts, in order to assess the surface temperature of the silicon. Thermal paste (Laird T-Putty 502) was coated on the reactor surface to improve the accuracy of thermocouple measurement. The objective of this experiment was to determine the flow of butane required to maintain the reactor at the design temperature (~400°C) in the absence of any heat removal from the heat sinks. The heating value of the butane required to stabilize the temperature provided an estimate of the heat loss from the system, primarily to the fluidic connections and the exhaust gas. It is important to note that the reactor used in this experiment was

known to have a leak (through the process described for verification of reactor and compression seal integrity) of approximately 15%. However, without knowing the location of the leak, it was impossible to properly discount the butane flow. Rather, the heat released was used as an upper bound for determining orders of magnitude of heat loss pathways and appropriate initial estimates for the later experiments.

The air flow was set at 6.15 slpm (with a mass flow controller set point of 30% of maximum), and the butane flow was adjusted to achieve center-point reactor temperatures near the design point of 400°C. The butane flow which achieved a reactor temperature above 400°C was approximately 47 sccm (with a mass flow controller set point of 8.8%). From this experiment, it can be concluded that the heat loss from the system given a reactor temperature of 400°C was at most 93 W, based on the lower heating value (LHV) of the fuel. Assuming a gas exhaust temperature of 350°C, the enthalpy loss to the hot exhaust gas was estimated to be 43 W (with air flow similar to the design point), which indicates that the conductive and convective losses from the manifolds and tubes was approximately 50 W. It is important to note that this experiment was carried out in the original system and, given the changes to the tubing, the relations between the heat loss pathways could change slightly in the final system. The results discussed here were primarily used to determine an initial estimate of reaction conditions in the final system.

6.2.3. Calibration of Calorimetry Estimate for Heat Removal through Heat Sinks

In order to confirm that the cooling water calorimetry was able to accurately determine the heat conducted through the heat sinks, as well as to confirm the precision of the surface thermocouples, experiments were conducted in which the combustor was replaced with an aluminum block of similar dimensions containing with four 100-W-cartridge heaters (Omega CSH-101100). The system was heavily insulated to avoid heat loss, and the electrical power input to the cartridge heaters was controlled using a variable autotransformer (Staco Energy Products) and both the current and voltage were measured with digital multimeters. The flow rates of the cooling water through the each

half of the cooling loop were 525 and 540 mL/min. A schematic of the calibration system is given as Figure 6-11.

Results from one calibration experiment, in which the input electrical power was increased in stages, are shown in Figure 6-12, and the calculated steady state heat removal rates as calculated are given in Table 6-2. In this experiment, cooling water temperature rise at steady state ranged from 2.9 to 4.6°C. There was good agreement between the input electrical power and the heat extracted through the heat sinks, with 97.4 and 95.1% of input power extracted at 176 and 356 W of electrical input, respectively. A second calibration experiment confirmed these results, where 341 W were extracted through the heat sinks from the cartridge heaters representing 97.4% of the input electrical power. The small deviation of the calculated heat removal through the heat sinks from the input electrical power is almost certainly caused by a small amount of convective, radiative, and conductive heat loss from the insulated system. These calibration experiments confirmed that the cooling water calorimetry provided an accurate measurement of the heat extracted via the heat sinks.

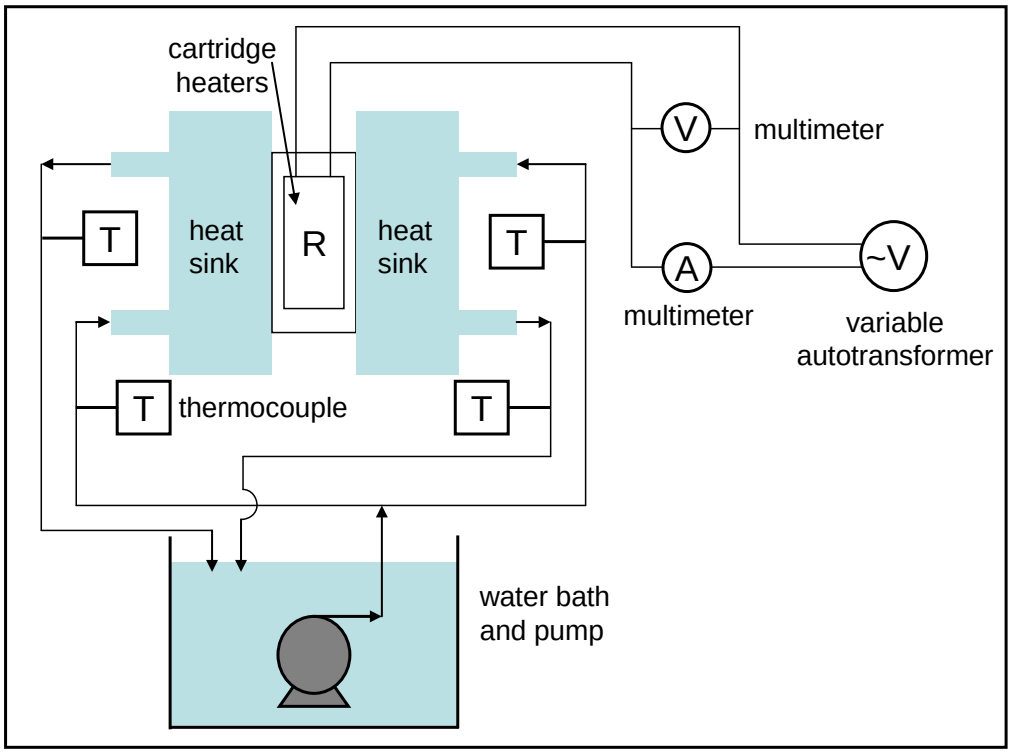

Figure 6-11: Flow and measurement paths for heat sink cooling water calorimetry calibration.

Table 6-2: Averaged values for extracted heat from cartridge heaters through heat sinks as determined by cooling water calorimetry.

Calculated Extracted Heat from Calorimetry	% of Input Electrical Power Extracted
133.6	102.7
171.6	97.4
218.8	96.1
275.1	96.2
339.0	95.1

6.3. Experimental Results and Discussion

6.3.1. System Performance at Design Conditions

The design-point performance of the combustor was demonstrated at conditions that most closely satisfied the system design target of 280 W heat transferred through the TE-mimicking heat sinks. The selected operating conditions consisted of a butane flow of 190 sccm (372 W LHV) and an air flow rate of ~6 slpm (for an equivalence ratio, Φ, of 1.0). The amount of catalyst in the two reactors was 193 and 161 mg, for a total catalyst weight of 354 mg and a total reactor weight of 5.47 g.

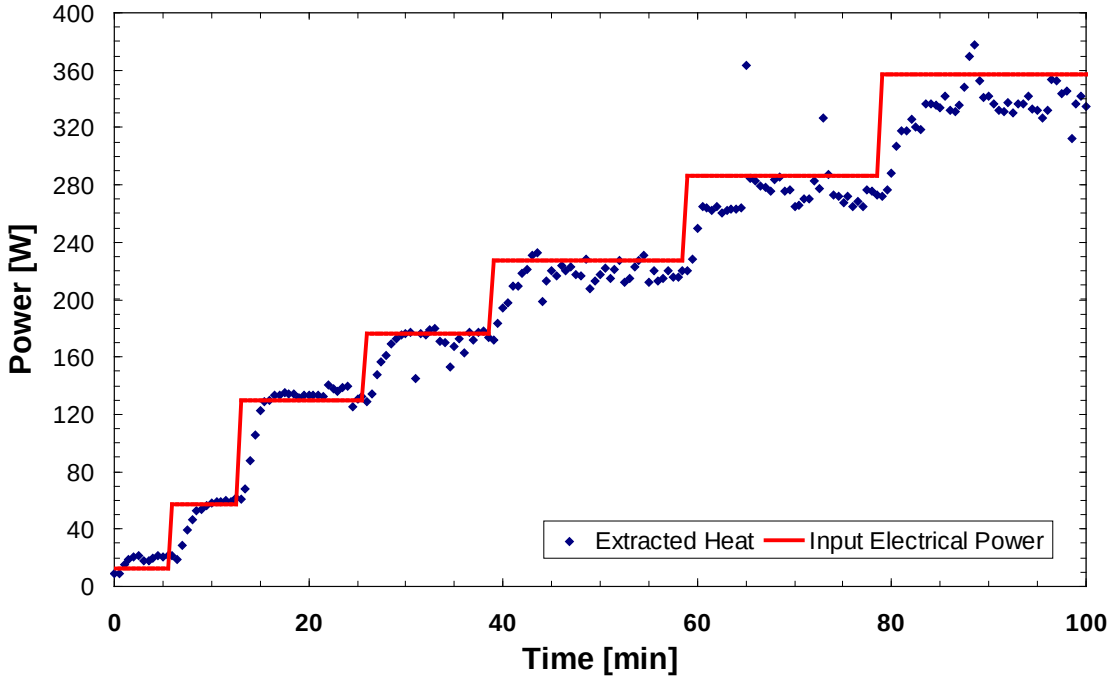

Figure 6-12: Calibration of heat sink cooling water calorimetry using cartridge heaters.

The dynamic profile of the total heat removed through the TE-mimicking heat sinks from the combustor at the design flow rate of butane is shown in Figure 6-13. In this

experiment, three steady state points at the design flow were identified, labeled A through C in the figure, as well as two periods with varying air flow. The dashed vertical lines on the figure indicate the points at which the air flow rate was changed, and the equivalence ratio bounded by these lines indicates the air flow during the enclosed time. As discussed previously, much of the scatter in the calculated heat removal rate is related to manual temperature control of the water bath. In this experiment, the water flow rates through the two legs of the cooling loop were 469 and 516 mL/min (+/- 3%, as estimated by repeat measurements).

At the design point, the average total heat removed from the catalytic combustor through the TE-mimicking heat sinks was 287 W (averaged across times A, B, and C) with a standard deviation of 4 W. The heat loss from the system was 88 W, which is in good agreement with the "adiabatic" experiment (as the enthalpy loss is slightly lower due to reduced air flow). The efficiency of the thermal conversion from chemical energy stored in the fuel (lower heating value) to heat conducted through the heat sinks is 76.6% (287 of 375 W). It is worth noting that despite the long time required to reach steady state after ignition, the heat removed through the heat sinks rapidly approaches the final value. This indicates that the dynamics for power production could be much faster than the experimental timescale.

The observed combustor surface dynamic temperature profiles for the design experiment are shown in Figure 6-14 to Figure 6-16. At steady state, the average maximum surface temperature was 395°C (with 1.4°C standard deviation), the average reactor center point surface temperature was 376°C (with 1.6°C standard deviation), and the average reactor exit temperature was 361°C (with 4.0°C standard deviation). The observed temperature gradient, though reasonable at 34°C over ~2.75 cm, could be further reduced with an additional conductive layer (such as a thicker layer of the eGraff material). It is possible that the heat sink (and the thermocouples on the surface) may not measure the hottest point on the reactor, given that the reactor is 3.5 cm in length and the heat sink is only 2.75 cm in length. However, in previous work, Blackwell has observed that for the

catalytic combustion of light hydrocarbons in a silicon microreactor, the maximum temperature is not observed immediately at the channel inlet but rather at some length into the channel[52]. Similar observations have been reported elsewhere in the literature[42, 101].

The maximum temperature profiles were consistent between the two reactors, since this was actively controlled through the manual adjustment of the fuel distribution valves. It was observed that there was a slight temperature difference between the two reactors for the center and exit surface temperatures (~ 2°C for the center temperature and ~8°C for the exit temperature). It was also observed that at the steady state points, there was still a slight increase in the reactor temperature; however, this increase was small and did not appear to be reflected in the heat removal through the heat sinks. As mentioned previously, the temperature rise was within the level of impact of increasing water bath temperature. Such an effect can be observed at the 140 - 145 min range in Figure 6-14, where the maximum temperature increases by 1°C in 5 min; where as, the cooling water temperature increased by 2°C over the same time period and there was no observed increase in the removed heat.

Earlier heat sink experiments with the original configuration were carried out at similar reactor temperatures, though in a reactor with a known leak of ~8%. In these experiments, the exit gas temperature was observed to be 20 – 50°C lower than the reactor exit temperature, likely owing to heat transferred to the gas distribution manifold from the hot exhaust (as the temperature was measured just after the manifold). Based on the 20 - 50°C temperature reduction range and the average reactor exit temperature of 361°C, the estimate of the enthalpy loss at the design conditions would be 46 - 42 W, respectively. The remaining heat loss from the system as a result of conduction, convection, radiation, and any unconverted fuel was estimated to be 42 - 46 W. As such, the enthalpy loss contributes ~50% of the total system heat loss at stoichiometric air flow, or ~12% of the input heating value of the fuel.

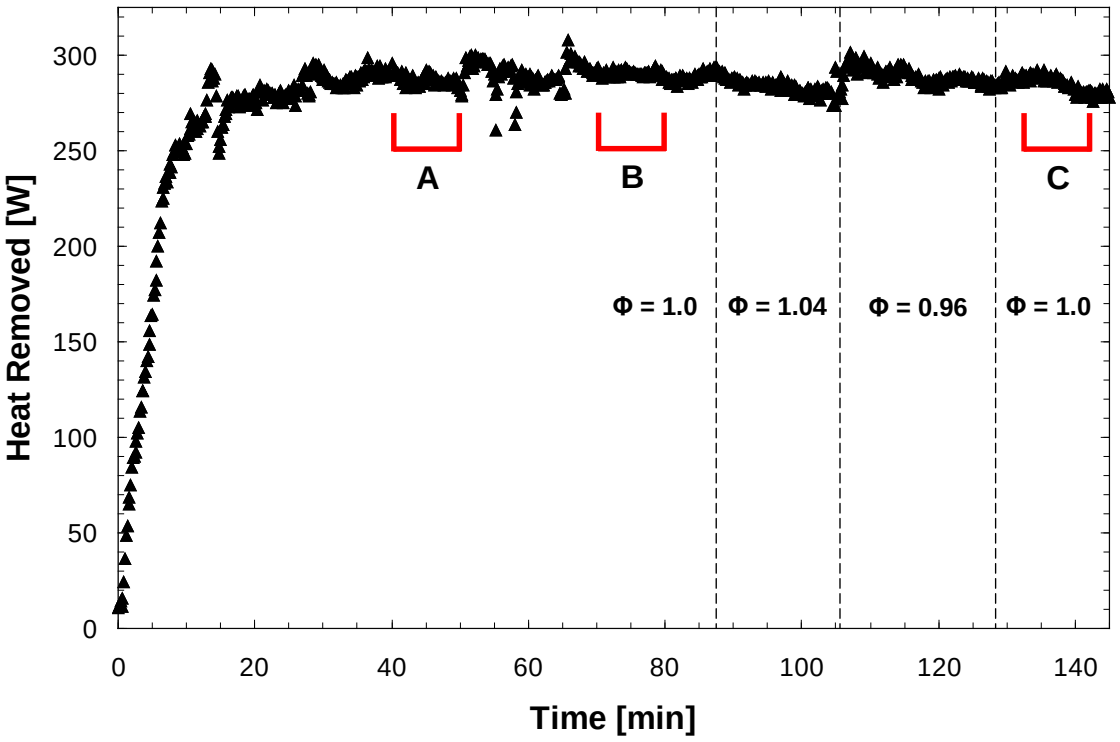

Figure 6-13: Dynamic profile of total heat removed from the combustor system through the TE-mimicking heat sinks at the design butane flow of 190 sccm. The time-spans marked A through C represent three periods considered as steady state. Vertical dashed lines indicate periods of different air flow, with the associated air equivalance ratio indicated on the figure. Data from April 10, 2010.

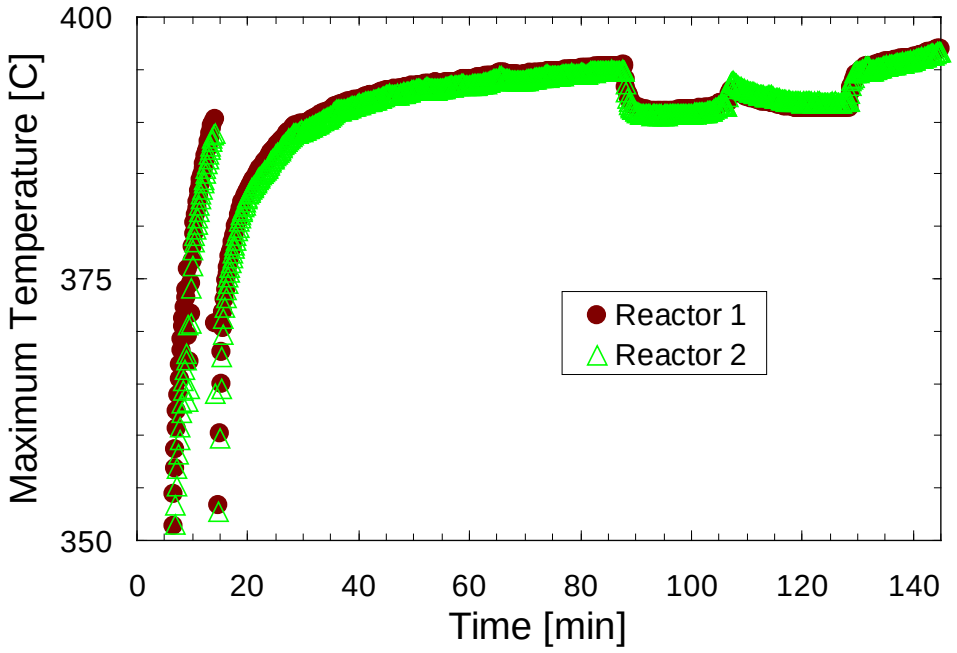

Figure 6-14: Maximum temperature profile for both reactors at the design butane flow rate of 190 sccm. Maximum temperature corresponds to thermocouple "25" for Reactor 1, "13" for reactor 2.

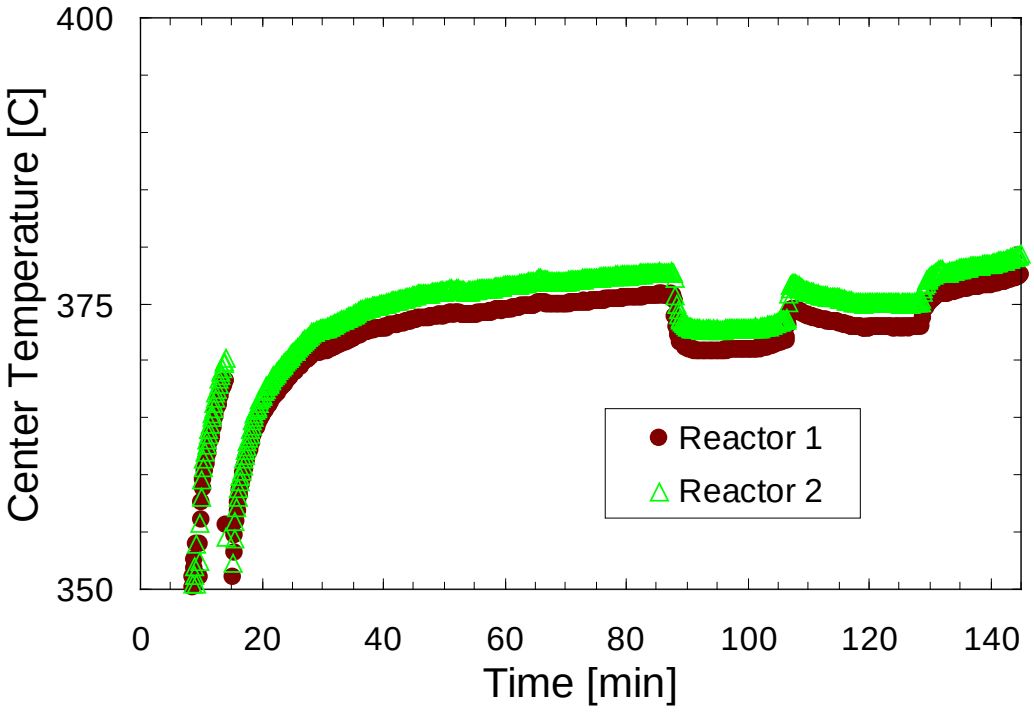

Figure 6-15: Center temperature profile for both reactors at the design butane flow rate of 190 sccm. Center temperature corresponds to thermocouple "24" for Reactor 1, "10" for reactor 2.

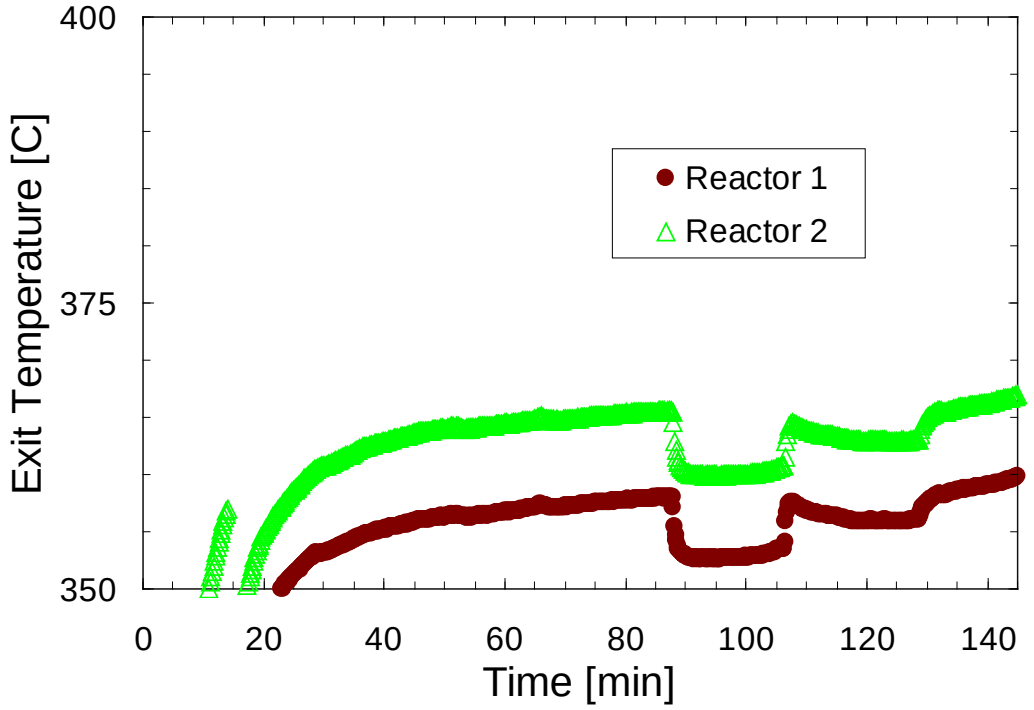

Figure 6-16: Exit temperature profile for both reactors at the design butane flow rate of 190 sccm. Center temperature corresponds to thermocouple "22" for Reactor 1, "4" for reactor 2.

In a separate experiment, the conversion of butane in the system at the design conditions was determined using a mass spectrometer. A small amount of argon was included in the fuel stream (at a flow rate of 10.7 sccm) to serve as an internal standard. The average butane flow in the exhaust stream was estimated as 5.6 sccm, based on five measurements spanning approximately one hour. This corresponds to a conversion of butane in the reactor of 97%. It is important to note that the reactor was observed to have a leak of ~7% during this experiment. It is possible that this leak may cause the conversion estimate to be higher than actual during the design point experiments described above, as the residence time in the leaking reactor may be higher than that in the intact reactor. However, this observation indicates that the conversion of butane in the reactor at the design conditions is nearly complete.

6.3.2. System Performance Over a Range of Fuel Flow Rates

In addition to demonstrating combustor performance close to the nominal design point, the range of the system was tested to demonstrate behavior under varying fuel flow rates. The system was operated with butane flow rates ranging from 135 to 253 sccm at an equivalence ratio of 1.0. The range of butane flow rates represented approximately 30% deviation from the design point of the system. The heat removed from the combustor through the TE-mimicking heat sinks as a function of the heating value of the input fuel flow is shown in Figure 6-17. Also shown in this figure are the 73, 75 and 78% thermal efficiency lines, where the thermal efficiency refers to the proportion of the heating value of the fuel that is transferred through the heat sinks. Also provided, for comparison, in this figure are experimental results from the original system configuration. For the original system experiment, the air equivalence was ~0.93 (indicating a small excess of air) and the reactor was known to have a leak of ~11%. The purpose of including these results is to demonstrate that the system performs similarly in the presence of a small leak, and it is noted that the heat removed in the original configuration for both measured values was 93% of the heat removed in the final configuration at the same conditions. Over the range of the system, heat fluxes to the heat sink ranged from 13.6 to 23.9 W/cm^2.

The measured reactor surface temperatures as a function of fuel flow rate are shown in Figure 6-18. Compared with the design limitation of 423°C, the maximum surface temperature was acceptable up to a butane flow rate of 417 W LHV (or 211 sccm), which corresponds to 320 W heat removed through the heat sinks (76.9% thermal efficiency). The surface temperature gradient from maximum to exit temperature increased with fuel flow rate, from 27°C at a butane flow of 135 sccm (267 W LHV) to 38°C at 253 sccm (500 W LHV). This increasing gradient was expected, as there is less mass transfer resistance at the hot spot with higher flow rates and an exponentially increasing reaction rate as temperature increases. A similar trend has been reported for other systems[42], and the magnitude of the thermal gradient observed in this work, which shows a normalized mean deviation of <0.02 (assuming a linear profile), is comparable with the results reported for combustor systems with 0.8-mm-thick copper thermal spreaders.

As the fuel (and air) flow rate increased, it was observed that the thermal efficiency of the system decreased slightly. This effect could be caused by increased contributions from one or more heat loss pathways from the system as a result of increased temperature. Radiation has a fourth-order dependence on temperature, but its contribution to the system heat loss is small. It is much more likely that the heat generation was reduced due to reduced butane conversion as the residence time approached and surpassed the characteristic timescale for diffusion. The characteristic residence, reaction and diffusion timescales for the reactor are shown in Figure 6-19, calculated at the average center surface temperature. Also shown in this figure is the observed thermal efficiency of the combustor at the corresponding fuel flow rate. While these estimates are best suited for order-of-magnitude comparisons, it can be observed that for most of the conditions considered in these experiments the residence time and the diffusion time were very similar, and that the residence time decreased as butane flow rate increased faster than the diffusion time decreased. As the kinetic timescale for reaction is much lower than the diffusion time at these conditions, the reaction was bulk diffusion limited in the range of conditions near to the design point.

Given that the system is not kinetically limited, it would be possible to improve the system performance, in terms of thermal efficiency, by decreasing the thermal resistance of the pathway through the TE modules. In principle, this would reduce the temperature of the reactor for a given heat flux through the TE modules (or heat sinks), decreasing the heat loss to the environment while allowing for equivalent conversion of butane. To optimize the system performance in this way, a better estimate of the reaction kinetics and a detailed CFD model of the heat and mass transport in the system would be of significant value. Without changing the thermal conductivity of the TE materials, a decrease in the thermal resistance could be achieved through additional TE-material area.

The combustion of 253 sccm of butane in the reactor corresponds with a volumetric heat generation of ~280 MW/m^3, which is reported by Suzuki, et al.,[124] to be comparable to that of industrial gas turbine combustors. At the design point, the weight hourly space velocity (WHSV) was 1 $sdm^3/(h\ mgcat)$ and the gas hourly space velocity (GHSV) was $2 \times 10^5\ h^{-1}$.

The amount of heat transferred through the heat sinks, when compared with the center surface temperature of the combustor and the measured temperature of the copper heat sink (~40°C), was used to calculate an effective heat transfer coefficient for the TE-interface surfaces of the reactor (based on an area per side of 9.975 cm^2). The heat transfer coefficient calculated based on the experimental observations at varying butane flow rates is shown in Figure 6-20. The predicted heat transfer resistance is similar to the estimates based on experimental results, though higher by ~10%. Possible factors contributing to this discrepancy include thermal contact resistances between the heat sink and reactor, inaccuracies in the temperature measurements (particularly that of the heat sink temperature), heat transfer resistance between the cooling water and copper heat sink, or even heat loss from the copper heat sinks.

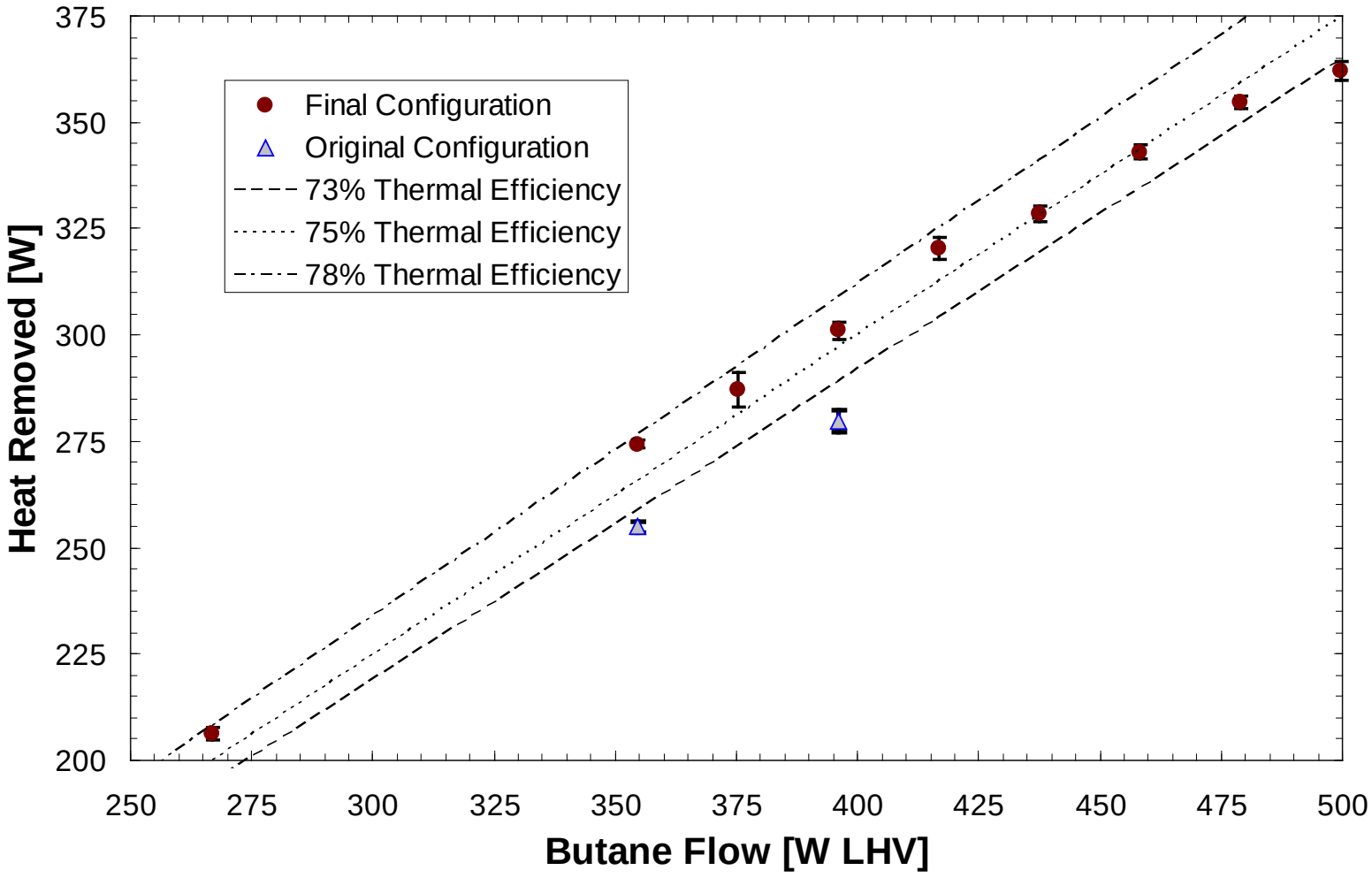

Figure 6-17: Performance map for catalytic combustor with TE-mimicking heat sinks. Shows heat removed from combustor through heat sinks at given butane flow [1 sccm = 1.974 W LHV]. Φ = 1.0 for "Final Configuration", and Φ ~ 0.93 for "Original Configuration". Error bars show standard deviation over the measurement period.

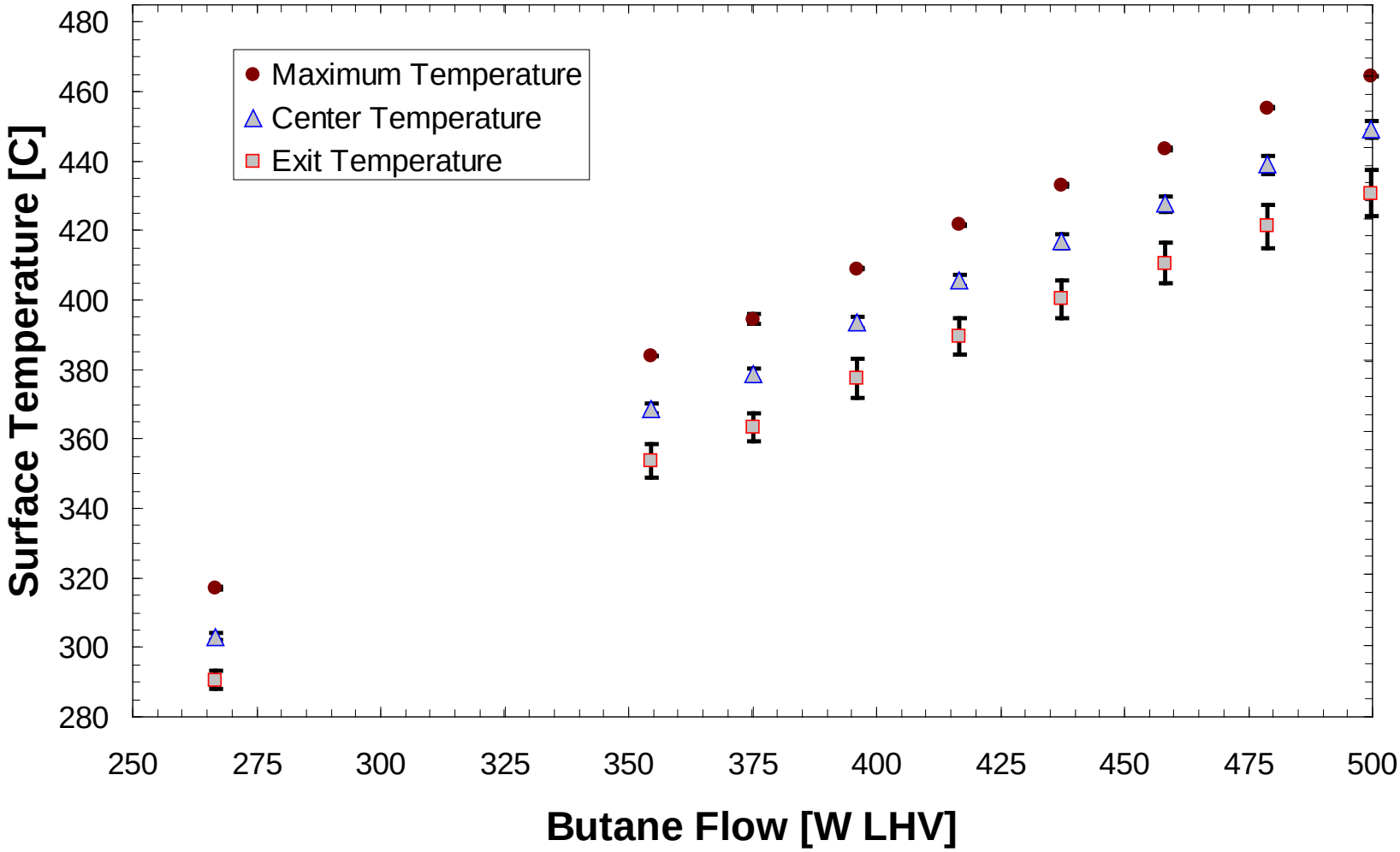

Figure 6-18: Surface temperature measurements over operating range for final configuration with butane flow [1 sccm = 1.974 W LHV], Φ = 1.0. Error bars indicate standard deviation over the measurement period.

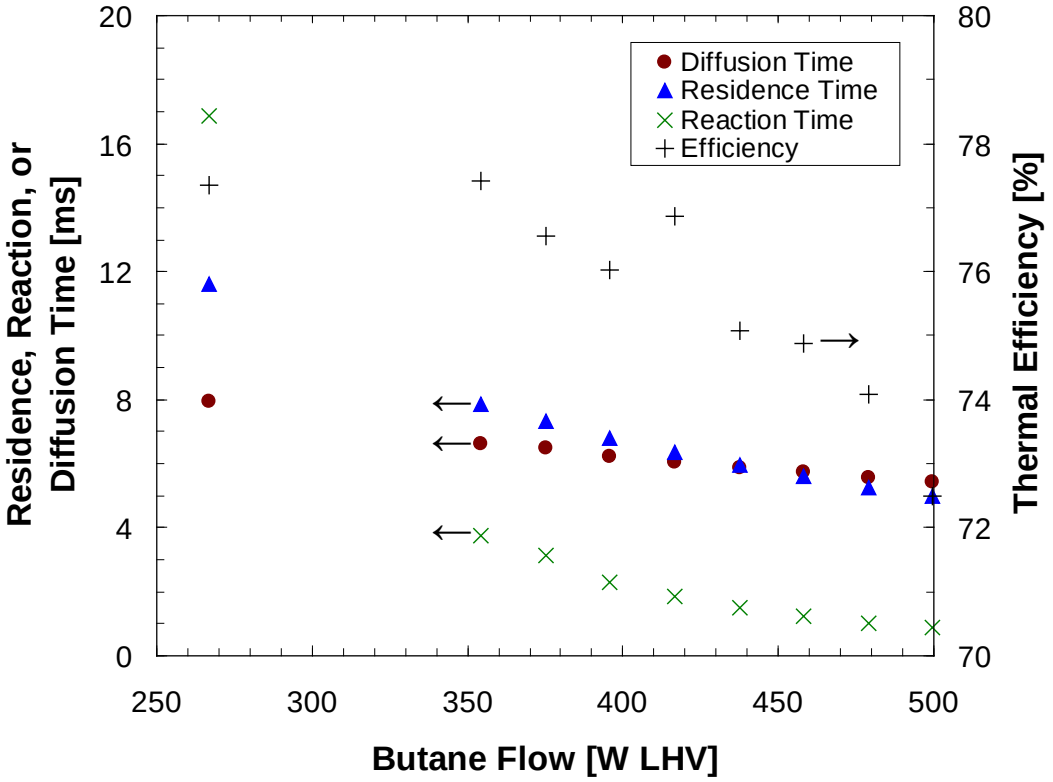

Figure 6-19: Estimated residence, reaction and diffusion timescales for the combustor, compared with observed thermal efficiency, over a range of butane flows. Timescales are calculated based on average combustor center temperature.

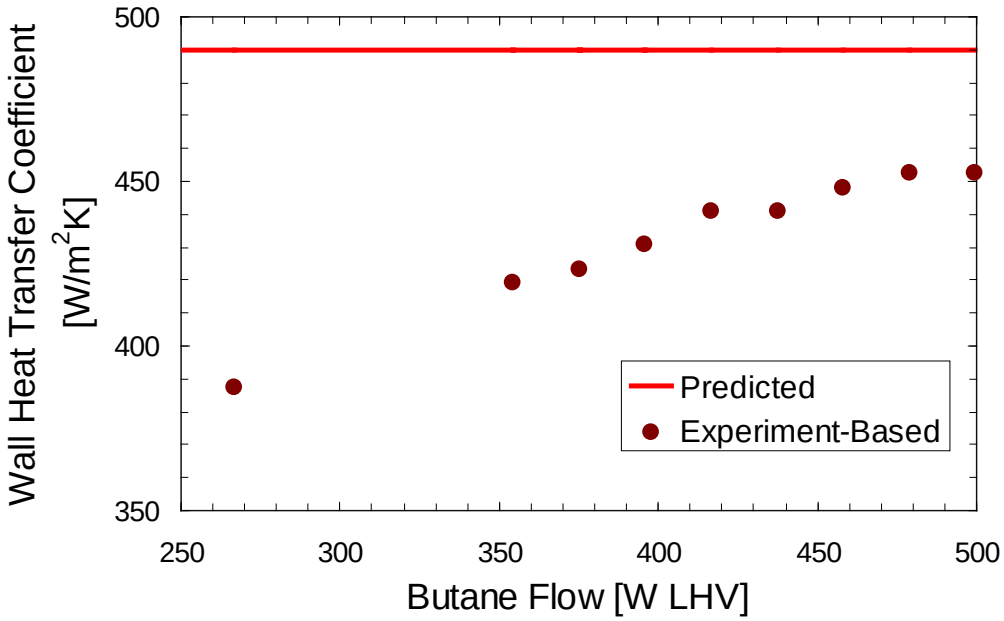

Figure 6-20: Comparison of predicted "effective" heat transfer coefficient for TE-mimicking heat sinks with observed heat transfer resistance.

6.4. Concluding Remarks for Design Performance with Heat Sinks

In this chapter, the performance of the combustor system at the design conditions with TE-mimicking heat sinks has been described. The demonstrated performance of the combustor compared well with the design targets for thermal efficiency, maximum temperature, axial temperature gradient, system pressure drop, and heat flux transferred to the heat sinks. The autothermal catalytic-combustion of butane in air was used to provide a heat source of 206 to 362 W at conditions suitable for a portable, air-breathing TE power generator.

Assuming a TE power conversion efficiency of 5%, the design point operation would result in thermoelectric power generation of 14.4 W, with an overall chemical-to-electrical conversion efficiency of 3.86% (based on LHV). Such performance, particularly given the low parasitic power loss required for air-pressurization, would represent a significant advancement in the field of portable TE power generators.

7. Power Generation with Thermoelectric Modules

Commercial thermoelectric modules from Hi-Z Technology, Inc. were obtained to assess the performance of the combustor system as a power generator. The bismuth-telluride-based Hi-Z modules were selected because they were capable of accommodating >250°C on a continuous operating basis and of approaching 400°C on an intermittent basis. This temperature limitation, though lower than the design temperature, was sufficient to allow a demonstration with butane combustion without the need for the addition of significant thermal barriers between the combustor and the TE module, as was required in other published works to allow stable catalytic combustion of an alkane[43]. The HZ-2 modules were selected based on the external dimensions (2.9 x 2.9 cm^2 surface area per module) similar to the design TE module.

7.1. Experimental Details

7.1.1. System Configuration

7.1.1.1. Combustor System Configuration

The system configuration for the combustor is largely the same as was used in the design experiments with the water-cooled heat sinks, which has been described previously in chapter 6. The system packaging for the TE power generation system has also been discussed previously in chapter 5. An image of the final TE power generation system is shown in Figure 7-1, and in this image it can be observed that the majority of the system volume consists of the air-cooled heat sinks..

7.1.1.2. Electrical System Configuration

A simplified way to conceive of a TE module in an electrical circuit is as a voltage source with a resistance (internal to the module) in series. Both the voltage (typically referred to as open circuit voltage) and the internal resistance are dependent on the temperatures of the "hot" and "cold" sides of the TE module. With two TE modules, there are three possible circuits that can be formed, and these are shown in Figure 7-2 to Figure 7-4. In these figures, R_I refers to the internal resistance, R_L refers to the load resistance (i.e., the device which is being powered by the TE power generator), and R_S refers to the shunt

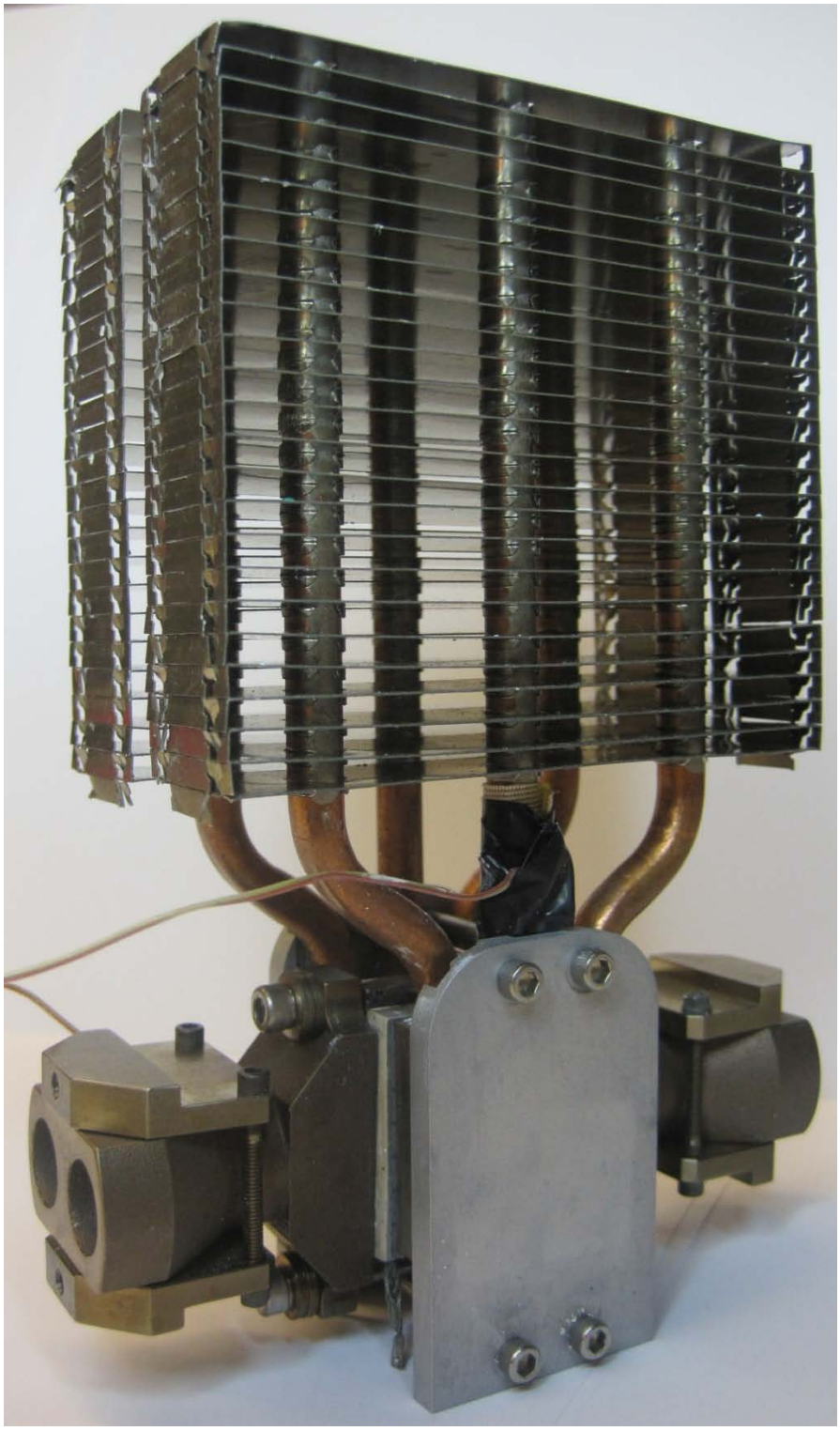

Figure 7-1: Image of thermoelectric power generator. For scale, aluminum fin banks are 8 x 8 x 2 cm.

resistance (i.e., a finely calibrated resistor used for current measurement). Similarly, V_{OC} refers to the maximum voltage gain, V_L refers to the voltage drop across the load, and V_S refers to the voltage drop across the shunt resistor. The series circuit connection provides power to the load with the highest voltage, while the parallel circuit provides power to the load with the highest current. The separate circuits eliminate any electrical interconnection between the two TE modules, which could be advantageous in the case of significantly different temperatures between the two reactors or heat sinks.

Electrical contacts to the terminals of the TE modules were made using alligator clips, and connections between circuit elements were made using 14-AWG wire. Wiring connections to the resistors were made using spade terminals.

7.1.2. Instrumentation and Control

7.1.2.1. Electrical Measurements

Load resistances were provided using adjustable tubular wirewound resistors (Ohmite), as shown in Figure 7-5, with resistances ranging from 0-1, 0-3, 0-5, and 0-10 Ohms. Two wires were connected to one end of the resistor using spade terminals, and two more wires were connected to the adjustable lug of the resistor. One of each of these wires was connected in the circuit, and the other wires were connected to the Agilent data acquisition system to measure the voltage drop across the load. By adjusting the position of the lug along the length of the resistor, the load resistance changed proportionally. The adjustable resistors were located outside the ventilated hood to allow for resistance adjustments to be made without otherwise disturbing the system.

Current measurement was accomplished using a shunt resistor (Simpson Electric), shown in Figure 7-6. This calibrated resistor exhibits a 50 mV voltage drop for a 5 A current flow, with a linear response from 0 – 50 mV for 0 – 5 A. The reported accuracy is 1%. Voltage measurements were carried out using the Agilent data acquisition system. The total resistance of the shunt was reported to be 0.065 Ohms; however, it was not included in the total power generation reported (as it was typically less than 1% of the power).

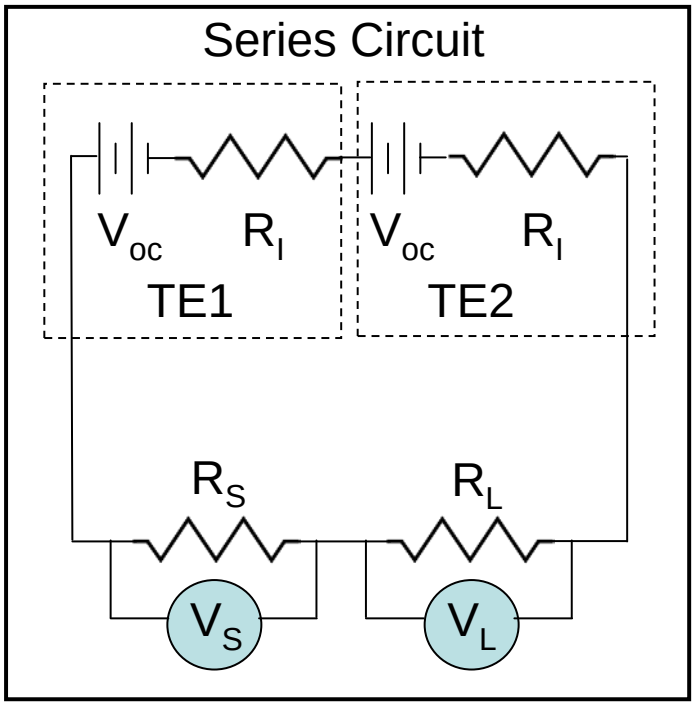

Figure 7-2: Series circuit connection. "V" refers to voltage and "R" refers to resistance. Subscript of "OC" indicates open circuit, "I" indicates internal to the TE module, "L" indicates the load of variable resistance, and "S" indicates the shunt resistance used to measure current flow.

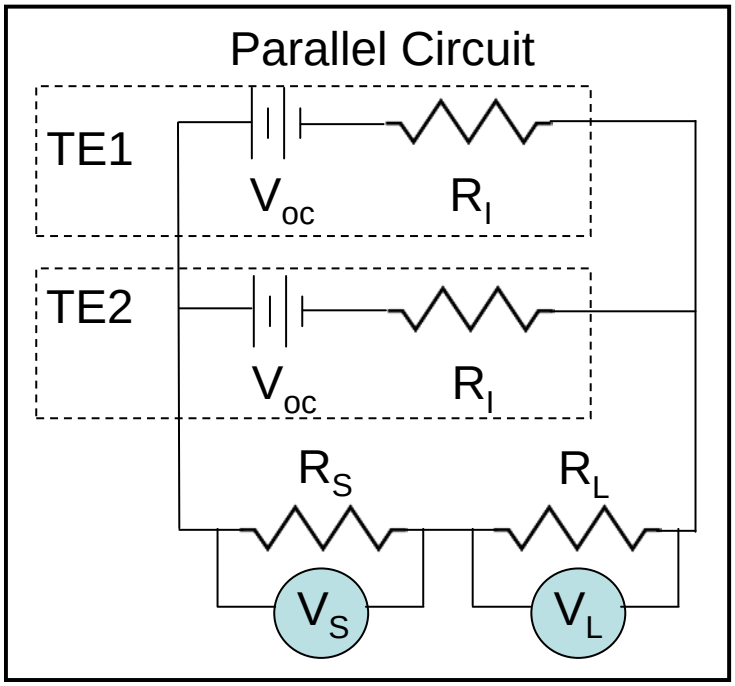

Figure 7-3: Parallel circuit connection for TE modules.

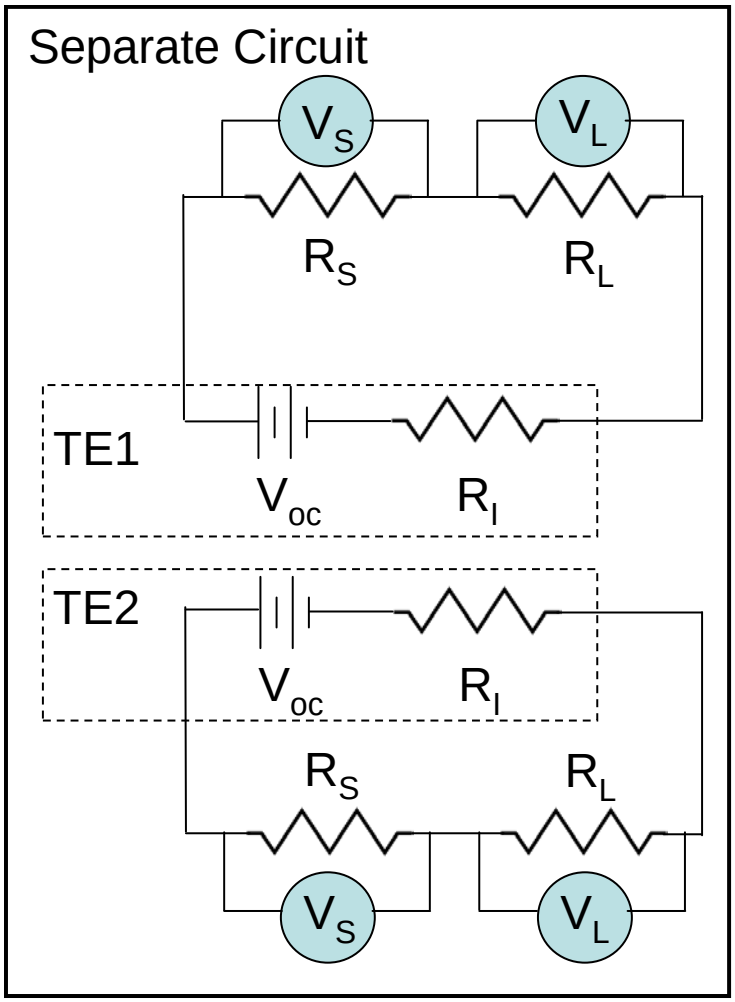

Figure 7-4: Separate circuit connection for TE modules.

Figure 7-5: Adjustable tubular wirewound resistor used as "electrical load".

Figure 7-6: Shunt resistor used to measure electrical current. Power from electrical circuit flows from one red wire, through the resistor, and into the other red wire. The black wires are used to measure the voltage drop across the shunt.

7.1.2.2. Temperature Measurements

Temperature measurements on the "cold" side of the device (on the exterior of the clamp plate and on the base of the heat sink pipe) were made using self-adhesive K-type thermocouples (Omega Engineering). The thermocouple on the clamp plate is shown in Figure 7-7, and the thermocouple on the heat sink pipe, covered over with electrical tape for increased adhesion, is shown in Figure 7-1. Both of these cold side measurements underestimated the temperature at the cold-side of the TE modules due to the low thermal conductivity of the electrical insulator.

To measure the combustor temperature, a slot was cut out of a sheet of graphite material (Graftech International eGraff) into which a 36-gage thermocouple was placed to align near the center of the reactor. This thermocouple arrangement is shown in Figure 7-8. The graphite layer, with embedded thermocouple, was coated on both sides with a layer of high-temperature thermal paste (Epoxyset Inc. HTG-72) and arranged between the silicon reactor and the alumina insulating wafer on the hot-side of the TE module. These thermocouples (one per reactor side) provided an estimate of the average reactor surface temperature, but they overestimated the temperature of the hot-side of the TE modules, again due to the low thermal conductivity of the electrical insulator.

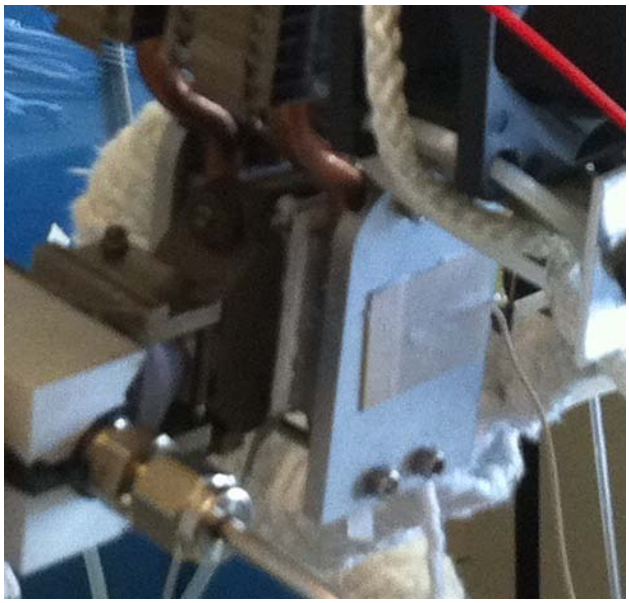

Figure 7-7: Self-adhesive thermocouple on exterior of clamp plate for estimate of cold-side temperature.

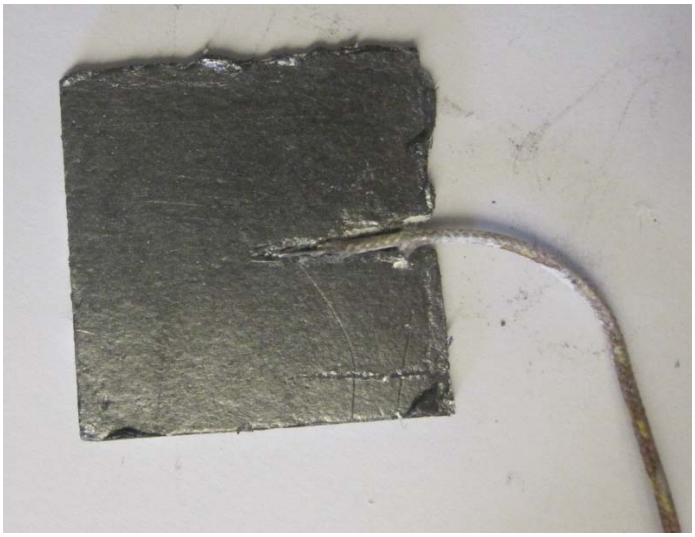

Figure 7-8: 36-gage thermocouple embedded in graphite layer and sandwiched between silicon reactor and alumina electrical insulator on hot-side of TE module. During packaging, both sides were coated with a layer of high-temperature thermal paste.

7.1.2.3. Butane Conversion Measurement

As discussed previously, the conversion of butane in the reactor was estimated from the measurement of butane in the exhaust gas, as determined by mass spectrometer (Inficon). The exhaust streams from the two reactors were combined and connected to a condenser, and a small portion of the exhaust from the condenser was drawn through a 50-µm-inner-diameter capillary to the mass spectrometer. Argon was included with the fuel stream at

a flow rate of 10.65 sccm and used as an internal standard. A calibration curve, shown in Figure 7-9, was created using known proportions of argon and butane in ~4 slpm of air. The charge number (m/z) used for butane was 43, which is the largest peak for the butane mass spectrum as reported by NIST[209]. It was experimentally observed that there was a lag time of approximately 1.5 minutes between changes in inlet flow rates and the observed change at the mass spectrometer, owing to the 25-ft length of capillary between the condenser and the instrument.

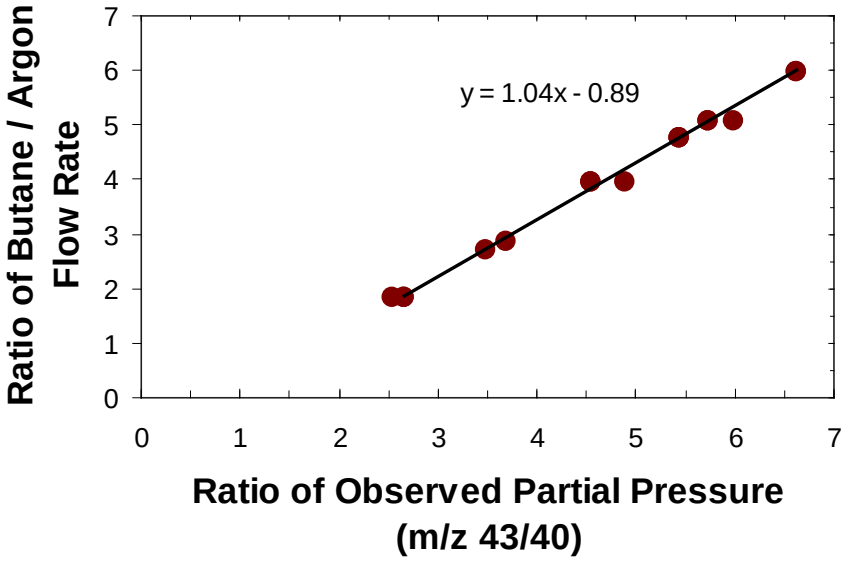

Figure 7-9: Mass spectrometer calibration curve for determining butane flow rate in exhaust gas. Line of best fit for most recent calibration is shown in figure.

7.1.3. Experimental Procedures

7.1.3.1. Reactor Start-up Procedure

The ignition procedure used in these experiments was to include hydrogen with the butane and air flow, similar to that described previously in chapter 6. A complicating factor was the relatively narrow operating window between the upper temperature limit imposed by the TE modules (approximately 300°C) and the lower temperature limit imposed by the butane kinetics (approximately 250°C). In order to achieve stable transition to autothermal butane combustion, the rates of decrease in hydrogen flow and increase in butane flow were significantly slower than in the heat sink experiments. Another factor that simplified start-up was that the electrical circuit was typically broken

during start-up, reducing the rate of heat removal from the combustor. Start-up times were typically longer for the TE-power generation system than those for the heat sink experiments, and finer flow adjustments were required.

An example profile of the dynamic reactor temperature is shown in Figure 7-10, and the dynamic profile of the fuel composition for the same experiment is shown in Figure 7-11. In this example, the transition from hydrogen-assisted combustion of butane to only butane began after 28 minutes, and the final hydrogen flow was cut off at 39 minutes. In the interim period, the butane flow was increased by approximately 5 sccm (10 W LHV) increments, and the hydrogen flow was decreased by approximately 55 sccm (10 W LHV) increments. The flow was then held stable, at 111 sccm of butane, until a steady state "open circuit" condition was observed, after which the circuit was closed. When higher flow of butane was used (e.g., 116 sccm butane flow), the same procedure described here was used, and the butane flow was increased after the circuit was closed.

7.1.3.2. Dynamics to Steady State

The system dynamics to steady state following start-up were similar to those discussed in chapter 6 for the heat sink experiments. The initial stabilization period can be observed in Figure 7-10 from approximately 40 to 50 minutes. In the TE power generation experiments, the fuel and air flow were held constant while the load resistance was varied. As discussed in chapter 3, an increase in the current flow through the TE modules, in response to a decrease in the load resistance, resulted in a slight increase in the heat removed from the reactor through the TE module (and vice versa). While the response time of the electrical circuit to the change in the resistor was nearly instantaneous, the small change to the heat balance necessitated some time to stabilize between observations. The changes in load resistance can be observed in Figure 7-10 as rapid, small increases in both reactor temperature and power production. The amount of time required to stabilize the system following a change in load resistance was somewhat dependent on the magnitude of the change; however, typically 5 – 10 minutes between measurements was sufficient. Upon stabilization, measurements (taken at 5 or 10 second intervals) were averaged over one minute or more to determine the steady state value.

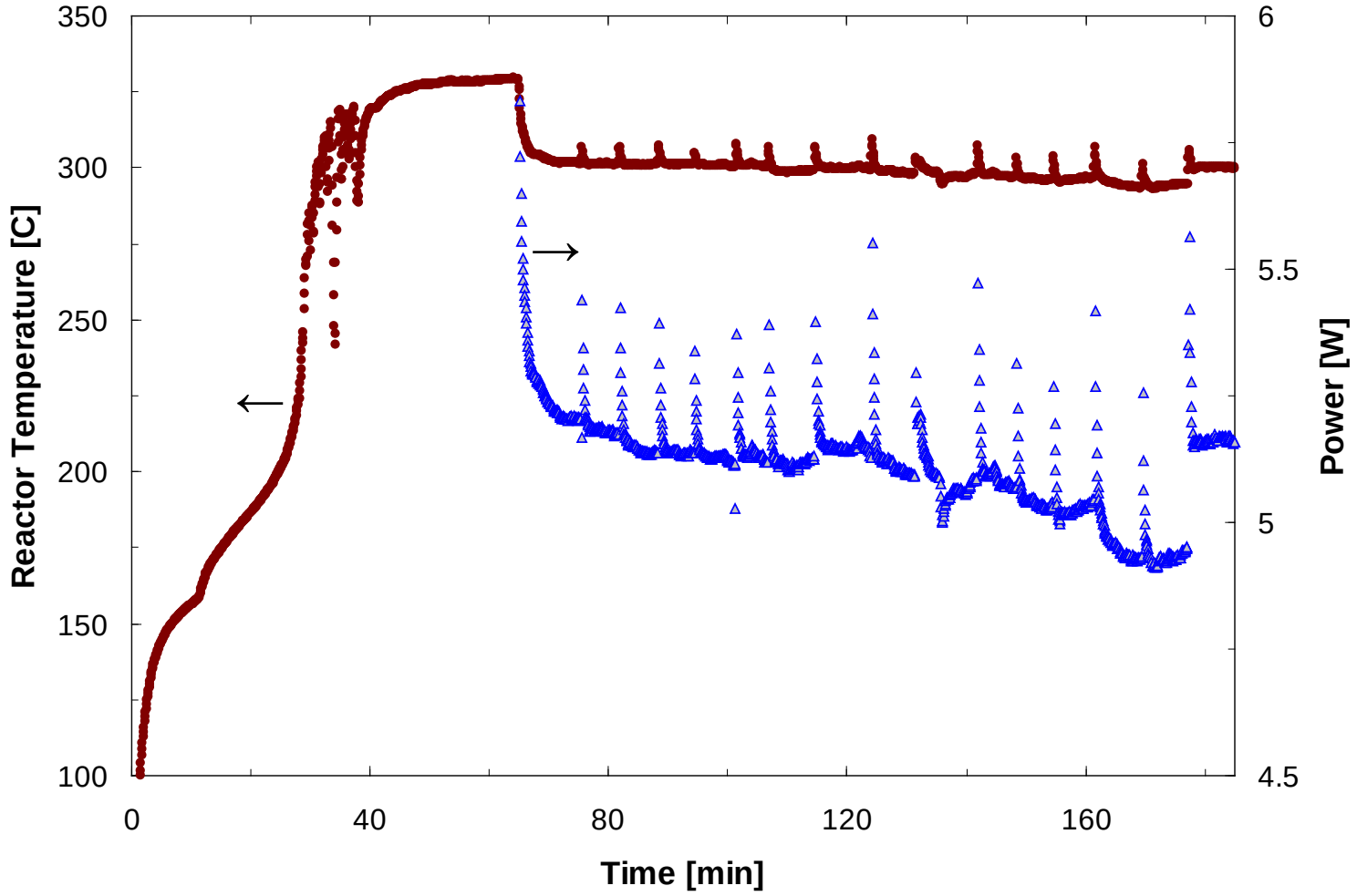

Figure 7-10: Dynamic profile of reactor temperature and power production for an example experiment. After 40 minutes, butane flow is 111 sccm (220 W LHV) and air flow is ~4 slpm. Brown dots indicate reactor temperature, and open blue triangles indicate electrical power provided to the load resistor. Series circuit connected after 65 minutes. Results from July 29, 2010.

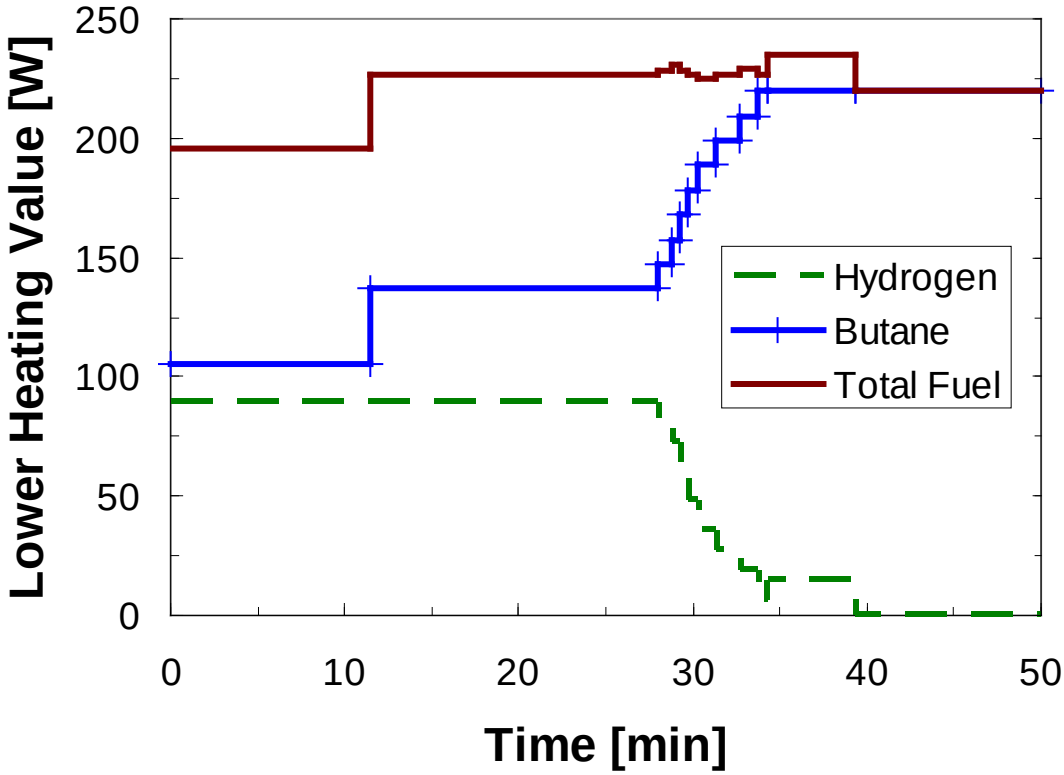

Figure 7-11: Example of lower heating value and composition of fuel during start-up period. Experimental conditions from July 29, 2010.

7.1.4. Calculations

7.1.4.1. Electrical Current

As described previously, the electrical current was measured using a shunt resistor connected in series with the load resistor. The voltage drop across the shunt resistor, V_S, can be used to calculate the current, I, based on the calibrated voltage drop, V_C, for a calibrated maximum current I_C, according to equation 37. The shunt used in this work was calibrated for 50 mV at 5 A.

$$I = \frac{V_S}{V_C} I_C \qquad [37]$$

7.1.4.2. Load Resistance

The load resistance was set by adjusting the lug position along the length of the resistor, and as such the exact value was not known *a priori*. Instead, the load resistance, R_L, was calculated based on the electrical current, I, determined from the shunt resistor and the

measured voltage drop across the resistor, V_L, according to Ohm's law as shown in equation 38.

$$R_L = \frac{V_L}{I} \qquad \textbf{[38]}$$

7.1.4.3. Electrical Power

The electrical power, P, produced from the TE power generator was calculated based on the product of the current, I, determined from the shunt resistor and the measured voltage drop, V_L, across the load resistance. As mentioned previously, this calculated value neglects the power dissipated by the shunt resistor (which is typically <0.04 W).

For the simplified TE power generation circuits shown in Figure 7-2 to Figure 7-4, the power, P, dissipated by the load, R_L, can be calculated according to equation 39, where V_{OCE} and R_{IE} refer to the effective open circuit voltage and internal resistance for the given circuit connection, respectively. For constant temperature sources, the maximum power is produced when the load is equal to the internal resistance. Other "optimal" ratios of the load resistance to the internal resistance have been suggested to maximize the conversion efficiency[32]; however, for a system such as the TE power generator, the load resistance should be optimized within a more complete model incorporating reaction kinetics, system heat loss pathways, and the temperature dependence of the thermoelectric properties.

$$P = R_L \left(\frac{V_{OCE}}{R_L + R_{IE}} \right)^2 \qquad \textbf{[39]}$$

7.2. Validation Experiments

7.2.1. Thermoelectric Module Testing

Before integration with the combustor, the TE modules from Hi-Z were tested with the same cartridge heaters and chuck used to test the TE-mimicking heat sinks (described in chapter 6). The purpose of the experiment was to investigate the packaging, to test the air-cooled heat sinks and fan, and to ensure that the TE modules were in good working order. The voltage applied to two cartridge heaters was controlled using a variable autotransformer, and the open circuit voltage across each of the two modules was

measured using a digital multimeter, and is shown in Figure 7-12 as a function of the measured temperature difference between the heater chuck and the exterior of the clamp plate. The actual temperature difference across the TE module was less than the measured value, primarily owing to thermal resistance of the alumina electrical insulating shims between the heater and the TE module, and between the TE module and heat sink.

What was observed from this experiment was that the two modules performed similarly to one another, indicating that they were undamaged. The slight difference in open-circuit voltages was very likely due to the fact that the air from the fan was forced past the heat sink cooling module 1 before that cooling module 2, likely increasing the cold side temperature of module 2. The other observation was that the voltage response to the total temperature difference was linear, as would be anticipated. The slope of the voltage response to the total temperature gradient was 25.8 mV/K, which is lower than the Seebeck coefficient of 32 mV/K that has been reported for these materials[44]. This difference indicated that the thermal resistance across the electrical insulators is considerable.

7.2.2. Initial System Testing with Damaged Reactor

Prior to final system integration with a pristine set of reactors, the TE Power generation system was tested using reactors with a known leak of ~ 27%. This was the same set of reactors that was used in the design point testing of the system, described in chapter 6 (and subsequently damaged). The objectives of these experiments were to indentify any issues with the packaging scheme or the design of the surrounding system, to gain insight into the performance of the system, and to identify appropriate fuel flow rates to accommodate the changed heat transfer pathway from the heat sink experiments. These experiments were also of value to identify appropriate experimental procedures for the final system testing. Experiments were conducted using either hydrogen or butane as the fuel, as well as with or without insulation on the gas distribution manifolds and tube adapters.

The experimental procedure, as described previously, was to stabilize the system under open circuit conditions and then to connect the load resistor and obtain measurements for power produced by the TE generator over a range of resistances. It was desired to test the system under a large enough range of resistances to observe the maximum in the power response to load resistance. An example response curve of power as a function of load resistance in shown in Figure 7-13. The results for hydrogen combustion in air, without insulation, are compared with a response modeled from equation 39, using 4.1 V as the V_{OC} (based on measured voltage immediately after the load resistor was opened) and a fitted value of 3.64 Ohms for the internal resistance of each module. The measured response follows the anticipated behavior, and the estimated internal resistance is similar to that reported by the manufacturer. The "Parallel" and "Series" responses were measured during separate experiments, which indicated repeatability in system performance.

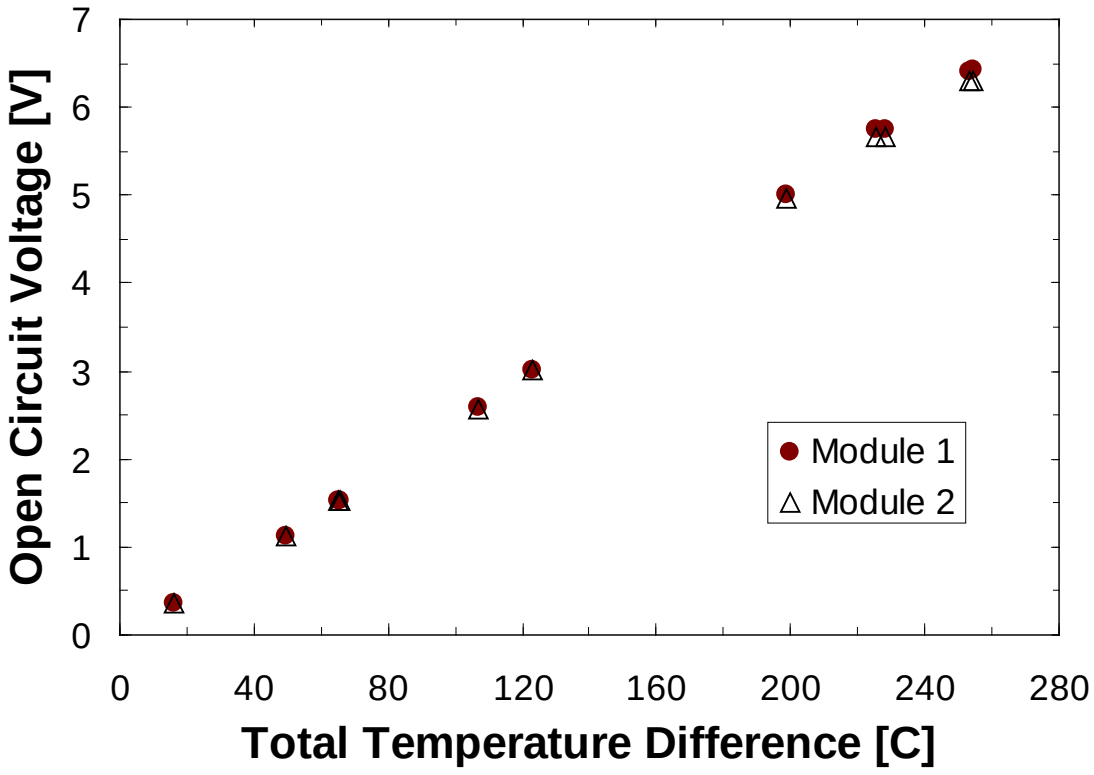

Figure 7-12: Testing of Hi-Z thermoelectric modules and air-cooled heat sinks using electrical heater. Total temperature difference refers to difference in temperature measured between heater chuck and exterior of clamp plate (across module 1). Actual difference across the TE module would be reduced as a result of electrical insulating shims.

In order to assess the impact of insulation surrounding the gas distribution manifolds and the tube adapters, power generation at two different hydrogen flow rates were compared for the system with and without insulation. The reactor integrity was assessed (as described in chapter 6) before and after the transition in order to remove any concerns that the system had been further damaged. The results of these experiments are shown in Figure 7-14, where voltage refers to V_L, the solid brown symbols indicate the insulated results, and the grey-filled symbols indicate the results of the system prior to the addition of insulation. It was observed that the impact of the insulation was considerable, allowing for increased production of power by approximately 10 – 15% at the same experimental conditions. Accordingly, all butane combustion experiments were carried out under insulation.

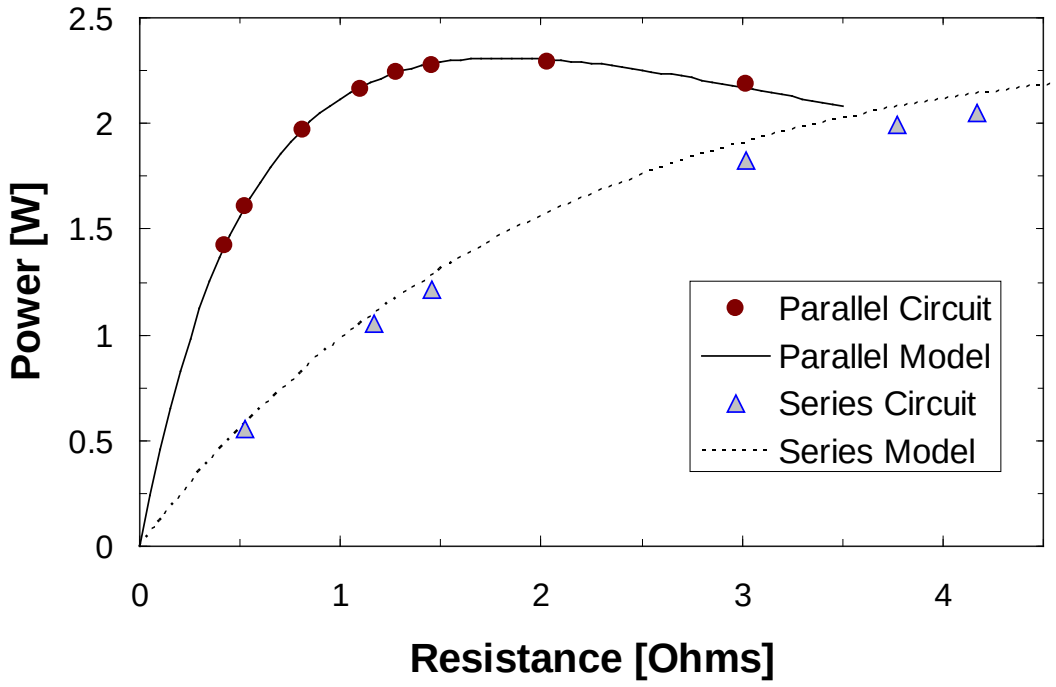

Figure 7-13: Uninsulated system results of power produced for a given load resistance for combustion of ~896 sccm oh hydrogen (160 W LHV). Points represent experimental measurements. Dashed line represents model prediction for Voc = 4.1 V (measurement estimate) and R_I = 3.64 Ohms per module (fitted value).

The preliminary system performance with butane combustion is shown in Figure 7-15. Power production results are shown for different load resistances with a parallel circuit connection at two different butane flow rates with approximately stoichiometric air (Φ =

1.0 at 272 W LHV, Φ = 0.96 at 282 W LHV). The models shown, of the form of equation 39, have both V_{OC} and R_I fit to only a few data points, and as such are provided only to guide the eye. These experiments demonstrated that it was possible to produce TE power with butane combustion in this system, even with a known leak from the reactor. A maximum of 6.2 W electric power was produced from 143 sccm butane flow (282 W LHV), which represents a conversion efficiency from chemical to electrical energy of 2.2%. These experiments were useful to provide a reference for final system performance (e.g., that the conversion efficiency shouldn't be less than 2.2% at similar power production levels) as well as to provide an estimate for operating conditions (i.e., combustion of ~110 sccm of butane when accommodating for the majority of the leak).

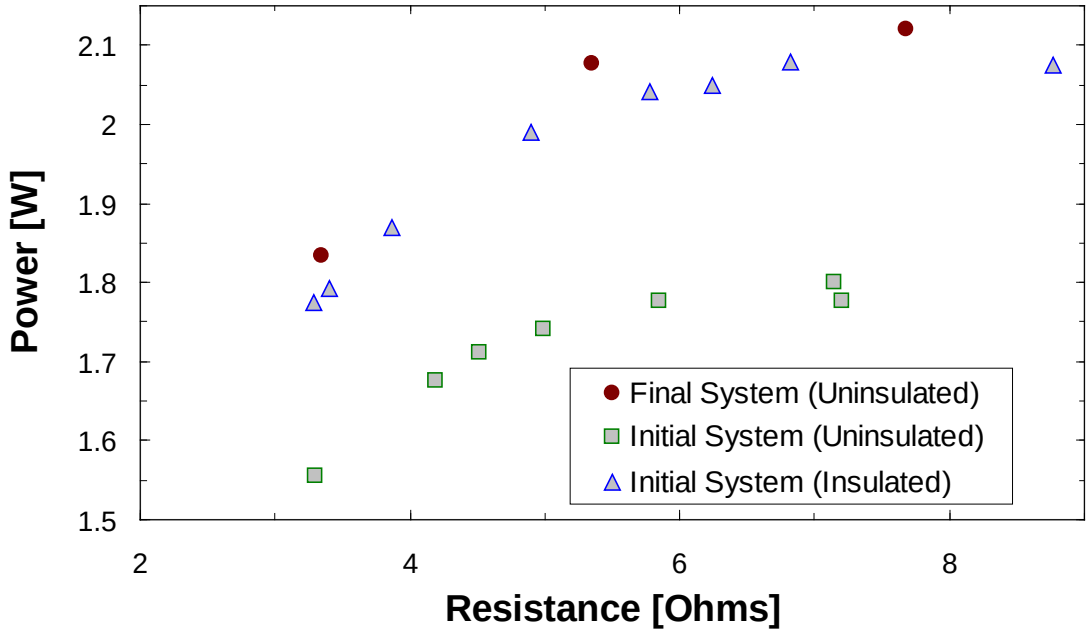

Figure 7-14: Preliminary experiment to assess impact of insulation over gas distribution manifolds on power output. Results for series circuit with ~780 sccm hydrogen (139 W LHV) and ~896 sccm hydrogen (160 W LHV). Air flow in all cases is ~4 slpm.

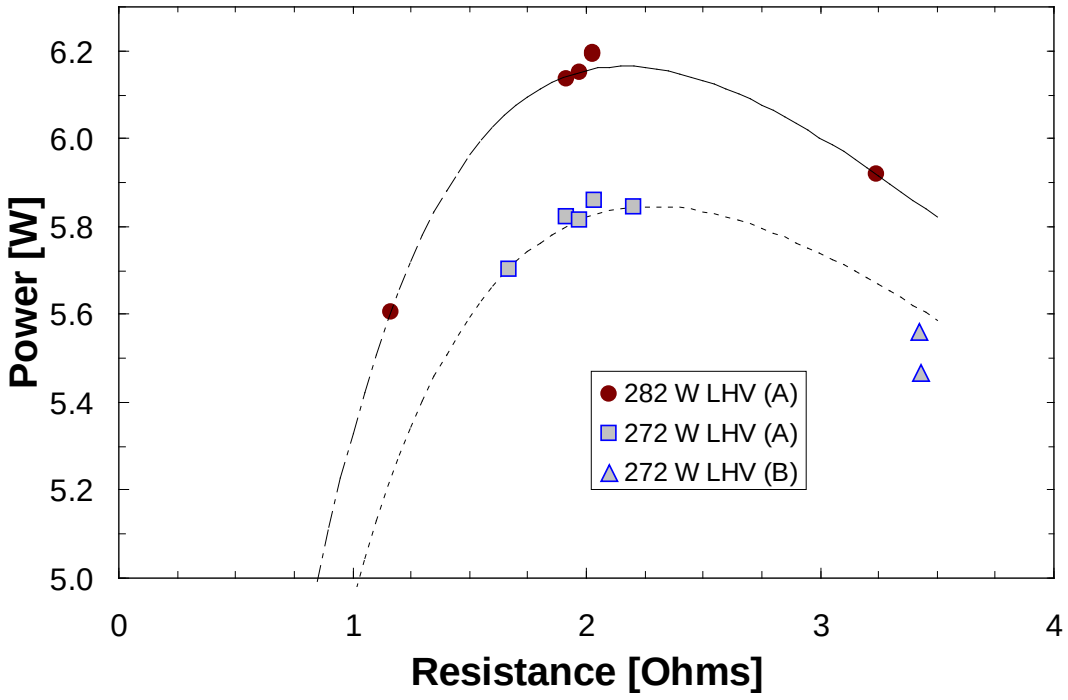

Figure 7-15: Thermoelectric power generation (insulated system) from butane combustion in air within a broken reactor. Φ ~ 1.0, and TE modules are connected in parallel. Legend identifies heating value of fuel flow and the experiment set (A or B) to which it belongs. V_{OC} and R_I parameters for models fit to data.

7.3. Final System Experimental Results and Discussion

The "final" TE power generation system included two silicon reactors that were wash coated with 229 and 243 mg of catalyst (for a total catalyst weight of 472 mg), and the other components which have been described in chapters 3 through 5. The reactor integrity was verified initially after assembly, and periodically between experiments, with no appreciable leak observed subsequent to any of the experiments reported here. It should be noted that in these experiments, the fuel flow distribution valves were adjusted in order to maximize the overall system performance rather than to equalize reactor temperature measurements (as there was no guarantee that the thermocouples were positioned identically). Reactor temperatures discussed below refer to the higher of the measurements, though the discrepancy was small.

7.3.1. Comparison of TE Power Generator with Initial System Testing Results

In order to assess the improvement in system performance as a result of the intact reactor, the system was tested with hydrogen combustion of 780 sccm (139 W LHV) with and without insulation on the gas distribution manifolds and tube adapters. The uninsulated system results show ~15% higher power production from the leaking reactor to the final system. The maximum power production for the final system after insulation is 14% higher than of that of the uninsulated system, which was similar to the improvement noted in the initial system testing. In addition to confirming that the final system behavior was representative of earlier observations, these results indicated that the leak from the initial system had a slightly larger impact on the power production than did the insulation on the manifolds and tube adapters. It is worth noting that the final insulated system produced 2.45 W electrical power from ~139 W LHV hydrogen flow, which corresponds to an efficiency of 1.76%

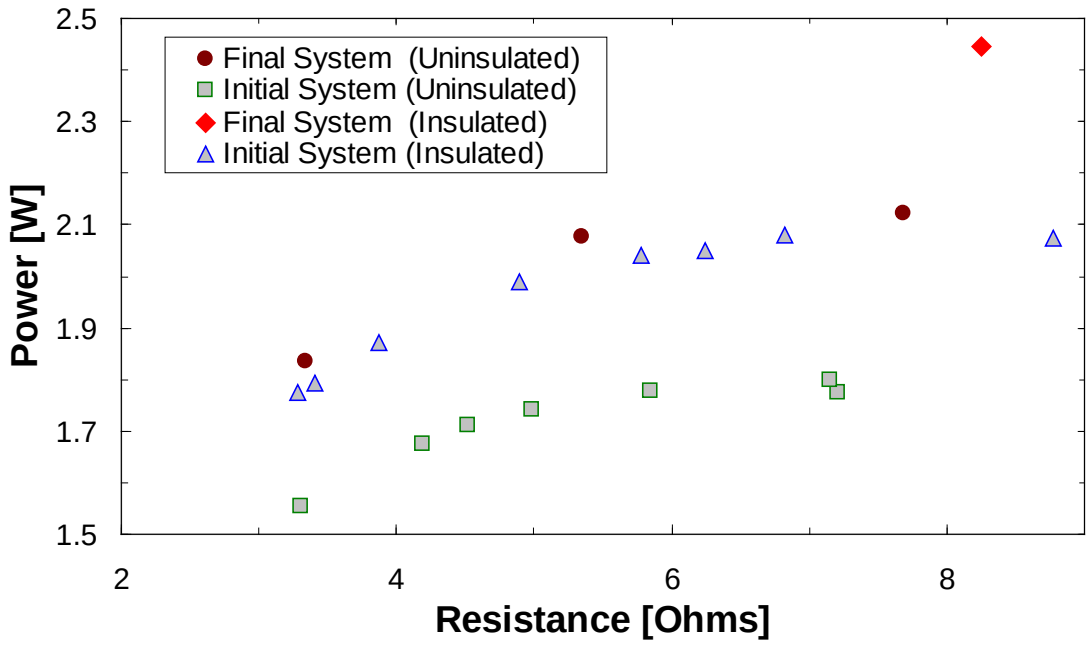

Figure 7-16: Comparison of final system with initial system testing experiments for power generation from hydrogen flow of ~780 sccm and Φ ~ 0.47. The TE modules were connected in series. Results generated with and without insulation on the gas distribution manifolds or tube adapters.

7.3.2. TE Power Generation from Catalytic Combustion of Butane

Three different flow rates of butane were used for TE power generation in this system. The lowest flow rate, 106 sccm (209 W LHV), was considered because it was on the stability boundary in terms of autothermal combustion of butane. The highest flow rate, 116 sccm (230 W LHV), was considered because it was estimated to provide a "hot-side" temperature at the TE module (accounting for the thermal resistance of the alumina insulating shim) close to 300°C, which was identified as a moderately "safe" limit for operation without damage to the modules. The third flow rate was chosen as an intermediate value between these two conditions. The TE power generated from the catalytic combustion of butane is shown in Figure 7-17, and the maximum power conditions for each flow rate and circuit connection are given as Table 7-1. In this figure, the power produced with a parallel circuit connection is represented by symbols with solid color, while the power produced with a series circuit connection is represented by gray-filled symbols. The symbol shape represents the flow rate of butane, as listed in the legend. The x-axis in this figure shows the voltage drop across the load resistance. The two down-arrows indicate the points at which the lowest flow rate was on the border of stability to sustain autothermal butane combustion (the system would be stable with resistances above the load resistance at this point, and unstable with load resistances below). The observed reactor temperatures at these two extinction points were similar (268°C for the series circuit and 272°C for the parallel circuit).

The maximum power produced from butane combustion in the final system was 5.82 W, with an overall chemical-to-electrical conversion efficiency of 2.53% (based on LHV). This performance compares quite favorably with other small TE power generators found in the literature. For example, in demonstrations using the same commercial thermoelectric module, 0.65 W (transient) electrical power was produced at 1.1% efficiency from catalytic combustion of methanol[44], ~0.44 W was produced at 0.5% efficiency from catalytic combustion of propane, and 1.08 W was produced at 1.08% efficiency from catalytic combustion of hydrogen[43].

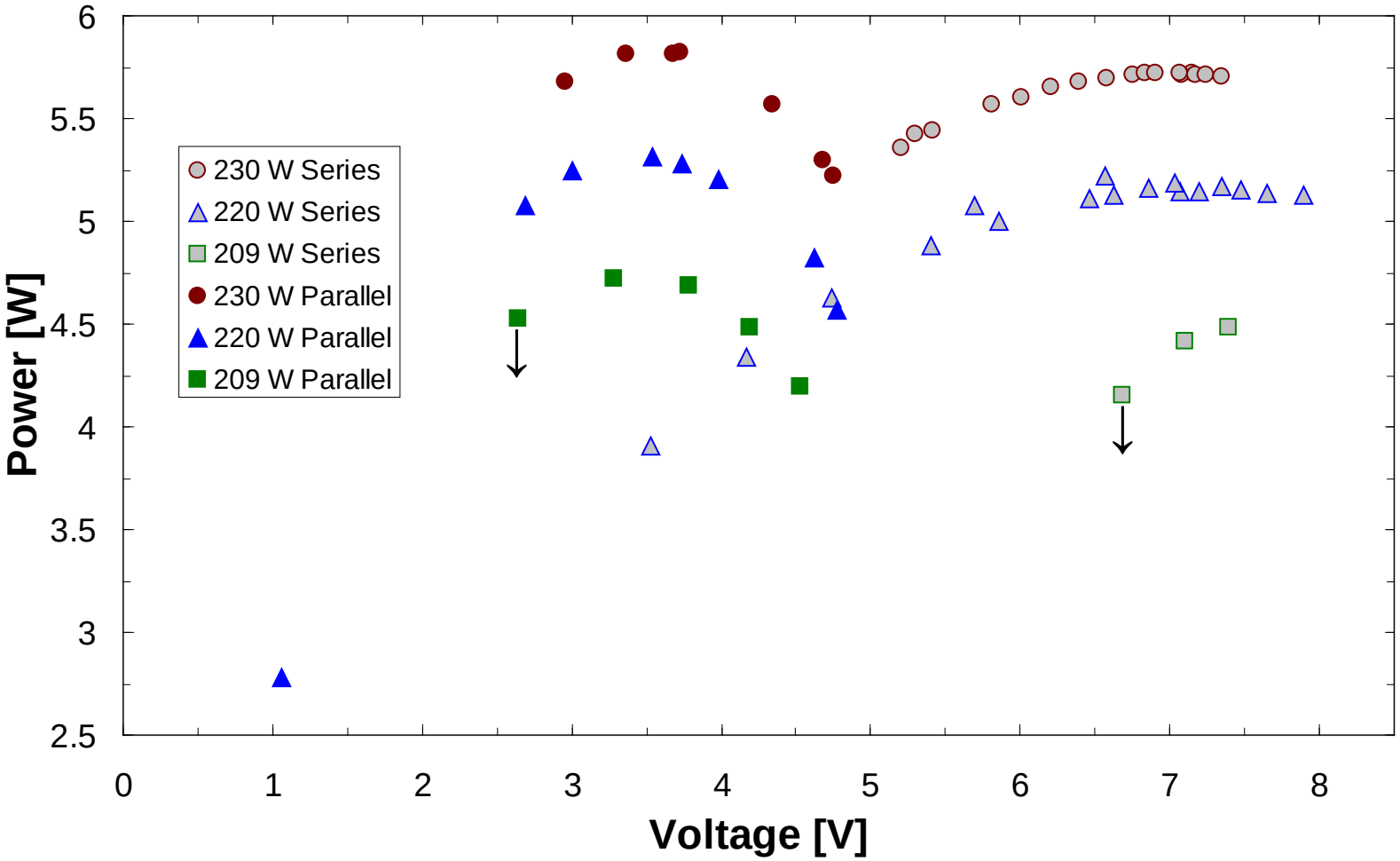

Figure 7-17: Power generation results for butane combustion in air. Solid color symbols indicate parallel circuit configuration, and grey-filled symbols indicate series circuit configuration. Butane flow indicated by symbol shape: circles indicate 116 sccm (230 W LHV), triangles indicate 111 sccm (220 W LHV), and squares indicate 106 sccm (209 W LHV). Down-arrows indicate extinction point for low butane flow.

Table 7-1: Experimentally observed maximum power conditions for TE power generation from butane. Efficiency refers to overall conversion from chemical to electrical energy, based on LHV.

Butane Flow [W LHV]	Φ	Circuit Configuration	Maximum Power [W]	Efficiency [%]	Voltage at P_{MAX} [V]	Current at P_{MAX} [A]
209	0.84	Parallel	4.72	2.25	3.29	1.44
220	0.85	Parallel	5.31	2.42	3.54	1.50
230	0.93	Parallel	5.82	2.53	3.73	1.56
209	0.84	Series	4.49	2.14	7.39	0.61
220	0.87	Series	5.22	2.38	6.56	0.80
230	0.89	Series	5.72	2.49	6.83	0.84
220	0.87	Separate	5.36	2.44	3.34 / 3.55	0.70 / 0.72

For a given butane flow, the performance of the TE power generator when the TE modules were connected in parallel was slightly higher than the performance when the modules were connected in series, as can be observed in Figure 7-17. This effect was expected, as there is an increase in the Peltier cooling for the series connection due to increased current flow through each module. For the 220 W LHV and 230 W LHV maximum power conditions, the temperature difference from reactor to heat sink was 2.6°C and 2.1°C larger, respectively, for the parallel compared with the series circuit. This effect can be observed in Figure 7-18. However, as it is often beneficial to produce power at higher voltage, the trade-off between power, efficiency, and voltage should be evaluated based on actual load requirements. For example, with a series connection, the TE power generator can meet the power requirements for USB standard devices (5 V DC, <0.9 A). The results with separate circuits were similar to that of the parallel circuit, with the slight difference possibly related to the observed maximum power points not reflecting the absolute maximum.

The current-voltage relationships for the TE generator are shown in Figure 7-19, and from the lines of best-fit the estimates for V_{OC}, short circuit current (I_{SC}) and internal resistance are given in Table 7-2. The internal resistance estimate is the ratio of V_{OC} to I_{SC}, adjusted to a per-module estimate based on the circuit connection. The estimates of internal resistance are lower for the parallel circuit than for the series circuit, which is likely because in the parallel circuit, more current passes through the lower internal resistance leg, while in the series circuit all current passes through both resistances.

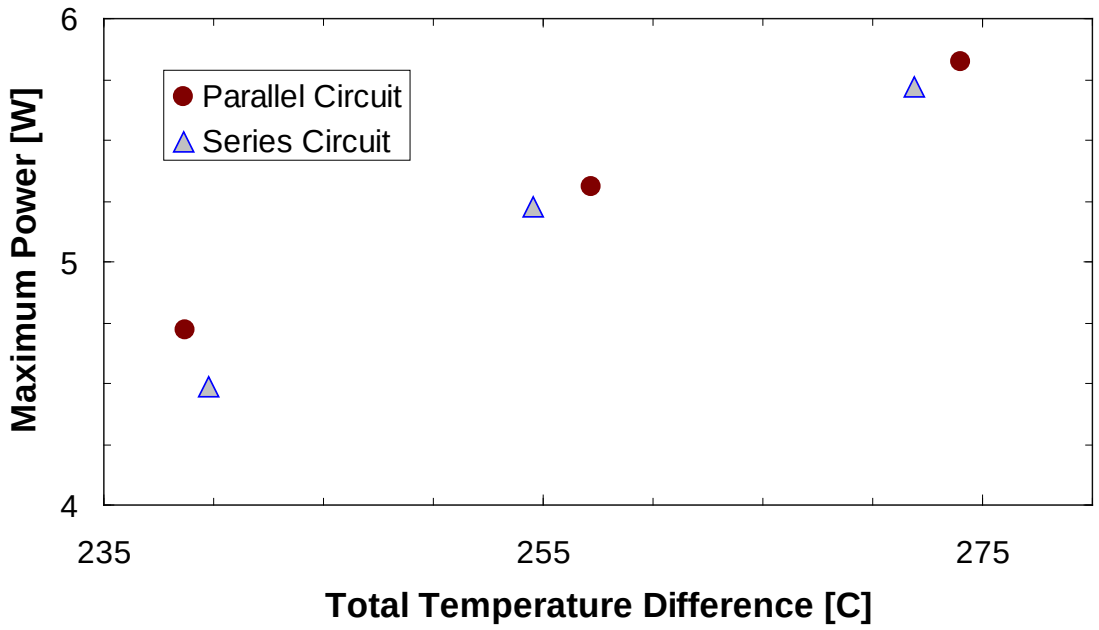

Figure 7-18: Maximum power produced for each flow rate compared with the total temperature difference between the reactor and heat sink. Total temperature difference is larger than that across the TE modules, due to thermal resistance of alumina shims.

The temperature of the air-cooled heat sink was observed to range from 18 to 25°C above ambient temperature on the side closer to the fan, and from 24 to 30°C above ambient temperature for the heat sink on the far side of the fan. The air cooling the heat sinks was observed to rise between 14 and 19°C above ambient temperature. The increased cold-side temperature of the TE modules that resulted was a necessary trade-off for having device-ready heat sinks (<80 g each) and a relatively-low-power fan (<1.35 W).

7.3.3. System Analysis

The butane conversion results measured for power generation from butane combustion with a series circuit configuration are shown in Figure 7-20 as a function of the observed reactor surface temperature. It is important to note that this system was operated autothermally, and as such the temperature and the butane conversion were not independent, as one would desire for a kinetic study. However, the conversion trend with increasing temperature has a very similar shape to those published in the literature for catalytic combustion of other hydrocarbons[113]. It is likely that the actual reaction temperature at the surface of the catalyst is slightly higher than this surface measurement;

though, with the high thermal conductivity of silicon and the good thermal contact between the catalyst wash coat and the reactor walls, it is not expected that this difference will be large. It was observed that the conversion for all measured operating points with the highest butane flow (230 W LHV) was nearly complete (>98%) within the precision of the instrument and calibration. The conversion for the intermediate butane flow (220 W LHV) was high, ranging from 92 to 98%. The conversion for the lowest butane flow (209 W LHV) was low during power production (80 to 90%) operation, but was ~97% for the open circuit condition. The extinction point observed during operation corresponds to the lowest butane conversion measurement, which supports the designation.

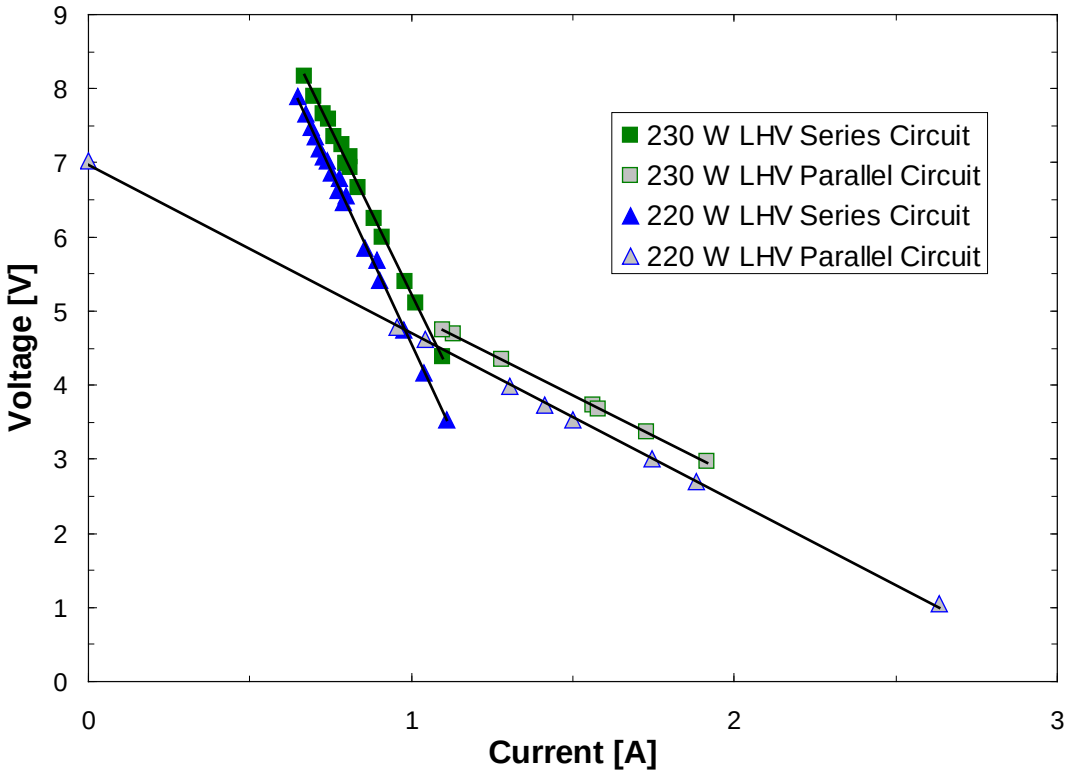

Figure 7-19: I-V Relationships for TE Power Generator. Filled symbols indicate series circuit connection and grey symbols indicate parallel circuit connection. Blue triangular symbols indicate butane flow of 111 sccm of butane (220 W LHV). Green square symbols indicate butane flow of 116 sccm (230 W LHV).

Table 7-2: Open circuit voltage, short circuit current and internal resistance as estimated from I-V curves. Internal resistance is estimated per module.

Butane Flow [W LHV]	Circuit Connection	V_{oc} [V]	I_{sc} [A]	R_I [Ohms]
220	Parallel	6.97	3.07	4.54
230		7.16	3.26	4.39
220	Series	13.99	1.48	4.72
230		14.19	1.58	4.48

In order to determine what regime the combustor is operating in at the operating conditions used for TE power generation, the characteristic timescales for reaction, diffusion, and residence were analyzed. These timescales are shown for varying conditions in Figure 7-20, estimated using the reactor surface temperature. As in chapter 6, these timescales are best suited for order-of-magnitude comparisons, though some indication as to performance can be drawn from their trends. Unlike the design experiments, the residence time in the TE power generator, with a minimum value of 11.7 ms, was always higher than the diffusion time, with a maximum value of 8.8 ms. This was expected, as a result of the reduced total flow rate and temperature characteristic of the TE power generator. The characteristic timescale for the reaction, however, changed significantly over the temperature span of interest (as the activation energy is estimated to be 71 kJ/mol), ranging from 45 to 11.7 ms. While the magnitude of this timescale is sensitive to small changes in temperature, the general trend indicates that the combustor may have been influenced by reaction kinetics for some of the conditions explored. The reaction time was similar to the residence time for reactor temperatures above ~310°C. This analysis suggests that if the system were to be operated at temperatures less than this cross-over point, it may be worthwhile to investigate the impact of improved catalyst activity, either through increased platinum concentration, doping with electronegative atoms such as vanadium or tungsten, or modifications to the support material.

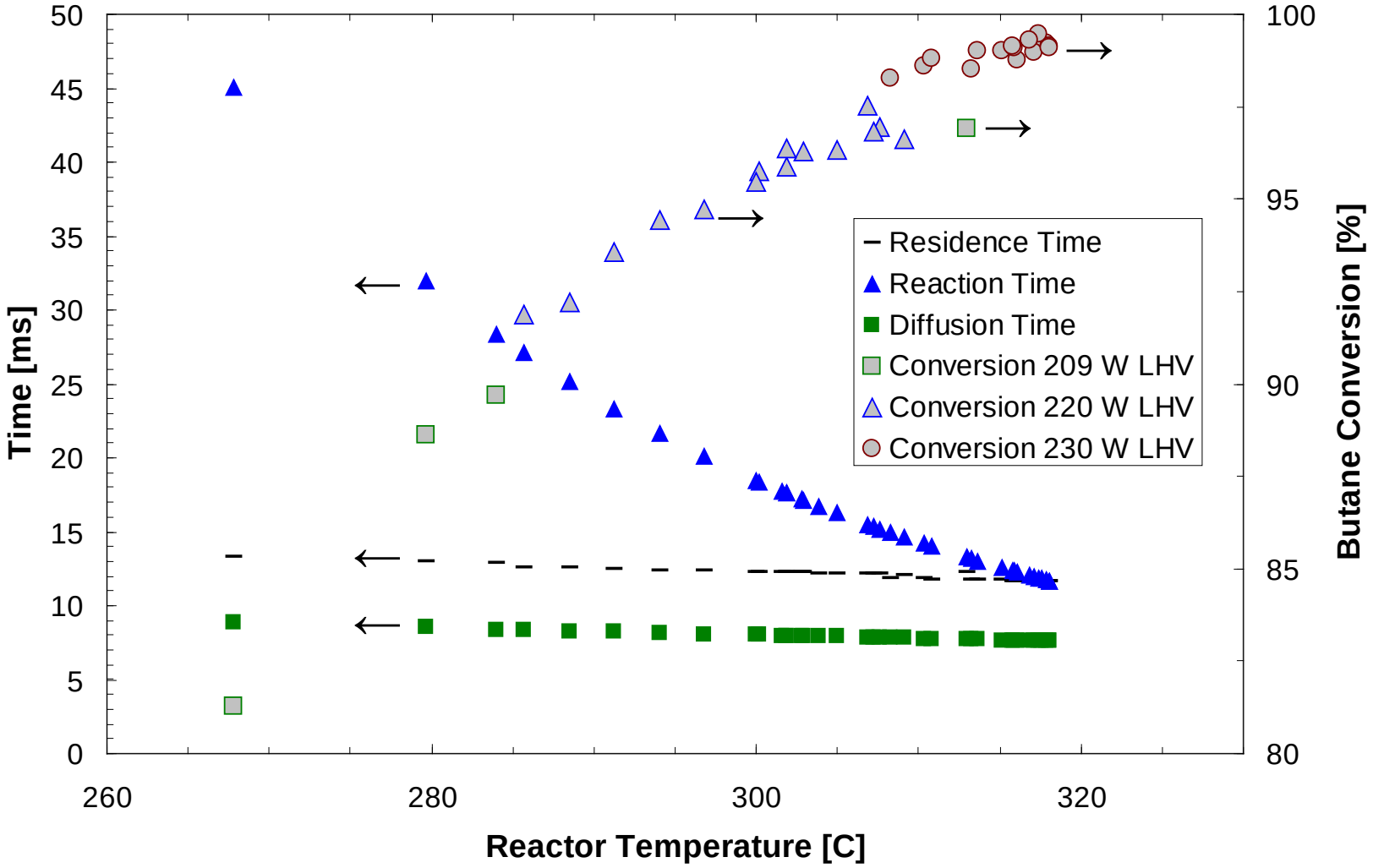

Figure 7-20: Comparison of characteristic timescales for residence, reaction, and diffusion compared with observed butane conversion at different reactor temperatures.

Given that the conversion of butane in the reactor was nearly complete for all experimental conditions with the highest butane flow rate, the total heat release in the reactor was constant at 230 W. Therefore, it was of interest to compare the system response to changing conditions with the heat transfer model described previously, in chapter 3, for these conditions. The reactor temperature for the highest butane flow rate is compared with the current through each TE module in Figure 7-21. There is a clear trend of decreasing reactor temperature with increasing current flow, as expected. The model equations are restated here as equations 28 to 32, where $(UA)_{loss}$ is the lumped heat loss term for conduction, convection and radiation, T is the reactor temperature, T_∞ is the ambient temperature, Q_i is the heat flux through pathway "i", H(T) is the enthalpy at temperature "T", N is the number of TE pairs in the two modules, A_e is the area of the TE elements, L_e is the length (thickness) of the TE elements, k_i is the thermal conductivity of TE material "i", T_H is the temperature on the hot-side of the TE, T_C is the temperature on the cold side of the TE, ρ_i is the electrical resistivity of TE material of type "i", I is the current, and α_i is the Seebeck coefficient of TE material of type "i". The temperature drop across the electrical insulation shim was assumed to be 18°C.

$$(UA)_{loss} = \frac{1}{(T - T_\infty)}\left(Q_{combustion} - Q_{enthalpy} - Q_{conduction} - Q_{Peltier} + Q_{Joule}\right) \quad \textbf{[40]}$$

$$Q_{enthalpy} = H_{exhaust}(T_H) - H_{exhaust}(T_C) \quad \textbf{[41]}$$

$$Q_{conduction} = \frac{N\,A_e\left(k_n + k_p\right)}{L_e}\left(T_H - T_C\right) \quad \textbf{[42]}$$

$$Q_{Peltier} = N\left(\alpha_p - \alpha_n\right)T_H\,I \quad \textbf{[43]}$$

$$Q_{Joule} = \frac{N\,L_e\left(\rho_p + \rho_n\right)}{A_e}I^2 \quad helpme \quad \textbf{[44]}$$

The properties of the TE materials were obtained from Hi-Z Technology[210] as polynomial functions of temperature, and were evaluated at the average temperature across the TE module. The polynomial functions are:

α_p = 10-3 x (-0.2559037+0.0023184 x T -3.181 E-6 x T^2 + 9.173E-10xT^3 -4.88E-13 x T^4) V/K

ρ_p = 10-3 x (-2.849603+0.01967684 x T -3.317 E-5 x T^2 + 3.4733E-8 x T^3 -1.9E-11 x T^4) Ohm-cm

k_p = 10-3 x (69.245746-0.5118914 x T+ 0.00199588 x T^2 -3.891 E-6 x T^3 + 3.0382E -9 x T^4) W/cm-K

α_n = 10-3 x ((0.07423215-0.0015018 x T + 2.9361E-6 x T^2 – 2.499E -9 X T^3 +1.361E-12 x T^4) V/K

ρ_n = 10-3 x (-1.95922+ 0.01791526 x T – 3.8181E-5 x T^2 + 4.9186E-8 X T^3 – 2.98E -11 x T^4) Ohm-cm

k_n = 10-3 x (14.25785 +0.06514882 x T- 0.0005162 x T^2 + 1.1246E- 6x T^3 -7.6 E – 10 x T^4) W/cm-K

Using this simple model, the lumped heat loss parameter was estimated at each experimental condition. The average estimated heat loss parameter for the system was 0.26 W/K, with a standard deviation of 1.7% of that value (0.0046 W/K). This is larger than the heat loss from the design system, which experienced 46 W heat loss at 376°C for an approximate value of 0.13 W/K. One likely contributing factor to the increased heat loss was the lack insulation over the inner surfaces of the gas manifolds (i.e., on the faces perpendicular parallel to the reactor compression seal), which had been insulated during the design experiments. These surfaces were exposed to ambient air, providing a significant area for convective heat loss. Another possible contributing factor to the increased heat loss was the significant air current observed to be passing the reactor from the fan used to cool the heat sinks, which could have increased the convective heat loss. It would certainly be possible to reduce these two sources of heat loss with improved packaging.

Based on this heat model, and the TE material properties provided by the manufacturer, the heat pathways in the system were assessed. For the conditions of maximum power production, 5.82 W of electrical power were generated at 2.53% efficiency with a parallel circuit connection. The enthalpy loss from the reactor, given the temperature of 316°C, was 38.4 W. The conductive heat loss through the TE modules was 99.8 W, while 2.2 W were transferred back to the reactor as a result of Joule heating in the TE modules. The Peltier heat transfer from the reactor, given the current of 1.56 A (distributed between the two modules), was 17.6 W. The heat released in the reactor was 230 W, which leaves 76.5 W of heat lost to the environment through conduction, convection and radiation. The estimated combustor efficiency (i.e., the fraction of heat released that was transferred to the TE modules) was 51%. It is important to note that these values are very sensitive

to the TE material property estimates, and as such should be taken as approximations. However, the above model would indicate conversion efficiency of 5% within the TE module, which is in good agreement with the manufacturer's claims.

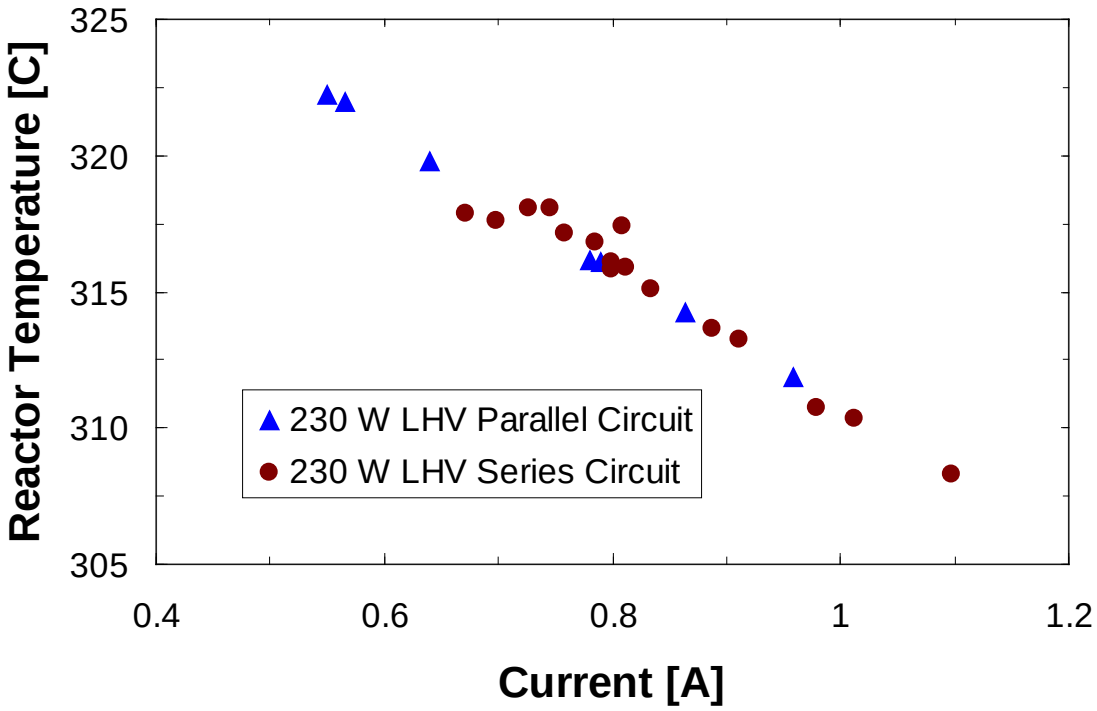

Figure 7-21: Reactor temperature variation for different current flow through the TE modules in series and in parallel circuit connection. Butane flow was 116 sccm (230 W LHV) with Φ = 0.91 for parallel circuit and Φ = 0.87 for series circuit.

7.4. System Testing Above Temperature Limits

A fresh combustor and a fresh pair of TE modules were used to test the performance of the system at temperatures above the recommended operating limits of the TE modules. The reactors were loaded with 215 and 202 mg of catalyst (for a total catalyst mass of 417 mg). The reactor was cracked during the loading process, likely due to a rough surface for compression sealing the manifolds as a result of an error during dicing. The leak was estimated to be ~8% of the inlet flow, and it also resulted in significant temperature inequality between the two reactors (~20 - 30°C). The TE modules were connected in a parallel circuit configuration.

The goal of these experiments was to assess the performance of the TE generator at temperatures above the stable operating range (which was assumed as ~300°C at the TE

module). During the initial system testing, 6.2 W of electrical power was generated in a cracked reactor prior to the integration of thermocouples between the combustor and the TE module. During the experiments to test the performance at elevated temperatures, thermocouples were included on the hot side to understand the elevated temperatures required to achieve the increased power production. The electrical power produced at the load as a function of the load voltage is given as Figure 7-22, and the conditions at the maximum (observed) power point are given in Table 7-3. In the figure, the power produced in the well-sealed combustor used in final system testing at the highest flow rate (corresponding with the upper limit on stable operating temperature) is shown for comparison. The chemical-to-electrical energy conversion efficiency in the cracked reactor is lower than that of the well-sealed reactor used in final system testing by 7 to 12%, which corresponds with the estimated reactor leak.

The maximum power produced was 7.37 W from a reactor temperature of 418°C, with an efficiency of 2.28%. Including the anticipated temperature drop across the alumina electrical insulating shim, this corresponded with the manufacturer's "intermittent limit" of 400°C for the TE module. The "intermittent limit" power production was 26.7% higher than that achieved near the stable operating temperature limit. It is important to note that the TE materials are not stable for long above 350°C because of appreciable oxidation. However, this demonstration shows the level of temporary increase in power production that could be accomplished if it was required, as well as the increased level of performance which could be achieved with TE materials capable of similar performance with expanded operating regions.

Table 7-3: Experimentally observed maximum power conditions above temperature limits. Reactor temperature refers to higher of two reactor surface temperatures.

Butane Flow [W LHV]	Φ	Maximum Power [W]	Efficiency [%]	Reactor Temp. at P_{MAX} [C]	Heat Sink Temp. at P_{MAX} [C]	Voltage at P_{MAX} [V]	Current at P_{MAX} [A]
230	0.91	5.11	2.22	313	53.6	3.46	1.48
292	0.92	6.88	2.35	391	62.5	4.22	1.63
313	0.95	7.22	2.31	409	64.5	4.01	1.80
323	0.96	7.37	2.28	418	65.6	4.03	1.83

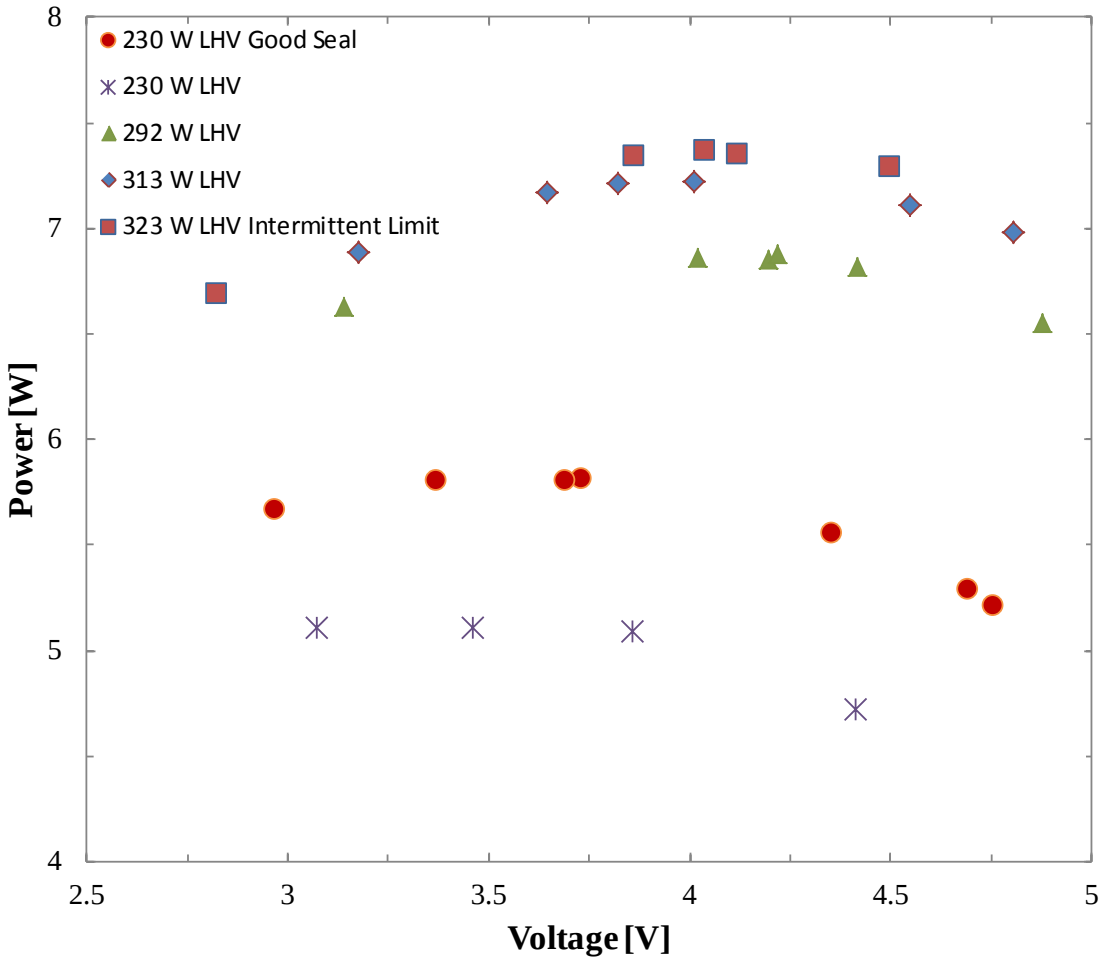

Figure 7-22: TE Power generated with a cracked reactor above the 300°C temperature limitation of the TE modules. TE modules connected in parallel. The red circles represent the best results from the well-sealed combustor below the temperature limits for comparison. All other curves generated from cracked reactor.

7.5. TE Power Generator Demonstration Limitations

There were several factors that limited the performance of the TE power generator in the demonstrations presented above. One such limitation was the temperature imbalance between the two reactors. One reactor was consistently hotter than the other, with a difference of approximately 8°C, as can be observed from the comparison of reactor temperatures for the case of 116 sccm butane flow with a series circuit configuration shown in Figure 7-23. Efforts to adjust the fuel distribution valves in order to eliminate this temperature difference were observed to reduce both reactor temperatures considerably. While it is possible that the thermocouple position was different between

the two sides, which would lead to an apparent temperature difference due to the axial thermal gradient, the open circuit voltage of the "colder" reactor was also observed to be lower than that of the "hotter" reactor, when measured with a digital multimeter, implying an actual temperature difference.

It is likely that the temperature difference was caused by some fraction of the channels in the "colder" reactor being blocked by the aluminum gasket. When the reactors used in these experiments were unloaded from the gas distribution manifolds, it was observed that one aluminum gasket had bent such that, at the inlet of the "colder" reactor, a few of the channels would have been at least partially obstructed. This can be observed in Figure 7-24. A very similar issue was observed for the aluminum gasket of a previously packaged reactor, so it is possible that the cause is related to the manifold itself or the packaging procedure. The impact of the gasket covering some channels is a reduction in the effective area of the reactor. It is quite possible that more butane was fed to the "hotter" reactor, which is supported by the observation that the reactor performed better with air flow greater than the stoichiometric equivalent (as the air was distributed evenly). Therefore, it is likely that, with improved packaging to prevent the aluminum gasket from obscuring any channels, the efficiency of the system and the power produced could be improved.

Another limitation of the present demonstration is the temperature limitation imposed by the TE material for stable operation. As demonstrated in chapter 6, the combustor is capable of processing greater flow rates of fuel than the 116 sccm demonstrated. As well, the TE generator is capable of generating power at temperatures above those explored in the final system demonstration. Indeed, the greatest amount of power produced from this system was 6.2 W, during the initial system testing. For that experiment, thermocouples had not yet been embedded between the reactor and TE modules, and so it was not clear that the temperature limitation had been exceeded during the experiment. However, it is clear that the temperature in the reactor must have been significantly higher than the 322°C maximum temperature exhibited in the final system experiments.

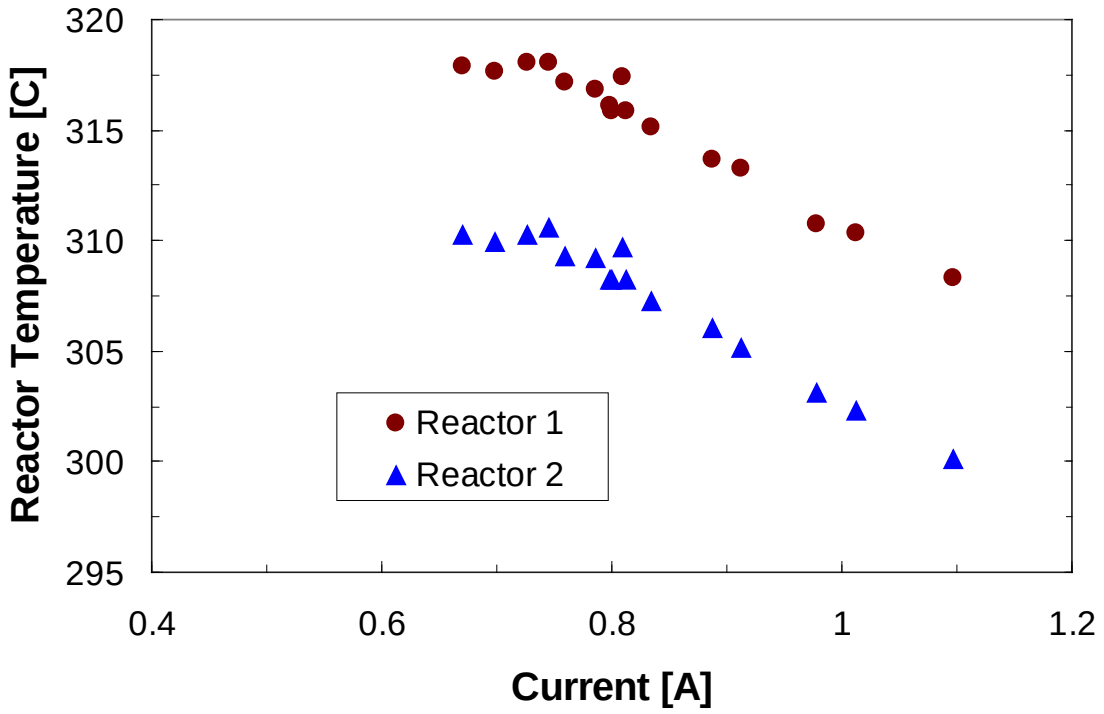

Figure 7-23: Comparison of reactor temperatures for experiments with series circuit configuration and 116 sccm (230 W LHV) butane flow.

Figure 7-24: Aluminum gasket after TE power generation experiments, which was observed to obstruct some of the channels. Bottom gap corresponds to inlet of "colder" reactor.

7.6. Concluding Remarks for Power Generation with Thermoelectric Modules

In this chapter, the performance of the integrated TE power generator has been described. The system achieved an order-of-magnitude increase in portable-scale TE power production from hydrocarbon fuel compared with the nearest competitor. The improved power was produced using the same commercial TE module, with similar system mass and an increase of at least 130% in the chemical-to-electrical energy conversion efficiency (from a fuel with greater heating value).

The catalytic combustion of butane in air has been used to produce as much as 5.82 W electrical power with 2.53% chemical-to-electrical conversion efficiency using commercially-available TE modules. The nearest comparison would be with work from the University of Delaware, where 0.65 W (transient) electrical power was produced at 1.1% efficiency from methanol and 0.44 W electrical power was produced at 0.5% efficiency from propane using the same TE module from Hi-Z Technology, Inc. And the pressure drop in the stainless steel sandwiched-gasket combustor, though not reported, is likely to be significantly larger than in the current work, so that a net-power-production comparison may show even more separation between the systems.

Based on the conversion efficiency, an energy density of 321 Wh/kg was demonstrated, which is greater than that of a lithium-ion battery. Given the mass of "essential" system components of 338 g and the 28 g mass of the commercial TE modules, the maximum power density was 17 W/kg, which is greater than that of non-hydrogen-based fuel cells. It is also important to consider the small resistance to flow through the reactor, and the device-ready heat sinks used in the demonstration. This system represents a significant advancement towards a viable air-breathing, hydrocarbon-fueled portable TE power generator which can surpass the performance of conventional batteries.

8. Concluding Remarks

8.1. Principal Accomplishments

The principal accomplishment from this thesis research was the model-assisted design of a mesoscale catalytic combustor that could facilitate thermoelectric power generation with a small parasitic power requirement for air pressurization. The designed system represents a significant advancement towards an air-breathing, hydrocarbon-fueled portable TE generator with high energy and power densities. Considerable design challenges associated with the use of ambient air as an oxidant were overcome, allowing for high gas flow rates without sacrificing fuel conversion, reactor pressure drop limitations, or thermal isolation. And the fabrication processes involved in the construction of the device are suitable to high-volume production with manageable costs. The demonstrated combustor performance motivates future efforts in the development of high-performance TE materials for portable generators.

Interfaced with heat sinks designed to mimic the behavior of high-performance (and high-heat-flux) TE modules, the autothermal catalytic-combustion of butane in air was used to provide a heat source of 206 to 362 W with conversion efficiency as high as 77%. The demonstrated performance of the combustor compared well with model predictions with respect to thermal efficiency, maximum temperature, axial temperature gradient, and system pressure drop. The pressure drop through the device was measured to be 258 Pa for 15 lpm of air at ambient conditions.

Interfaced with commercial TE modules and light-weight heat sinks, the catalytic combustion of butane in air has been used to produce as much as 5.82 W electrical power with 2.53% chemical-to-electrical conversion efficiency. Based on the conversion efficiency, an energy density of 321 Wh/kg was demonstrated, which is greater than that of a lithium-ion battery. And based on the mass of the system components the maximum power density was 17 W/kg, which is greater than that of non-hydrogen-based fuel cells.

8.2. Limitations and Challenges

8.2.1. Fabrication of Stacked Reactors by Multiple Silicon Wafer Bonds

The concept of a stacked-reactor design, described in chapter 3, was based on an underlying assumption of good thermal contact between the two reactors. One of the intended results of the stacked design was the transfer of heat from the hot inlet sections in one reactor to the cold outlet sections of the other reactor in order to reduce the surface-temperature gradient, which depends on cross-reactor conductive heat transfer. The intended fabrication process, involving the sequential de-protection of bonding faces to achieve a four-wafer fusion bonded stack, would guarantee good thermal contact between the reactors given their linkage by covalent bonds. The challenges faced with selective removal of silicon nitride from the bonding faces has been described in chapter 4, with the final result that reactors were fabricated from two bonded wafers and paired after dicing.

Several different approaches were considered and attempted to ensure good thermal contact between the reactors, including copper thermocompression bonding, adhesive bonding with a high-temperature polyimide layer, adhesive bonding with a thermally-conductive (silver-filled) ceramic paste, and even a thin layer of 5-minute epoxy. The major issues that had to be considered were the alignment of the two reactors during the bonding process (or, alternately, the ability of the adhesive to survive the dicing process and in particular the cooling water flow), the temperature limitations of the adhesive material, the stability of the adhesive material during high-temperature operation in proximity with silicon, the coefficient of thermal expansion of the adhesive material (compared with that of silicon), and the ability of the adhesive material to form a thin and homogeneous layer between the silicon reactors. A survey of available adhesives was conducted to obtain possible candidates; however, the operating temperature of the combustor was relatively high for epoxies and similarly compliant and easily applied adhesives, while the desired layer properties were not well suited to ceramic adhesives. Additionally, a challenge was faced to align and bond reactors without the adhesive interfering with the smoothness of the faces to which the gas distribution manifolds were attached.

None of the bonding techniques identified were implemented successfully with a combustor that could be compression-sealed to the gas manifolds and operated at high temperature (~400°C). Only the 5-minute epoxy was used to bond reactors with alignment sufficient for compression-sealing of fluidic connections; however, when heated to 400°C the 5-minute epoxy was not stable, and either combusted or melted and flowed out of the gap between reactors. The removal of the epoxy likely left an air gap between the reactors, which would certainly not have provided good thermal contact. The final packaging procedure used in this work involved light force to hold the two reactors together (either by hand or with Kapton tape) while the manifolds were connected. While no noticeable gaps were observed between the reactors, it is possible that the thermal contact between the reactors could be improved. An improvement in this aspect of the packaging would likely result in decreased axial temperature gradients, which would improve the performance of the combustor as a TE generator.

8.2.2. Reactor Fracture During or After Packaging

Significant difficulties were faced with the fracturing of reactors, both during the integration of the reactor with the fluidic connections and heat sinks (or TE modules) and after successful integration as a result of force applied to the fluidic connections. The fracture of reactors during packaging was a result of the design of the system, which necessitated two (thermally) separated systems to be compressed onto the silicon reactor from two directions. Once one of the two systems was connected to the reactor (i.e., the fluidic connections or the heat sinks / TE modules), the mechanical connections of that system to the rest of the experimental set-up also restricted, if not fixed, the "global" position and orientation of the reactors. Therefore, the alignment and compliance of the two systems were crucial to successful integration, as any stress resulting from misalignment was borne by the silicon reactor. The issue was complicated by the need to have thermal isolation between the hot fluidic connections near the reactor and the cold heat sinks for thermal isolation of the reactor. The change to flexible metal tubes, described in chapter 5, facilitated successful packaging of the system.

Reactor fracturing was also a problem after packaging, in the event that there was significant movement in the external piping system. It would be desirable, in a

redesigned system, to have the fluidic connections and the TE modules and heat sinks rigidly fixed to one another to avoid any stress on the silicon. This would have to be implemented with some integrated insulation (or other thermal barrier) to prevent parasitic heat transfer between the hot tubes and the cold side of the TE system, as that would increase the cooling load on the system. A rigid configuration would be essential for a portable device.

8.3. Recommendations for Improved System Performance

8.3.1. Integrated Enthalpy Recovery

As detailed in the system models in chapter 3 and again in chapter 6, the portion of the combustion heat which is lost from the system in the enthalpy of the hot exhaust gas is considerable (~16% of fuel LHV). The most common method of making use of this heat is to warm the inlet gas stream while cooling the exhaust stream. Such a recuperator system requires for the hot exhaust and the cold inlet gases to be brought into thermal contact with sufficient area for heat transfer as well as a suitable length such that a temperature gradient can exist in the system. The effectiveness of a recuperator should be evaluated based on the net impact on the system energy balance, with consideration also given to added system mass and volume (i.e., net power density impact), pressure requirements (i.e., impact on "net" power), and the overall viability of the system design (i.e., impact on fragility, production cost, packaging, etc.). One of the key characteristics for a recuperator is that the heat loss to the environment from the added surface should be less than that from directly discharging the exhaust.

There has been discussion of "on-chip" recuperation, where the recuperator is integrated into the silicon device. However, the high thermal conductivity of silicon can be a hindrance in this aspect, as an "on-chip" recuperator would require thermally isolated regions of the device, with each section likely serving as a "transfer unit". For example, the microcombustor developed by Arana, et al., used silicon slabs connecting insulating silicon nitride tubes as an integrated recuperator[76]. Aside from the use of low-conductivity capillary tubing, two demonstrated ways to introduce thermal isolation zones in silicon reactors are "halo-etches"[155] (where a significant amount of material is

removed and an air gap provides the isolation) or "refilled trenches", where an etched region of silicon is refilled with a low-conductivity material such as silicon oxide[211] or parylene-C[156]. The advantage of the halo-etch is that the thermal conductivity of air is very low, while the refilled trench provides significantly more mechanical stability.

An example concept for a combustor with an on-chip recuperator is shown in Figure 8-1. In this example, the isolation zones are used to separate three thermal equilibration regions, which would be characterized as having temperatures T_1, T_2, and T_3 as labeled in the figure, with $T_c > T_3 > T_2 > T_1$. While the equilibration regions wouldn't necessarily be isothermal, given the relatively large thermal conductivity of silicon the assumption is sufficient for the description here. The effectiveness of the recuperator is related to the heat conducted by the remaining silicon bridge, which depends on the area for conduction (the width "H" in the figure multiplied by the thickness of the silicon, minus the channel area) and the length of the isolation region (shown as "L"). However, the pressure drop in the device (and, in the case of a halo-etched device, the fragility) increases as H is reduced and L is increased, so a model-based design would be of use to identify the optimal structure. In order to limit the convective heat loss from the recuperator, a layer of insulation would likely be required. The heat loss through the fluidic connections would almost certainly be reduced, however, because the temperature of the device at the inlets and outlets would necessarily have to be reduced significantly. The decreased temperature at the fluidic connections would also greatly simplify the packaging, as low temperature sealants and high-CTE materials could be used. The example design would require selective catalyst layer deposition to avoid combustion in the preheating zones, as well as an integrated gas distribution manifold.

Another possibility for improved thermal efficiency, and one that could be integrated quite easily with the current design, is to use an external recuperator. One example concept that was considered in this work is to use steel tubes within which the inlet and outlet streams would be separated by a thin steel wall, with insulation on the outside to reduce heat loss. A schematic of this example external recuperator is shown in Figure 8-2. The shape and size of the tubes could be optimized with some simple heat transfer

modeling and a pressure drop calculation, possibly including some static mixing to reduce the required length. Depending on the design of the remaining system, such a recuperator could be incorporated with little or no additional system mass or pressure drop, and with no decrease in the mechanical robustness of the system.

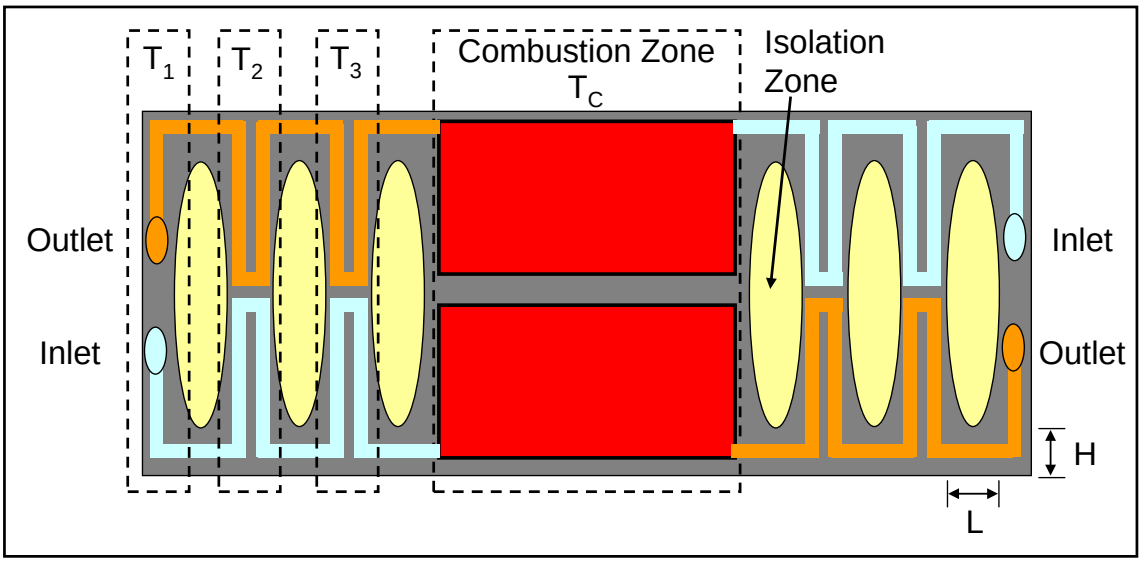

Figure 8-1: Schematic of an on-chip recuperator design, shown here with three isolation zones. Red boxes indicate the combustion zones, blue rectangles represent the inlet gas channels, and orange rectangles represent the exhaust channels.

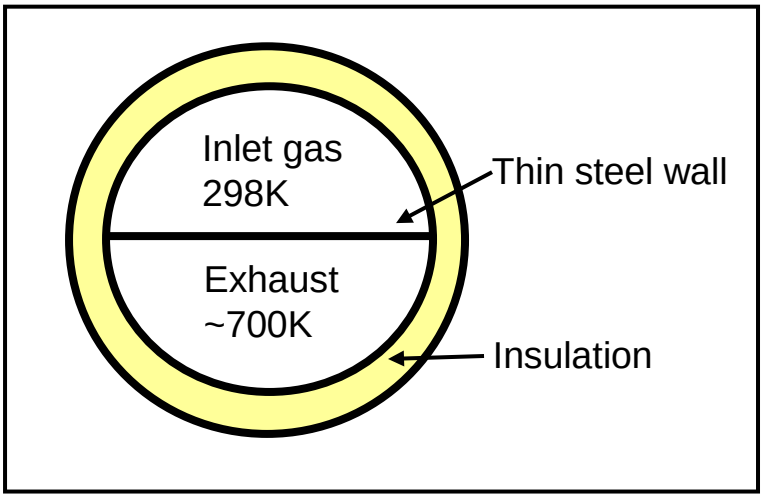

Figure 8-2: Schematic of a half-cylinder tube enthalpy recuperator.

8.3.2. Improved Gas Distribution Manifolds

The mass of the current system was dominated by the gas distribution manifolds and by the air-cooled heat sinks. And the heat loss from the manifolds was a significant fraction of the overall heat generated. The reduction of the mass of the manifolds seems to be the easiest way to improve the power density of the current device. As mentioned previously,

the mass could be reduced by reduced tolerances in the current direct metal laser sintering process, or also through post-process machining where material could be removed. The distributor mass could also be reduced through the use of an "on-chip" distributor, as the added silicon mass is likely to be a small fraction of that of the current metal distributors. However, the challenge with an on-chip distributor is that the characteristic length scale for pressure drop is likely to be on the order of 1-mm, so it would require a significant design effort to produce an "optimal" manifold. It is possible to use multiple fusion bonded wafers to create a silicon manifold with larger dimensions, but the added processing complexity may limit the suitability of this design. The optimization of the manifold design would balance the reduced system mass, the increased system pressure drop, and the changes to the heat loss pathways in order to improve the power density and the energy density (for fixed mission duration) of the system.

Another option for improved gas distribution manifolds would be to investigate the use of a ceramic structure similar to the current metal design, which would have the advantages of reduced density and thermal conductivity relative to stainless steel. The reduction in the thermal conductivity would result in reduced heat loss to the environment (as there would be a larger temperature drop across the manifold for an equivalent heat flux), similar to the low-conductivity tubes used by Arana[110], Nielsen[109], and Blackwell[52]. The combination of reduced system heat loss and reduced system mass could make a significant improvement in the energy and power densities, provided that the materials integration issues between the ceramic, the silicon, and the steel tubes could be solved.

8.3.3. Increased Heat Flux Through TE Modules

The difference in the effective thermal resistance of the commercial TE modules compared with the estimate for the design TE modules was significant. Given that the heat loss from the system scales with the system temperature (though the enthalpy loss also scales with the gas flow rate), the thermal efficiency of the combustor would be improved as the relative resistance in the "active" pathway of heat flux through the TE modules is decreased. This trend was observed between the design testing experiments, where the combustor was ~77% efficient, and the TE power generation experiments, where the combustor was ~50% efficient. Clearly, the design of improved TE modules

would increase the power generation from the current device. It may also be possible to decrease the effective heat transfer resistance at the combustor surface with an increase in the TE module area, possibly with the use of a thermal spreader; however, the increased surface area for heat loss to the environment may limit the effectiveness of such a design.

8.3.4. Selective Catalyst Layer Deposition for Reduced Thermal Gradients

The issue of axial thermal gradients in this device was addressed through the use of parallel channels, thermally conductive materials, and a counter-current reactor arrangement. However, the catalyst washcoating technique which was developed was observed to create axial gradients in the deposited catalyst layer thickness. While not explored in this work, it may be possible to localize the catalyst layers in alternating channels at different axial positions. The "hot spot" within each channel would then be distributed at different axial positions across the surface of the reactor, and when combined with the thermally conductive silicon this may result in a smooth surface temperature distribution. The gradient in catalyst layer deposition, as well as its dependence on the slurry, surface and process parameters, could be investigated experimentally by ESEM measurements of the catalyst layer at different axial positions. A model-based design procedure could be used to localize the "hot spots" such that the surface temperature gradient was reduced below some target value.

9. References

1. Blomgren, G. E. In *Perspectives on portable lithium ion batteries liquid and polymer electrolyte types*, The Seventeenth Annual Battery Conference on Applications and Advances, 2002.
2. Release: China Laptop Industry Report. *Research and Markets* 2006.
3. Release. *Semiconductor Industry Association* 2006.
4. Hassoun, J.; Panero, S.; Reale, P.; Scrosati, B., A New, Safe, High-Rate and High-Energy Polymer Lithium-Ion Battery. *Advanced Materials* **2009,** *21* (47), 4807-4810.
5. Mitsos, A.; Chachuat, B.; Barton, P. I., What is the design objective for portable power generation: Efficiency or energy density? *Journal of Power Sources* **2007,** *164* (2), 678-687.
6. Cowey, K.; Green, K. J.; Mepsted, G. O.; Reeve, R., Portable and military fuel cells. *Current Opinion in Solid State and Materials Science* **2004,** *8* (5), 367-371.
7. Baxter, J.; Bian, Z.; Chen, G.; Danielson, D.; Dresselhaus, M. S.; Fedorov, A. G.; Fisher, T. S.; Jones, C. W.; Maginn, E.; Kortshagen, U.; Manthiram, A.; Nozik, A.; Rolison, D. R.; Sands, T.; Shi, L.; Sholl, D.; Wu, Y., Nanoscale design to enable the revolution in renewable energy. *Energy & Environmental Science* **2009,** *2* (6), 559-588.
8. Palo, D. R.; Holladay, J. D.; Rozmiarek, R. T.; Guzman-Leong, C. E.; Wang, Y.; Hu, J.; Chin, Y.-H.; Dagle, R. A.; Baker, E. G., Development of a soldier-portable fuel cell power system: Part I: A bread-board methanol fuel processor. *Journal of Power Sources* **2002,** *108* (1-2), 28-34.
9. Kundu, A.; Jang, J. H.; Gil, J. H.; Jung, C. R.; Lee, H. R.; Kim, S. H.; Ku, B.; Oh, Y. S., Micro-fuel cells--Current development and applications. *Journal of Power Sources* **2007,** *170* (1), 67-78.
10. Holladay, J. D.; Jones, E. O.; Phelps, M.; Hu, J., Microfuel processor for use in a miniature power supply. *Journal of Power Sources* **2002,** *108* (1-2), 21-27.
11. Choi, D.; Wang, D.; Viswanathan, V. V.; Bae, I.-T.; Wang, W.; Nie, Z.; Zhang, J.-G.; Graff, G. L.; Liu, J.; Yang, Z.; Duong, T., Li-ion batteries from LiFePO4 cathode and anatase/graphene composite anode for stationary energy storage. *Electrochemistry Communications* **2010,** *12* (3), 378-381.
12. Linden, D.; Reddy, T. B., *Handbook of batteries*. 3rd ed.; McGraw-Hill: New York, 2002.
13. Atwater, T. B.; Cygan, P. J.; Leung, F. C., Man portable power needs of the 21st century: I. Applications for the dismounted soldier. II. Enhanced capabilities through the use of hybrid power sources. *Journal of Power Sources* **2000,** *91* (1), 27-36.
14. Mitsos, A.; Hencke, M. M.; Barton, P. I., Product engineering for man-portable power generation based on fuel cells. *AIChE Journal* **2005,** *51* (8), 2199-2219.
15. Yunt, M.; Chachuat, B.; Mitsos, A.; Barton, P. I., Designing man-portable power generation systems for varying power demand. *AIChE Journal* **2008,** *54* (5), 1254-1269.

16. Mitsos, A.; Palou-Rivera, I.; Barton, P. I., Alternatives for Micropower Generation Processes. *Industrial & Engineering Chemistry Research* **2004,** *43* (1), 74-84.
17. Takashi, O.; Gwang-Goo, L.; Yuji, S.; Nobuhide, K.; Shin, M., Development of a micro catalytic combustor using high-precision ceramic tape casting. *Journal of Micromechanics and Microengineering* **2006,** *16* (9), S198.
18. Cohen, A. L.; Ronney, P. D.; Frodis, U.; Sitzki, L.; Meiburg, E. H.; Wussow, S. Microcombustor and combustion-based thermoelectric microgenerator. US Patent Number 6951456, 2005.
19. Ju, Y.; Xu, B., Theoretical and experimental studies on mesoscale flame propagation and extinction. *Proceedings of the Combustion Institute* **2005,** *30* (2), 2445-2453.
20. Kaisare, N. S.; Vlachos, D. G., Optimal reactor dimensions for homogeneous combustion in small channels. *Catalysis Today* **2007,** *120* (1), 96-106.
21. Prakash, S.; Armijo, A. D.; Masel, R. I.; Shannon, M. A., Flame dynamics and structure within sub-millimeter combustors. *AIChE Journal* **2007,** *53* (6), 1568-1577.
22. Miesse, C. M.; Masel, R. I.; Jensen, C. D.; Shannon, M. A.; Short, M., Submillimeter-scale combustion. *AIChE Journal* **2004,** *50* (12), 3206-3214.
23. Miesse, C.; Masel, R. I.; Short, M.; Shannon, M. A., Diffusion flame instabilities in a 0.75 mm non-premixed microburner. *Proceedings of the Combustion Institute* **2005,** *30* (2), 2499-2507.
24. Jiang, L. Q.; Zhao, D. Q.; Wang, X. H.; Yang, W. B., Development of a self-thermal insulation miniature combustor. *Energy Conversion and Management* **2009,** *50* (5), 1308-1313.
25. Zhou, J.; Wang, Y.; Yang, W.; Liu, J.; Wang, Z.; Cen, K., Combustion of hydrogen-air in catalytic micro-combustors made of different material. *International Journal of Hydrogen Energy* **2009,** *34* (8), 3535-3545.
26. Karagiannidis, S.; Mantzaras, J.; Jackson, G.; Boulouchos, K., Hetero-/homogeneous combustion and stability maps in methane-fueled catalytic microreactors. *Proceedings of the Combustion Institute* **2007,** *31* (2), 3309-3317.
27. Norton, D. G.; Vlachos, D. G., Hydrogen assisted self-ignition of propane/air mixtures in catalytic microburners. *Proceedings of the Combustion Institute* **2005,** *30* (2), 2473-2480.
28. Maruta, K.; Takeda, K.; Ahn, J.; Borer, K.; Sitzki, L.; Ronney, P. D.; Deutschmann, O., Extinction limits of catalytic combustion in microchannels. *Proceedings of the Combustion Institute* **2002,** *29* (1), 957-963.
29. Wood, C., Materials for thermoelectric energy conversion. *Reports on Progress in Physics* **1988,** *51* (4), 459.
30. Federici, J. A.; Norton, D. G.; Brüggemann, T.; Voit, K. W.; Wetzel, E. D.; Vlachos, D. G., Catalytic microcombustors with integrated thermoelectric elements for portable power production. *Journal of Power Sources* **2006,** *161* (2), 1469-1478.
31. Stefanidis, G. D.; Vlachos, D. G., Controlling Homogeneous Chemistry in Homogeneousâˆ'Heterogeneous Reactors: Application to Propane Combustion. *Industrial & Engineering Chemistry Research* **2009,** *48* (13), 5962-5968.

32. Rowe, D. M., *CRC handbook of thermoelectrics*. CRC Press: Boca Raton, FL, 1995.
33. Venkatasubramanian, R.; Siivola, E.; Colpitts, T.; O'Quinn, B., Thin-film thermoelectric devices with high room-temperature figures of merit. *Nature* **2001,** *413* (6856), 597-602.
34. Kajikawa, T., Approach to the Practical Use of Thermoelectric Power Generation. *Journal of Electronic Materials* **2009,** *38* (7), 1083-1088.
35. Hicks, L. D.; Dresselhaus, M. S., Effect of quantum-well structures on the thermoelectric figure of merit. *Physical Review B* **1993,** *47* (19), 12727.
36. Harman, T. C.; Taylor, P. J.; Walsh, M. P.; LaForge, B. E., Quantum Dot Superlattice Thermoelectric Materials and Devices. *Science* **2002,** *297* (5590), 2229-2232.
37. Vineis, C. J.; Harman, T. C.; Calawa, S. D.; Walsh, M. P.; Reeder, R. E.; Singh, R.; Shakouri, A., Carrier concentration and temperature dependence of the electronic transport properties of epitaxial PbTe and PbTe/PbSe nanodot superlattices. *Physical Review B* **2008,** *77* (23), 235202.
38. Pichanusakorn, P.; Bandaru, P., Nanostructured thermoelectrics. *Materials Science and Engineering: R: Reports* **2009,** *67* (2-4), 19-63.
39. Koh, Y. K.; Vineis, C. J.; Calawa, S. D.; Walsh, M. P.; Cahill, D. G., Lattice thermal conductivity of nanostructured thermoelectric materials based on PbTe. *Applied Physics Letters* **2009,** *94* (15), 153101-3.
40. Ahn, K.; Li, C.; Uher, C.; Kanatzidis, M. G., Improvement in the Thermoelectric Figure of Merit by La/Ag Cosubstitution in PbTe. *Chemistry of Materials* **2009,** *21* (7), 1361-1367.
41. Yoshida, K.; Tanaka, S.; Tomonari, S.; Satoh, D.; Esashi, M., High-energy density miniature thermoelectric generator using catalytic combustion. *Microelectromechanical Systems, Journal of* **2006,** *15* (1), 195-203.
42. Norton, D. G.; Wetzel, E. D.; Vlachos, D. G., Thermal Management in Catalytic Microreactors. *Industrial & Engineering Chemistry Research* **2005,** *45* (1), 76-84.
43. Norton, D. G.; Voit, K. W.; Brüggemann, T.; Vlachos, D. G., Portable power generation via integrated catalytic microcombustion-thermoelectric devices. In *24th Army Science Conference*, Orlando, FL, 2004.
44. Karim, A. M.; Federici, J. A.; Vlachos, D. G., Portable power production from methanol in an integrated thermoeletric/microreactor system. *Journal of Power Sources* **2008,** *179* (1), 113-120.
45. O'Sullivan, F.; Celanovic, I.; Jovanovic, N.; Kassakian, J.; Akiyama, S.; Wada, K., Optical characteristics of one-dimensional Si/SiO[sub 2] photonic crystals for thermophotovoltaic applications. *Journal of Applied Physics* **2005,** *97* (3), 033529-7.
46. Bermel, P.; Ghebrebrhan, M.; Chan, W.; Yeng, Y. X.; Araghchini, M.; Hamam, R.; Marton, C. H.; Jensen, K. F.; Soljačić, M.; Joannopoulos, J. D.; Johnson, S. G.; Celanovic, I., Design and global optimization of high-efficiency thermophotovoltaic systems. *Opt. Express* **2010,** *18* (S3), A314-A334.

47. Nielsen, O. M.; Arana, L. R.; Baertsch, C. D.; Jensen, K. F.; Schmidt, M. A. In *A thermophotovoltaic micro-generator for portable power applications*, TRANSDUCERS, Solid-State Sensors, Actuators and Microsystems, 12th International Conference on, 2003; pp 714-717.
48. Yang, W.; et al., Research on micro-thermophotovoltaic power generators with different emitting materials. *Journal of Micromechanics and Microengineering* **2005,** *15* (9), S239.
49. Yang, W. M.; Chou, S. K.; Shu, C.; Xue, H.; Li, Z. W.; Li, D. T.; Pan, J. F., Microscale combustion research for application to micro thermophotovoltaic systems. *Energy Conversion and Management* **2003,** *44* (16), 2625-2634.
50. Xue, H.; Yang, W.; Chou, S. K.; Shu, C.; Li, Z., MICROTHERMOPHOTOVOLTAICS POWER SYSTEM FOR PORTABLE MEMS DEVICES. *Microscale Thermophysical Engineering* **2005,** *9* (1), 85 - 97.
51. Chia, L. C.; Feng, B., The development of a micropower (micro-thermophotovoltaic) device. *Journal of Power Sources* **2007,** *165* (1), 455-480.
52. Blackwell, B. S.; Massachusetts Institute of Technology. Dept. of Chemical Engineering. Design, fabrication, and characterization of a micro fuel processor. Thesis Ph. D. --Massachusetts Institute of Technology Dept. of Chemical Engineering February 2008.
53. Mitsos, A.; Barton, P. I., *Microfabricated power generation devices : design and technology*. Wiley-VCH: Weinheim, 2009.
54. Jacobson, S. A.; Epstein, A. H., AN INFORMAL SURVEY OF POWER MEMS. In *The International Symposium on Micro-Mechanical Engineering*, 2003.
55. Fernandez-Pello, A. C., Micropower generation using combustion: Issues and approaches. *Proceedings of the Combustion Institute* **2002,** *29* (1), 883-899.
56. Mehra, A.; Xin, Z.; Ayon, A. A.; Waitz, I. A.; Schmidt, M. A.; Spadaccini, C. M., A six-wafer combustion system for a silicon micro gas turbine engine. *Microelectromechanical Systems, Journal of* **2000,** *9* (4), 517-527.
57. Cho, J.-H.; Lin, C. S.; Richards, C. D.; Richards, R. F.; Ahn, J.; Ronney, P. D., Demonstration of an external combustion micro-heat engine. *Proceedings of the Combustion Institute* **2009,** *32* (2), 3099-3105.
58. Cho, J. H.; et al., Power production by a dynamic micro heat engine with an integrated thermal switch. *Journal of Micromechanics and Microengineering* **2007,** *17* (9), S217.
59. Whalen, S.; Thompson, M.; Bahr, D.; Richards, C.; Richards, R., Design, fabrication and testing of the P3 micro heat engine. *Sensors and Actuators A: Physical* **2003,** *104* (3), 290-298.
60. Spadaccini, C. M.; Zhang, X.; Cadou, C. P.; Miki, N.; Waitz, I. A., Preliminary development of a hydrocarbon-fueled catalytic micro-combustor. *Sensors and Actuators A: Physical* **2003,** *103* (1-2), 219-224.
61. Kamarudin, S. K.; Achmad, F.; Daud, W. R. W., Overview on the application of direct methanol fuel cell (DMFC) for portable electronic devices. *International Journal of Hydrogen Energy* **2009,** *34* (16), 6902-6916.
62. Evans, A.; Bieberle-Hütter, A.; Rupp, J. L. M.; Gauckler, L. J., Review on microfabricated micro-solid oxide fuel cell membranes. *Journal of Power Sources* **2009,** *194* (1), 119-129.

63. NTT prototype micro PEM for cell phones. *Fuel Cells Bulletin* **2005,** *2005* (4), 6.
64. Holladay, J. D.; Wang, Y.; Jones, E., Review of Developments in Portable Hydrogen Production Using Microreactor Technology. *Chemical Reviews* **2004,** *104* (10), 4767-4790.
65. Cheng, X.; Shi, Z.; Glass, N.; Zhang, L.; Zhang, J.; Song, D.; Liu, Z.-S.; Wang, H.; Shen, J., A review of PEM hydrogen fuel cell contamination: Impacts, mechanisms, and mitigation. *Journal of Power Sources* **2007,** *165* (2), 739-756.
66. Shah, K.; Ouyang, X.; Besser, R. S., Microreaction for Microfuel Processing: Challenges and Prospects. *Chemical Engineering & Technology* **2005,** *28* (3), 303-313.
67. Xuan, J.; Leung, M. K. H.; Leung, D. Y. C.; Ni, M., A review of biomass-derived fuel processors for fuel cell systems. *Renewable and Sustainable Energy Reviews* **2009,** *13* (6-7), 1301-1313.
68. Itoh, N.; Kaneko, Y.; Igarashi, A., Efficient Hydrogen Production via Methanol Steam Reforming by Preventing Back-permeation of Hydrogen in a Palladium Membrane Reactor. *Industrial & Engineering Chemistry Research* **2002,** *41* (19), 4702-4706.
69. Wilhite, B.; Weiss, S.; Ying, J.; Schmidt, M.; Jensen, K., High-Purity Hydrogen Generation in a Microfabricated 23 wt % Ag–Pd Membrane Device Integrated with 8:1 LaNi0.95Co0.05O3/Al2O3 Catalyst. *Advanced Materials* **2006,** *18* (13), 1701-1704.
70. Mu, X.; Pan, L.; Liu, N.; Zhang, C.; Li, S.; Sun, G.; Wang, S., Autothermal reforming of methanol in a mini-reactor for a miniature fuel cell. *International Journal of Hydrogen Energy* **2007,** *32* (15), 3327-3334.
71. Moreno, A. M.; Wilhite, B. A., Autothermal hydrogen generation from methanol in a ceramic microchannel network. *Journal of Power Sources* **2010,** *195* (7), 1964-1970.
72. Kwon, O. J.; Yoon, D. H.; Kim, J. J., Silicon-based miniaturized reformer with methanol catalytic burner. *Chemical Engineering Journal* **2008,** *140* (1-3), 466-472.
73. Kuei-Sung, C.; et al., A micro-fuel processor with trench-refilled thick silicon dioxide for thermal isolation fabricated by water-immersion contact photolithography. *Journal of Micromechanics and Microengineering* **2005,** *15* (9), S171.
74. Chen, Y.; Wang, Y.; Xu, H.; Xiong, G., Integrated One-Step PEMFC-Grade Hydrogen Production From Liquid Hydrocarbons Using Pd Membrane Reactor. *Industrial & Engineering Chemistry Research* **2007,** *46* (17), 5510-5515.
75. Casanovas, A.; Saint-Gerons, M.; Griffon, F.; Llorca, J., Autothermal generation of hydrogen from ethanol in a microreactor. *International Journal of Hydrogen Energy* **2008,** *33* (7), 1827-1833.
76. Arana, L. R.; Schaevitz, S. B.; Franz, A. J.; Schmidt, M. A.; Jensen, K. F., A microfabricated suspended-tube chemical reactor for thermally efficient fuel processing. *Microelectromechanical Systems, Journal of* **2003,** *12* (5), 600-612.

77. Moreno, A. M.; Damodharan, S.; Wilhite, B., Influence of Two-Dimensional Distribution Schemes upon Reactor Performance in a Ceramic Microchannel Network for Autothermal Methanol Reforming. *Industrial & Engineering Chemistry Research* **2010,** *Accepted for Publication*.
78. Kim, T.; Kwon, S., MEMS fuel cell system integrated with a methanol reformer for a portable power source. *Sensors and Actuators A: Physical* **2009,** *154* (2), 204-211.
79. Kamarudin, S. K.; Daud, W. R. W.; Ho, S. L.; Hasran, U. A., Overview on the challenges and developments of micro-direct methanol fuel cells (DMFC). *Journal of Power Sources* **2007,** *163* (2), 743-754.
80. Zhu, Y.; Khan, Z.; Masel, R. I., The behavior of palladium catalysts in direct formic acid fuel cells. *Journal of Power Sources* **2005,** *139* (1-2), 15-20.
81. Kim, H. S.; Morgan, R. D.; Gurau, B.; Masel, R. I., A miniature direct formic acid fuel cell battery. *Journal of Power Sources* **2009,** *188* (1), 118-121.
82. Jayashree, R. S.; Yoon, S. K.; Brushett, F. R.; Lopez-Montesinos, P. O.; Natarajan, D.; Markoski, L. J.; Kenis, P. J. A., On the performance of membraneless laminar flow-based fuel cells. *Journal of Power Sources* **2009,** *195* (11), 3569-3578.
83. Miesse, C. M.; Jung, W. S.; Jeong, K.-J.; Lee, J. K.; Lee, J.; Han, J.; Yoon, S. P.; Nam, S. W.; Lim, T.-H.; Hong, S.-A., Direct formic acid fuel cell portable power system for the operation of a laptop computer. *Journal of Power Sources* **2006,** *162* (1), 532-540.
84. Huang, H.; Nakamura, M.; Su, P.; Fasching, R.; Saito, Y.; Prinz, F. B., High-Performance Ultrathin Solid Oxide Fuel Cells for Low-Temperature Operation. *Journal of The Electrochemical Society* **2007,** *154* (1), B20-B24.
85. Bieberle-Hütter, A.; Beckel, D.; Infortuna, A.; Muecke, U. P.; Rupp, J. L. M.; Gauckler, L. J.; Rey-Mermet, S.; Muralt, P.; Bieri, N. R.; Hotz, N.; Stutz, M. J.; Poulikakos, D.; Heeb, P.; Müller, P.; Bernard, A.; Gmür, R.; Hocker, T., A micro-solid oxide fuel cell system as battery replacement. *Journal of Power Sources* **2008,** *177* (1), 123-130.
86. Shao, Z.; Haile, S. M.; Ahn, J.; Ronney, P. D.; Zhan, Z.; Barnett, S. A., A thermally self-sustained micro solid-oxide fuel-cell stack with high power density. *Nature* **2005,** *435* (7043), 795-798.
87. Glassbrenner, C. J.; Slack, G. A., Thermal Conductivity of Silicon and Germanium from 3^{o}K to the Melting Point. *Physical Review* **1964,** *134* (4A), A1058.
88. Landolt-Börnstein Numerical data and functional relationships in science and technology. Group III: Condensed Matter. http://www.springerlink.com/content/1619-4810.
89. Satoh, D.; Tanaka, S.; Yoshida, K.; Esashi, M., Micro-ejector to supply fuel-air mixture to a micro-combustor. *Sensors and Actuators A: Physical* **2005,** *119* (2), 528-536.
90. Gardner, W. G.; Jaworski, J. W.; Camacho, A. P.; Protz, J. M., Experimental results for a microscale ethanol vapor jet ejector. *Journal of Micromechanics and Microengineering* **2010,** *20* (4), 045019.
91. Felder, R. M.; Rousseau, R. W., *Elementary principles of chemical processes*. 3rd ed.; John Wiley: New York, 1999.

92. Hu, J.; Wang, Y.; VanderWiel, D.; Chin, C.; Palo, D.; Rozmiarek, R.; Dagle, R.; Cao, J.; Holladay, J.; Baker, E., Fuel processing for portable power applications. *Chemical Engineering Journal* **2003,** *93* (1), 55-60.
93. Jin, J.; Kwon, S., Microcatalytic Combustion of H2 on Pt/Al2O3-Coated Nickel Foam. *Combustion Science and Technology* **2009,** *181*, 211-225.
94. Salge, J. R.; Deluga, G. A.; Schmidt, L. D., Catalytic partial oxidation of ethanol over noble metal catalysts. *Journal of Catalysis* **2005,** *235* (1), 69-78.
95. Guan, G.; Zapf, R.; Kolb, G.; Men, Y.; Hessel, V.; Loewe, H.; Ye, J.; Zentel, R., Low temperature catalytic combustion of propane over Pt-based catalyst with inverse opal microstructure in a microchannel reactor. *Chemical Communications* **2007,** (3), 260-262.
96. Guan, G.; Kusakabe, K.; Taneda, M.; Uehara, M.; Maeda, H., Catalytic combustion of methane over Pd-based catalyst supported on a macroporous alumina layer in a microchannel reactor. *Chemical Engineering Journal* **2008,** *144* (2), 270-276.
97. Geus, J. W.; van Giezen, J. C., Monoliths in catalytic oxidation. *Catalysis Today* **1999,** *47* (1-4), 169-180.
98. Tacchino, S.; Vella, L. D.; Specchia, S., Catalytic combustion of CH4 and H2 into micro-monoliths. *Catalysis Today* **2010,** *In Press, Corrected Proof.*
99. Giani, L.; Groppi, G.; Tronconi, E., Mass-Transfer Characterization of Metallic Foams as Supports for Structured Catalysts. *Industrial & Engineering Chemistry Research* **2005,** *44* (14), 4993-5002.
100. Chen, G.-B.; Chen, C.-P.; Wu, C.-Y.; Chao, Y.-C., Effects of catalytic walls on hydrogen/air combustion inside a micro-tube. *Applied Catalysis A: General* **2007,** *332* (1), 89-97.
101. Kaisare, N. S.; Deshmukh, S. R.; Vlachos, D. G., Stability and performance of catalytic microreactors: Simulations of propane catalytic combustion on Pt. *Chemical Engineering Science* **2008,** *63* (4), 1098-1116.
102. Vican, J.; Gajdeczko, B. F.; Dryer, F. L.; Milius, D. L.; Aksay, I. A.; Yetter, R. A., Development of a microreactor as a thermal source for microelectromechanical systems power generation. *Proceedings of the Combustion Institute* **2002,** *29* (1), 909-916.
103. Won, J. Y.; Jun, H. K.; Jeon, M. K.; Woo, S. I., Performance of microchannel reactor combined with combustor for methanol steam reforming. *Catalysis Today* **2006,** *111* (3-4), 158-163.
104. Hardesty, D. R.; Weinberg, F. J., Burners Producing Large Excess Enthalpies. *Combustion Science and Technology* **1973,** *8* (5), 201 - 214.
105. Ronney, P. D., Analysis of non-adiabatic heat-recirculating combustors. *Combustion and Flame* **2003,** *135* (4), 421-439.
106. Chen, M.; Buckmaster, J., Modelling of combustion and heat transfer in 'Swiss roll' micro-scale combustors. *Combustion Theory and Modelling* **2004,** *8* (4), 701 - 720.
107. Yoshida, K.; Tomonari, S.; Yoshioka, H.; Tanaka, S.; Satoh, D.; Esashi, M. In *High energy density miniature electrical and thermal power source using catalytic combustion of butane*, Micro Electro Mechanical Systems. 17th IEEE International Conference on. (MEMS), 2004; pp 316-321.

108. Mitsos, A.; Chachuat, B. t.; Barton, P. I., Methodology for the Design of Man-Portable Power Generation Devices. *Industrial & Engineering Chemistry Research* **2007,** *46* (22), 7164-7176.
109. Nielsen, O. M.; Massachusetts Institute of Technology. Dept. of Electrical Engineering and Computer Science. A thermally efficient micro-reactor for thermophotovoltaic power generation. Thesis Ph. D. --Massachusetts Institute of Technology Dept. of Electrical Engineering and Computer Science., 2006.
110. Arana, L. R.; Massachusetts Institute of Technology. Dept. of Chemical Engineering. High-temperature microfluidic systems for thermally-efficient fuel processing. Thesis Ph. D. --Massachusetts Institute of Technology Dept. of Chemical Engineering., 2003.
111. O'Malley, A.; Hodnett, B. K., The influence of volatile organic compound structure on conditions required for total oxidation. *Catalysis Today* **1999,** *54* (1), 31-38.
112. Burch, R.; Hayes, M. J., C---H bond activation in hydrocarbon oxidation on solid catalysts. *Journal of Molecular Catalysis A: Chemical* **1995,** *100* (1-3), 13-33.
113. Diehl, F.; Barbier Jr, J.; Duprez, D.; Guibard, I.; Mabilon, G., Catalytic oxidation of heavy hydrocarbons over Pt/Al2O3. Influence of the structure of the molecule on its reactivity. *Applied Catalysis B: Environmental* **2010,** *95* (3-4), 217-227.
114. Rader, C. G.; Weller, S. W., Ignition on catalytic wires: Kinetic parameter determination by the heated-wire technique. *AIChE Journal* **1974,** *20* (3), 515-522.
115. Staicu, O.; Razus, D.; Munteanu, V.; Oancea, D., Heterogeneous catalytic ignition of n-butane/air mixtures on platinum. *Central European Journal of Chemistry* **2009,** *7* (3), 478-485.
116. Yao, Y.-F. Y., Oxidation of Alkanes over Noble Metal Catalysts. *Industrial & Engineering Chemistry Product Research and Development* **1980,** *19* (3), 293-298.
117. Garetto, T. F.; Rincón, E.; Apesteguía, C. R., The origin of the enhanced activity of Pt/zeolites for combustion of C2-C4 alkanes. *Applied Catalysis B: Environmental* **2007,** *73* (1-2), 65-72.
118. Choudhary, T. V.; Banerjee, S.; Choudhary, V. R., Catalysts for combustion of methane and lower alkanes. *Applied Catalysis A: General* **2002,** *234* (1-2), 1-23.
119. Terribile, D.; Trovarelli, A.; de Leitenburg, C.; Primavera, A.; Dolcetti, G., Catalytic combustion of hydrocarbons with Mn and Cu-doped ceria-zirconia solid solutions. *Catalysis Today* **1999,** *47* (1-4), 133-140.
120. Brunelle, J. P., Preparation of catalysts by metallic complex adsorption on mineral oxides. *Pure and Applied Chemistry* **1978,** *50*, 1211-1229.
121. Pinna, F., Supported metal catalysts preparation. *Catalysis Today* **1998,** *41* (1-3), 129-137.
122. Burch, R.; Loader, P. K., Investigation of Pt/Al2O3 and Pd/Al2O3 catalysts for the combustion of methane at low concentrations. *Applied Catalysis B: Environmental* **1994,** *5* (1-2), 149-164.
123. Saracco, G.; Specchia, V., Catalytic combustion of propane in a membrane reactor with separate feed of reactants. IV. Transition from the kinetics- to the transport-controlled regime. *Chemical Engineering Science* **2000,** *55* (18), 3979-3989.

124. Suzuki, Y.; Saito, J.; Kasagi, N., Development of Micro Catalytic Combustor with Pt/Al2O3 Thin Films. *JSME International Journal Series B Fluids and Thermal Engineering* **2004,** *47* (3), 522-527.
125. Nishibori, M.; Shin, W.; Tajima, K.; Houlet, L. F.; Izu, N.; Itoh, T.; Matsubara, I., Long-term stability of Pt/alumina catalyst combustors for micro-gas sensor application. *Journal of the European Ceramic Society* **2008,** *28* (11), 2183-2190.
126. Otto, K.; Andino, J. M.; Parks, C. L., The influence of platinum concentration and particle size on the kinetics of propane oxidation over Pt/[gamma]-alumina. *Journal of Catalysis* **1991,** *131* (1), 243-251.
127. Yoshida, H.; Yazawa, Y.; Hattori, T., Effects of support and additive on oxidation state and activity of Pt catalyst in propane combustion. *Catalysis Today* **2003,** *87* (1-4), 19-28.
128. Yazawa, Y.; Kagi, N.; Komai, S.-i.; Satsuma, A.; Murakami, Y.; Hattori, T., Kinetic study of support effect in the propane combustion over platinum catalyst. *Catalysis Letters* **2001,** *72* (3), 157-160.
129. Gawthrope, D. E.; Lee, A. F.; Wilson, K., Physicochemical properties of Pt-SO4/Al2O3 alkane oxidation catalysts. *Physical Chemistry Chemical Physics* **2004,** *6* (14), 3907-3914.
130. Yazawa, Y.; Yoshida, H.; Komai, S.-i.; Hattori, T., The additive effect on propane combustion over platinum catalyst: control of the oxidation-resistance of platinum by the electronegativity of additives. *Applied Catalysis A: General* **2002,** *233* (1-2), 113-124.
131. Oancea, D.; Staicu, O.; Munteanu, V.; Razus, D., Catalytic Combustion of the Stoichiometric n-Butane/Air Mixture on Isothermally Heated Platinum Wire. *Catalysis Letters* **2008,** *121* (3), 247-254.
132. Maluf, N., *An introduction to microelectromechanical systems engineering*. Artech House: Boston, 2000.
133. Ni, Z.; Seebauer, E. G.; Masel, R. I., Effects of Microreactor Geometry on Performance:â€‰ Differences between Posted Reactors and Channel Reactors. *Industrial & Engineering Chemistry Research* **2005,** *44* (12), 4267-4271.
134. Tomasic, V.; Jovic, F., State-of-the-art in the monolithic catalysts/reactors. *Applied Catalysis A: General* **2006,** *311*, 112-121.
135. Heck, R. M.; Gulati, S.; Farrauto, R. J., The application of monoliths for gas phase catalytic reactions. *Chemical Engineering Journal* **2001,** *82* (1-3), 149-156.
136. Williams, J. L., Monolith structures, materials, properties and uses. *Catalysis Today* **2001,** *69* (1-4), 3-9.
137. Janna, W. S., *Introduction to fluid mechanics*. 4th ed.; CRC Press: Boca Raton, 1993.
138. Kiwi-Minsker, L.; Renken, A., Microstructured reactors for catalytic reactions. *Catalysis Today* **2005,** *110* (1-2), 2-14.
139. Peles, Y.; Srikar, V. T.; Harrison, T. S.; Protz, C.; Mracek, A.; Spearing, S. M., Fluidic packaging of microengine and microrocket devices for high-pressure and high-temperature operation. *Microelectromechanical Systems, Journal of* **2004,** *13* (1), 31-40.

140. Ajmera, S. K.; Delattre, C.; Schmidt, M. A.; Jensen, K. F., Microfabricated Differential Reactor for Heterogeneous Gas Phase Catalyst Testing. *Journal of Catalysis* **2002,** *209* (2), 401-412.
141. Amador, C.; Gavriilidis, A.; Angeli, P., Flow distribution in different microreactor scale-out geometries and the effect of manufacturing tolerances and channel blockage. *Chemical Engineering Journal* **2004,** *101* (1-3), 379-390.
142. Commenge, J. M.; Falk, L.; Corriou, J. P.; Matlosz, M., Optimal design for flow uniformity in microchannel reactors. *AIChE Journal* **2002,** *48* (2), 345-358.
143. Labalme, V.; Garbowski, E.; Guilhaume, N.; Primet, M., Modifications of Pt/alumina combustion catalysts by barium addition II. Properties of aged catalysts. *Applied Catalysis A: General* **1996,** *138* (1), 93-108.
144. Aryafar, M.; Zaera, F., Kinetic study of the catalytic oxidation of alkanes over nickel, palladium, and platinum foils. *Catalysis Letters* **1997,** *48* (3), 173-183.
145. Oancea, D.; Staicu, O.; Munteanu, V., Kinetics of Isothermal Ignition of Lower Alkane/Air Mixtures on Platinum. In *European Combustion Meeting*, 2009.
146. Deshmukh, S. R.; Vlachos, D. G., A reduced mechanism for methane and one-step rate expressions for fuel-lean catalytic combustion of small alkanes on noble metals. *Combustion and Flame* **2007,** *149* (4), 366-383.
147. Chen, G.-B.; Chao, Y.-C.; Chen, C.-P., Enhancement of hydrogen reaction in a micro-channel by catalyst segmentation. *International Journal of Hydrogen Energy* **2008,** *33* (10), 2586-2595.
148. Federici, J. A.; Wetzel, E. D.; Geil, B. R.; Vlachos, D. G., Single channel and heat recirculation catalytic microburners: An experimental and computational fluid dynamics study. *Proceedings of the Combustion Institute* **2009,** *32* (2), 3011-3018.
149. Shakun, W., A Technique for Calculating the Performance of a Two-stage Cascaded Peltier Device Operating between Heat Source and Heat Sink with Finite Heat Transfer Coefficients. *Energy Conversion* **1971,** *11*, 55-61.
150. Rodriguez, A.; Vian, J. G.; Astrain, D.; Martinez, A., Study of thermoelectric systems applied to electric power generation. *Energy Conversion and Management* **2009,** *50*, 1236-1243.
151. Plummer, J. D.; Deal, M.; Griffin, P. B., *Silicon VLSI technology : fundamentals, practice and modeling / James D. Plummer, Michael Deal, Peter B. Griffin*. Prentice Hall: Upper Saddle River, NJ, 2000; p xiv, 817 p.
152. Ayon, A. A.; Braff, R.; Lin, C. C.; Sawin, H. H.; Schmidt, M. A., Characterization of a Time Multiplexed Inductively Coupled Plasma Etcher. *Journal of The Electrochemical Society* **1999,** *146* (1), 339-349.
153. Mehra, A.; Ayon, A. A.; Waitz, I. A.; Schmidt, M. A., Microfabrication of high-temperature silicon devices using wafer bonding and deep reactive ion etching. *Microelectromechanical Systems, Journal of* **1999,** *8* (2), 152-160.
154. Losey, M. W.; Jackman, R. J.; Firebaugh, S. L.; Schmidt, M. A.; Jensen, K. F., Design and fabrication of microfluidic devices for multiphase mixing and reaction. *Microelectromechanical Systems, Journal of* **2002,** *11* (6), 709-717.
155. Marre, S.; Park, J.; Rempel, J.; Guan, J.; Bawendi, M. G.; Jensen, K. F., Supercritical Continuous-Microflow Synthesis of Narrow Size Distribution Quantum Dots. *Advanced Materials* **2008,** *20* (24), 4830-4834.

156. Lei, Y.; et al., A parylene-filled-trench technique for thermal isolation in silicon-based microdevices. *Journal of Micromechanics and Microengineering* **2009,** *19* (3), 035013.
157. Robbins, H.; Schwartz, B., Chemical Etching of Silicon. *Journal of The Electrochemical Society* **1960,** *107* (2), 108-111.
158. Zaborenko, N.; Massachusetts Institute of Technology. Dept. of Chemical Engineering. Continuous-Flow Study and Scale-up of Conventionally Difficult Chemical Processes. Thesis Ph. D. --Massachusetts Institute of Technology Dept. of Chemical Engineering., 2010.
159. Seidel, H.; Csepregi, L.; Heuberger, A.; Baumgartel, H., Anisotropic Etching of Crystalline Silicon in Alkaline Solutions. *Journal of The Electrochemical Society* **1990,** *137* (11), 3612-3626.
160. Peeters, E. Process Development for 3D Silicon Microstructures, with Application to Mechanical Sensor Design. Catholic University of Louvain: Belgium, 1994.
161. Quiram, D. J.; Jensen, K. F.; Schmidt, M. A.; Mills, P. L.; Ryley, J. F.; Wetzel, M. D.; Kraus, D. J., Integrated Microreactor System for Gas-Phase Catalytic Reactions. 1. Scale-up Microreactor Design and Fabrication. *Industrial & Engineering Chemistry Research* **2007,** *46* (25), 8292-8305.
162. Schmidt, M. A., Wafer-to-wafer bonding for microstructure formation. *Proceedings of the IEEE* **1998,** *86* (8), 1575-1585.
163. Klaassen, E. H.; Petersen, K.; Noworolski, J. M.; Logan, J.; Maluf, N. I.; Brown, J.; Storment, C.; McCulley, W.; Kovacs, G. T. A., Silicon fusion bonding and deep reactive ion etching: a new technology for microstructures. *Sensors and Actuators A: Physical* **1996,** *52* (1-3), 132-139.
164. Zaborenko, N.; Murphy, E. R.; Kralj, J. G.; Jensen, K. F., Synthesis and Kinetics of Highly Energetic Intermediates by Micromixers: Direct Multistep Synthesis of Sodium Nitrotetrazolate. *Industrial & Engineering Chemistry Research* **2010,** *49* (9), 4132-4139.
165. Huff, M. A.; Schmidt, M. A. In *Fabrication, packaging, and testing of a wafer-bonded microvalve*, Solid-State Sensor and Actuator Workshop. 5th Technical Digest., IEEE, 1992; pp 194-197.
166. Qin-Yi, T.; Cha, G.; Gafiteanu, R.; Gosele, U., Low temperature wafer direct bonding. *Microelectromechanical Systems, Journal of* **1994,** *3* (1), 29-35.
167. Maszara, W. P.; Jiang, B. L.; Yamada, A.; Rozgonyi, G. A.; Baumgart, H.; de Kock, A. J. R., Role of surface morphology in wafer bonding. *Journal of Applied Physics* **1991,** *69* (1), 257-260.
168. Barth, P. W., Silicon fusion bonding for fabrication of sensors, actuators and microstructures. *Sensors and Actuators A: Physical* **1990,** *23* (1-3), 919-926.
169. Zhou, X.; Virasawmy, S.; Quan, C., Wafer-level BCB bonding using a thermal press for microfluidics. *Microsystem Technologies* **2009,** *15* (4), 573-580.
170. Niklaus, F.; Kumar, R. J.; McMahon, J. J.; Yu, J.; Lu, J. Q.; Cale, T. S.; Gutmann, R. J., Adhesive Wafer Bonding Using Partially Cured Benzocyclobutene for Three-Dimensional Integration. *Journal of The Electrochemical Society* **2006,** *153* (4), G291-G295.

171. Hwang, T.; Popa, D.; Sin, J.; Stephanou, H. E.; Leonard, E. M. In *BCB wafer bonding for microfluidics*, Micromachining and Microfabrication Process Technology IX, San Jose, CA, USA, SPIE: San Jose, CA, USA, 2004; pp 182-191.
172. Choi, Y.-S.; Park, J.-S.; Park, H.-D.; Song, Y.-H.; Jung, J.-S.; Kang, S.-G., Effects of temperatures on microstructures and bonding strengths of Si-Si bonding using bisbenzocyclobutene. *Sensors and Actuators A: Physical* **2003,** *108* (1-3), 201-205.
173. Tsau, C. H.; Spearing, S. M.; Schmidt, M. A., Fabrication of wafer-level thermocompression bonds. *Microelectromechanical Systems, Journal of* **2002,** *11* (6), 641-647.
174. Tsau, C. H.; Massachusetts Institute of Technology. Dept. of Materials Science and Engineering. Fabrication and characterization of wafer-level gold thermocompression bonding. Thesis Ph. D. --Massachusetts Institute of Technology Dept. of Materials Science and Engineering., 2003.
175. Olesinski, R.; Abbaschian, G., The Cu-Si (Copper -Silicon) system. *Journal of Phase Equilibria* **1986,** *7* (2), 170-178.
176. Hymes, S.; Kumar, K. S.; Murarka, S. P.; Ding, P. J.; Wang, W.; Lanford, W. A., Thermal stability of copper silicide passivation layers in copper-based multilevel interconnects. *Journal of Applied Physics* **1998,** *83* (8), 4507-4512.
177. Chang, C.; x; An, Formation of copper silicides from Cu(100)/Si(100) and Cu(111)/Si(111) structures. *Journal of Applied Physics* **1990,** *67* (1), 566-569.
178. Seibt, M.; Hedemann, H.; Istratov, A. A.; Riedel, F.; Sattler, A.; Schröter, W., Structural and Electrical Properties of Metal Silicide Precipitates in Silicon. *physica status solidi (a)* **1999,** *171* (1), 301-310.
179. Chromik, R. R.; Neils, W. K.; Cotts, E. J., Thermodynamic and kinetic study of solid state reactions in the Cu--Si system. *Journal of Applied Physics* **1999,** *86* (8), 4273-4281.
180. Reid, J. S.; Sun, X.; Kolawa, E.; Nicolet, M. A., Ti-Si-N diffusion barriers between silicon and copper. *Electron Device Letters, IEEE* **1994,** *15* (8), 298-300.
181. Knitter, R.; Liauw, M. A., Ceramic microreactors for heterogeneously catalysed gas-phase reactions. *Lab on a Chip* **2004,** *4* (4), 378-383.
182. Meille, V., Review on methods to deposit catalysts on structured surfaces. *Applied Catalysis A: General* **2006,** *315*, 1-17.
183. Nijhuis, T. A.; Beers, A. E. W.; Vergunst, T.; Hoek, I.; Kapteijn, F.; Moulijn, J. A., Preparation of monolithic catalysts. *Catalysis Reviews: Science and Engineering* **2001,** *43* (4), 345 - 380.
184. Vengallatore, S.; Peles, Y.; Arana, L. R.; Spearing, S. M., Self-assembly of micro- and nanoparticles on internal micromachined silicon surfaces. *Sensors and Actuators A: Physical* **2004,** *113* (1), 124-131.
185. Hwang, S.-M.; Kwon, O. J.; Kim, J. J., Method of catalyst coating in micro-reactors for methanol steam reforming. *Applied Catalysis A: General* **2007,** *316* (1), 83-89.
186. Kwon, O. J.; Hwang, S.-M.; Ahn, J.-G.; Kim, J. J., Silicon-based miniaturized-reformer for portable fuel cell applications. *Journal of Power Sources* **2006,** *156* (2), 253-259.

187. Kwon, O. J.; Hwang, S.-M.; Song, I. K.; Lee, H.-I.; Kim, J. J., A silicon-based miniaturized reformer for high power electric devices. *Chemical Engineering Journal* **2007,** *133* (1-3), 157-163.
188. Gonzalez-Velasco, J. R.; Gutierrez-Ortiz, M. A.; Marc, J. L.; Botas, J. A.; Gonzalez-Marcos, M. P.; Blanchard, G., Pt/Ce0.68Zr0.32O2 Washcoated Monoliths for Automotive Emission Control. *Industrial & Engineering Chemistry Research* **2002,** *42* (2), 311-317.
189. Bravo, J.; Karim, A.; Conant, T.; Lopez, G. P.; Datye, A., Wall coating of a CuO/ZnO/Al2O3 methanol steam reforming catalyst for micro-channel reformers. *Chemical Engineering Journal* **2004,** *101* (1-3), 113-121.
190. Beers, A. E. W.; Nijhuis, T. A.; Kapteijn, F.; Moulijn, J. A., Zeolite coated structures for the acylation of aromatics. *Microporous and Mesoporous Materials* **2001,** *48* (1-3), 279-284.
191. Valentini, M.; Groppi, G.; Cristiani, C.; Levi, M.; Tronconi, E.; Forzatti, P., The deposition of [gamma]-Al2O3 layers on ceramic and metallic supports for the preparation of structured catalysts. *Catalysis Today* **2001,** *69* (1-4), 307-314.
192. Roumanie, M.; Pijolat, C.; Meille, V.; De Bellefon, C.; Pouteau, P.; Delattre, C., Deposition of Pt-catalyst in a micro-channel of a silicon reactor: Application to gas micro-TAS working at high temperature. *Sensors and Actuators B: Chemical* **2006,** *118* (1-2), 297-304.
193. Agrafiotis, C.; Tsetsekou, A.; Ekonomakou, A., The effect of particle size on the adhesion properties of oxide washcoats on cordierite honeycombs. *Journal of Materials Science Letters* **1999,** *18* (17), 1421-1424.
194. Agrafiotis, C.; Tsetsekou, A., The effect of powder characteristics on washcoat quality. Part I: Alumina washcoats. *Journal of the European Ceramic Society* **2000,** *20* (7), 815-824.
195. Blachou, V.; Goula, D.; Philippopoulos, C., Wet milling of alumina and preparation of slurries for monolithic structures impregnation. *Industrial & Engineering Chemistry Research* **1992,** *31* (1), 364-369.
196. Cristiani, C.; Valentini, M.; Merazzi, M.; Neglia, S.; Forzatti, P., Effect of ageing time on chemical and rheological evolution in [gamma]-Al2O3 slurries for dip-coating. *Catalysis Today* **2005,** *105* (3-4), 492-498.
197. Meille, V.; Pallier, S.; Rodriguez, P., Reproducibility in the preparation of alumina slurries for washcoat application--Role of temperature and particle size distribution. *Colloids and Surfaces A: Physicochemical and Engineering Aspects* **2009,** *336* (1-3), 104-109.
198. Meille, V.; Pallier, S.; Santa Cruz Bustamante, G. V.; Roumanie, M.; Reymond, J.-P., Deposition of -Al2O3 layers on structured supports for the design of new catalytic reactors. *Applied Catalysis A: General* **2005,** *286* (2), 232-238.
199. Evanko, C. R.; Dzombak, D. A.; Novak, J. W., Influence of surfactant addition on the stability of concentrated alumina dispersions in water. *Colloids and Surfaces A: Physicochemical and Engineering Aspects* **1996,** *110* (3), 219-233.
200. Thomas, R. R.; Kaufman, F. B.; Kirleis, J. T.; Belsky, R. A., Wettability of Polished Silicon Oxide Surfaces. *Journal of The Electrochemical Society* **1996,** *143* (2), 643-648.

201. Agrafiotis, C.; Tsetsekou, A.; Leon, I., Effect of Slurry Rheological Properties on the Coating of Ceramic Honeycombs with Yttria-Stabilized-Zirconia Washcoats. *Journal of the American Ceramic Society* **2000,** *83* (5), 1033-1038.
202. Haldeman, G., Personal communication with Dr. George Haldeman regarding appropriate compression with Belleville washers. 2008.
203. Fogler, H. S., *Elements of chemical reaction engineering*. 3rd ed.; Prentice Hall PTR: Upper Saddle River, N.J., 1999.
204. Seshadri, V.; Kaisare, N. S., Simulation of hydrogen and hydrogen-assisted propane ignition in pt catalyzed microchannel. *Combustion and Flame* **2010,** *In Press, Corrected Proof*.
205. Deutschmann, O.; Maier, L. I.; Riedel, U.; Stroemman, A. H.; Dibble, R. W., Hydrogen assisted catalytic combustion of methane on platinum. *Catalysis Today* **2000,** *59* (1-2), 141-150.
206. Zhong, B.-J.; Yang, Q.-T.; Yang, F., Hydrogen-assisted catalytic ignition characteristics of different fuels. *Combustion and Flame* **2010,** *157* (10), 2005-2007.
207. Seshadri, V.; Kaisare, N. S. In *Simulation of Ignition Characteristics of Various Fuels in a Catalytic Microreactor*, European Combustion Meeting, 2009.
208. Perry, R. H.; Green, D. W.; Maloney, J. O., *Perry's Chemical engineers' handbook*. 6th ed.; McGraw-Hill: New York, 1984.
209. Butane Mass Spectrum. http://webbook.nist.gov/cgi/cbook.cgi?ID=C106978&Mask=200 (accessed 06/06/2010).
210. Bass, J. C., Vice President, Hi-Z Technology, Inc. 2010; pp Personal Communication of fourth-order property equations for Hi-Z thermoelectric materials.
211. Chunbo, Z.; Khalil, N., Fabrication of thick silicon dioxide layers for thermal isolation. *Journal of Micromechanics and Microengineering* **2004,** *14* (6), 769.

10. Appendix A: Fabrication Process

All reactors were fabricated in the Microsystems Technology Laboratories at MIT. The "Machine" name corresponds to the identifier used in the MTL "Coral" scheduling system. The cleanliness code describes the compatibility of the process step, where brown is CMOS compatible, green indicates metal-free silicon processing, yellow is KOH etch or Pyrex® compatible, and red is for gold and III-V metals general processing. In the following sections, please note that the masks may not be actual size, but are to scale. The horizontal boxes at the bottom of each mask, for alignment with the wafer flat, are 6 cm in length in the actual mask.

10.1. Final Two-Wafer Stack Design

The final combustors used in this work were fabricated from two silicon wafers with flats cut to the <100> direction. Identical "frontside" masks with channel features were used for both wafers, as shown in Figure 10-1. The "backside" mask with alignment and diesaw marks is shown in Figure 10-2.

Project Name: 2-Wafer Stack Combustors

Start date: **Christopher Marton**
Process Users:

General process: Start with bare Si wafers, and deposit oxide and nitride. LAM-etch half the nitride coating from one half (frontside). Coat both sides of the wafer with resist. Pattern the channels on the frontside and alignment marks on the backside. LAM-etch the nitride, BOE-etch the oxide to expose the silicon. Then, KOH etch the silicon wafer to create flow channels and marks. Remove the nitride and oxide from the frontside using H3PO4 and then HF. Next, fusion bond the top and bottom wafers to seal the flow channels. Finally, diesaw the devices.

Starting material: 2 6-inch, 1mm thick, Double Side Polished Silicon Wafers

STEP	DATE	FAC	# WAFS	MACHINE	ACTION	NOTES	CODE
1					**DEPOSIT THERMAL OXIDE**		
1.1		ICL	1,2	RCA	RCA clean wafers		Br
1.2		ICL	1,2	5C	Deposit 400nm Thermal (wet) Oxide both sides of wafers		Br
2					**DEPOSIT NITRIDE LAYER**		
2.1		ICL	1,2	RCA	RCA clean wafers for CVD		Br
2.2		ICL	1,2	VTR	Deposit 400nm VTR SiN on both sides of wafers		Br
3					**PATTERN CHANNELS AND ALIGNMENT MARKS**		
3.1		TRL	1,2	HMDS	Coat wafer with HMDS		G
3.2		TRL	1,2	coater	Spincoat OCG 825 on the backside to define ports		G
3.3		TRL	1,2	prebake	Bake at 95°C for 15 minutes		G
3.4		TRL	1,2	coater	Spincoat OCG 825 on the frontside to define channels		G
4.5		TRL	1,2	prebake	Bake at 95°C for 25 minutes		G
3.6		TRL	1,2	EV1	Expose backside for 2 seconds (backside mask)		G
3.7		TRL	1,2	photowet-1	Develop OCG 934 1:1, 7 seconds		G
3.8		TRL	1,2	EV1	Expose frontside for 2 seconds (channel mask)		G
3.9		TRL	1,2	photowet-1	Develop OCG 934 1:1, 1-3 minutes		G
3.10		TRL	1,2	postbake	Postbake at 120°C for 30 minutes		G
3.11		ICL	1,2	LAM-490B	Etch exposed nitride (nitride on Ox)		G
3.12		ICL	1,2	oxEtch-BOE	BOE exposed oxide		G
3.13		TRL	1,2	acidhood	piranha clean wafer		G
5					**ETCH CHANNELS AND ALIGNMENT MARKS**		
		ICL	1,2	TMAH-KOH hood	25%, 80°C KOH etch wafer to ~500 um (~6.5 hr)		Y
5.1		TRL	1,2	acidhood	post KOH clean (2 piranhas)		G
5.2		ICL	1,2	hot phos	180C H3PO4-etch Nitride from wafers (40 A/min etch rate for VTR Nitride, ~100 min + overetch)		G
5.3		TRL	1,2	acidhood	49% HF-etch oxide from wafers		G
6					**BOND WAFERS**		
6.1		TRL	1,2	RCA-TRL	RCA clean wafers		Br
6.2		TRL	1,2	EV620	Align wafers for bonding		Br
6.3		TRL	1,2	EV501	Fusion Bond Wafers		Br

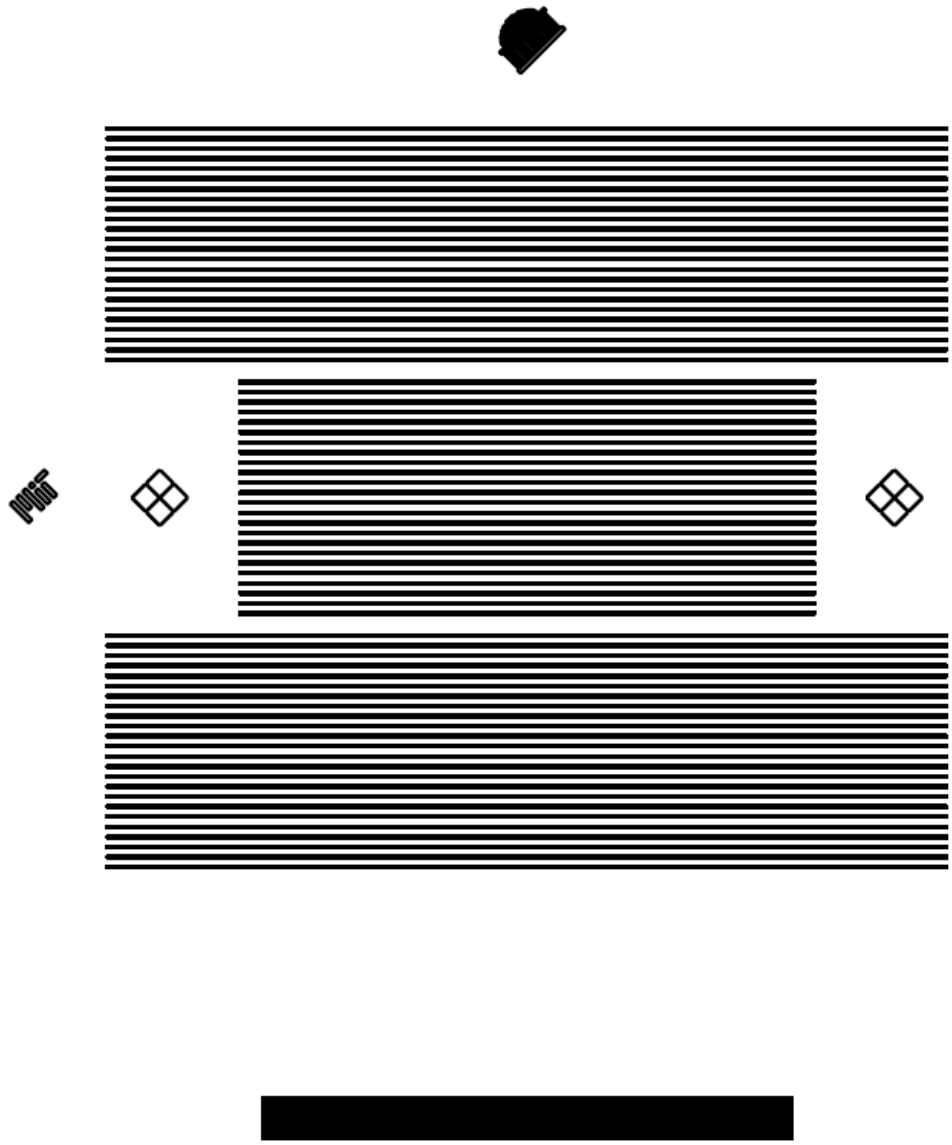

Figure 10-1: Frontside channel mask for 2-wafer stack combustors.

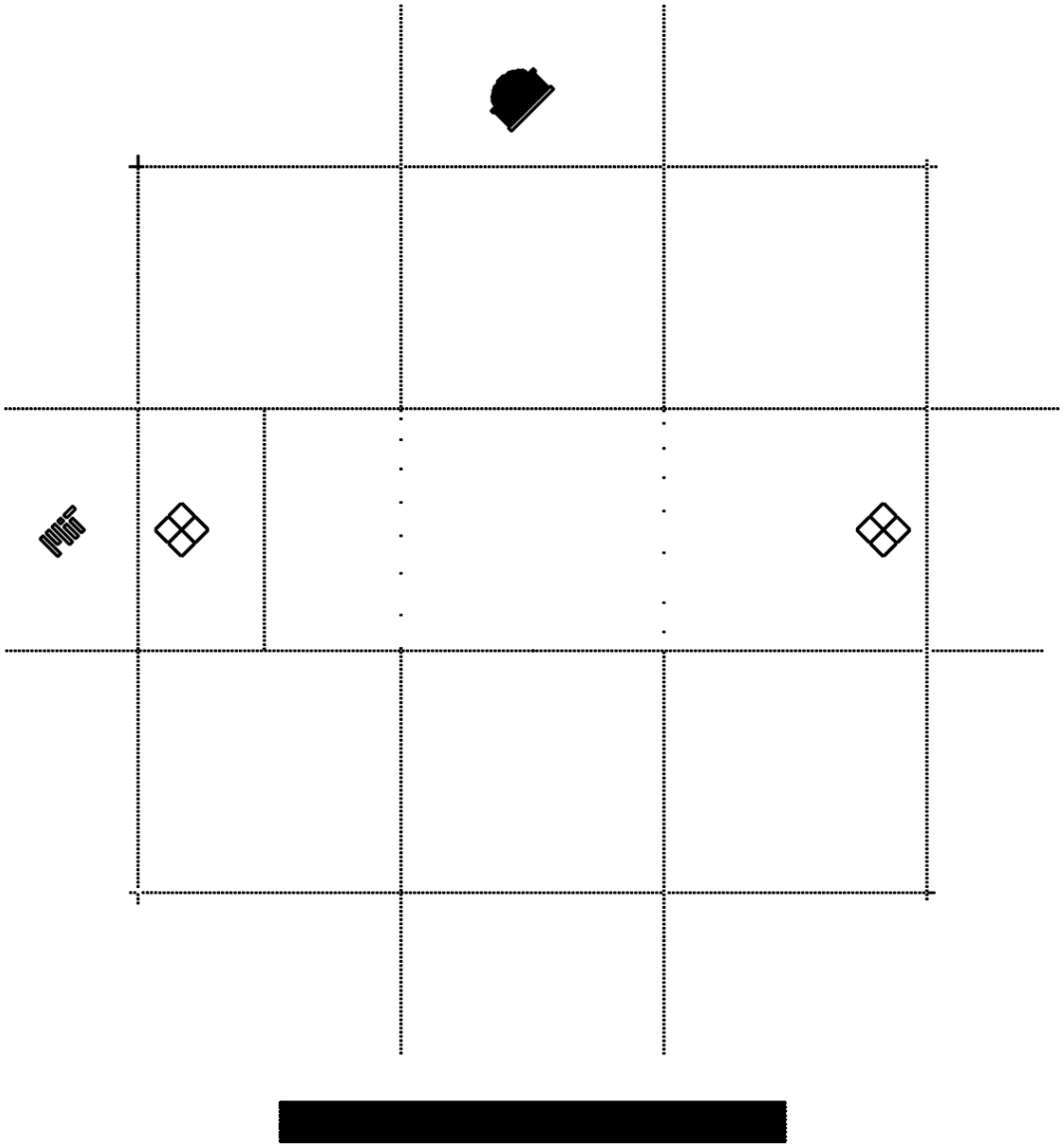

Figure 10-2: Backside mask for 2-wafer stack combustors.

10.2. Original Four-Wafer Stack Process

The original four-wafer stack process involved selective deprotection of the silicon bonding faces for the formation of two-wafer stacks, and subsequently the two stacks were to be bonded together. As described in chapter 4, this process was not successful due to issues with silicon nitride strands released in the KOH etch protecting the silicon nitride to be removed. This process was performed with wafers with the flat cut to the <110> crystal plane, and two different frontside and backside masks were used. The frontside masks A and B are shown in Figure 10-3 and Figure 10-4, respectively, and the backside masks for wafers A and B are shown in Figure 10-5 and Figure 10-6, respectively.

Project Name: 4-Wafer Stack Combustors
Start date:
Process Lead: **Christopher Marton**
Process Users:

General process: Start with bare Si wafers, and deposit oxide and nitride. LAM-etch half the nitride coating from one half (frontside). Coat both sides of the wafer with resist. Pattern the channels on the frontside and alignment marks on the backside. LAM-etch the nitride, BOE-etch the oxide to expose the silicon. Then, KOH etch the silicon wafer to create flow channels and marks. Remove the nitride and oxide from the frontside using HF. Next, fusion bond the top and bottom wafers to seal the flow channels. Remove the rest of the nitride and oxide from the backside using HF. Then fusion bond the two, two-wafer stacks together to form a four-wafer stack. Finally, diesaw the devices.

Starting material: 4 6-inch, 1mm thick, Double Side Polished Silicon Wafers

STEP	DATE	FAC	# WAFS	MACHINE	ACTION	NOTES	CODE
1					**DEPOSIT THERMAL OXIDE**		
1.1		ICL	1,2,3,4	RCA	RCA clean wafers		Br
1.2		ICL	1,2,3,4	5C	Deposit 400nm Thermal (wet) Oxide both sides of wafers		Br
2					**DEPOSIT NITRIDE LAYER**		
2.1		ICL	1,2,3,4	RCA	RCA clean wafers for CVD		Br
2.2		ICL	1,2,3,4	VTR	Deposit 400nm VTR SiN on both sides of wafers		Br
3					**REMOVE HALF OF FRONTSIDE NITRIDE LAYER**		
3.1		ICL	1,2,3,4	LAM490B	Remove 200nm VTR SiN layer from frontside of wafers only		G
4					**PATTERN CHANNELS AND ALIGNMENT MARKS**		
4.1		TRL	1,2,3,4	HMDS	Coat wafer with HMDS		G
4.2		TRL	1,2,3,4	coater	Spincoat OCG 825 on the backside to define ports		G
4.3		TRL	1,2,3,4	prebake	Bake at 95°C for 15 minutes		G
4.4		TRL	1,2,3,4	coater	Spincoat OCG 825 on the frontside to define channels		G
4.5		TRL	1,2,3,4	prebake	Bake at 95°C for 25 minutes		G
4.6		TRL	1,2,3,4	EV1	Expose backside for 2 seconds (backside mask)		G
4.7		TRL	1,2,3,4	photowet-1	Develop OCG 934 1:1, 7 seconds		G
4.8		TRL	1,2,3,4	EV1	Expose frontside for 2 seconds (channel mask)		G
4.9		TRL	1,2,3,4	photowet-1	Develop OCG 934 1:1, 1-3 minutes		G
4.10		TRL	1,2,3,4	postbake	Postbake at 120°C for 30 minutes		G
4.11		ICL	1,2,3,4	LAM-490B	Etch exposed nitride (nitride on Ox)		G
4.12		ICL	1,2,3,4	oxEtch-BOE	BOE exposed oxide		G
4.13		TRL	1,2,3,4	acidhood	piranha clean wafer		G
5					**ETCH CHANNELS AND ALIGNMENT MARKS**		
5.1		ICL	1,2,3,4	TMAH-KOH hood	20%, 80°C KOH etch wafer to ~500 um (~6.5 hr)		Y
5.2		TRL	1,2,3,4	acidhood	post KOH clean (2 piranhas)		G
5.3		TRL	1,2,3,4	acidhood2	49% HF-etch Nitride and oxide from frontside of wafers (40 min - only partial nitride removal from backside)		G
6					**BOND WAFERS**		
6.1		TRL	1,2,3,4	RCA-TRL	RCA clean wafers		Br
6.2		TRL	1-2, 3-4	EV620	Align wafers for bonding		Br
6,3		TRL	1-2, 3-4	EV501	Fusion Bond Wafers		Br
6.4		TRL	1-2, 3-4	tube B3	Anneal at 1000C for 1 hour		G
7					**BOND WAFER STACKS**		
7.1		TRL	1-2, 3-4	acidhood	Backside nitride and oxide removal (49% HF, ~40min)		G
7.2		TRL	1-2, 3-4	RCA-TRL	RCA clean wafers		Br
7.3		TRL	(1-2) - (3-4)	EV620	Align wafers for bonding		Br
7.4		TRL	(1-2) - (3-4)	EV501	Fusion Bond Wafers		Br
7.5		TRL	(1-2) - (3-4)	tube B3	Anneal at 1000C for 1 hour		G
8		ICL		diesaw	**DIESAW DEVICES**		

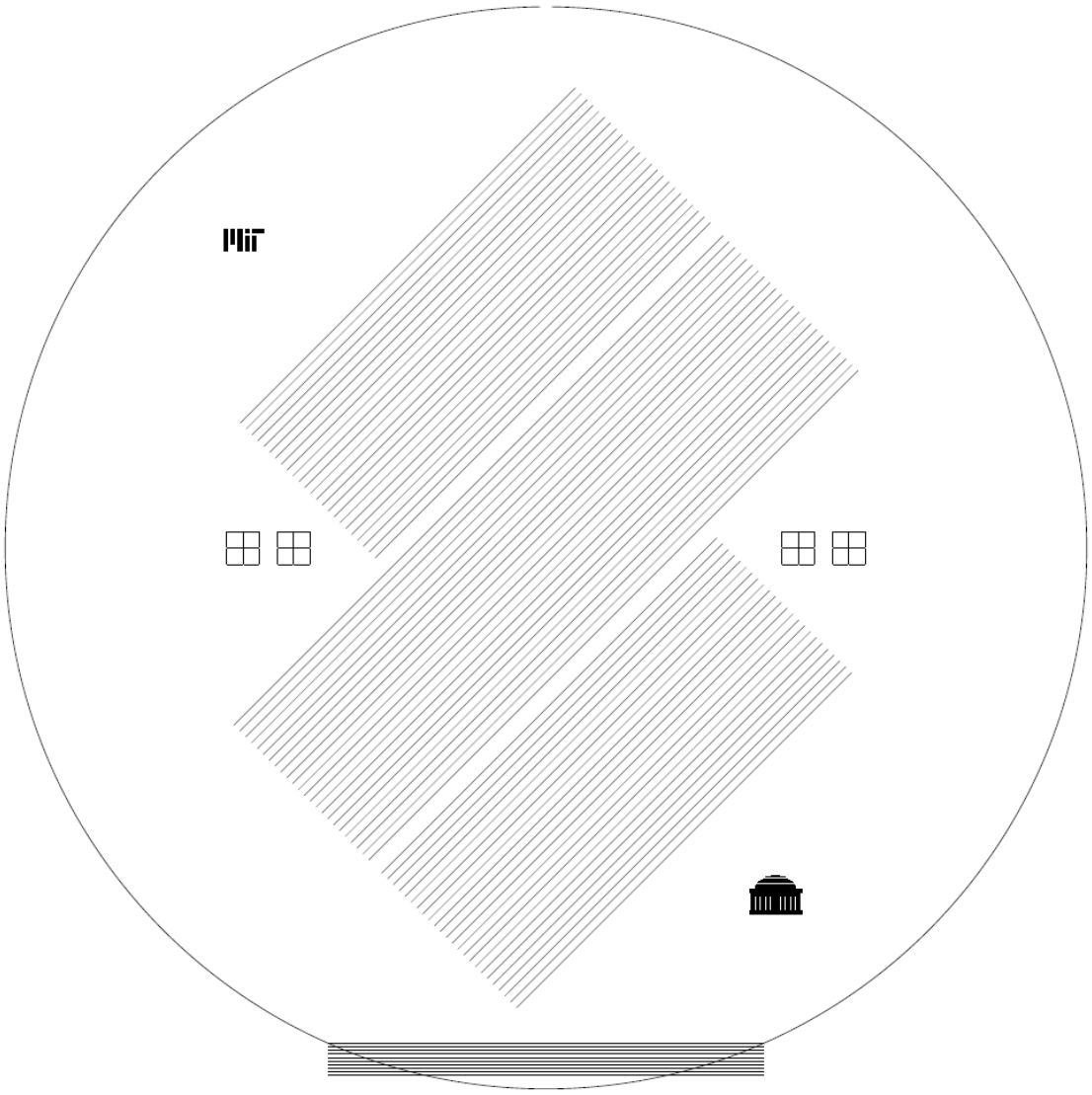

Figure 10-3: Four-wafer stacked combustor frontside mask "A".

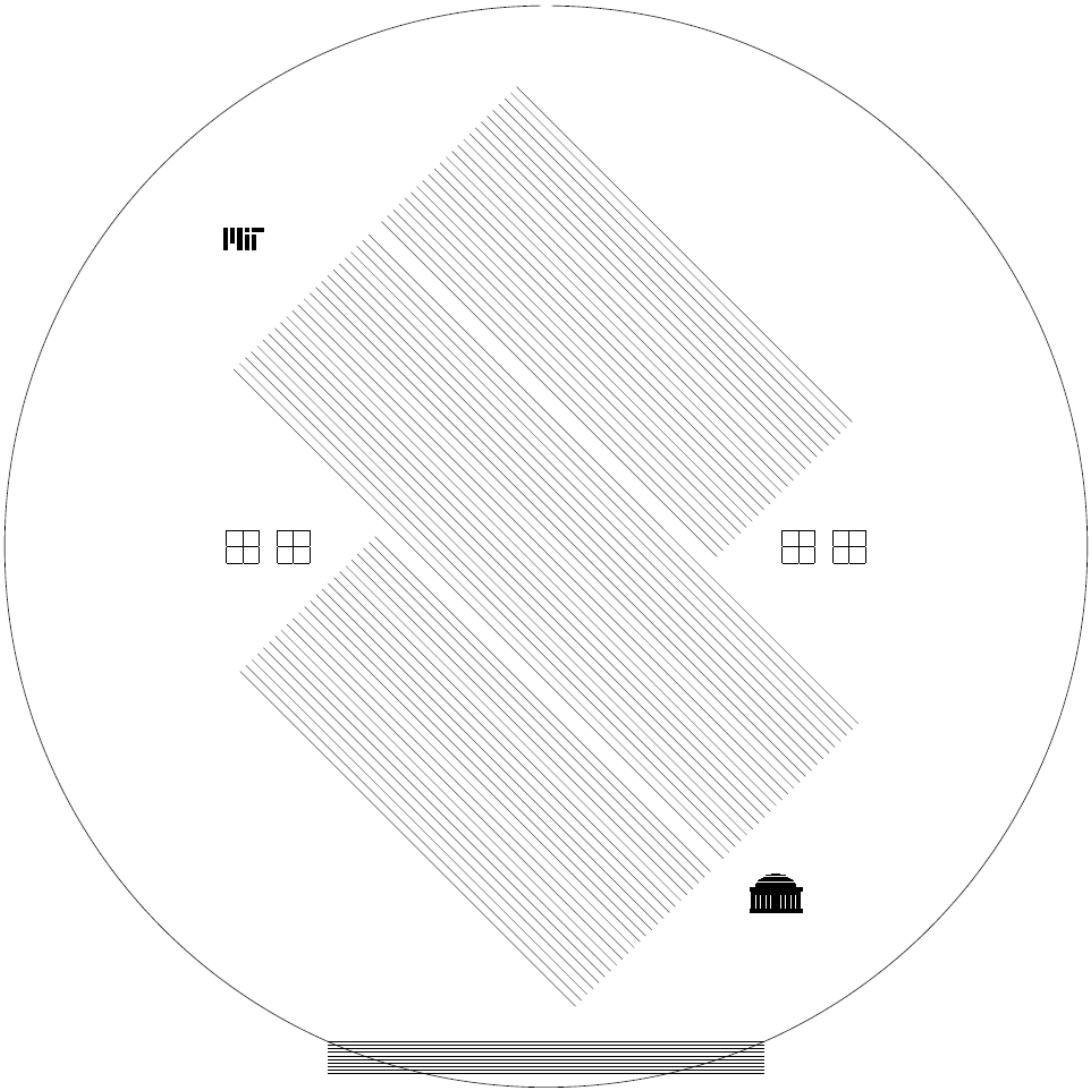

Figure 10-4: Four-wafer stacked combustor frontside mask "B".

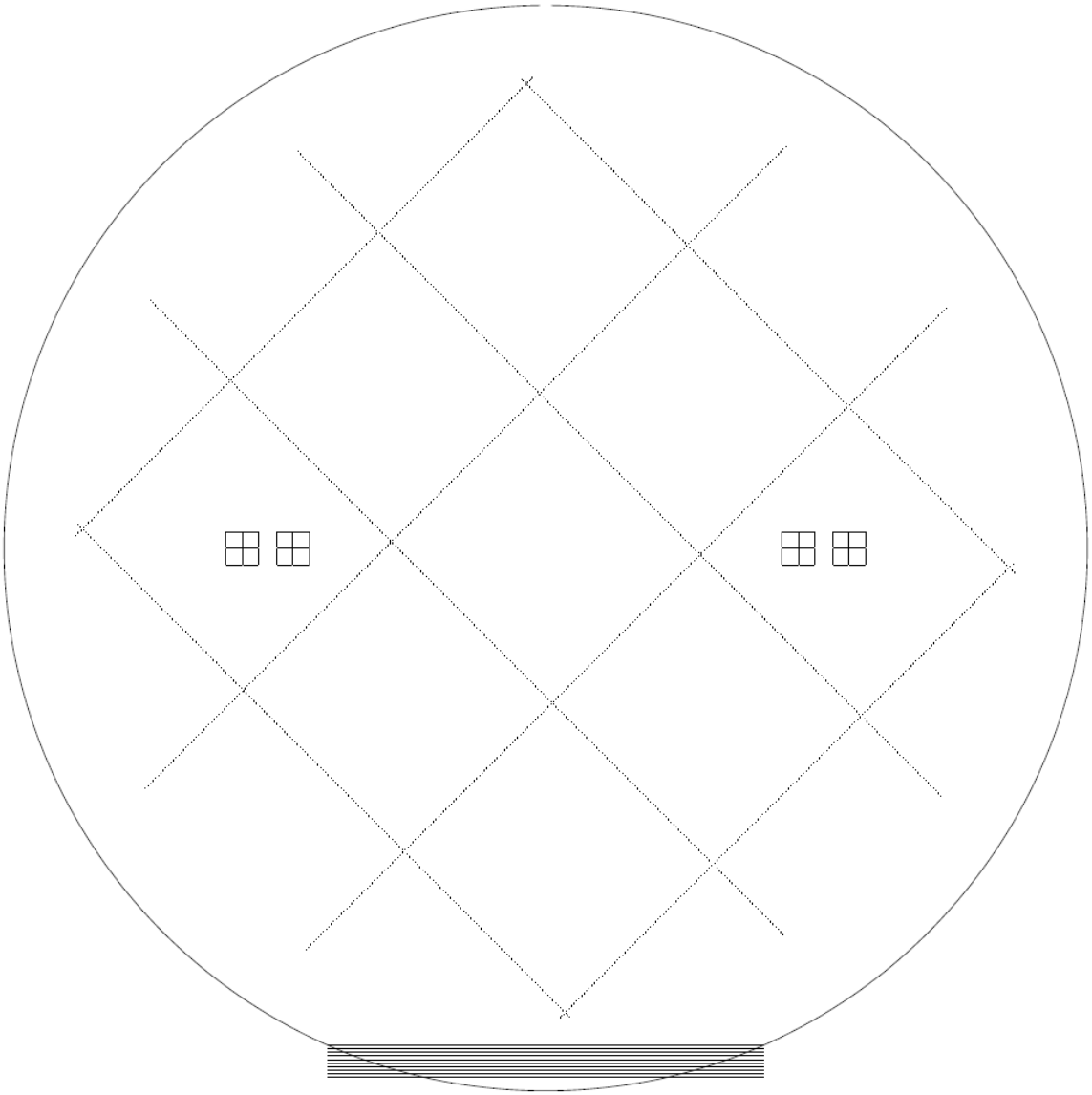

Figure 10-5: Four-wafer stacked combustors backside mask "A".

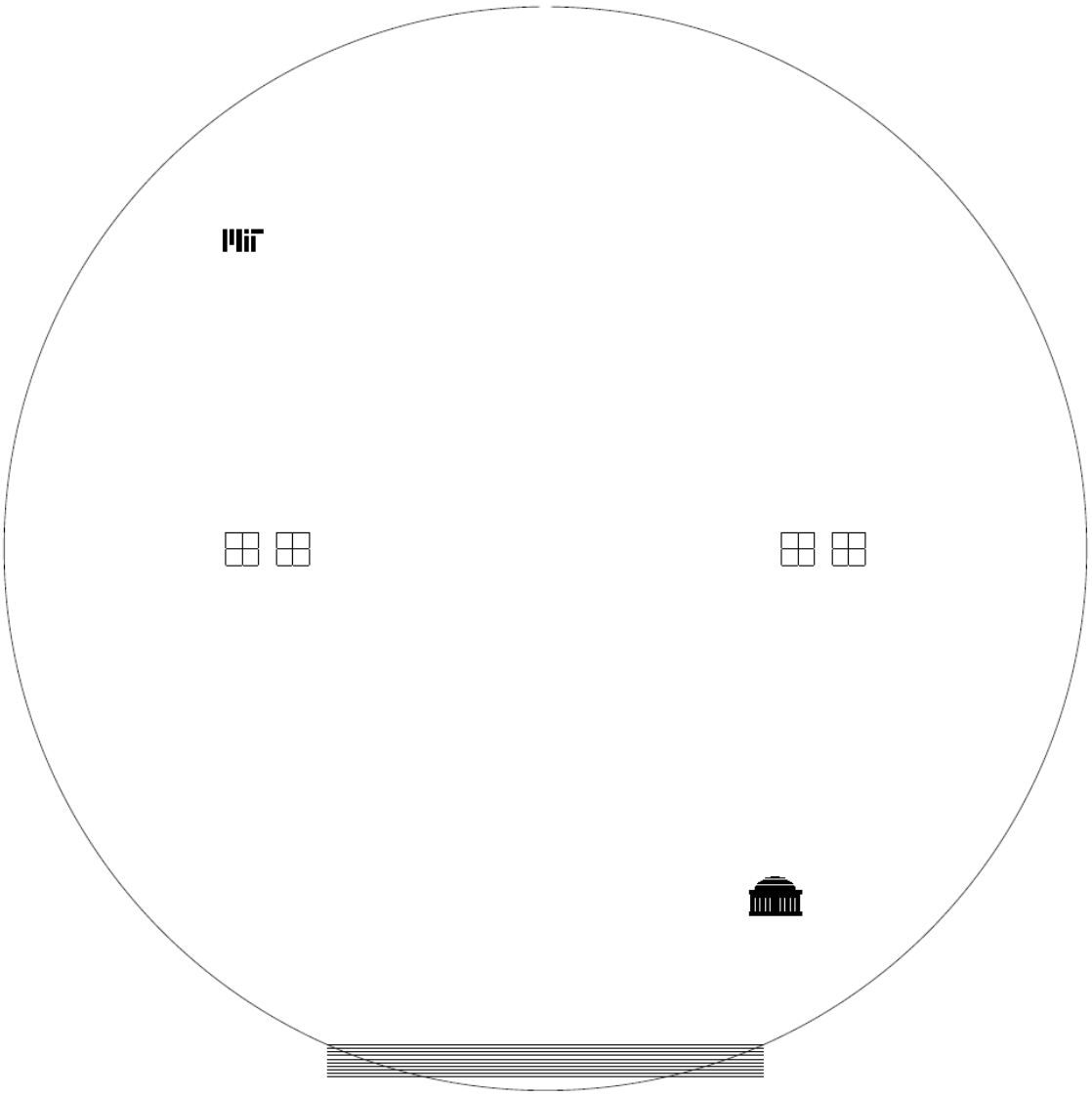

Figure 10-6: Four-wafer stacked combustors backside "B".